

LAL 11-299  
December 2011

# Université Paris-sud 11

## THÈSE

présentée pour obtenir le grade de

Docteur ès Sciences de l'Université Paris-Sud 11

Spécialité : physique des particules

par

**Leonid BURMISTROV**

**A detector for charged particle identification  
in the forward region of *SuperB***

**Un détecteur pour l'identification des  
particules chargées dans la région avant de  
*SuperB***

Soutenue le 9 december 2011 devant le Jury composé de :

M.	N. Arnaud	Examinateur
M.	O. Bezshyyko	Rapporteur
M.	D. Breton	Examinateur
M.	J. S. Real	Examinateur
M.	P. Schune	Examinateur
M.	L. Serin	Président du Jury
M.	A. Stocchi	Directeur de thèse
M.	J. Va'vra	Rapporteur



# Contents

<b>1</b>	<b>Introduction</b>	<b>11</b>
<b>2</b>	<b>The <i>SuperB</i> experiment</b>	<b>15</b>
2.1	The Standard Model of the elementary particles . . . . .	15
2.1.1	Conservation laws and symmetries . . . . .	17
2.1.2	The CKM Matrix and the source of the $CP$ -violation . . . . .	18
2.1.3	The Unitarity Triangle . . . . .	19
2.1.4	B-factories . . . . .	20
2.1.5	State of the art in the B-physics . . . . .	21
2.2	Accelerator . . . . .	23
2.2.1	Luminosity and the "crabbed waist" beam crossing schemes . . . . .	24
2.3	The <i>SuperB</i> Detector . . . . .	25
2.3.1	The Silicon Vertex Tracker . . . . .	28
2.3.2	The Drift Chamber . . . . .	29
2.3.3	The Electromagnetic Calorimeter . . . . .	30
2.3.4	The Instrumented Flux Return . . . . .	33
2.3.5	Particle Identification system . . . . .	34
<b>3</b>	<b>The DIRC-like TOF detector</b>	<b>39</b>
3.1	The time-of-flight technique . . . . .	39
3.2	The DIRC-like TOF detector . . . . .	42
3.3	Time resolution of the DIRC-like TOF detector . . . . .	44

3.4	Study of $\sigma_{\text{trk}}$	45
3.5	Study of $\sigma_{\text{detector}}$ and geometry optimization	51
3.5.1	Geant4 - the full simulation tool for particle physics.	51
3.5.2	Standard simulated processes for charged tracks and $\gamma's$	52
3.5.3	Cherenkov light propagation and propagation in quartz	52
3.5.4	Simulation of the PMT response	58
3.5.5	$\sigma_{\text{chromaticity}}$ and $\sigma_{\text{transit}}$ production	59
3.5.6	Geometry optimization	62
3.5.7	Comparison of time versus channel distributions for DIRC-like TOF configurations with and without photon absorber	80
3.5.8	Recommended geometries for the DIRC-like TOF detector	81
3.6	Mechanical installation and readout electronics	84
<b>4</b>	<b><i>SuperB-related background studies</i></b>	<b>87</b>
4.1	Introduction and overview of the <i>SuperB</i> backgrounds	87
4.2	Full simulation of <i>SuperB</i> : the Bruno software	88
4.2.1	Introduction	88
4.2.2	Geometry description	88
4.2.3	Simulation I/O	89
4.2.4	Implementation of the DIRC-like TOF detector into Bruno	89
4.3	$e^+e^-$ annihilation into anything but electron(s)-positron(s)	91
4.4	$e^+e^-$ pair production	92
4.5	Elastic Bhabha background in the DIRC-like TOF detector	93
4.6	Radiative Bhabha	95
4.6.1	Introduction	95
4.6.2	Impact of the radiative Bhabha background on the DIRC-like TOF detector	97
4.6.3	Background production of light in the DIRC-like TOF	99
4.6.4	Method to estimate the light background rate in the DIRC-like TOF photodetectors	100

4.6.5	Absorbed dose by the DIRC-like TOF and its front-end electronics	102
4.7	Touschek effect	104
4.8	Summary of the DIRC-like TOF detector background analysis	109
4.9	Studying of the Touschek background at DAΦNE $e^- e^+$ collider	111
4.9.1	Upgrading the DAΦNE $\phi$ -factory	111
4.9.2	Geant4 simulation of the modified DAΦNE interaction region	114
4.9.3	Touschek generator	116
4.9.4	Calibration of the low-angle photon detectors	118
4.9.5	Background rate measurement and comparison with simulation	118
<b>5</b>	<b>Test of the DIRC-like TOF prototype at SLAC CRT</b>	<b>121</b>
5.1	Experimental setup	121
5.1.1	Cosmic Ray Telescope	122
5.1.2	DIRC-like TOF prototype	129
5.1.3	Readout electronics and data acquisition software	133
5.2	Waveform analysis	141
5.3	Laser tests of the DIRC-like TOF prototype	147
5.4	Full simulation of the DIRC-like TOF prototype	151
5.4.1	Waveform and PMT response simulation	154
5.4.2	Cosmic muon generator	164
5.4.3	Simulation results	166
5.5	Measurements	175
5.5.1	CRT and USBWC DAQs merging	175
5.5.2	Summary of data taking	179
5.5.3	Comparison between runs without and with photon absorber	181
5.5.4	Measurements of the DIRC-like TOF prototype time resolution	181
5.6	Conclusions	201
<b>6</b>	<b>Selection of a photodetector for DIRC-like TOF detector</b>	<b>203</b>

6.1	Introduction . . . . .	203
6.2	Experimental setup . . . . .	203
6.3	Measurements . . . . .	208
6.3.1	Burle MCP-PMT . . . . .	208
6.3.2	Hamamatsu MCP-PMT . . . . .	213
6.3.3	SiPM . . . . .	213
6.4	Conclusions . . . . .	215
<b>7</b>	<b>Conclusions</b>	<b>217</b>
	<b>References</b>	<b>219</b>
<b>8</b>	<b>Likelihood based particle selector</b>	<b>229</b>
	<b>Acknowledgements</b>	<b>233</b>

# Résumé

Dans cette thèse nous présentons la conception, l'étude des performances et les premiers tests, effectués au Cosmic Ray Telescope situé au SLAC, d'un nouveau détecteur d'identification des particules émises dans la région "avant" du détecteur *SuperB*.

Ce détecteur est basé sur une technique de mesure du temps de vol (TOF). Pour identifier les particules avec une impulsion jusqu'à 3 GeV/c et une distance de vol de l'ordre de deux mètres nous avons besoin d'un détecteur TOF capable de mesurer le temps avec une précision typique de 30 ps. Pour atteindre cet objectif nous avons conçu un appareillage pour lequel le passage d'une particule chargée produit de la lumière Cherenkov dans une tuile en quartz qui est ensuite détectée par des photodétecteurs très rapides et une électronique rapide dédiée. Nous l'appelons le détecteur "DIRC-like TOF".

Les photodétecteurs HAMAMATSU SL-10 MCP-PMT ont été caractérisés au LAL et une résolution en temps d'environ 37 ps a été mesurée. La nouvelle électronique 16-canaux USB WaveCatcher développée au LAL(CNRS/IN2P3) et au CEA/IRFU montre un jitter de moins de 10 ps. La géométrie du détecteur à quartz a été étudiée avec une attention particulière à l'aide d'une simulation Geant4. Celle-ci montre que la meilleure géométrie permet d'atteindre une résolution en temps d'environ 90 ps par photoélectron avec au moins 10 photoélectrons détectés, donnant donc en moyenne la résolution totale désirée de 30 ps.

Nous avons construit un prototype d'un tel détecteur, avec des barres de quartz de réserve de l'expérience *BaBar* et nous l'avons installé dans le Cosmic Ray Telescope au SLAC. Une résolution en temps d'environ 70 ps par photoélectron a été obtenue, en accord avec la simulation.

Cette preuve de principe a convaincu la Collaboration *SuperB* d'adopter notre détecteur comme solution de base pour l'identification des particules émises vers l'avant dans *SuperB*. Le point délicat, encore ouvert, est celui de la résistance de ce détecteur aux bruits de fond de la machine.

Dans cette thèse nous présentons aussi les études préliminaires de différents types de bruit de fond et leur effet sur les performances du détecteur DIRC-like TOF. Le processus Bhabha radiatif est de loin la source dominante de bruit de fond. Le taux de photoélectrons de bruit de fond principalement due aux gammas d'énergie d'environ

1.4 MeV est estimé à  $\sim 480$  kHz/cm<sup>2</sup> ce qui correspond à 2 C/cm<sup>2</sup> de charge d'anode intégrée sur 5 ans. Le flux de neutrons traversant l'électronique de front end du détecteur DIRC-like TOF est estimé à  $\sim 10^{11}$ /cm<sup>2</sup>/an. Ces résultats préliminaires sont rassurants.

# Abstract

In this thesis, we present the conception, the performances studies and the first tests in the SLAC Cosmic Ray Telescope of a new detector for charged particle identification in the forward region of the *SuperB* detector.

This detector is based on the time-of-flight (TOF) technique. To identify particles with momentum up to 3 GeV/c and flying around two meters, we need a TOF detector able to measure the time with a precision of about 30 ps. To achieve this goal we have conceived a device in which charged particle produce Cherenkov light in a fused silica (quartz) radiator. This light is then detected by very fast photodetectors and a dedicated ultrafast electronics. We call this device, the "DIRC-like TOF" detector.

For what concern the photodetectors, the HAMAMATSU SL-10 MCP-PMT has been characterized at LAL test bench and a time resolution of about 37 ps per photoelectron has been measured. The new 16-channel USB WaveCatcher electronics developed by LAL (CNRS/IN2P3) and CEA/IRFU has been shown to have a jitter smaller than 10 ps. The geometry of the quartz detector has been then carefully studied with Geant4 simulations. They show that the best detector geometry allows to reach a time resolution of about 90 ps per photoelectron with at least 10 photoelectrons detected, giving in average the expected 30 ps total time resolution.

We have constructed a prototype of such device, using quartz bars available from the *BaBar* experiment, and we have installed it in the SLAC Cosmic Ray Telescope. A time resolution of about 70 ps per photoelectron was obtained, in agreement with simulation.

This proof-of-principle has convinced the *SuperB* Collaboration to adopt our device as the baseline for the *SuperB* charged particle identification detector in the forward region. The delicate point which is still under study is the resistance of this detector to the machine background.

In this thesis we also present preliminary studies of different types of background and their effect on the performances of the DIRC-like TOF detector. Radiative Bhabha process is by far the dominant source of background. The rate of the background photoelectrons caused mainly by the gammas with energy around 1.4 MeV is estimated to be  $\sim 480 \text{ kHz/cm}^2$  which corresponds to  $2 \text{ C/cm}^2$  of integrated anode charge in 5 years. The neutron flux thought the DIRC-like TOF front end electronics is  $\sim 10^{11}/\text{cm}^2/\text{year}$ .

These preliminary results are reassuring.

# Chapter 1

## Introduction

The search for evidence of physics beyond the Standard Model (SM) is the main goal of particle physics in the next decades. The LHC at CERN is looking for the Higgs boson, the last missing building block of the SM. At the same time it will intensively search for New Physics (NP) which has solid theoretical motivations related to the quantum stabilization of the Fermi scale to show up around 1 TeV.

However, pushing the high-energy frontier, i.e. increasing the available center of mass energy in order to produce and observe new particles, is not the only way to look for NP. New particles could reveal themselves through their virtual effects in processes involving SM particles only. For this kind of searches, often called indirect, the production thresholds are not an issue. Since quantum effects become typically smaller as the mass of the virtual particles increases, the name of the game is rather high precision. As a matter of fact, high-precision measurements allow to probe NP energy scales inaccessible at present and next-generation colliders.

Flavour physics is the best candidate as a tool for indirect NP searches for several reasons. First, Flavour Changing Neutral Currents (FCNC), neutral meson-antimeson mixing and  $CP$  violation occur at the loop level in the SM and therefore are potentially subject to order one NP virtual corrections. In addition, quark flavour violation in the SM is governed by the weak interaction and suppressed by the small quark mixing angles. Both these features are not necessarily shared by NP which, in such cases, could produce very large effects. Indeed, the inclusion in the SM of generic NP flavour-violating terms with natural order one couplings is known to violate present experimental constraints unless the NP scale is pushed up to 10-100 TeV or even more depending on the flavour sector. The difference between the NP scale emerging from flavour physics and the one suggested by Higgs physics is very intriguing. It clearly indicates that flavour physics has either the potential to push the explored NP scale in the 100 TeV region or, if the NP scale is indeed close to 1 TeV, that the flavour structure of NP is highly non-trivial and the experimental determination of the flavour-violating couplings is particularly interesting. A short description of the flavour sector in SM is given in the first part of Chapter 2.

In this thesis we present the project of a high luminosity asymmetric collider known as the *SuperB* factory. This machine is capable to reach a luminosity exceeding  $10^{36} \text{ cm}^{-2}\text{s}^{-1}$  at the energy of the  $\Upsilon(4S)$  production. This represents an increase of two orders of magnitude with respect to the luminosity reached at the present B factories: PEP-II (SLAC) and KEKB (KEK). It should be noted that the measurements which can be performed at *SuperB* will allow one to study in a unique manner the structure of the NP beyond the SM, if discovered at LHC, and/or eventually to extent the domain of the NP search at energy scales larger and not accessible to the LHC. To achieve the ambitious goal for luminosity the design of the machine is innovative. The successful tests of the new collision scheme ("crab waist" scheme) performed in Frascati since beginning of 2008 have shown that this machine can be constructed (see second part of Chapter 2).

In this thesis we mainly discuss the design of the new *SuperB* detector (see third part of Chapter 2). The *SuperB* detector is based on the current *BaBar* detector which has been successfully operated for about 10 years at the PEP-II B-Factory (SLAC). Part of the *BaBar* hardware (in particular the 1.5 T superconducting coil, the CsI crystals from the barrel electromagnetic calorimeter and the quartz bars from the ring-imaging Cerenkov detector, the DIRC) will be reused in *SuperB* which will also benefit from the experience accumulated in various fields: mechanics, electronics, computing, etc. The new *SuperB* design will take into account the luminosity increase (from  $10^{34}$  to  $10^{36} \text{ cm}^{-2}\text{s}^{-1}$ ) and the reduced forward boost ( $\beta\gamma=0.24$  instead of 0.56 for *BaBar*).

In order to study new rare decay channels, the charged particle identification (PID) has to be more performing than in present B-factories. In particular it is now understood that there is a number of cases where the *BaBar*/Belle physics outputs would have benefited from a better coverage of the PID system in the forward end-cap as well as in the barrel. Even though the end-cap covers only a modest portion of the geometrical acceptance, a more hermetic detector than *BaBar* would allow higher efficiencies for exclusive B physics channel and could be especially valuable for some of the types of studies expected to be important at *SuperB*. For this reasons improvements of the detector are also being investigated, either to cope with the higher level of physical backgrounds or to improve the detector hermiticity. In particular, the *SuperB* collaboration has decided to look at the possibility of extending the particle PID of *SuperB* in the forward region.

The polar acceptance of the DIRC detector (the barrel PID) only starts around  $25.5^\circ$ . Tracks more forward can only be identified through energy loss ( $dE/dx$ ) measurements in the tracking system. This method is limited in efficiency and suffers from high mis-identification probability. Therefore, covering the detector forward end cap (down to  $\sim 16^\circ$ ) with a dedicated PID detector would enhance the physics potential of the experiment as discussed in the third part of Chapter 2 of this document.

In this thesis we present the studies on a new Cherenkov time-of-flight detector called the DIRC-like TOF (see Chapter 3). In order to fulfill the PID requirements the total time resolution of the DIRC-like TOF detector should be 30 ps per track. It sets challenging requirements on detector, photomultipliers and electronics. In Chapter 5 we present the

experiment which has been performed at SLAC Cosmics Ray Telescope in order to test this detector concept.

In Chapter 4 we describe in details the most important background sources for the DIRC-like TOF detector and their impact on the photodetector lifetime and on the front end electronics.

In Chapter 6 we finally describe in some details the setup which is now available at LAL and the tests which have been performed to study the characteristics of different photodetectors and in particular their timing characteristics.



# Chapter 2

## The *SuperB* experiment

In the first section of this chapter, we discuss the Standard Model of strong, weak and electromagnetic interactions and with particular attention the fermion sector and thus the CKM matrix. We introduce the  $CP$ -violation phenomena and show the role of  $B$ -physics and from the experimental point of view of the  $B$ -Factories facilities. We briefly discuss physics motivation and show the importance of the *SuperB* factory construction. In the second section, we describe the *SuperB* accelerator and the new accelerating schemes which will allow *SuperB* to reach a luminosity of about a factor 100 better than the past generation of  $B$ -factories (the *BaBar* experiment at the PEP-II collider at SLAC in USA and the *Belle* experiment at the KEK-B collider in Japan). And finally, in the last section, we describe the *SuperB* detector which will be built in Frascati, Italy.

### 2.1 The Standard Model of the elementary particles

The role of the Standard Model (SM) is to establish and group in families the list of all existing elementary particles and to describe their interactions. Table 2.1 summarizes the main characteristics of twelve fermions (six quarks and six leptons, which are classified in three generations) and four gauge bosons.

An important type of physical theory based on local symmetries is called a gauge theory and the symmetries natural to such a theory are called gauge symmetries. The observation of various symmetries can help to build a theory of a given interaction. For example, the observation that the electric charge of the system is conserved in the electromagnetic process indicates that the Lagrangian describing the electromagnetic interaction has to be invariant under the  $U(1)$  gauge transformation. Gauge symmetries in the SM, used to describe three of the four fundamental interactions, are based on the  $SU(3)_C \times SU(2)_L \times U(1)_Y$  group. The symmetries of the  $SU(3)_C$  group describe the

Table 2.1: Table of elementary particles

Particle	Where it was found	Year of discovery	Charge	Mass
Quarks	Hadrons	1905-1995	-1/3-2/3	2 Mev/c <sup>2</sup> -176 GeV/c <sup>2</sup>
up-down (u,d)	proton neutron	proton (1905) neutron (1932)	up 2/3 down -1/3	2-4 MeV/c <sup>2</sup>
strange (s)	strange particles (K, $\Lambda$ ...)	kaon (1947)	-1/3	$\sim$ 100 MeV/c <sup>2</sup>
charm (c)	hadrons: J/ $\Psi$ , D	J/ $\Psi$ (1974)	2/3	$\sim$ 1.4 GeV/c <sup>2</sup>
beauty (b)	hadrons: B	$\Upsilon$ (1977)	-1/3	$\sim$ 5.2 GeV/c <sup>2</sup>
top (t)		top(1995)	2/3	$\sim$ 176 GeV/c <sup>2</sup>
Leptons		1898-2000	0,-1	0-1784 MeV/c <sup>2</sup>
electron (e)		1898	-1	$\sim$ 0.5 MeV/c <sup>2</sup>
neutrino e ( $\nu_e$ )		1956	0	$\sim$ 0
muon ( $\mu$ )		1937	-1	$\sim$ 106.5 MeV/c <sup>2</sup>
neutrino $\mu$ ( $\nu_\mu$ )		1962	0	$\sim$ 0
tau ( $\tau$ )		1975	-1	$\sim$ 1784 MeV/c <sup>2</sup>
neutrino $\tau$ ( $\nu_\tau$ )		2000	0	$\sim$ 0
Boson			0, $\pm$ 1,	0-90 MeV/c <sup>2</sup>
photon ( $\gamma$ )		1923	0	0
gluon ( $g$ )	$e^+e^-$ collision	1979	0	0
$W^-$ , $W^+$	$p\bar{p}$ collision	1983	$\pm$ 1	$\sim$ 80 GeV/c <sup>2</sup>
Z	$p\bar{p}$ collision	1983	0	$\sim$ 91 GeV/c <sup>2</sup>

strong force, the  $SU(2)_L$  group describes the weak interaction and the  $U(1)_Y$  group the electromagnetic force. In the theory of the electroweak interaction, the carriers of the electromagnetic and weak forces are the massless photon and three massive gauge bosons called the  $W^\pm$  and  $Z^0$  bosons respectively. The strong interaction is mediated by gluons, acting upon quarks, antiquarks, and other gluons.

For the last decades, the SM has been very successful in explaining numerous experimental data. However, the SM leaves open questions. The SM particles acquire their masses from the Higgs mechanism of the spontaneous symmetry breaking. It is known that the scalar field theory contains a quadratic divergence due to the quantum loop corrections. In order to make the Higgs boson mass around 100 GeV one has to introduce a very high cut-off of the theory of the order of the Plank scale ( $M_{\text{Pl}} \sim 10^{19}$  GeV). This fine-tuning, often called the hierarchy problem, is rather unnatural. Therefore, the SM must be considered as an effective theory of some more fundamental theory. Secondly, the SM does not explain the observed hierarchical pattern of the quark and lepton mass spectra. The quarks and leptons of the second generation are several orders of magnitude heavier than the corresponding particles of the first generation, and the third generation is even heavier by another order of magnitude. The quark flavour mixing CKM matrix, discussed later in this chapter, has also a typical hierarchical structure. Moreover, the number of generations is still an open question. All these questions and problems require a very precise test of the SM and beyond.

### 2.1.1 Conservation laws and symmetries

The symmetry properties of a physical system are intimately related to the conservation laws characterizing that system. Noether's theorem states that each symmetry of a physical system implies that some physical property of the system is conserved. Conversely, each conserved quantity has a corresponding symmetry.

The parity transformation (also called parity inversion,  $P$ ) is the simultaneous flip in the sign of all three spatial coordinates ( $\vec{x}$ ). It affects also the momentum of the particle ( $\vec{p}$ ), but leaves the spin unchanged, so that the helicity ( $h$ ) is also changed in to its opposite:

$$\begin{aligned} \vec{x} &\xrightarrow{P} -\vec{x} \\ \vec{p} &\xrightarrow{P} -\vec{p} \\ h &\xrightarrow{P} -h \end{aligned} \tag{2.1}$$

The parity symmetry appears to be valid for all reactions involving electromagnetic and strong interactions. Until 1956, the parity conservation was believed to be one of the fundamental conservation laws (along with the energy and momentum conservation).

However, it was observed that it is violated in the weak interaction: neutrinos, which can interact and be created only through the weak interaction, exist only as a left-handed particle ( $\nu_L$ ,  $h = -1$ ). The  $P$ -parity transformation applied to this particle leads to a right-handed neutrino ( $\nu_R$ ,  $h = 1$ )

$$P(\nu_L) = \nu_R \quad (2.2)$$

which does not exist in nature.

The charge conjugation operator  $C$  changes the charge of the particle and interchanges the particle with its antiparticle. Notice that this transformation does not alter the chirality of the particle. Thus, a left-handed neutrino would be taken by charge conjugation into a left-handed antineutrino, which does not exist in the Standard Model:

$$C(\nu_L) = \bar{\nu}_L \quad (2.3)$$

This property manifests the  $C$ -symmetry violation in the weak interaction.

It was believed for some time that the  $C$ -symmetry could be combined with the parity-inversion transformation to preserve a combined  $CP$ -symmetry which changes a particle into its antiparticle and inverts its momentum and helicity. In 1957, this  $CP$ -symmetry was proposed by Lev Landau to be the true symmetry between matter and antimatter. But in 1964  $CP$ -violation in the weak interactions was observed in the study of rare decays in the neutral kaon system and in  $B$ -meson decays. However, if  $CP$  is combined with time reversal ( $T$ -symmetry), the resulting  $CPT$ -symmetry is universally obeyed what is confirmed by all experimental studies up to now.

### 2.1.2 The CKM Matrix and the source of the $CP$ -violation

Fermion masses are generated via a Yukawa interaction with the Higgs scalar field. Using global unitary transformations in the flavour space, the Yukawa interaction can be diagonalized to obtain the physical eigenstates (and thus the diagonal mass terms in the SM Lagrangian). In this way the *weak eigenstates* ( $d'$ ,  $s'$ ,  $b'$ ) are the linear combinations of the *mass eigenstates* ( $d$ ,  $s$ ,  $b$ ). They are rotated by a  $3 \times 3$  unitary matrix, referred to as Cabibbo-Kobayashi-Maskawa (CKM) matrix [1, 2]:

$$\begin{pmatrix} d' \\ s' \\ b' \end{pmatrix} = \begin{pmatrix} V_{ud} & V_{us} & V_{ub} \\ V_{cd} & V_{cs} & V_{cb} \\ V_{td} & V_{ts} & V_{tb} \end{pmatrix} \begin{pmatrix} d \\ s \\ b \end{pmatrix} = V_{\text{CKM}} \begin{pmatrix} d \\ s \\ b \end{pmatrix} \quad (2.4)$$

The non-diagonal elements of the CKM matrix allow for the transitions between the quark generations in the charged weak current

$$J_\mu^+ = (\bar{u} \ \bar{c} \ \bar{t})_L \gamma_\mu V_{\text{CKM}} \begin{pmatrix} d \\ s \\ b \end{pmatrix}_L \quad (2.5)$$

A unitary complex  $N \times N$  matrix can be described by  $N^2$  real parameters. If this matrix mixes  $N$  families each with two quarks one can remove  $2N - 1$  phases through a redefinition of the quark states, which leaves the Lagrangian invariant. Since an orthogonal  $N \times N$  matrix has  $N(N - 1)/2$  real parameters (angles) we are left with  $N^2 - (2N - 1) - N(N - 1)/2 = (N - 1)(N - 2)/2$  independent physical phases in the quark mixing matrix. Therefore, it is real if it mixes only two generations. On the other hand, the three-generation mixing matrix can be described by three angles and one complex phase. The later one is the only source of  $CP$ -violation in the SM.

Among various proposed parametrizations of the CKM matrix, the most convenient one for practical purposes is the Wolfenstein parametrization [3]. Starting from the observed hierarchy of the mixing angles ( $\theta_{13} \ll \theta_{23} \ll \theta_{12}$  where  $\theta_{ij}$  denotes the mixing angle between the  $i$ -th and  $j$ -th generations), the Wolfenstein parametrization emphasizes a hierarchy in the magnitudes of the CKM elements: the ones on the diagonal are of order 1, and the others become smaller the further they are far from the diagonal. In this parametrization, expanding the matrix elements in terms of the small parameter  $\lambda = |V_{us}|$ , the CKM matrix can be written to order  $\mathcal{O}(\lambda^4)$  in the following traditional form:

$$V_{\text{CKM}} = \begin{pmatrix} 1 - \frac{\lambda^2}{2} & \lambda & A\lambda^3(\rho - i\eta) \\ -\lambda & 1 - \frac{\lambda^2}{2} & A\lambda^2 \\ A\lambda^3(1 - \rho - i\eta) & -A\lambda^2 & 1 \end{pmatrix} + \mathcal{O}(\lambda^4) \quad (2.6)$$

The Wolfenstein parameters have the following experimentally measured values:  $\lambda = 0.2257^{+0.0009}_{-0.0010}$ ,  $A = 0.814^{+0.021}_{-0.022}$ ,  $\rho = 0.135^{+0.031}_{-0.016}$ ,  $\eta = 0.349^{+0.015}_{-0.017}$  [4].

### 2.1.3 The Unitarity Triangle

The unitarity of the CKM matrix,  $V_{\text{CKM}} V_{\text{CKM}}^\dagger = 1$ , imposes

$$\sum_i V_{ij} V_{ik} = \delta_{jk}, \quad \sum_j V_{ij} V_{kj} = \delta_{ik} \quad (2.7)$$

The six vanishing combinations in Eq. (2.7) can be represented as triangles in a complex plane, of which ones obtained by taking scalar products of neighbouring rows or columns are nearly degenerate. The most commonly used unitarity triangle (UT), see Figure 2.1 arises from

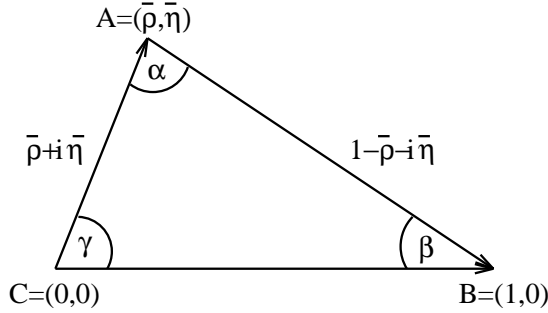


Figure 2.1: Unitarity Triangle in the  $\bar{\rho} - \bar{\eta}$  plane with  $\bar{\rho} = \rho(1 - \lambda^2/2)$  and  $\bar{\eta} = \eta(1 - \lambda^2/2)$ . Adapted from [5].

$$V_{ud}V_{ub}^* + V_{cd}V_{cb}^* + V_{td}V_{tb}^* = 0 \quad (2.8)$$

by dividing each side of Eq. (2.8) by the well-known  $V_{cd}V_{cb}^*$ :

$$\frac{V_{ud}V_{ub}^*}{V_{cd}V_{cb}^*} + 1 + \frac{V_{td}V_{tb}^*}{V_{cd}V_{cb}^*} = 0 \quad (2.9)$$

Its vertices are exactly  $(0, 0)$ ,  $(1, 0)$  and  $(\bar{\rho}, \bar{\eta})$  with  $\bar{\rho} = \rho(1 - \lambda^2/2)$  and  $\bar{\eta} = \eta(1 - \lambda^2/2)$ . Note that the phase transformation (Eq. (2.8)  $\rightarrow$  Eq. (2.9)) only rotates the triangle but leaves its shape unchanged. Therefore, the angles of the triangle, which are called  $\beta$ ,  $\alpha$  and  $\gamma$  (according to the *BaBar* collaboration) or  $\phi_1$ ,  $\phi_2$  and  $\phi_3$  (according to the *Belle* collaboration), and the sides of the unitary triangle are the physical observables which can be measured.

The CKM matrix elements are ones of the fundamental parameters of the SM, so an important goal of flavour physics is to overconstrain the CKM matrix elements by their measurements as precisely as possible in order to search for the evidence of potential effects of New Physics (NP) beyond the SM. One possibility of achieving this goal is to measure the sides and the angles of the Unitarity Triangle in various independent ways with very good precision. The consistency of the various measurements tests the unitarity in the three-generation SM. Any discrepancy with the SM expectations would imply the presence of new channels or new particles beyond the SM. In particular, the deviation from the triangle shape will be a clear signal of NP.

### 2.1.4 B-factories

In the last decade the main role in B physics has been played by the B-factories. The PEP – II and KEK – B  $e^+e^-$  asymmetric colliders, at Stanford Linear Accelerator Center (SLAC) and the Tsukuba High Energy Accelerator Research Organization (KEK) respectively, produced  $\sim 10^9 B\bar{B}$  pairs at the  $\Upsilon(4S)$  resonance. This accumulated statistics is not enough yet to find a deviation from the SM, as shown in next subsection.

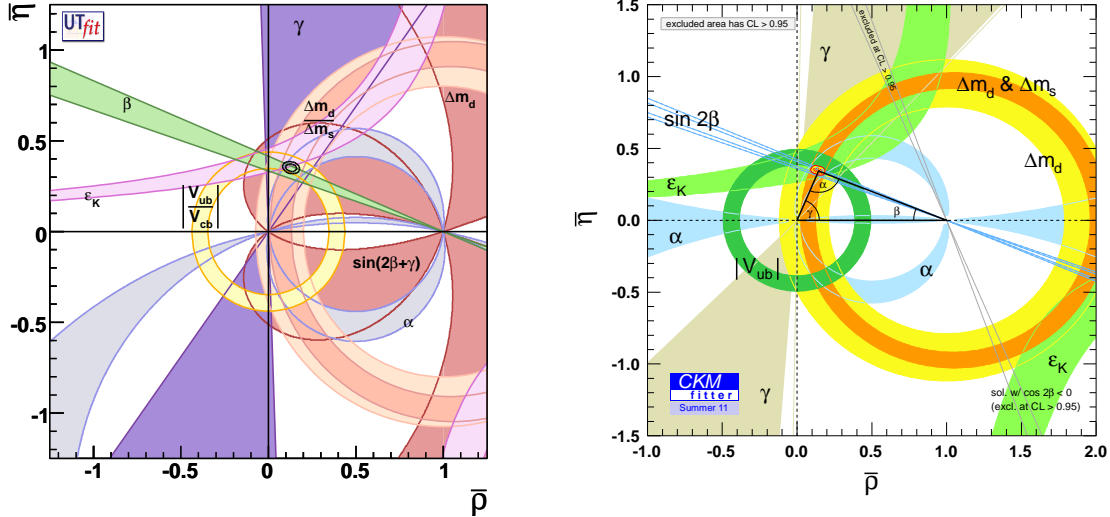


Figure 2.2: Constraints on the  $(\bar{\rho} - \bar{\eta})$  plane obtained by the UTfit collaboration [5] and the CKMfitter collaboration [6].

Therefore, it is crucial to build a new improved B-factory which will be able to produce 100 times more ( $\sim 10^{11}$ )  $B\bar{B}$  pairs.

### 2.1.5 State of the art in the B-physics

B-factories have recently performed several measurements of the sides and angles of the unitarity triangle using a set of numerous observables from the  $B$ -mesons and kaons decays. In Figure 2.2 we show the allowed regions for  $\bar{\rho}$  and  $\bar{\eta}$  as given by all measurements available at present moment. As it can be seen from Figure 2.2, the SM description of the  $CP$ -violation through the CKM mechanism appears to be a very successful framework which turns out to be in a very good agreement with all the measured observables accessible at the present moment. In this situation, any effect of NP beyond the SM will appear as a correction to the CKM picture.

In order to be able to look for NP, the precision of the measurements has to be improved substantially. In Figure 2.3 we show the allowed regions on the  $(\bar{\rho} - \bar{\eta})$  plane coming from different constraints assuming the current measurement precision and the one expected to be achieved at the *SuperB* factory. With the precision estimated for *SuperB* assuming the central values of the measured parameters to be the same as the current ones, the present picture will be drastically changed as one can see in Figure 2.3 (Right). This discrepancy would clearly indicate the presence of NP effects.

Therefore, a very precise measurement of the unitarity triangle parameters with sig-

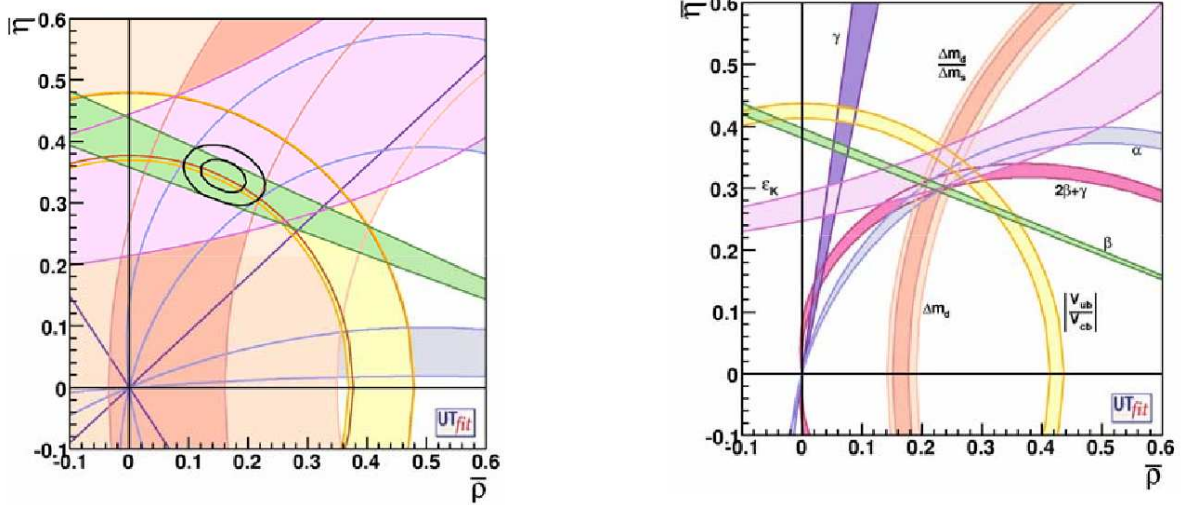


Figure 2.3: 95% probability regions for  $\bar{\rho}$  and  $\bar{\eta}$  selected by different constraints, assuming the present central values with the present errors (left) or with the errors expected at SuperB (right). Adapted from [7].

nificantly reduced experimental errors using a *SuperB* factory is very important for the test of the SM, search of NP and making strong constraints on the NP parameters.

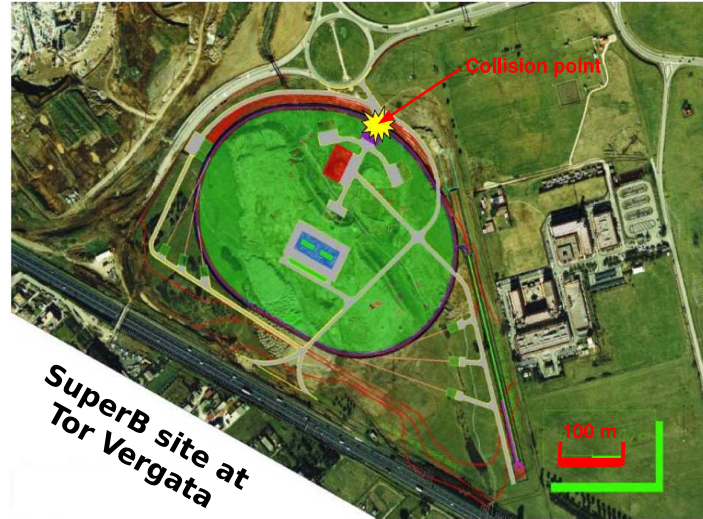


Figure 2.4: Layout of the *SuperB* site on the Tor Vergata University campus. The *SuperB* detector is installed in the collision point.

## 2.2 Accelerator

The *SuperB* accelerator is a high-luminosity two-ring asymmetric energy  $e^+e^-$  collider which is going to be built at the Tor Vergata University campus in Italy (see Figure 2.4). This project is a logical continuation of the  $e^+e^-$  colliders built at SLAC in California, USA (PEP-II [8]) and at KEK in Tsukuba, Japan (KEKB [9]). The key ideas and technologies, which are used in the design of this accelerator come from successful recent tests of the new concepts in the beam manipulation in the interaction region (IP) called "crabbed waist" performed at the DAΦNE collider at INFN in Frascati, Italy (2008) (see [10] for more details). This technique allows to produce an extraordinary high luminosity (by minimization of the transverse beam size) without increasing the beam currents or power consumption.

The energies of the colliding beams are tuned to sum up to a center-of-mass energy of 10.58 GeV, corresponding to the mass of the  $\Upsilon(4S)$  vector meson resonance. The effective cross section for the production of the  $\Upsilon(4S)$  at  $\sqrt{s} = 10.58$  GeV is about 1.1 nb. This resonance decays nearly with 100 % probability into a pair of B mesons,  $B^0\bar{B}^0$  or  $B^+B^-$ . The design luminosity is foreseen to be  $L = 10^{36}$  cm $^{-2}$ s $^{-1}$ . With this luminosity *SuperB* factory will produce in one running year ( $2 \times 10^7$  s)  $2.2 \times 10^{10}$   $B\bar{B}$  pairs providing an ideal laboratory for the study of B mesons.

If the  $\Upsilon(4S)$  resonance was produced at rest, then the B mesons would have a residual momentum such that their average flight distance would be of the order of 30  $\mu$ m: it would be experimentally very difficult to measure the separation between the decay points of the two B mesons. To avoid this problem, positron and electron beams are accelerated at the

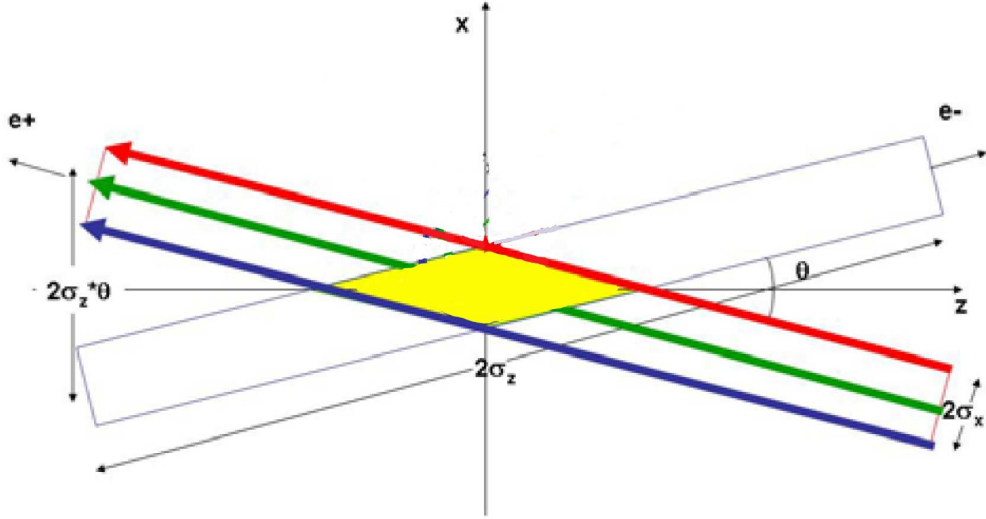


Figure 2.5: Bunch crossing scheme with large Piwinski angle.  $\theta$  is the angle between bunches,  $2\sigma_x$  ( $2\sigma_z$ ) is the horizontal (longitudinal) bunch size. The collision area is shown in yellow. The Figure is adapted from [7].

energies of  $E_{e^+} = 6.694$  GeV (HER, high-energy ring, in which the positrons circulate) and  $E_{e^-} = 4.18$  GeV (LER, low-energy ring, in which polarized electrons circulate). This provides the Lorentz boost of the  $\Upsilon(4S)$  to be  $\beta\gamma = 0.237 = \frac{E_{e^+} - E_{e^-}}{E_{cm}}$ , with  $E_{cm}$  being the center-of-mass energy, resulting in an average separation between the two B mesons of the order of  $\sim 120$   $\mu\text{m}$ . Note the boost is reduced with respect to *BaBar* ( $\beta\gamma = 0.56$ ). The measurement of this distance is possible in an experiment, providing a precise tracking device which placed as close as possible to the interaction point.

## 2.2.1 Luminosity and the "crabbed waist" beam crossing schemes

The luminosity  $L$  of an  $e^+e^-$  collider is given by the following expression:

$$L = \frac{N^+ N^-}{4\pi\sigma_y \sqrt{(\sigma_z \tan\theta/2)^2 + \sigma_x^2}} f_c \quad (2.10)$$

where  $f_c$  is the frequency of collision of the bunches,  $N^+$  ( $N^-$ ) is the number of particles in the positron (electron) bunches,  $\sigma_x$ ,  $\sigma_y$ ,  $\sigma_z$  are the beam sizes in the horizontal ( $x$ ), vertical ( $y$ ) and longitudinal ( $z$ ) directions and  $\theta$  is the crossing angle between the beam lines at the IP.  $\sigma_{x,y}$  is a function of the beam emittance ( $\varepsilon_{x,y}$ ) and of the beta function ( $\beta_{x,y}$ ) at the collision point in each plane:

$$\sigma_{x,y} = \sqrt{\beta_{x,y}\varepsilon_{x,y}} \quad (2.11)$$

Table 2.2: *SuperB* accelerator parameters.

Parameter	Units	HER ( $e^+$ )	LER ( $e^-$ )
Energy	GeV	6.7	4.18
$\beta_x$ @ IP	cm	2.6	3.2
$\beta_y$ @ IP	cm	0.0253	0.0205
Emittance x	nm rad	2.0	2.46
Emittance y	pm rad	5	6.15
Bunch length	mm	5	5
$\sigma_x$ effective	$\mu\text{m}$	165.22	165.30
$\sigma_y$ @ IP	$\mu\text{m}$	0.036	0.036
Energy spread ( $10^{-4}$ )	dE/E	6.43	7.34
CM energy spread ( $10^{-4}$ )	dE/E	5.0	5. 0
Total beam lifetime	min	4.23	4.48
Luminosity	$\text{cm}^{-2}\text{s}^{-1}$	$10^{36}$	

From Eq. (2.10) and Eq. (2.11) one can see that the small horizontal and vertical emittances as well as small beam spot sizes and beta functions have to be produced at the interaction region in order to increase the luminosity without increasing the beam current. However, reduction of the  $\beta_y$  requires very short bunches to keep the "hourglass" effect small. The use of large Piwinski angle [11] ( $\phi$ ) allows to decrease the effective bunch length (see Figure 2.5). The Piwinski angle is defined by:

$$\phi = \frac{\sigma_z}{\sigma_x} \tan \frac{\theta}{2} \quad (2.12)$$

To minimize the beam-beam effect (which increases together with large Piwinski angle implementation) the crabbed waist innovation [7] is required (see Figure 2.6). This bunch transformation mainly suppress the betatron and synchrobetatron resonances.

Table 2.2 shows the values of the main baseline parameters.

## 2.3 The *SuperB* Detector

The *SuperB* detector [7, 12] concept is based on the *BaBar* detector [13], with certain modifications required to operate at a luminosity of  $10^{36}\text{cm}^{-2}\text{s}^{-1}$  or more, and with a reduced center-of-mass boost. Further improvements are needed to cope with higher beam-beam and other beam-related backgrounds, as well as to improve detector hermeticity and performance. Its design is optimized for *CP* violation studies, but it is also well suited to do precise measurements in other B and non B physics. To achieve the goal of performing accurate measurements there are many requirements:

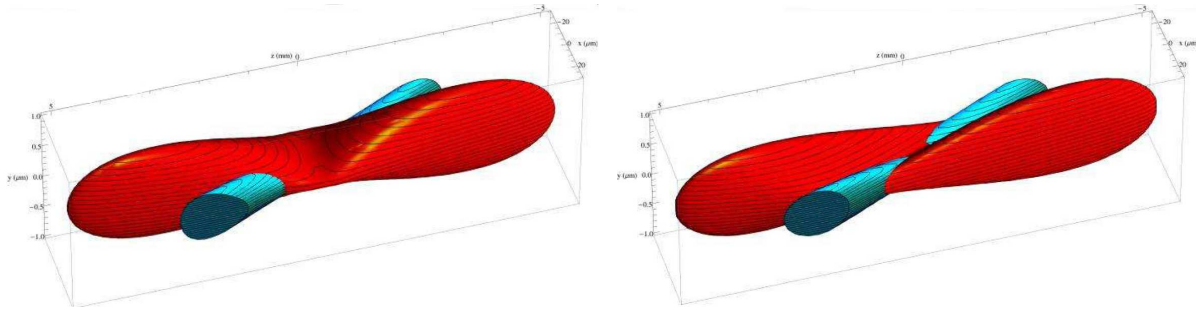


Figure 2.6: Bunch charge density envelops at the IP when colliding without (left) and with (right) the crabbed waist bunch transformation enabled. The low energy beam (in red) and high energy beam (in blue) are shown only near the overlap regions. The Figure is adapted from [7].

- a large and uniform acceptance in the center-of-mass system. Although the boost originated by the asymmetric beams is not large, optimizing the detector acceptance leads to an asymmetric detector;
- an excellent vertex resolution, in particular along the collision axis, since the B mesons travel almost parallel to it;
- an excellent detection efficiency and high precision on the momentum measurement for charged particles with transverse momentum ranging between 60 MeV/c and 4 GeV/c;
- an excellent energy and angular resolution for photons and  $\pi^0$  with energy down to 20 MeV and up to 5 GeV;
- a good discrimination between  $e$ ,  $\mu$ ,  $\pi$ ,  $K$  and  $p$  over a wide kinematic range;
- neutral hadrons identification capability.

Furthermore, since the average momentum of B decay products is less than 1 GeV/c, the precision of the measured track parameters is primarily influenced by multiple Coulomb scattering, rather than by the intrinsic devices resolutions. Similarly, for low energy photons, the detection efficiency and energy resolution are impacted by the amount of material traversed before the calorimetry system. For these reasons, the material in the active volume of the detector has been kept at the minimum.

A schematic view of the detector is shown in Figure 2.7 where the major subsystems are indicated. The Silicon Vertex Tracker (SVT) provides precise position information for charged tracks, and contributes to charged tracks identification with very low momentum ( $< 100$  MeV/c). The Drift Chamber (DCH) is used for momentum ( $0.12 \text{ GeV}/c < p_T < 5.00 \text{ GeV}/c$ ) measurements and kaon pion separation (for momentum smaller

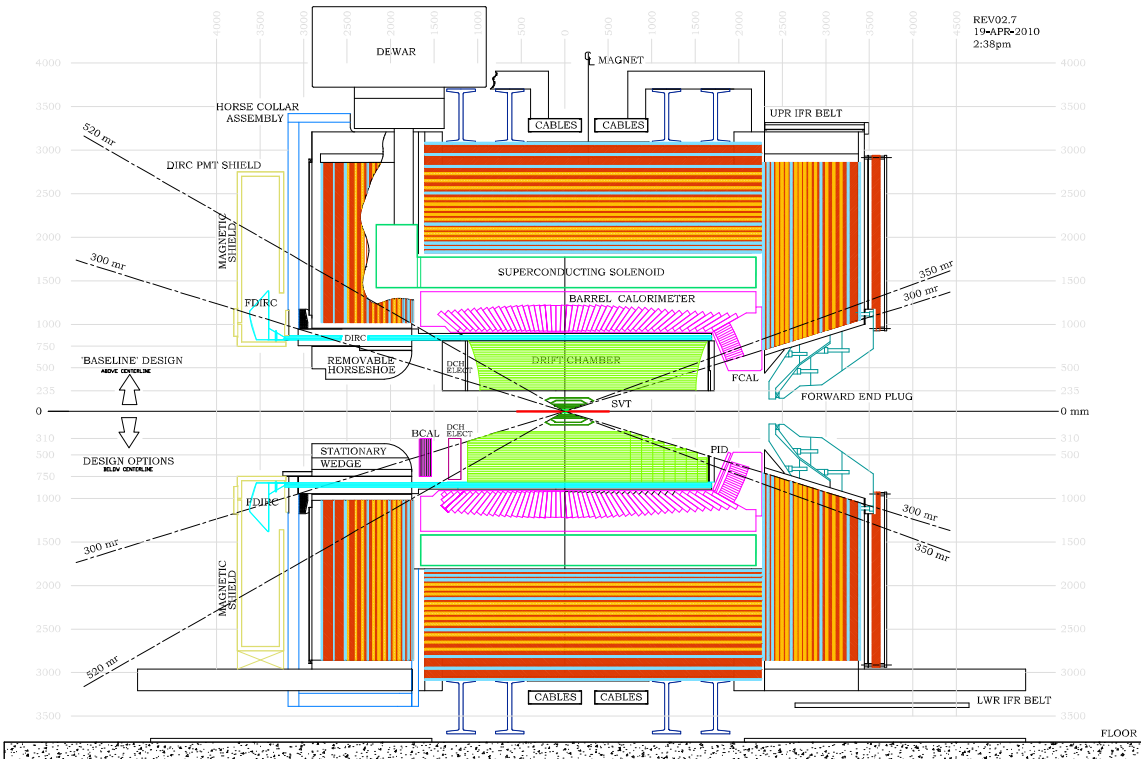


Figure 2.7: The *SuperB* detector. The upper half shows the baseline configuration, and the bottom half adds a number of optional detectors (most of them are the forward particle identification system and backward EMC).

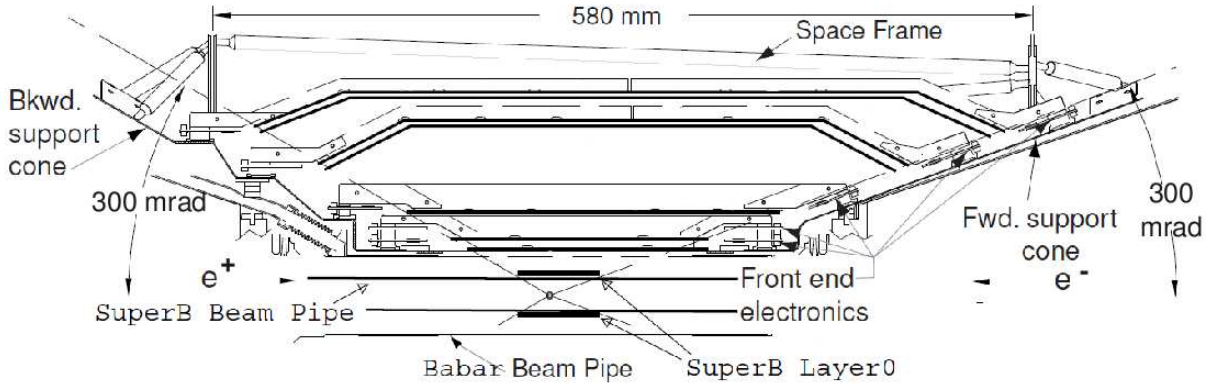


Figure 2.8: Longitudinal section of the SVT.

than 600 MeV/c). The Detector of Internally Reflected Cherenkov light (Focusing DIRC) is optimized for charged hadrons identification. The Electromagnetic Calorimeter (EMC) provides electron and neutral particle identification (PID). These detectors are located inside a 1.5 T magnetic field supplied by a superconducting solenoid. The Instrumented Flux Return (IFR) is used for muon (momentum more than 1 GeV/c) identification and long-living neutral hadron detection. The next sections are dedicated to a more detailed description of each subsystem.

The convention adopted in *SuperB* for the coordinate system follows a standard spherical coordinate system centered at the IP, the  $z$  axis being parallel to the high energy beam direction, and  $\theta$  and  $\phi$  being the usual polar and azimuthal angles. The  $y$  axis points upwards and  $x$  axis is in the direction to form a right-handed cartesian system of coordinates.

### 2.3.1 The Silicon Vertex Tracker

The main task of the *SuperB* vertex detector is to reconstruct the decay vertices of the two B mesons with a precision better than one half their mean separation ( $120 \mu\text{m}$ ), in order to allow the determination of the B mesons decay times for the measurement of time-dependent  $CP$  asymmetries. In addition, the charged particles with a transverse momentum ( $p_T$ ) smaller than 100 MeV/c do not reach the drift chamber and the SVT provides the only tracking information for them. Finally, the SVT also plays a role in particle identification through its own measurements of the rate of energy loss, and by giving the best determination of the polar angle of high momentum tracks, which is a necessary input to fully exploit the FDIRC.

The *SuperB* SVT design (see Figure 2.8) is based on the *BaBar* vertex detector layout with the addition of an innermost layer closer to the IP (Layer0). The Layer0 close-in position measurements lead to an improved vertex resolution, which is expected to

largely compensate for the reduced boost at the *SuperB*, thus retaining the resolution for B decays achieved in *BaBar*. The Layer0 design, is driven by the background condition, are the following: radius of about 1.5 cm, high granularity ( $50 \times 50 \mu\text{m}^2$  pitch); low material budget (about 1%  $X_0$ ); and adequate radiation resistance. The current baseline configuration of the SVT Layer0 is based on the triplets technology, which has been shown to provide the best physics performance (see [12] for more details).

The external SVT layers: Layer1-Layer5, located at radii between 3 and 15 cm, will be built with the same technology used for the *BaBar* SVT (double sided silicon strip sensor), which is adequate for the machine background conditions expected in the *SuperB* accelerator scheme.

To achieve the necessary resolution in  $\Delta t$  (0.6 ps), a resolution of  $40 \mu\text{m}$  must be attained in z for single-vertex measurements. In the  $x$  and  $y$  plane, distances of approximately  $100 \mu\text{m}$  must be resolved for the correct reconstruction of secondary vertices such as those from D and  $\tau$  decays.

The SVT angular acceptance, constrained by the interaction region design, will be down to 300 mrad in both the forward and backward directions, corresponding to a solid angle coverage of 95% in the center-of-mass frame.

### 2.3.2 The Drift Chamber

The SuperB Drift Chamber (DCH) provides measurements of the charged particle momenta and of the ionization energy losses used for particle identification. This is the primary device in *SuperB* to measure velocities of particles having momenta below approximately 700 MeV/c. It is based on the *BaBar* design, with 40 layers of centimeter-sized cells strung approximately parallel to the beamline [13]. A subset of layers are strung at a small stereo angle in order to provide measurements along  $z$  axis.

The DCH is required to provide momentum measurements with the same precision as the *BaBar* DCH (approximately 0.4% for tracks with a transverse momentum of 1 GeV/c). Like in *BaBar* it uses a helium-based gas mixture in order to minimize the measurement degradation from multiple scattering. However the  $p_T$  resolution of low momentum tracks is dominated by the multiple Coulomb scattering.

Figure 2.9 shows two possible endcap layouts, either with spherical or stepped endplates. Stepped endplates would provide a better match to the geometry of the forward PID and calorimeter systems, and would reduce the impact of the endplate material on the performance of these detectors. In addition at low  $\theta$  angle the very forward region of the DCH would suffer from the background.

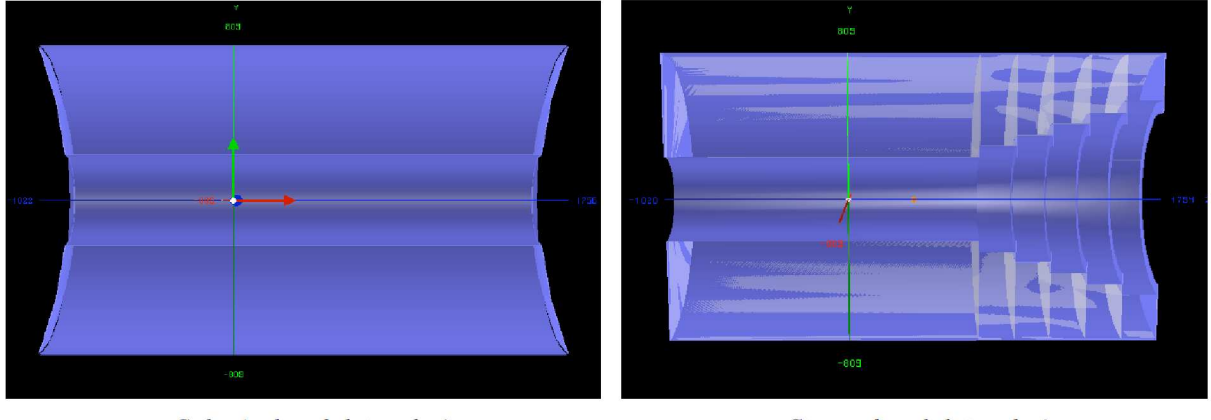


Figure 2.9: Longitudinal section view of the two possible *SuperB* DCH layouts with different endcaps: spherical (from the left) or stepped endplates (from the right).

Table 2.3: Solid angle coverage of the electromagnetic calorimeters. Values are obtained assuming the barrel calorimeter is in the same location with respect to the collision point as in *BaBar*. The center of mass (CM) numbers are for massless particles and initial "nominal" 4 GeV on 7 GeV beam energies. The barrel *SuperB* row includes one additional ring of crystals over *BaBar*.

Calorimeter	$\cos \theta(\text{lab})$		$\cos \theta(\text{CM})$		$\Omega(\text{CM})(\%)$
	minimum	maximum	minimum	maximum	
Backward	-0.974	-0.869	-0.985	-0.922	3.1
Barrel ( <i>BaBar</i> )	-0.786	0.893	-0.870	0.824	84.7
Barrel ( <i>SuperB</i> )	-0.805	0.893	-0.882	0.824	85.2
Forward	0.896	0.965	0.829	0.941	5.6

### 2.3.3 The Electromagnetic Calorimeter

The *SuperB* electromagnetic calorimeter (EMC) provides energy and direction measurement of photons and electrons, and is an important component in the identification of electrons versus other charged particles. The system contains three components, shown in Figure 2.10 – the barrel calorimeter, reused from *BaBar*; the forward endcap calorimeter, replacing the *BaBar* forward endcap; and the backward endcap calorimeter, a new device improving the backward solid angle coverage. Table 2.3 details the solid angle coverage of each calorimeter. The total solid angle covered for a massless particle in the center-of-mass (CM) is 94.1% of  $4\pi$ .

#### The barrel calorimeter.

The barrel calorimeter for *SuperB* is the existing *BaBar* CsI(Tl) crystal calorimeter [13]. Estimated rates and radiation levels indicate that this system will successfully continue to

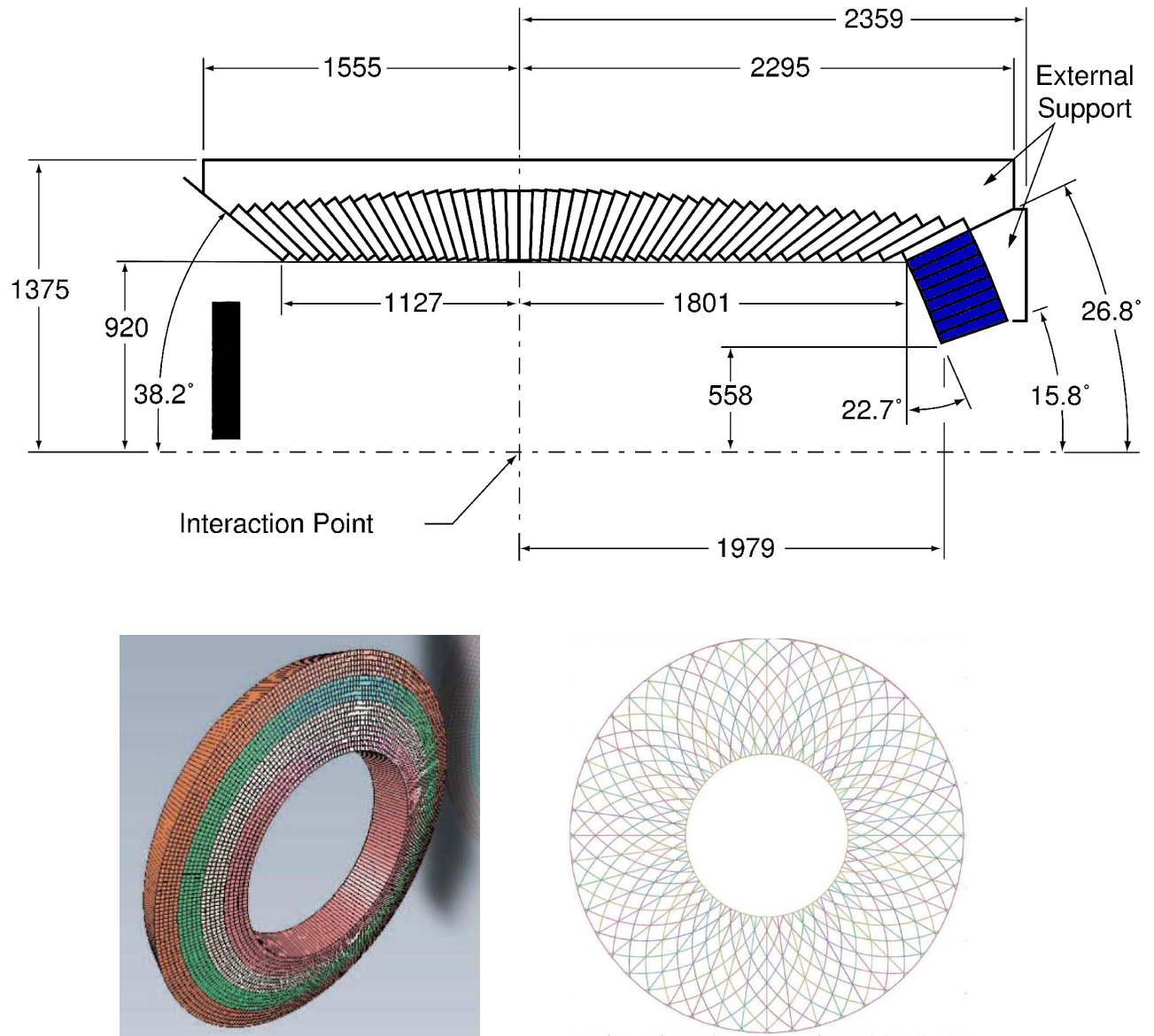


Figure 2.10: **Top:** Longitudinal section of the top half of the barrel EMC. Note: the forward part of the EMC (shown in blue color) is replaced by the new LYSO forward EMC. The backward EMC represented by the black box. **Bottom left:** Arrangement of the LYSO crystals in groups of rings in the forward EMC. **Bottom right:** View of the backward EMC showing the scintillator strip geometry for pattern recognition.

function in the *SuperB* environment. It covers  $2\pi$  in azimuth and polar angles from  $26.8^\circ$  to  $141.8^\circ$  in the lab frame. There are 48 rings of crystals in polar angle, with 120 crystals in each azimuthal ring (5,760 crystals in total). The crystal length ranges from  $16X_0$  to  $17.5X_0$ . They are read out by two redundant PIN diodes connected to a multirange amplifier. A source calibration system allows calibrating the calorimeter with 6.13 MeV photons from the  $^{16}N$  decay chain. Adding one more ring of crystals at the backward end of the barrel is under consideration. These crystals would be obtained from the current *BaBar* forward calorimeter, that will not be reused in *SuperB*. Space is already available for the additional crystals in the existing mechanical structure. In addition, the new readout electronics (analog-to-digital boards) have been designed to reduce the failure rate and to keep it at an acceptable level.

The existing barrel PIN diode readout (from *BaBar*) is kept at *SuperB*. They are expected to continue to perform satisfactorily. In addition they are epoxied to the crystals and changing them would be a difficult operation. In order to accommodate the higher event rate, the shaping time is decreased.

### **Forward Endcap Calorimeter.**

The forward electromagnetic calorimeter for *SuperB* is a new device replacing the *BaBar* CsI(Tl) forward calorimeter, with coverage starting at the end of the barrel and extending down to 270 mrad ( $\cos \theta = 0.965$ ) in the laboratory frame. Because of the increased background levels, a faster and more radiation hard material, such as LYSO (Lutetium Yttrium Orthosilicate, with Cerium doping) or pure CsI, is required in the forward calorimeter. The baseline design is based on LYSO crystals. The advantages of LYSO include a much shorter scintillation time constant (LYSO: 40 ns, CsI(Tl): 680 ns), a smaller Moliere radius (LYSO: 2.1 cm, CsI: 3.6 cm), and a wider resistance to radiation damage. One radiation length is 1.14 cm in LYSO and 1.86 cm in CsI. An alternative choice is pure CsI [14]; however, the light output would be much smaller, making LYSO preferable. There are 20 rings of crystals, arranged in four groups of 5 layers each. The crystals maintain the almost projective geometry of the barrel. Each group of five layers is arranged in five crystals wide modules. The grouping of crystals is illustrated in Figure 2.10 (Bottom left). Each crystal is up to  $2.5 \times 2.5 \text{ cm}^2$  at the back end, with a projective taper to the front. The maximum transverse dimensions are dictated by the Moliere radius. The length of each crystal is approximately 20 cm, or  $17.5X_0$ .

The LYSO crystals are readout by Avalanche Photodiodes (APD), with a low-noise and a gain of order 50, which offer the possibility of measuring signals from sub-MeV radioactive sources. This would obviate the need for a step with photomultipliers during the uniformity measurement process during calorimeter construction. The disadvantage of APDs is the gain dependence on temperature, which can be of order  $2\%/\text{C}^\circ$  (e.g. [15]). This requires good control of the readout temperature. Downstream on the acquisition chain, the same electronics as for the barrel EMC is used.

### **The backward electromagnetic calorimeter.**

The backward electromagnetic calorimeter for *SuperB* is a new device with the principal

intent of improving the detector hermeticity at modest cost. Excellent energy resolution is not a requirement, since there is significant material from the drift chamber in front of it. Thus a high quality crystal calorimeter is not planned for the backward region. The proposed device is based on a multi-layer lead-scintillator stack with longitudinal segmentation providing capability for  $\pi/e$  separation. In addition, a 100 ps time resolution would allow to achieve a  $3\sigma$   $K/\pi$  separation. The backward calorimeter is located starting at  $z = -1320$  mm, allowing room for the drift chamber front end electronics. The inner radius is 310 mm, and the outer radius 750 mm. The total thickness is  $12X_0$ . It is constructed from a sandwich of 2.8 mm Pb alternating with 3 mm plastic scintillator (e.g., BC-404 or BC-408). The scintillator light is collected for readout in wavelength-shifting fibers (e.g., 1 mm Y11). To provide for transverse spatial shower measurement, each layer of scintillator is segmented into strips. The segmentation alternates among three different patterns for different layers:

- Right-handed logarithmic spiral;
- Left-handed logarithmic spiral;
- Radial wedge.

This set of patterns is repeated eight times to make a total of 24 layers. With this arrangement, all fibers are emerge at the outer radius of the detector. There are 48 strips per layer, making a total of 1152 strips. The strip geometry is illustrated in Figure 2.10 (Bottom right).

### 2.3.4 The Instrumented Flux Return

The Instrumented Flux Return (IFR) is designed primarily to identify muons, and in conjunction with the electromagnetic calorimeter, to identify neutral hadrons, such as  $K_L^0$ . The iron yoke of the detector magnet provides the large amount of material needed to absorb hadrons. The IFR system must have high efficiency for selecting penetrating particles such as muons, while at the same time rejecting charged hadrons (mostly pions and kaons).

The total amount of material in the *BaBar* detector flux return (about 5 interaction lengths at normal incidence in the barrel region including the inner detectors) is not optimal for muon identification [13]. Adding iron with respect to the *BaBar* IFR for the upgrade to the *SuperB* detector can produce an increase in the pion rejection rate at a given muon identification efficiency, and one of the goals of the simulation studies is to understand whether the *BaBar* iron structure can be upgraded to match the *SuperB* muon detector requirements. A possible longitudinal segmentation of the iron is shown in Figure 2.11. The three inner detector layers are most useful for  $K_L^0$  identification; the coarser segmentation in the following layers preserves the efficiency for low momentum

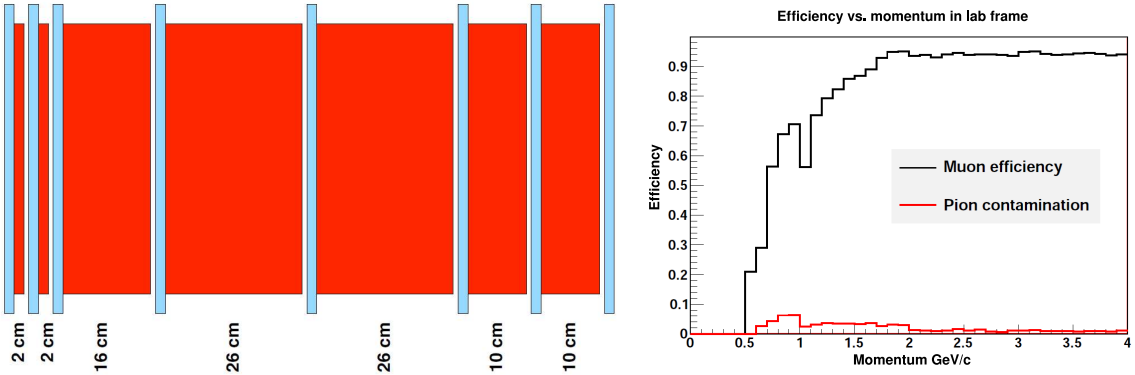


Figure 2.11: **Left:** Sketch of the longitudinal segmentation of the iron absorber (red) and the limited streamer tube (blue) in the baseline configuration. Active detector positions are shown in light blue from the innermost (left) to the outermost (right) layers. **Right:** Efficiency and misidentification probability for muons and charged pions as a function of the particle momentum. Study performed with full Geant4 based simulation.

muons. The presented layout has a total of 92 cm of iron and allows the reuse of the *BaBar* flux return with some mechanical modifications.

The main tool to perform the detector optimization and performances study is a Geant4 based simulation. Single muons and pions with momentum ranging between 0.5 GeV/c and 4 GeV/c enter the detector and their tracks are reconstructed and analyzed to extract relevant quantities for a cut-based muon selector. Preliminary results obtained using the baseline *SuperB* detector configuration give an average muon efficiency of  $\sim 87\%$  with a pion contamination of  $\sim 2\%$  over the entire momentum range. The efficiency and misidentification probability for muons and charged pions as function of the particle momentum are shown in Figure 2.11 (Right).

### 2.3.5 Particle Identification system

#### Focusing DIRC.

The DIRC (Detector of Internally Reflected Cherenkov light) [16] is an example of innovative detector technology that has been crucial to the performance of the *BaBar* science program. Excellent flavor tagging will continue to be essential for the program of physics anticipated at *SuperB*. The challenge for *SuperB* is to retain (or even improve) the outstanding performance attained by the *BaBar* DIRC, while also gaining an essential factor of 100 in background rejection to deal with the much higher luminosity. A new Cherenkov ring imaging detector, called the Focusing DIRC, or FDIRC is being planned for the *SuperB* barrel. It will use the existing *BaBar* bar boxes and mechanical support structure. This structure will be attached to a new photon "camera", which will be optically coupled to the bar box window. The new camera design combines a small modular focusing

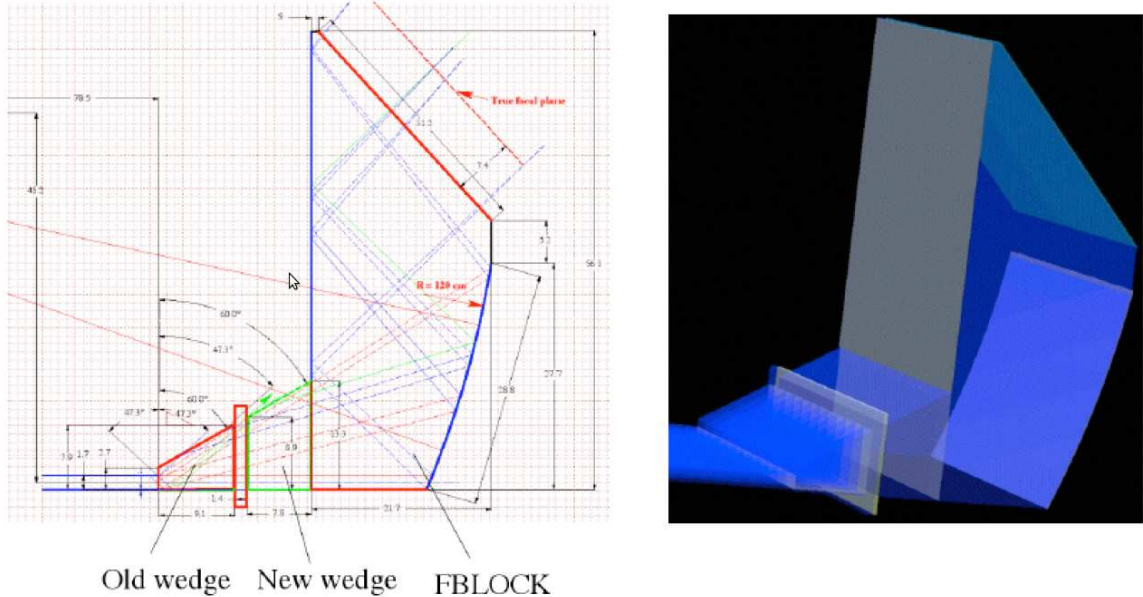


Figure 2.12: Barrel FDIRC Design. **Left:** FDIRC optical design (dimensions in cm). **Right:** Geant4 model of the FDIRC.

structure that images the photons onto a focal plane instrumented with very fast (with TTS around  $\sim 100$  ps), highly pixelated, photon detectors (PMTs). These elements should combine to attain the desired performance levels while being at least 100 times less sensitive to backgrounds than the *BaBar* DIRC.

Figure 2.12 shows the new FDIRC camera design (see Ref. [17] for more detail). It consists of two parts: a focusing block (FBLOCK) with cylindrical and flat mirror surfaces, and a new wedge. The wedge at the end of the bar rotates rays with large transverse angles (in the focusing plane) before they emerge into the focusing structure. The old wedge is too short so that an additional wedge element must be added to insure that all rays strike the cylindrical mirror. The cylindrical mirror is rotated appropriately to make sure that all rays reflect onto the FBLOCK flat mirror, preventing reflections back into the bar box itself: The flat mirror then reflects rays onto the detector focal plane with an incidence angle of almost  $90^\circ$ , thus avoiding reflections.

There are several important advantages over the *BaBar* DIRC: less sensitivity to the background (reduction of the detector volume), precise timing that can be used to measure the chromatic dispersion (thus improving performance); the total number of photomultipliers is reduced by about one half compared to a non-focusing design.

#### Forward PID device.

The barrel FDIRC detector combined with  $dE/dx$  from the DCH and SVT provides good  $K/\pi$  separation up to about 4 GeV/c, however hadron identification in the forward and backward regions in *SuperB* is limited unless dedicated PID devices are added there.

Any such device needs to cover the "cross-over"  $K/\pi$  ambiguity region for  $dE/dx$  near 1 GeV/c, and should also provide high momentum  $K/\pi$  separation where the  $dE/dx$  separation power is rather poor.

The DIRC-like TOF detector (see Figure 2.13) is the base line option for the *SuperB* forward PID. The physical gain is limited by the small solid angle coverage ( $15^\circ < \theta_{\text{lab.}} < 25.5^\circ$ ) and is equal to 4.7% per charged track . On Figure 2.13 (Bottom)  $S/\sqrt{S+B}$  of  $B \rightarrow K\nu\bar{\nu}$  as a function of the integrated luminosity in three different detector configurations is shown (study has been done with FastSim [18]). The configuration with forward PID detector does increase sensitivity of the *SuperB* detector.

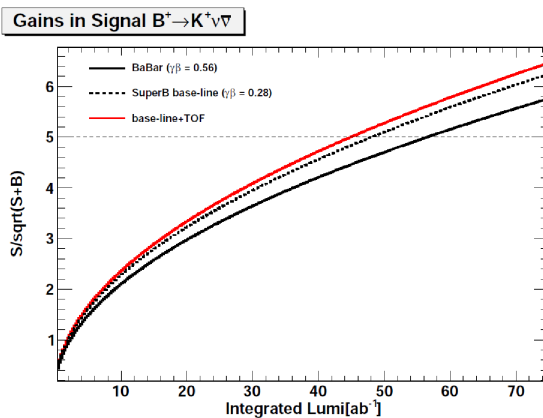
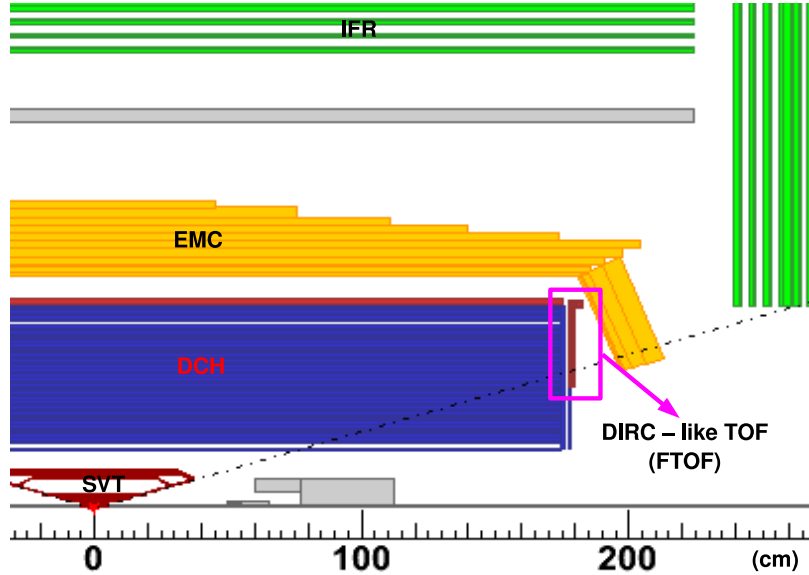


Figure 2.13: **Top:** Location of the DIRC-like TOF detector. **Bottom :**  $S(\text{signal})/\sqrt{S(\text{signal}) + B(\text{background})}$  of  $B \rightarrow K\nu\bar{\nu}$  as a function of the integrated luminosity in three different detector configurations. The black solid curve correspond to *BaBar* configuration. The dashed line represent the *SuperB* base line configuration (no backward EMC and no forward PID). The red line corresponds to the *SuperB* configuration with forward PID device.



# Chapter 3

## The DIRC-like TOF detector

In this chapter the principles of the DIRC-like TOF detector are described. We start with a general description of the time-of-flight (TOF) technique and compute the needed time precision in order to achieve a good  $K/\pi$  separation in the 0.8 - 3.0 GeV/c momentum range. Then we describe the DIRC-like TOF detector and in particular the full simulation which has been developed for geometry optimization and performances estimation. We focus on the time resolution and on the main contributions entering in its evaluation. Finally the electronics and the mechanical integration in the *SuperB* detector are discussed.

### 3.1 The time-of-flight technique

The time-of-flight of a particle with mass  $m$  and constant momentum  $p$ , flying over a distance  $L$  is defined by the formula:

$$t = \frac{L}{c} \sqrt{1 + \left(\frac{mc}{p}\right)^2} \quad (3.1)$$

where  $c$  is the speed of light. One can see from Eq. (3.1) that particles with different masses will have different TOFs. By measuring this time, if momentum is known, one can determine the mass of the particle, hence perform charged particle identification (PID). The DIRC-like TOF is located about 2 m away from interaction point (IP). Using formula (3.1) with  $L = 2$  m, one can compute the time-of-flight to DIRC-like TOF detector for different particles types, see Figure 3.1 (Left).

If the momentum of the particle is much bigger than its rest mass ( $p \gg mc$ ) the Eq. (3.1) can be written as follows:

$$t = \frac{L}{c} \left( 1 + \frac{1}{2} \left( \frac{mc}{p} \right)^2 \right). \quad (3.2)$$

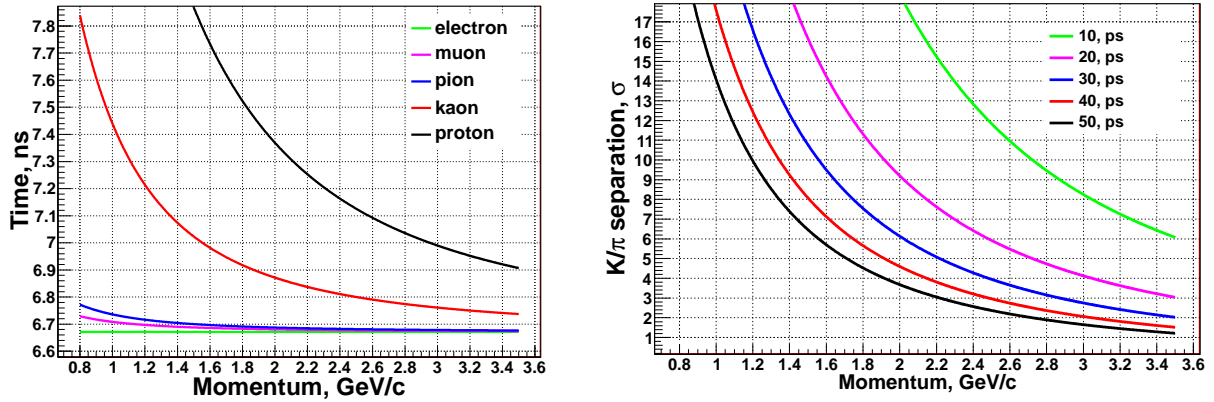


Figure 3.1: **Left:** Time-of-flight from IP to TOF detector (located about 2 m away from IP) as a function of momentum for different particle types, shown in different colors.  $t = 0$  corresponds to the particle at the IP. **Right:**  $K/\pi$  separation power (see Eq. (3.4)) of the TOF detector with different time resolutions.

Using Eq. (3.2) the TOF difference  $\Delta t$  between two particles with masses  $m_1$ ,  $m_2$  and momentum  $p$  can be computed to be:

$$\Delta t = \frac{Lc}{2p^2} (m_1^2 - m_2^2) \quad (3.3)$$

One can see from Eq. (3.3) that  $\Delta t$  decreases quadratically with momentum. To perform good PID for momentum up to few GeV/c the TOF has to be measured very precisely.

It is convenient to define the separation power between two particle hypothesis in numbers of  $\sigma$ , where  $\sigma$  is the time resolution of a given detector:

$$\text{separation power} = \frac{|\Delta t|}{\sigma} \quad (3.4)$$

On Figure 3.1 (Right),  $K/\pi$  separation power of a TOF detector with different time resolutions are shown. As it will be shown in the following the proposed DIRC-like detector could achieve a time resolution of about 30ps. One can see from Figure 3.1 (Right) that this corresponds to more than  $\sigma$   $K/\pi$  separation up to momentum of 3 GeV/c.

An important remark about particle decay in flight has to be done. Before producing Cherenkov light in the DIRC-like TOF detector, particles will travel around two meters from IP. For low momentum tracks this distance would be bigger because of their helix trajectory. The number of particles  $N$  which reach the DIRC-like TOF can be estimated using this formula:

$$N(t) = N_0 \exp \left( -\frac{t}{\tau\gamma} \right), \quad t = \frac{L}{\beta c} \quad (3.5)$$

where  $N_0$  is initial number of particles,  $\beta = v/c$ ,  $v$  is speed of the particle in laboratory frame,  $\gamma = 1/\sqrt{1-\beta^2}$ ,  $t/\gamma$  is the time in rest frame of the particle,  $\tau$  is the mean lifetime.

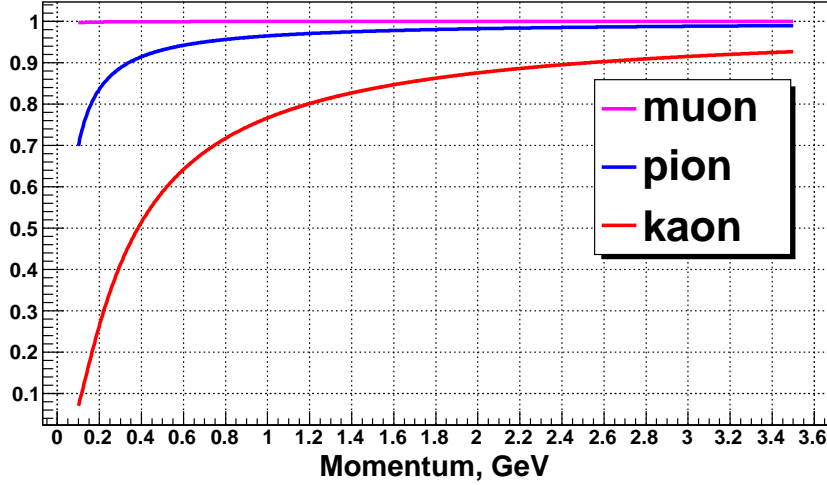


Figure 3.2: Fraction ( $N/N_0$ ) of particles which reach the DIRC-like TOF detector without decaying in flight as a function of momentum.

In Figure 3.2 the fraction ( $N/N_0$ ) of the different particle types which reach the DIRC-like TOF without decaying in flight as a function of momentum is shown. One can see that around 70 % of 0.8 GeV/c kaons will reach the DIRC-like TOF detector. This gives the upper limit of the kaon identification efficiency for this momentum, using only the DIRC-like TOF.

The separation power would define level of the PID ability of the DIRC-like TOF detector. Intuitively, one can say that if the purity of the selected particle sample is very high (which means that the number of wrongly-identified particles is low), the efficiency of the identification (ID) would be low too. And vice-versa: if the purity is low (which means that the miss-identification (misID) is high) the selection efficiency is high as well. Depending on the goals of a specific physics analysis, high-purity or high-efficiency samples would have to be selected. Therefore, one needs criteria to tune and monitor the efficiency and the purity of a PID selector.

A common way to separate two hypothesis – labelled ‘1’ and ‘2’ in the following, for instance ‘kaon’ and ‘pion’ – is to use a selector based on a ratio of likelihoods  $R_{LH}$ :

$$R_{LH} = \frac{LH_1}{LH_1 + LH_2} = \frac{1}{1 + \frac{LH_2}{LH_1}} \quad (3.6)$$

In the above formula,  $LH_1$  and  $LH_2$  are the likelihoods of the hypothesis (1) and (2) respectively.

In the (ideal) case for which the measurement is Gaussian-distributed, there is a direct correspondence between the (misID, ID) probabilities and the following two numbers: the  $\sigma$ -separation between the two hypothesis and the likelihood ratio threshold. Figure 3.3

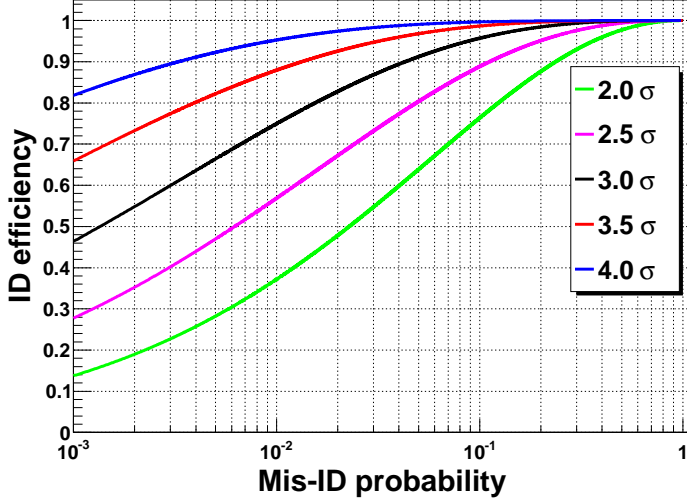


Figure 3.3: ID efficiency versus Mis-ID probability for different ' $\sigma$ ' separation.

plots the ID vs. misID evolution for different separation powers. More details can be found in Appendix 8. One can see that for a  $3\ \sigma$   $K/\pi$  separation, an efficiency of 90 % corresponds to 4 % mis-identification probability.

## 3.2 The DIRC-like TOF detector

The DIRC-like TOF detector is a ring imaging Cherenkov counter which use the time-of-flight technique to identify charged particles. The main goal of PID detector, located in the forward region, is to improve the  $K/\pi$  separation in the 0.8-3.0 GeV/c momentum range. In the *SuperB* baseline design this region is only covered by the DCH which provides limited PID for particles with momentum bigger than 0.7 GeV/c. The main requirements for such device are the following.

- Small radiation length as it will be located just in front of the forward EMC which resolution should not be degraded by additional material upstream.
- Compactness: there is a very limited space ( a few cm at most) between the DCH and the forward EMC.
- Radiation hardness as the DIRC-like TOF will be located not far from the IP ( $\approx$  2 m).
- Good  $K/\pi$  separation in (0.8-3.0) GeV/c momentum range, which requires a large number of photo electrons (p.e.) for all tracks (at least 10) and a precise timing measurement.

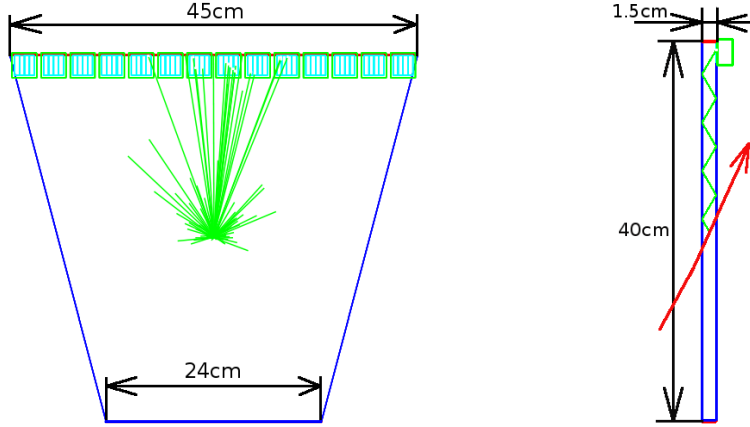


Figure 3.4: **Left:** Front view of one DIRC-like TOF sector; the 14 MCP-PMTs are connected to the outer side of the quartz tile, the Cherenkov photons are shown in green. **Right:** Side view of the same sector; the charged track crossing the quartz is indicated by the red arrow; an example of Cherenkov photon path is shown as well in green. The coordinates of the photon hit are defined by the touched PMT position and channel number, hence its resolution equal to channel size ( $22 \times 5.5 \text{ mm}^2$  for SL10 MCP-PMT).

The DIRC-like TOF measures the particle time-of-flight to separate kaons from pions. The start time is given by the bunch crossing while the detection of Cherenkov photons produced by the charged tracks while crossing a quartz volume provides the stop time for the TOF measurement. The DIRC-like TOF is based on the same principle as the *BaBar* DIRC [19, 20] and *SuperB* FDIRC [21, 22]. The detector material (quartz) is used in two ways: first as a Cherenkov radiator, then as a light guide for the Cherenkov light trapped in the radiator by total internal reflection – see Figure 3.4. Unlike for the DIRC, the Cherenkov angle is not measured by the DIRC-like TOF: what matters is the arrival time of the photons to the photo-multiplier (PMT) channels, which are then converted into photoelectrons. One will have several independent time measurements per track.

In our baseline configuration, the overall detector is made of 12 quartz (fused silica) sectors (optically isolated one from another) with thickness 15 mm (about 15%  $X_0$ ) and covering  $30^\circ$  in azimuth each. The Cherenkov light is detected by Hamamatsu SL10 [23] multi-channel plate (MCP)-PMTs: 14 per sector, hence 168 in total – see Figure 3.4. The DIRC-like TOF is a 2-dimensional device: both the time and the position, given by the coordinate of the touched MCP-PMT, are needed to perform PID. The DIRC-like TOF will be located about 2 meters away from the *SuperB* IP and will cover the polar angle range between  $[15^\circ; 25^\circ]$ .

### 3.3 Time resolution of the DIRC-like TOF detector

The total time resolution can be estimated using the following formula:

$$\sigma_{\text{tot}}^2 \sim \left( \frac{\sigma_{\text{electronics}}}{\sqrt{N_{\text{p.e.}}}} \right)^2 + \left( \frac{\sigma_{\text{detector}}}{\sqrt{N_{\text{p.e.}}}} \right)^2 + \left( \frac{\sigma_{\text{TTS}}}{\sqrt{N_{\text{p.e.}}}} \right)^2 + \sigma_{\text{trk}}^2 + \sigma_{t0}^2 \quad (3.7)$$

where :

- $N_{\text{p.e.}}$  is the number of p.e.

$N_{\text{p.e.}}$  depends on the track parameters (mass, momentum, angles with respect to the quartz tiles) and geometry of the detector. A full Geant4 [24, 25] simulation of the DIRC-like TOF shows that  $N_{\text{p.e.}}$  is at least 9 (18) for 0.8 GeV/c (2 GeV/c) kaons (see later).

- $\sigma_{\text{electronics}}$  describes the electronics accuracy and the quality of the signal. It has two main components:

- $\sigma_{\text{waveform}}$  which includes all possible effects coming from the signal itself – finite  $\frac{S}{N}$  ratio, imperfect quality and bandwidth [26] of the amplifier, quality of the cable and ground connections, electromagnetic noise in the experimental hall and many others.
- $\sigma_{S/N \rightarrow \infty}$  which models the resolution coming from the electronics itself and from algorithm of time computation. It becomes dominant when the signal-to-noise ratio  $S/N$  is very large.

- $\sigma_{\text{detector}}$  is the time spread coming from detector effects and is the superposition of different contributions listed in the following.

- $\sigma_{\text{chromaticity}}$  is driven by the refraction index, which depends on wavelength (dispersion [27, 28]). Photons with different wavelengths have different speeds, hence different propagation times.

- $\sigma_{\text{channel size}}$  is due to the finite size of the PMT channels: 'close' photons produced by a charged track can follow slightly different paths to a given channel, which cause additional time smearing.

- $\sigma_{\text{transit production}}$  appears due to the fact that charged particle emits photons all along its trajectory (hence at different times) while it is crossing the quartz radiator. This term is estimated to be around 14 ps – see later in section 3.5.5.

- $\sigma_{\text{TTS}}$  is the transit time spread (TTS) of the MCP-PMT (about 37 ps according to published reference [23]). One have to say that this particular MCP-PMT has a long tail in the timing distribution which (caused by recoil photoelectron from first MCP surface) this effect would degrade the overall performances of the DIRC-like TOF detector.

- $\sigma_{\text{trk}}$  is due to the track parameter reconstruction (at most 20 ps for a 0.8 GeV/c kaon).

$\sigma_{\text{trk}}$  contains the following terms:

- $\sigma_p, \sigma_L$  the time uncertainties coming from the precision of the track momentum and pathlength reconstructions.
- $\sigma_{\text{coupling to bar}}$ : in order to match photons detected by PMTs with a given track, the tracking system should provide its intersection with the DIRC-like TOF detector. This position is known with a finite precision which induces an additional time smearing.
- $\sigma_{t_0}$  is the time start resolution.

The longitudinal profile ( $\sigma_z$ ) of the *SuperB*  $e^-$  and  $e^+$  bunches is, to first approximation, described with a Gaussian distribution with RMS of about 6 mm [7]. Therefore, the time when the interaction occurs is known with uncertainty  $\sigma_{t_0} = \sigma_z/c = 20$  ps.

Most of these contributions are only relevant because of the high accuracy of the DIRC-like TOF – few tens of ps for the whole measurement, from the detector raw data to the final reconstruction. Finding, understanding and mitigating such tiny effects are significant parts of this thesis. From Eq. (3.7), one can see the two ways to reduce  $\sigma_{\text{tot}}$ : either by decreasing the dominant terms of the equation or by increasing  $N_{\text{p.e.}}$ .  $\sigma_{\text{trk}}$  has been studied within the *SuperB* FastSim framework [18] – see next section. In parallel, a full Geant4-based simulation of the DIRC-like TOF has been developed to study (and to minimize)  $\sigma_{\text{detector}}$  which is one of the leading terms in the Eq. (3.7) and which cannot be estimated analytically.

Finally, one can note that the number of readout channels per quartz sector is  $56 = 14(\text{PMT}) \times 4(\text{channel})$ , which is significantly more than the expected number of p.e. ( $> 10$ ) coming from the charged track. Hence, we can consider with good approximation that the number of touched PMT channels to be equal to the number of p.e.  $N_{\text{ch}} \simeq N_{\text{p.e.}}$ .

## 3.4 Study of $\sigma_{\text{trk}}$

In order to study  $\sigma_{\text{trk}}$  one first needs to estimate the expected momentum resolution ( $\sigma_{\text{mom}}$ ) of the detector.

The inner part of the *SuperB* detector operates in a 1.5 T magnetic field parallel to z-axis. A charged particles follow helix trajectory within this field. By measuring its radius a transfers momentum ( $p_\perp$ ) can be evaluated. The trajectories of the charged particles are reconstructed from the spacial hits in the SVT and the DCH.

Similar to *BaBar* reconstruction software – *SuperB* would use Kalman filter track fitting algorithm [29, 30] for charged track reconstruction. This algorithm performs hits pattern recognition and determined five parameters characterizing each track:

- $d_0$ , the distance in the x–y plane to the z-axis;
- $z_0$ , the coordinate along the z-axis;
- $\phi_0$ , the azimuthal angle of the POCA (position of the closest approach) to the z-axis;
- $\lambda$ , the dip angle of the track with respect to the transverse (x–y) plane. It is related to the polar angle  $\theta$  via the relation  $\theta = \frac{\pi}{2} - \lambda$ ;
- $\omega$ , the (signed) curvature of the track, whose sign and magnitude are related, respectively, to the charge of the associated particle and its transverse momentum.

All the quantities are defined at the POCA to the z-axis (POCAz). The momentum  $\vec{p}(l)$ , where  $l$  is the flight length from POCAz can be written in this way:

$$\vec{p}(l) = \frac{qcB_z}{\omega} \begin{pmatrix} \cos(\phi_0 + \omega l) \\ \sin(\phi_0 + \omega l) \\ \tan(\lambda) \end{pmatrix} \quad (3.8)$$

From Eq. (3.8) one can derive:

$$\tan(\lambda) = \frac{p_z}{p_{\perp}} \quad (3.9)$$

where  $p_z$  is the projection of the momentum on z-axis. The full momentum can be expressed via  $p_{\perp}$  and  $p_z$ :

$$p = \sqrt{p_{\perp}^2 + p_z^2} \quad (3.10)$$

Hence the resolution of the momentum can be written in this way:

$$\sigma_{\text{mom}} = \sqrt{\frac{(p_{\perp}\sigma_{p_{\perp}})^2 + (p_z\sigma_{p_z})^2}{p_{\perp}^2 + p_z^2}} \quad (3.11)$$

where  $\sigma_{p_z}$  can be found from the Eq. (3.9):

$$\sigma_{p_z} = \sqrt{(p_{\perp}\sigma_{\tan(\lambda)})^2 + (\tan(\lambda)\sigma_{p_{\perp}})^2} \quad (3.12)$$

Taking into account the  $p_{\perp}$  resolution as a function of  $p_{\perp}$  for *BaBar* DCH<sup>1</sup>:

$$\frac{\sigma_{p_{\perp}}}{p_{\perp}} = (0.13 \pm 0.01)\% \frac{p_{\perp}}{1 \text{ GeV}/c} + (0.45 \pm 0.03)\% \quad (3.13)$$

---

<sup>1</sup>here we assume that *SuperB* DCH would be at least as good as Babar one.

and resolution of the  $\tan(\lambda)$ :  $\sigma_{\tan(\lambda)} = 0.53 \cdot 10^{-3}$  [13] the  $\sigma_{\text{mom}}$  can be evaluated as a function of momentum as shown in Figure 3.5 (Top). One can see that for momentum of 3 GeV/c the resolution is  $\sim 15$  MeV/c.

However DIRC-like TOF detector is located in the forward endcap and hence the tracks would not cross all the layers of the DCH which cause momentum resolution degradation. According to study done with FastSim the muons with momentum  $> 2$  GeV/c with  $\theta = 23^\circ$  would produce signal on 25 layers out of 40 [31] and the momentum resolution drops down to  $\sim 20$  MeV/c [32] – see Figure 3.5 (Bottom).

Now that momentum resolution of the *SuperB* tracking system is understood we can study its effect on the timing characteristic of the DIRC-like TOF detector.

As explained above,  $\sigma_{\text{trk}}$  receive contributions from three main components:  $\sigma_p$ ,  $\sigma_L$ ,  $\sigma_{\text{coupling to bar}}$ .

Let's have a look on the effect on the time resolution coming from uncertainties of the momentum  $p$  and track length  $L$ :  $\sigma_{\text{mom}}$  and  $\sigma_{\text{Length}}$  respectively. Using Eq. (3.1), one can compute:

$$\sigma_p = \frac{dt(p)}{dp} \Big|_{L=\text{const}} dp = -\frac{L}{p^2} \frac{m^2 c}{\sqrt{1 + \left(\frac{mc}{p}\right)^2}} \frac{\sigma_{\text{mom}}}{p} \quad (3.14)$$

$$\sigma_L = \frac{dt(L)}{dL} \Big|_{p=\text{const}} dL = \frac{1}{c} \sqrt{1 + \left(\frac{mc}{p}\right)^2} \sigma_{\text{Length}} \quad (3.15)$$

From Eq. (3.14) one can see that  $\sigma_p$  decreases very quickly with momentum. Hence we can expect that  $\sigma_p$  would be small for high momentum tracks where we need best performances of the DIRC-like TOF detector. At contrary  $\sigma_L$  is almost a constant and in addition time is linearly proportional to the  $\sigma_{\text{Length}}$ . For these reasons we expect  $\sigma_L$  to be the dominant contribution to the time resolution.

Using toy Monte Carlo<sup>2</sup> method behavior of the  $\sigma_p$  and  $\sigma_L$  has been studied as a function of momentum resolution  $\sigma_{\text{mom}}$  and track path length resolution  $\sigma_{\text{Length}}$  respectively.

Figure 3.6 (Left) shows  $\sigma_p$  versus  $\sigma_{\text{mom}}$  for kaon at different momenta, for example :  $\sigma_p = 12$  ps, 2.2 ps and 1.2 ps correspond to  $\sigma_{\text{mom}} = 20$  MeV/c, 12 MeV/c, 5 MeV/c respectively. Time resolution is much more sensitive to the precision of the track length measurement. This dependency ( $\sigma_L$  vs  $\sigma_{\text{Length}}$ ) is almost constant for high momentum and it starts to be slightly different at low momentum. To keep  $\sigma_L$  below 10 ps,  $\sigma_{\text{Length}}$  should be less than 3mm. We can conclude that  $\sigma_p$  does not affect much the timing performances of the DIRC-like TOF detector, whereas  $\sigma_{\text{Length}}$  has to be studied more accurately.

Difference between true and reconstructed time of the track arrival ( $t_{\text{true}} - t_{\text{reco}}$ ) was

---

<sup>2</sup>Method based on Monte Carlo, usually used for simple estimations.

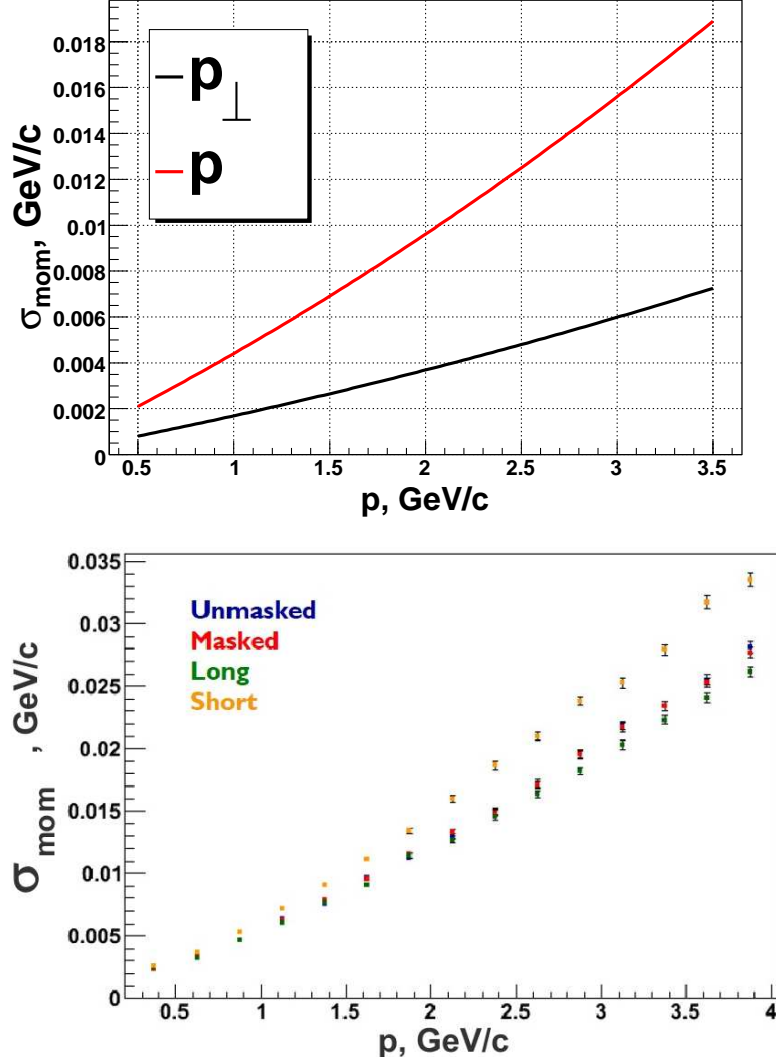


Figure 3.5: **Top:** The  $p_{\perp}$  and  $p$  resolution as a function of the momentum using analytical approach: Eq. (3.13) and Eq. (3.11) respectively, ( $\theta$  of the tracks is equal  $23^{\circ}$ ). **Bottom:** The  $p$  resolution as a function of momentum using *SuperB* FastSim (for more information see [32]). Different configuration of the *SuperB* DCH are shown in different colors. The unmasked – standard configuration of the DCH (shown in blue). Masked (shown in red) – configuration with masked forward and backward regions of the DCH where background rates expected to be very high. Long – is the configuration with extended DCH (there are no place for forward PID and backward EMC). Short – is the compact (in forward region) configuration of the DCH in order to give a space for FARICH detector [33, 34]. The DCH configuration which goes with DIRC-like TOF detector is shown in red and blue.  $\sigma_{mom}$  for charged tracks at  $\theta = 23^{\circ}$  with momentums 0.8 GeV/c, 2 GeV/c, 3 GeV/c equal to 5 MeV/c, 12 MeV/c, 20 MeV/c respectively.

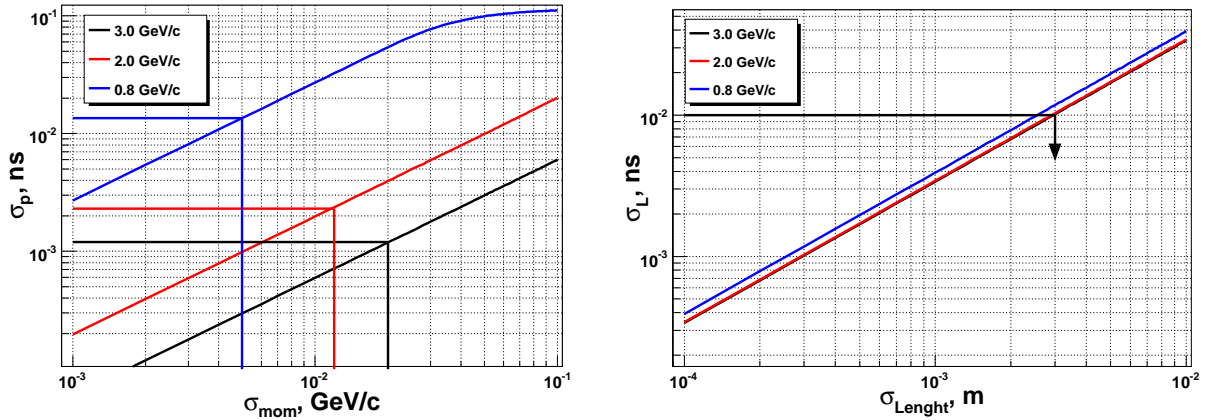


Figure 3.6: **Left:** The time resolution  $\sigma_p$  as a function of momentum resolution  $\sigma_{\text{mom}}$  for kaon with different momenta. **Right:** The time resolution  $\sigma_L$  as a function of track length resolution  $\sigma_{\text{Length}}$  for kaon with different momenta.

studied with FastSim. We produce two sets of Monte Carlo: one for kaon and one with same parameters for pion. The  $\theta$  of the track has been fixed at  $20^\circ$  while momentum has been fixed at several constant values (0.7, 0.8, 0.9, 1.5, 2.0, 2.5, 3.0, 3.5) GeV/c. To reconstruct the time we use the reconstructed flight length  $L_{\text{reco}}$  and momentum  $p_{\text{reco}}$ :

$$t_{\text{reco}} = \frac{L_{\text{reco}}}{c\beta_{\text{reco}}} = \frac{1}{c} L_{\text{reco}} \sqrt{1 + \left(\frac{mc}{p_{\text{reco}}}\right)^2} \quad (3.16)$$

We assume that contribution from  $\sigma_p$  is small, hence the error of the time difference ( $t_{\text{true}} - t_{\text{reco}}$ ) is defined by  $\sigma_L$ . On the Figure 3.7 (Left)  $\sigma_L$  as a function of momentum for kaon and pion are shown. This information can be used to extract  $\sigma_{\text{Length}}$ , which is shown on the Figure 3.7 (Right). One can see that for 3 GeV/c kaon  $\sigma_L = 2.2$  ps which correspond to  $\sigma_{\text{Length}} = 0.7$  mm.

Another contribution to the  $\sigma_{\text{trk}}$  is  $\sigma_{\text{coupling to bar}}$ . For this study we use same set of Monte Carlo data as one described above. The position of the impact point of the charged particles to the quartz detector is needed in order to properly evaluate the time propagation of the photons inside the detector. We define precision of this impact position as:

$$dR = \sqrt{(\Delta x)^2 + (\Delta y)^2} \quad (3.17)$$

where  $\Delta x + \Delta y$  are:

$$\begin{aligned} \Delta x &= x_{\text{true}} - x_{\text{reco}} \\ \Delta y &= y_{\text{true}} - y_{\text{reco}} \end{aligned} \quad (3.18)$$

where  $x_{\text{true}}$ ,  $x_{\text{reco}}$  and  $y_{\text{true}}$ ,  $y_{\text{reco}}$  are true and reconstructed  $x$  and  $y$  positions of the track intersection point with DIRC-like TOF detector. These uncertainties mainly occur

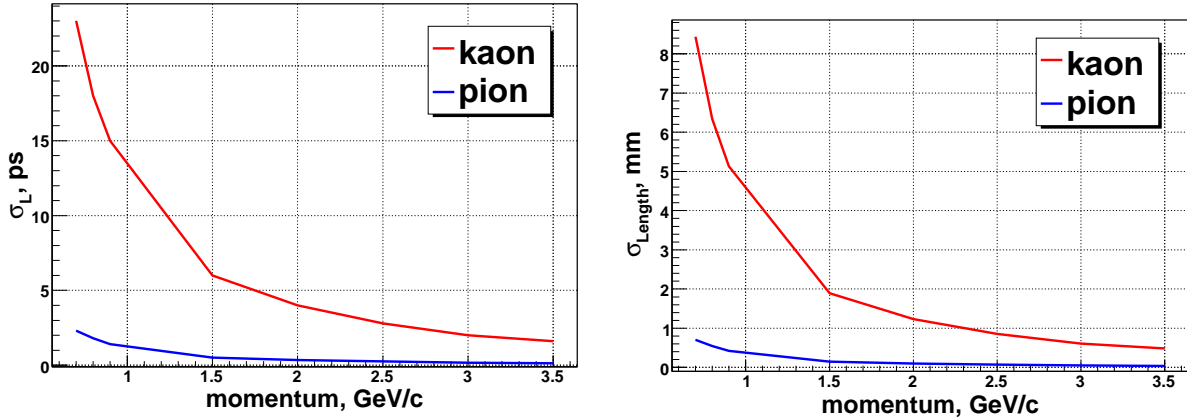


Figure 3.7: **Left:**  $\sigma_L$  as the function of the momentum for  $K$  and  $\pi$ . **Right:**  $\sigma_{\text{Length}}$  as the function of the momentum for  $K$  and  $\pi$ . Study were done with FastSim tool, angle of the track  $\theta = 20^\circ$ .

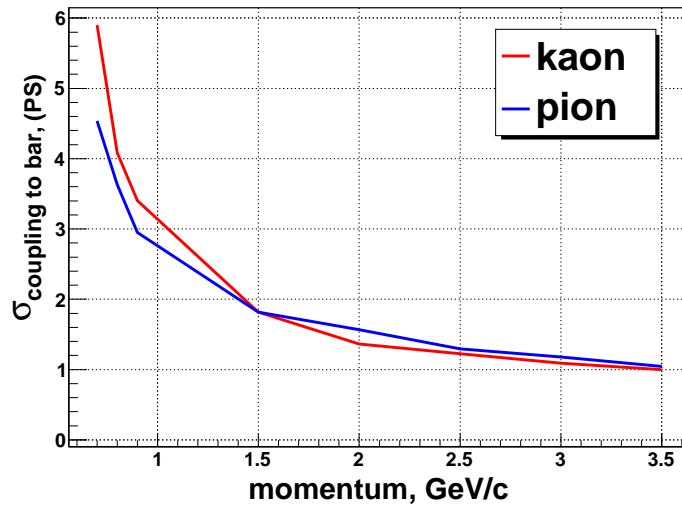


Figure 3.8:  $\sigma_{\text{coupling to bar}}$  as the function of the momentum for  $K$  and  $\pi$ . Study were done with FastSim tool, angle of the track  $\theta = 20^\circ$ .

due to multiple interaction of the charged particles with surrounded material. The  $dR$  uncertainty would cause time smearing:

$$\sigma_{\text{coupling to bar}} = \frac{dR}{c/n} \quad (3.19)$$

$\sigma_{\text{coupling to bar}}$  has been studied with FastSim. Figure 3.8 shows the dependence of  $\sigma_{\text{coupling to bar}}$  as a function of momentum for  $\theta = 20^\circ$ . One can see that this term is small  $< 6$  ps. For kaon and pion at 3 GeV/c,  $\sigma_{\text{coupling to bar}} \approx 1$  ps.

## 3.5 Study of $\sigma_{\text{detector}}$ and geometry optimization

Full simulation of the DIRC-like TOF detector has been developed. Its main goals are:

- Optimize the geometry in terms of number of p.e. and timing.
- Estimate the time resolution per channel.
- Study the different contributions to the time resolution.

1.5 T *SuperB* magnetic field is included in the simulation. The Cherenkov photon production and the propagation inside the DIRC-like TOF detector is done with Geant4. An additional standalone simulation which uses the output from the Geant4 simulation has been developed in order to include effects coming from PMT and tracking.

### 3.5.1 Geant4 - the full simulation tool for particle physics.

*"Geant4 is a toolkit for simulating the passage of particles through matter. It includes a complete range of functionality including tracking, geometry, physics models and hits. The physics processes offered cover a comprehensive range, including electromagnetic, hadronic and optical processes, a large set of long-lived particles, materials and elements, over a wide energy range starting, in some cases, from 250 eV and extending in others to the TeV energy range. It has been designed and constructed to expose the physics models utilized, to handle complex geometries, and to enable its easy adaptation for optimal use in different sets of applications. The toolkit is the result of a worldwide collaboration of physicists and software engineers. It has been created exploiting software engineering and object-oriented technology and implemented in the C++ programming language. It has been used in applications in particle physics, nuclear physics, accelerator design, space engineering and medical physics."* [24] This is an abstract from the main publication by Geant4 collaboration. One has to add that this is commonly used open source software which is frequently updated and have a lot of available examples. That is why we have been using it for our needs.

In the following two subsections we describe the physical processes simulated in the Geant4 including the production Cherenkov light.

### 3.5.2 Standard simulated processes for charged tracks and $\gamma$ 's

The physical processes taken into account in the dedicated simulation of the DIRC-like TOF detector are the following:

- $\gamma$  : gamma conversion [35, 36], Compton scattering [37, 38], photoelectric effect [39, 40, 41].
- $e, \mu$  : ionization [42, 43, 44], multiple scattering [45, 46, 47, 48], bremsstrahlung [49], annihilation (only for  $e^+$ ) [50]. Note that delta-rays has been taken into account as well.
- $\pi, K, p$  : ionization [51], multiple scattering [45].

We do not include particle decay in flight since we want to study the response of the DIRC-like TOF detector for a given particle type. We did not include hadronic interactions into our simulation.

Detailed description of the available physical processes in Geant4 can be found elsewhere [52].

### 3.5.3 Cherenkov light propagation and propagation in quartz

#### Cherenkov effect

Cherenkov radiation [53, 54], is electromagnetic radiation emitted when a charged particle passes through a dielectric medium of refractive index  $n$  with a velocity  $v$  greater than the speed of light  $c/n$  in that medium. The charged particles polarize the molecules of that medium, which then turn back rapidly to the ground state, emitting photons with energy of a few eV. They are emitted within the Cherenkov cone and are called Cherenkov photons. The opening angle  $\theta_c$  of the Cherenkov cone is a function of the velocity of the charged particle. Taking into account that the wavefront of the electromagnetic excitation is perpendicular to the photon direction,  $\cos(\theta_c)$  can be calculated from the simple geometrical representation. In Figure 3.9 (Left) a charged particle passes through an optical transparent medium emitting Cherenkov photons. One can see that emitted photon at time  $t$  would travel the distance equal  $\frac{c}{n}t$  while the charged particle will travel  $\beta ct$  together with wavefront these three length would build the right-angled triangle with cathetus  $\frac{c}{n}t$  and hypotenuse  $\beta ct$ , the  $\cos \theta_c$  can be found:

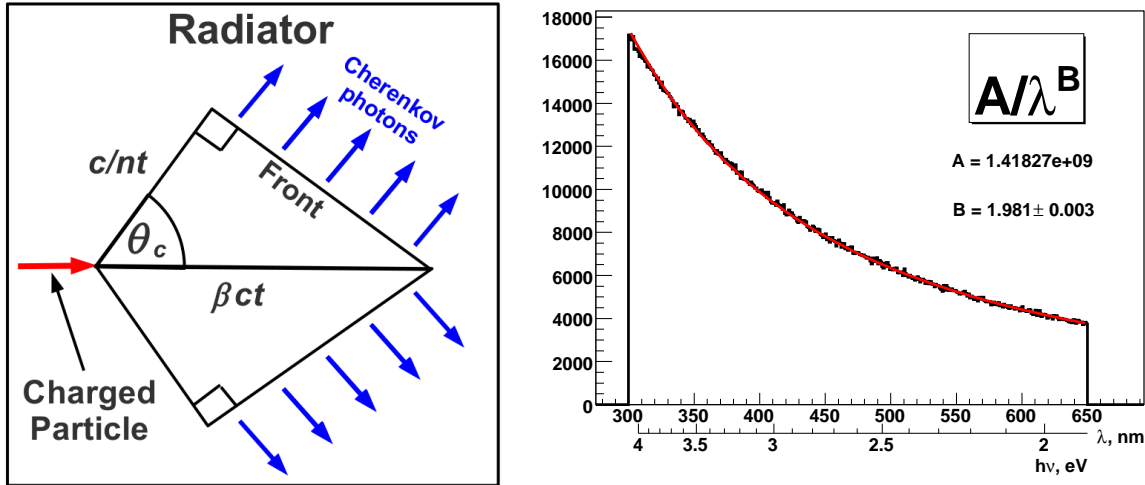


Figure 3.9: **Left:** Cherenkov effect. A charged particle (red arrow) passes through an optical transparent medium emit Cherenkov photons (blue arrows),  $\theta_c$  is the Cherenkov angle. **Right:** Spectrum of the Cherenkov photons obtained from the simulation. The fit function  $A/\lambda^B$ , where  $A = 1.41827e+09$  is unphysical scaling factor and  $B = 1.981 \pm 0.003$  (expected to be around 2 see Eq. (3.21)).

$$\cos \theta_c = \frac{1}{n\beta} \quad (3.20)$$

One has to say that yield of Cherenkov light have no decay time (unlike scintillation), which is very important for timing resolution. The number of Cherenkov photons emitted per unit path length  $x$  and per unit wavelength  $\lambda$  is given by:

$$\frac{\partial^2 N}{\partial x \partial \lambda} = \frac{2\pi\alpha z^2}{\lambda^2} \left( 1 - \frac{1}{(n(\lambda))^2 \beta^2} \right) \quad (3.21)$$

where  $z$  is the electric charge of the particle producing Cherenkov radiation (in unit of the proton charge) and  $\alpha$  the fine-structure constant. Assuming weak dependence of the refractive index from wavelength of the photon it is easy to see that spectrum of the Cherenkov photons per unit length is proportional to  $1/\lambda^2$ . A fit of the simulated spectrum gives  $1/\lambda^{1.981 \pm 0.003}$  see Figure 3.9 (Right).

The refractive index  $n(\lambda) \geq 1$  is a function of the phase velocity  $v_p(\lambda)$ :

$$n(\lambda) = \frac{c}{v_p(\lambda)} \quad (3.22)$$

The refractive index  $n(\lambda)$  depends on the wavelength  $\lambda$  see Figure 3.10. This dependency can be parameterized with Sellmeier equation:

$$n^2(\lambda) = 1 + \frac{B_1 \lambda^2}{\lambda^2 - C_1} + \frac{B_2 \lambda^2}{\lambda^2 - C_2} + \frac{B_3 \lambda^2}{\lambda^2 - C_3} \quad (3.23)$$

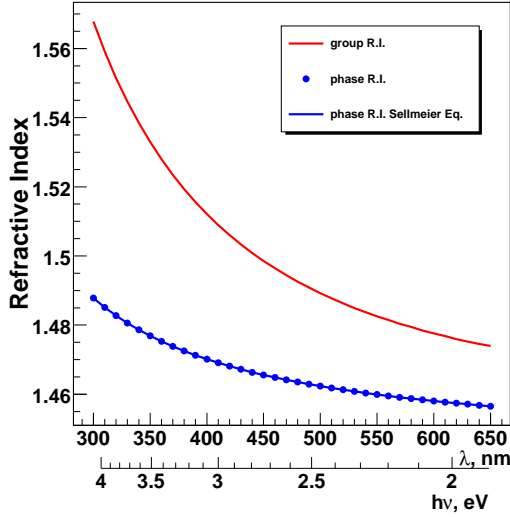


Figure 3.10: Refractive index (R.I.) (blue dots) and group refractive index (red) of the quartz as a function of wavelength. Blue dots correspond to values used by Geant4 simulation (exported from full simulation of the *BaBar* DIRC). Blue line was obtained with Sellmeier Eq. (3.23) using parameters from Table 3.1.

Coefficients ( $B_1, B_2, B_3, C_1, C_2, C_3$ ) for fused silica are taken from [55] and shown in Table 3.1.

Table 3.1: Coefficients for fused silica (see Eq. (3.23))

Coefficient	Value
$B_1$	0.6961663
$B_2$	0.4079426
$B_3$	0.8974794
$C_1$	$4.67914826 \times 10^{-3}$
$C_2$	$1.35120631 \times 10^{-2}$
$C_3$	97.9340025

The time-of-propagation (TOP)  $t_{\text{TOP}}$  of the photon with wavelength  $\lambda$  over the path  $L$  in the medium is defined by this equation:

$$t_{\text{TOP}} = \frac{L}{v_g(\lambda)} \quad (3.24)$$

where  $v_g(\lambda)$  is the group velocity. Usually refractive index  $n(\lambda)$  as a function of  $\lambda$  is given which mean that phase velocity  $v_p$  can be found using Eq. (3.22). Then using link between  $v_g$  and  $v_p$ :

$$v_g = v_p \left( 1 + \frac{\lambda}{n} \frac{\partial n}{\partial \lambda} \right) \quad (3.25)$$

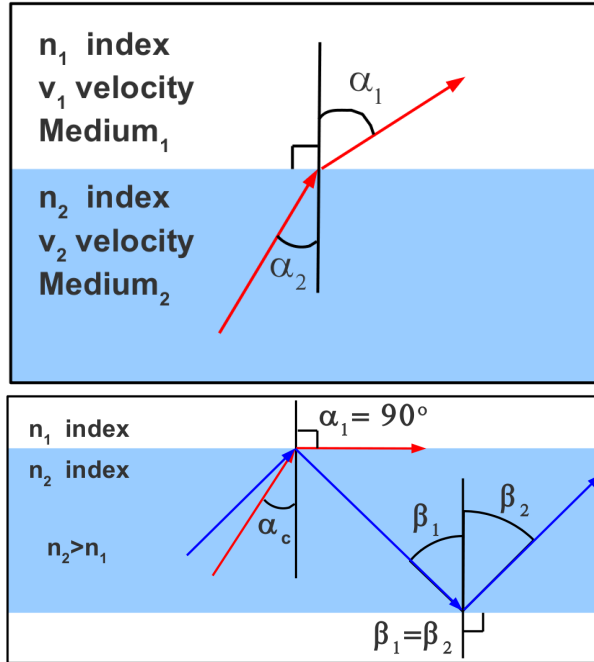


Figure 3.11: **Top:** Snell's law ( $\sin(\alpha_1)n_1 = \sin(\alpha_2)n_2$ ). Optical photon penetrates the edge between media with different refractive indices  $n_1 < n_2$ ,  $\alpha_1 > \alpha_2$  and  $v_1 > v_2$ . **Bottom:** Total internal reflection. If the incident angle of the photon bigger then critical angle  $\alpha_{\text{critical}}$  ( $\alpha_c$  on the figure) total internal reflection occur. In this case incident angel  $\beta_1$  equal to angle of reflection  $\beta_2$ .

and Eq. (3.24) the  $t_{\text{TOP}}$  can be calculated.

Another useful expression for group refractive index  $n_g$  can be obtain using these Eq. (3.25) and (3.22) :

$$n_g = \frac{c}{v_g} = \frac{n}{1 + \frac{\lambda}{n} \frac{\partial n}{\partial \lambda}} \quad (3.26)$$

$n_g$  is shown in the Figure 3.10.

### Total internal reflection

When light is passing through a boundary between two different isotropic media with refractive indexes  $n_1$ ,  $n_2$ , (see Figure 3.11 (Top)) the relation between incident angles  $\alpha_1$  and  $\alpha_2$  is the following:

$$\frac{\sin(\alpha_1)}{\sin(\alpha_2)} = \frac{v_1}{v_2} = \frac{n_2}{n_1} \quad (3.27)$$

where  $v_1$  and  $v_2$  are the light speeds in Medium<sub>1</sub> and Medium<sub>2</sub> respectively. This formula is known as the Snell's law. The law comes from Fermat's principle of least time, which in

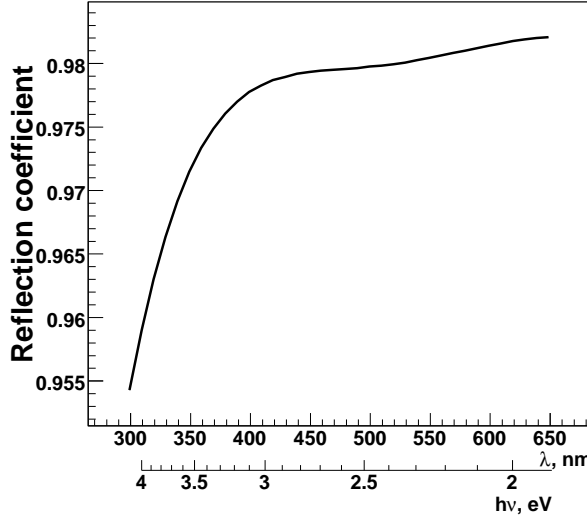


Figure 3.12: Reflection coefficient after 20 bounds in quartz as a function of wavelength (for *BaBar* DIRC bars [56]).

turn comes from the propagation of light as waves. When  $\sin(\alpha_1 = 90^\circ) = \frac{n_2}{n_1} \sin(\alpha_2) = 1$ ,  $\alpha_2$  in this case called critical angle ( $\alpha_{\text{critical}}$ ) (see Figure 3.11 (Bottom)). For example the  $\alpha_{\text{critical}}$  for the DIRC quartz in air interface photon with  $\lambda = 400$  nm is  $42.9^\circ$ .

If the photon propagates from more optically dense medium to less optical dense medium with incidence angle  $\beta_1 > \alpha_{\text{critical}}$  total internal reflection occurs see Figure 3.11 (Bottom). In case of well-polished surface one need to know two important consequences:

- The incident angel  $\beta_1$  equal to angle of reflection  $\beta_2$ . This will give as possibility of reconstruction the photon path length in the quartz radiator.
- The reflection coefficient can be very close to one ( $\sim 0.9992$ ) for *BaBar* DIRC bars. This value can be compared with the reflection coefficient of good aluminum mirror which would be around 0.92. In Figure 3.12 the reflection coefficient after 20 bounces in quartz as a function of wavelength is shown.

## Absorption

During light propagation inside the quartz bar, the photon can be absorbed by the material. This absorption is usually described in terms of free (or mean) path length: the depth at which the initial flux of the photons with given  $\lambda$  decreases by a factor of  $e$ . In our case, this effect is very small: the mean path length for photons at  $\lambda = 400$  nm is 350 m, see Figure 3.13.

## Mirror reflectivity

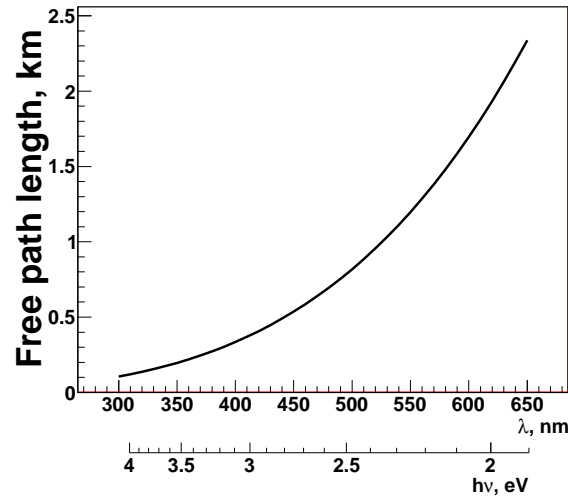


Figure 3.13: Free path length of the photons inside the quartz as a function of  $\lambda$  (for *BaBar* DIRC bars [56]).

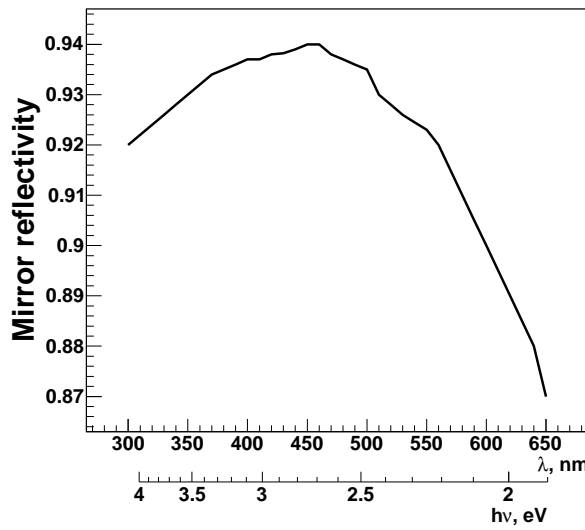


Figure 3.14: Aluminum mirror reflectivity as a function of  $\lambda$  (for *BaBar* DIRC mirrors [56]).

Some of the studied configurations of the DIRC-like TOF detector have an additional mirror in order to improve photon collection. Each time when a photon gets reflected there is non zero probability of absorption. One has to take this effect into account. The mirror reflectivity as a function of wavelength is shown on the Figure 3.14. We assume the mirror properties are the same as these of the *BaBar* DIRC mirrors.

### 3.5.4 Simulation of the PMT response

A geometrical description of the MCP-PMT has been implemented in Geant4 simulation see Figure 3.15. The base line PMT which we are going to use for the DIRC-like TOF detector is SL10 [23]. The full size MCP-PMT and 4 channels per PMT have been simulated. The big box in green (Figure 3.15) is a dummy volume (total detector volume) which has been implemented in order to have realistic overall dimensions of the whole system. The active area of the MCP-PMT is in light blue color. We simulate separately each PMT channel<sup>3</sup>. So the packing efficiency and active area of the PMT are naturally taken into account.

When the optical photon hits a PMT channel we store wavelength, time, position, channel number<sup>4</sup>, and photon path length information, and we stop simulating this photon.

Using as input information from Geant4, the offline analysis takes into account effects coming from the tube itself:

- Photon Detection Efficiency

Not all incident photons produce p.e. which are then detected by the PMT. The ratio between detected and total number of incident photons is known as Photon Detection Efficiency (PDE):

$$\text{PDE} = \frac{\text{Number of detected photons}}{\text{Total number of photons}} \quad (3.28)$$

For MCP-PMT the PDE mainly depends on two parameters: the quantum efficiency (QE) of the photocathode and the collection efficiency (CE) of the photoelectrons. The QE is the mean number of p.e. produced per incident photon. Usually QE is a function of the photon wavelength. Various type of photocathodes has been simulated. For the most popular bialkali photocathode the QE reaches 25 % for a wavelength around 400 nm. After the p.e. has been produced it goes into the MCP and creates an avalanche to amplify the signal. The collection efficiency is a probability that the photoelectron is collected into MCP hole. For 10  $\mu\text{m}$  pore

---

<sup>3</sup>Usually in simulation the sensitive area is a global volume. Then the actual geometric coverage of PMT has to be taken into account.

<sup>4</sup>FTOF sector contain 14 pmt which have four channels each. So the channels are numbered from 0 to 55

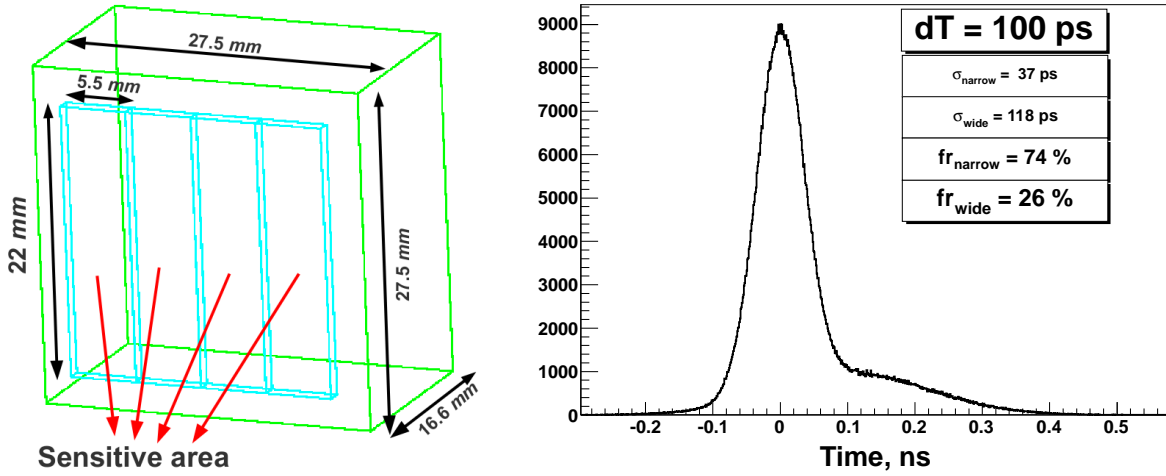


Figure 3.15: **Left:** Description of the MCP-PMT within Geant4 simulation. The green box is dummy volume which represent the MCP-PMT ( $27.5 \times 27.5 \times 16.6$ ) mm<sup>3</sup>. The light blue boxes are the MCP-PMT channels ( $22 \times 5.5$ ) mm<sup>2</sup> they are actual active area. **Right:** The transit time spread of the SL10 MCP-PMT. The two Gaussian structure can be observed - narrow and wide. The RMS of the time resolution for narrow and wide components are  $\sigma_{\text{narrow}} = 37$  ps,  $\sigma_{\text{tail}} = 118$  ps. The relative probabilities (fractions) are  $fr_{\text{narrow}} = 74\%$ ,  $fr_{\text{tail}} = 26\%$ . The narrow and wide components are separated in time  $dT \sim 100$  ps.

MCP-PMT this number is usually around 60 % [23]. Figure 3.16 shows the different types of simulated photocathodes.

- Transit Time Spread of the MCP-PMT.

The transit time is the time between the p.e. production and the moment when the amplified output signal exits from the PMT. This time has a jitter known as TTS (Transit Time Spread). For SL10 the TTS (see Figure 3.15 from the right) is the sum of two Gaussian distributions, one narrow and the other wide. The wide (tail) component is produced by recoil electron inside the MCP-PMT and is delayed in time. The time resolutions for narrow and wide components are:  $\sigma_{\text{narrow}} = 37$  ps,  $\sigma_{\text{tail}} = 118$  ps. The corresponding fractions are:  $fr_{\text{narrow}} = 74\%$ ,  $fr_{\text{tail}} = 26\%$ . The narrow and wide components are separated in time by  $dT \sim 100$  ps. The TTS distribution is assumed to be the same for all photocathodes.

### 3.5.5 $\sigma_{\text{chromaticity}}$ and $\sigma_{\text{transit}}$ production

As the group velocity is a function of  $\lambda$ , photons with different wavelength travel at different speeds. This introduces an additional smearing of the optical photon timing.

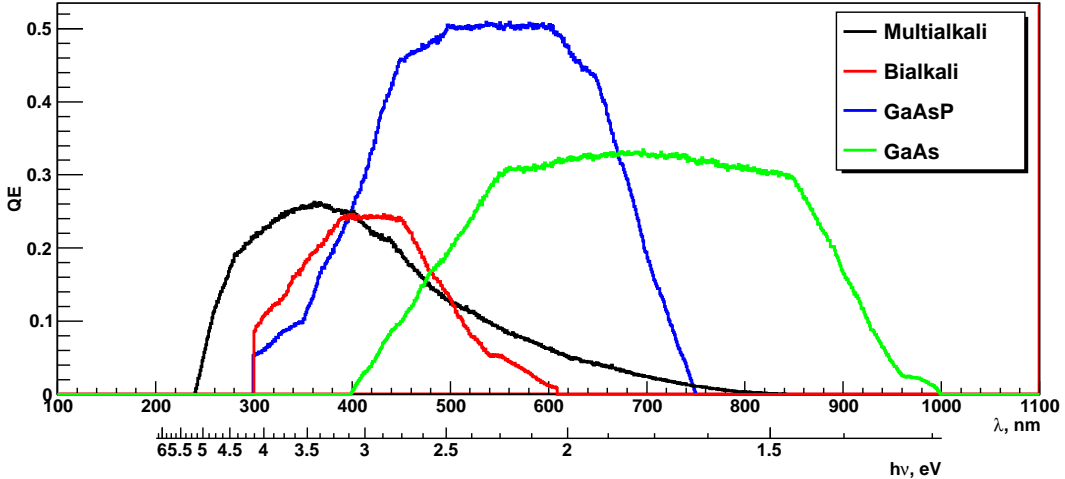


Figure 3.16: Quantum efficiency vs wavelength for different photocathodes [57].

This effect is proportional to the photon path length and its RMS is  $\sigma_{\text{chromaticity}}$ . This term matters for DIRC-like TOF detector since it cannot be corrected unlike for the FDIRC [22] (FDIRC prototype was the very first Cherenkov detector ever which successfully corrected the chromatic error by timing), or TORCH [58, 59, 60] (TORCH is a proposal, it does not exist yet) detectors which measure both  $\theta_{\text{Cherenkov}}$  and the photon propagation time. However the DIRC-like TOF detector is small so the photon path length and hence  $\sigma_{\text{chromaticity}}$  will not be larger than 40 ps.

The chromatic term is an important effect to estimate in order to have an idea about intrinsic time resolution of the DIRC-like TOF detector. In order to make this estimate we use the Geant4 simulation. We simulate the Kaons with 3.5 GeV/c momentum perpendicular to the quartz tile with flat distributed position. In Figure 3.17 time distribution of photons with fixed path length are shown. In case of very short photon path length (for example between 10 mm and 11 mm),  $\sigma_{\text{chromaticity}}$  is very small: Figure 3.17(Left). The time of the Cherenkov photon arrival is almost flat-distributed in the 50 ps window which is equal to the time taken by the tracks to cross quartz radiator: this phenomena is transit production. This term does not depend on the photon path length, but only on the quartz radiator particle crossing time. The RMS of the photon transit production effect is given by the formula:

$$\sigma_{\text{transit production}} = \frac{1}{\sqrt{12}} t_{\text{transit}} = \frac{1}{\sqrt{12}} \frac{w}{\beta c} \quad (3.29)$$

where:  $t_{\text{transit}}$  is the time taken by the particle to cross the quartz radiator of thickness  $w$ . In the example described above:  $\sigma_{\text{transit production}} = \frac{50 \text{ ps}}{\sqrt{12}} \sim 14 \text{ ps}$ .

If we increase the photon path length in the quartz (between 300 mm and 303 mm),

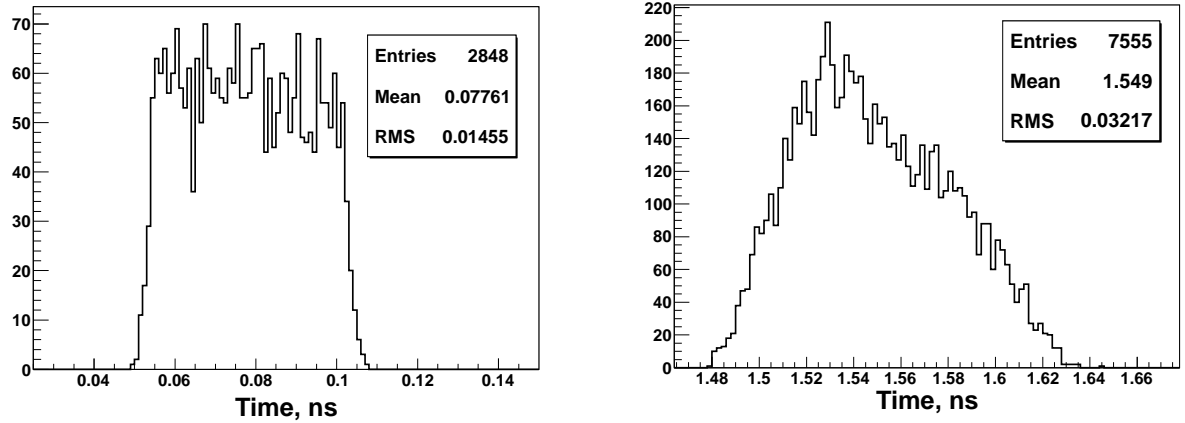


Figure 3.17: **Left:** Time distribution of the Cherenkov photon arrival, the photon path length is fixed between 10 mm and 11 mm.  $\sigma_{\text{chromaticity}}$  is very small in this case the RMS of the distribution dominated by  $\sigma_{\text{transit production}}$ . One can see that it is almost flat distributed. **Right:** Time distribution of the Cherenkov photon arrival, the photon path length is fixed between 300 mm and 303 mm. The  $\sigma_{\text{chromaticity}}$  is not small any more. This time distribution defined by convolution between chromatic and transit production effect. Note we did not simulate the photocathode in this particular case.

the time distribution becomes wider (see Figure 3.17(Right)) because the chromatic effect contributes more. Therefore to choose the best photocathode one should not only study the number of p.e. but also the chromatic term. On Figure 3.18 (Left)  $\sigma_{\text{chromaticity}} \oplus \sigma_{\text{transit production}}$  as a function of photon path length for different photocathodes is shown. One can see that for photon path length = 0 mm  $\sigma_{\text{chromaticity}} \oplus \sigma_{\text{transit production}}$  is around 14 ps, which is equal to  $\sigma_{\text{transit production}}$ . Using this equation:

$$\sigma_{\text{chromaticity}}^2 = (\sigma_{\text{chromaticity}} \oplus \sigma_{\text{transit production}})^2 - \sigma_{\text{transit production}}^2 \quad (3.30)$$

$\sigma_{\text{chromaticity}}$  can be measured directly see Figure 3.18(Right).

As expected in case of 100% quantum (all photons are converted into p.e.) efficiency  $\sigma_{\text{chromaticity}}$  is maximum. But the minimal  $\sigma_{\text{chromaticity}}$  is for the GaAs photocathode. One can see from Figure 3.16 that GaAs is sensitive in a very wide  $\lambda$  region in comparison to GaAsP and Bialkali: hence it should have a bigger  $\sigma_{\text{chromaticity}}$ . But if we look at 3.10(Right) where the quartz refractive index is shown we see that this index is almost constant at high  $\lambda$ . So the group velocity of the photons does not change much too, which explains why  $\sigma_{\text{chromaticity}}$  is minimal for GaAs. GaAs is not sensitive in blue region where the majority of the Cherenkov photon are produced (see Figure 3.10 (Left)). Hence, the GaAs photocathode is not satisfactory as it would not collect much light.

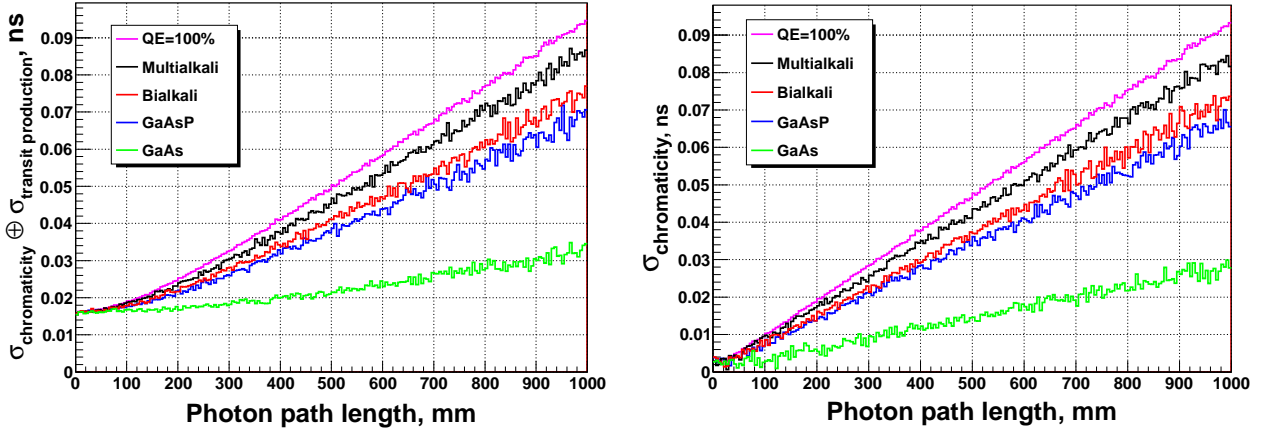


Figure 3.18: **Left:**  $\sigma_{\text{chromaticity}} \oplus \sigma_{\text{transit production}}$  as a function of photon path length.  
**Right:**  $\sigma_{\text{chromaticity}}$  as a function of photon path length.

### 3.5.6 Geometry optimization

Geometry optimization of the DIRC-like TOF detector has been studied with Geant4 simulation. One has to optimize the time spread and the number of detected photons. For this reason we studied many different geometries; the main ones are listed in Table 3.2.

Table 3.2: Description of the different geometries.

Configuration/GeomID	0	1	2	3	4	5	6	7	8
PMT position	A	B	B	B	D	B	B	C	D
PMT orientation	V	V	H	H	V	V	V	V	V
Mirror	-	+	+	-	+	+	-	+	+
Absorber	SB	SB	SB	SB	ST	B	B	B	T
Tilting	-	-	-	-	+	-	-	-	+

**Time resolution for the different geometries.** In this section the effect of the geometry on the time resolution of the photon arrivals is studied. The larger the particle momentum the better the timing accuracy is needed to separate efficiently kaons and pions. That is why we generate kaons with 3.5 GeV/c momentum which enter the DIRC-like TOF detector in the center of the tile. We put a material to absorb photons (called 'photon absorber' in the following) on all sides but the one with PMTs. In this way, only direct photons reach the detectors; photons with complicated paths (reflections, etc.) are absorbed by this material and do not contribute to timing. In this way we compare five different geometries (0, 1, 2, 3, 4) and study effects coming from:

- Position of the PMT. The PMT itself can be located in four different ways. In

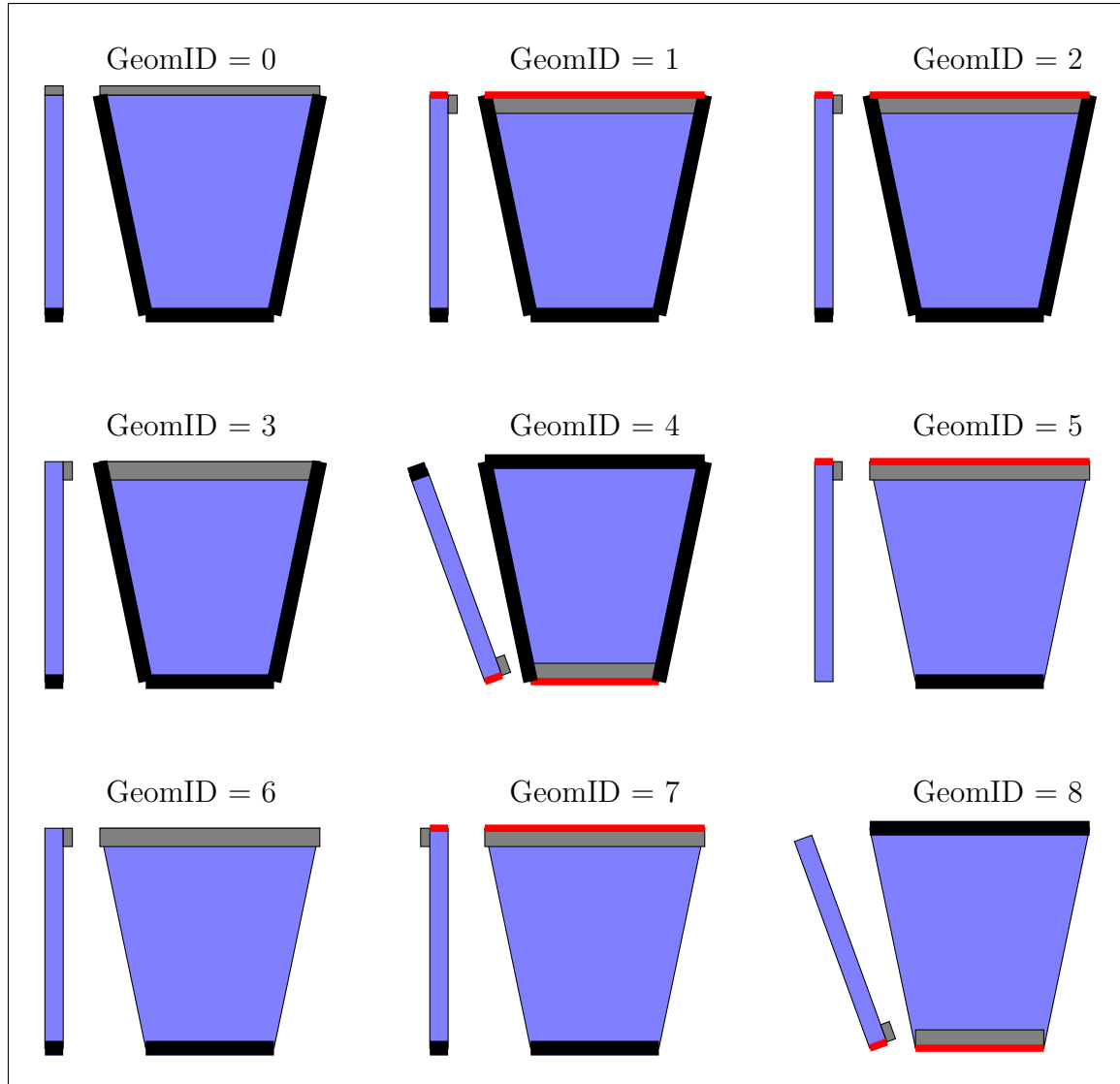


Figure 3.19: Schematic drawings of the different geometries which have been studied. For each geometry two different views (side and front) are shown. The trapezoid in blue represents the quartz radiator, the gray box the PMTs, the black box the absorber (see text for details) and the red box the mirror. Each geometry is associated with its identification number called GeomID, ranging from 0 to 8.

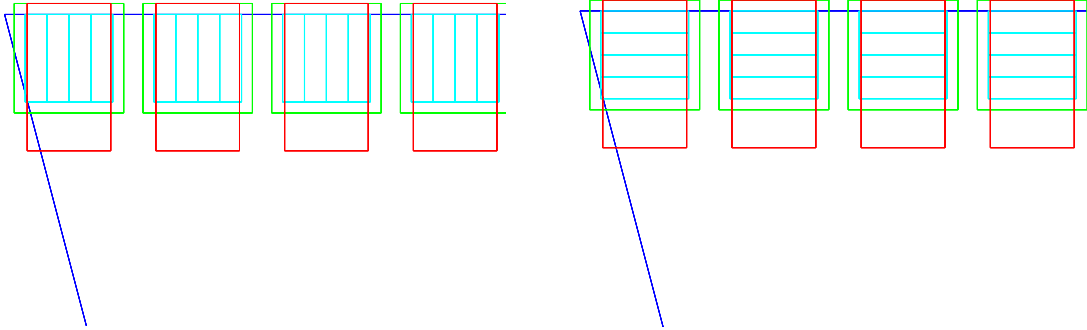


Figure 3.20: The PMT channel orientation vertical (V) from the left and horizontal (H) from the right. In dark blue is the quartz tile radiator, the light blue correspond to the sensitive area of the PMT, green box is the PMT body and in red the electronics are shown.

Table 3.2 we call them A, B, C and D.

**A)** the PMT is on the face of the quartz tile. As we will see later this is the best position for timing but it is not possible to use MCP-PMT due to bad angle to the magnetic field. One could use SiPM [61] but they are sensitive to neutron background; studies are in progress within SuperB [62] to test their performances after irradiation.

**B)** the PMT is attached from the top of the quartz tile: this is our baseline position for the PMTs as it takes into account the magnetic field of the *SuperB* detector.

**C)** same as B but the PMT attached from the opposite side of the quartz sector. This particular configuration (GeomID=7) will be used later to study effects on the number of collected photons; it should not have any effect on their timing.

**D)** the PMT is attached to the bottom of the detector. All configurations with this PMT position have tilted quartz radiators (by 22.7° degrees) in order to collect more light – see configurations 4 and 8 in Figure 3.19.

- Orientation of the PMT. Our baseline PMT is the Hamamatsu SL10 with 4 channels. The size of each channel is  $5.5 \times 22 \text{ mm}^2$  and so the PMT can be oriented in two different ways: horizontal (**H**) or vertical (**V**) see Figure 3.20.
- Mirror. In order to collect more light, a mirror can be attached to the face of the DIRC-like TOF detector on the top or on the bottom. But this will increase the number of possible photon path lengths and affect their time distribution.

We observe interesting behavior of the time resolution per channel depending on the PMT position. On Figure 3.21, the time of the photo electron arrival vs channel for kaon at 3.5 GeV/c hitting the DIRC-like TOF detector in the center of the sector for different geometries (0 on the left and 1 on the right) are shown. One can see that these two

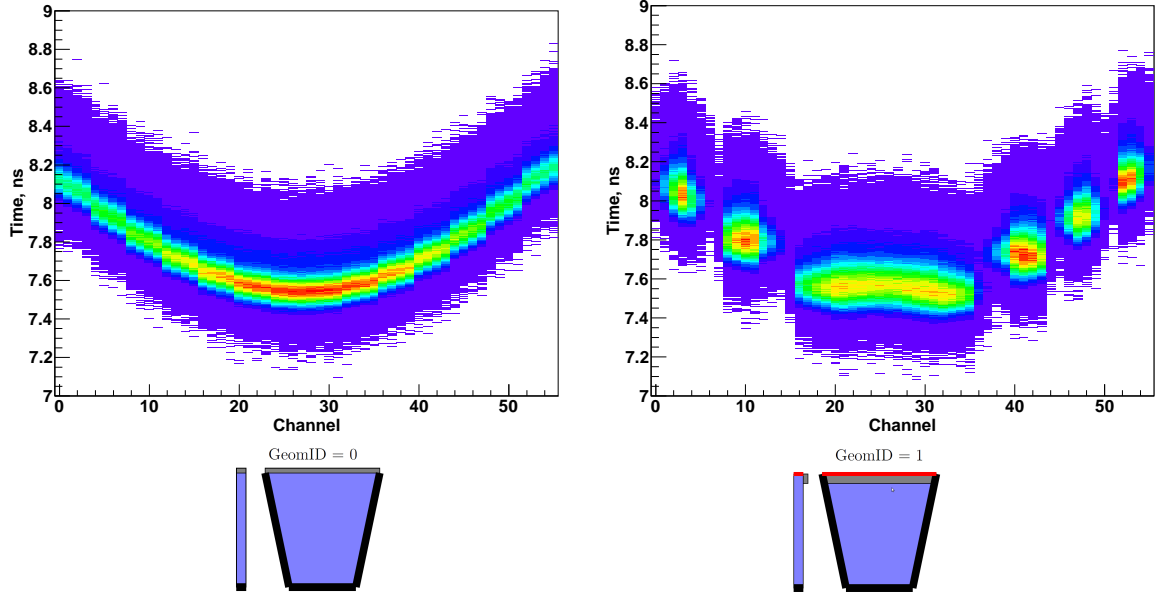


Figure 3.21: Time of the photo electron arrival vs channel for kaon at 3.5 GeV/c hitting the DIRC-like TOF detector in the center of the sector for different geometries: GeomID=0 in the left and GeomID=1 in the right.

patterns are very different: smooth for GeomID = 0 and with an "island" structure for GeomID=1. Geometry 0 is the one with PMTs installed on the top face of the quartz tile while for geometry 1 PMTs are on the side of the sector. Patterns for geometries 2 and 3 (see Figure 3.22) are similar to pattern 1 but have more timing steps (sharp changing of the mean values) between neighbor channels. Figure 3.23 (Left) shows the Full Width at Half Maximum (FWHM) of the photon time distribution channel by channel for geometries 0, 1 and 2. One can see that, as expected from the comparison of the 2D-distributions above, the best timing is achieved with geometry 0 which cannot work with MCP-PMT due to the strong longitudinal *SuperB* magnetic field ( $\sim 1.5$  T); the only option in this case would be to use SiPM.

The effect on time distribution coming from the mirror can be seen on Figure 3.24: on the left, the FWHM of the time distribution vs. channel with and without mirror are compared. One can see that for some channels the FWHM is larger with a mirror while they are the same for the other channels. On the right side of the plots the time distributions for channel 30 (taken as an example) are shown. The reflected photons travel more, hence they are late in time and form a second peak.

Two configurations of the DIRC-like TOF detector have PMTs located at the quartz tile inner radius (GeomID=4, 8). In this case, the quartz radiator is tilted by approximately the same angle as the forward EMC to have more photons internally reflected – that is why we call these geometries 'tilted'. In Figure 3.25 (Left) the distribution of the

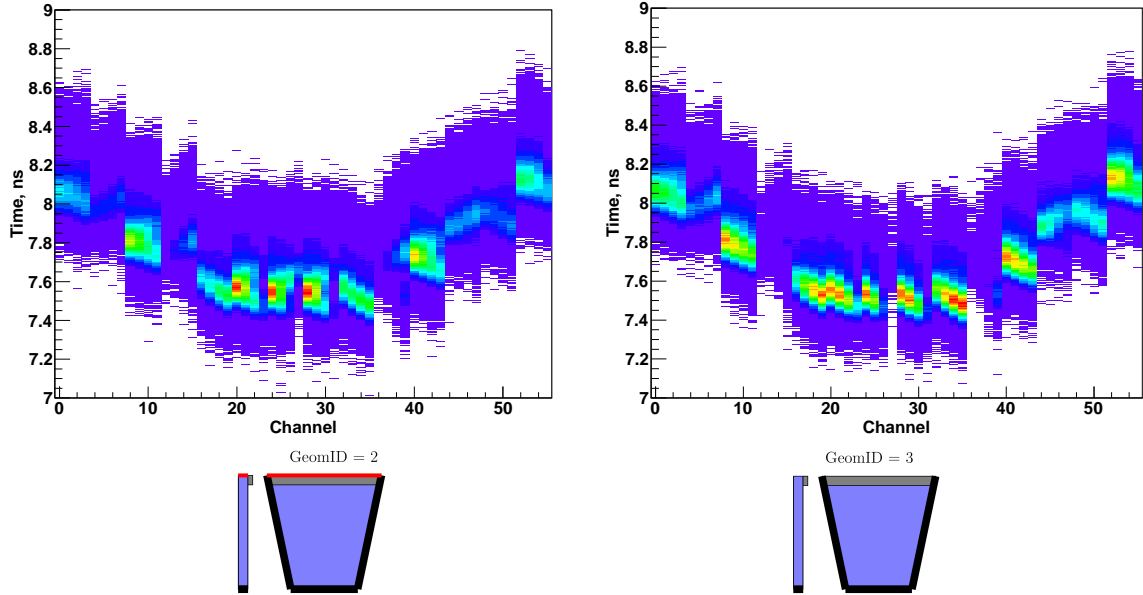


Figure 3.22: Time of the photo electron arrival vs channel for kaon at 3.5 GeV/c hitting the DIRC-like TOF detector in the center of the sector for different geometries: GeomID=2 on the left and GeomID=3 on the right.

time of the photon arrival vs channel is shown. One can see a pattern quite similar to GeomID=1 but the number of PMTs is obviously smaller. The timing is quite good, as seen in Figure 3.25(Right).

**Number of photons for different geometries.** In order to study the effect of the different geometries on the amount of detected light, we generate from the interaction point 0.8 GeV/c kaons with uniformly distributed polar angle  $\theta$  and azimuthal angle  $\phi$  for 7 (configuration 2 is equivalent to 4 in term of number of photons; configuration 4 is worse than configuration 8 by definition) different configurations (0, 1, 3, 5, 6, 7 and 8) of the DIRC-like TOF detector. We know from Eq. (3.21) that charged particles with higher momentum produce more light. That is why we choose to look at number of photoelectrons coming from low momentum kaon. As we will see later for geometries which use photon absorber, the amount of light depends on the position and the direction of the charged track entering the quartz sector. That is why we generate uniform distribution of tracks in  $\theta$  and  $\phi$ . The main goal is to study effects coming from:

- The absorber. In order to only detect direct photons, absorber can cover the sides of the tile. In this case, the time vs. channel distribution is very simple but we detect less light. In Table 3.2 the presence of absorber is indicated by letters: **S** absorber on left and right faces, **T** top face, **B** bottom face. Geometries without absorber on the left and right sides will be called 'unscreened'. We always assume a 100 % efficient absorber.

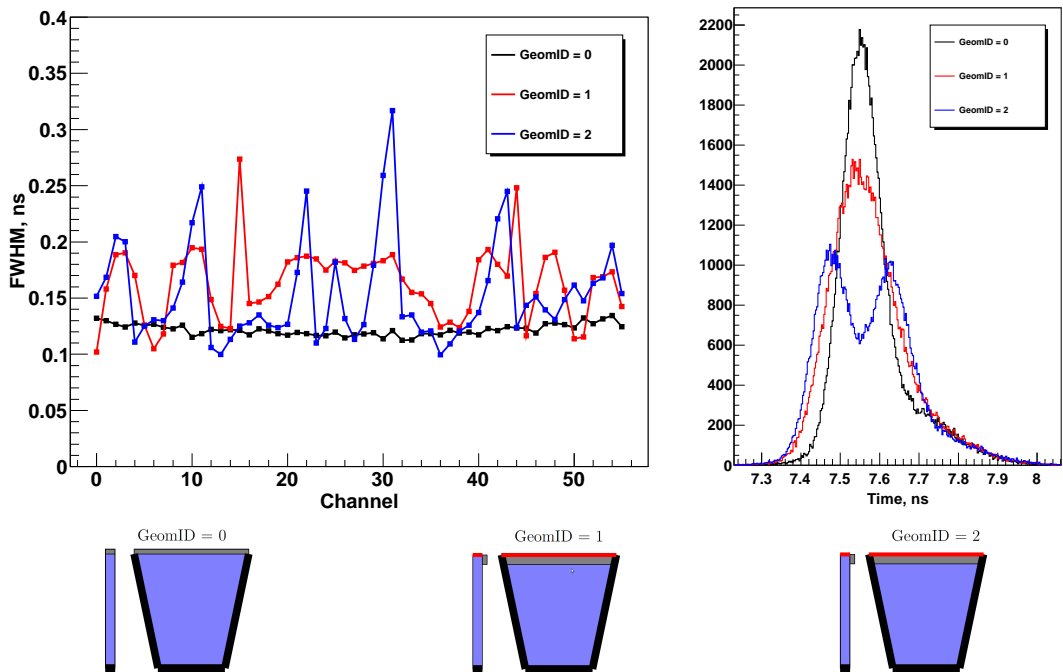


Figure 3.23: **Left:** FWHM of the time distribution vs. channel, for different geometry configurations. **Right:** Time distribution of the photons for channel 30 taken as a representative example. Both plots are for 3.5 GeV/c kaon hitting the DIRC-like TOF detector in the center of the sector.

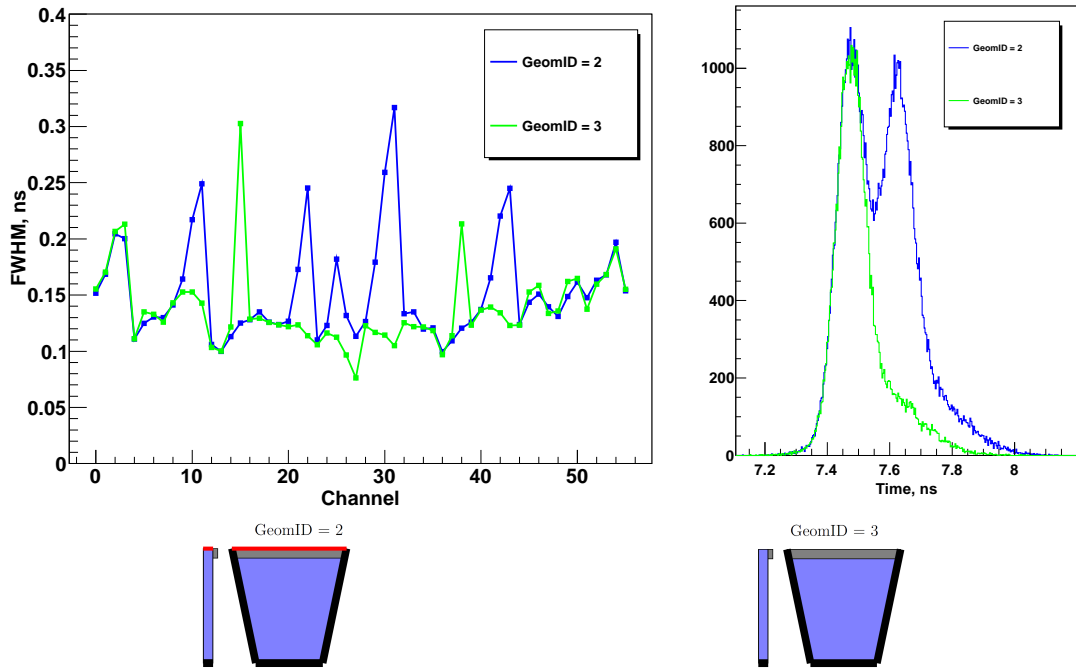


Figure 3.24: **Left:** FWHM of the time distribution vs. channel, for different geometries with and without mirror. **Right:** Time distribution of the photons in channel 30. Both plots are for 3.5 GeV/c kaon hitting the DIRC-like TOF detector in the center of the sector. One should really work with a variable " $\text{Time}_{\text{expected}} - \text{Time}_{\text{measured}}$ " as this is the only variable which will have a Gaussian distribution. This was suggested by J. Va'vra in Orsay, 2009, slide 13, where DIRC-like TOF counter was proposed first time: <http://agenda.infn.it>

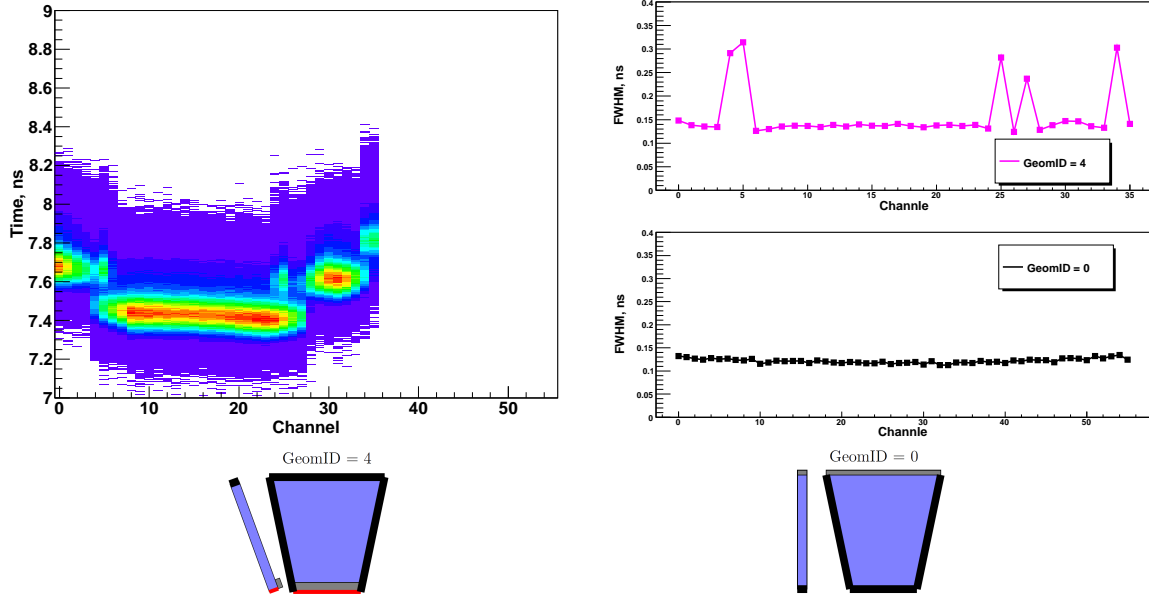


Figure 3.25: **Left:** Time of the photon arrival vs. channel for GeomID=4; the PMTs are located on the inner radius of the quartz tiles which explains why they are less channel available. **Right:** FWHM of the time distribution vs. channel, for geometries 0 and 4. This is for kaon at 3.5 GeV/c hit the DIRC-like TOF tile in the middle.

- The mirror. The mirror increases the number of photons but degrades the time resolution.
- The PMT position. Different positions (A, B, C and D) change the number of detected photo electrons.
- The thickness of the radiator. In order to increase the amount of detected light, the thickness of the radiator can be increased. This has been studied for different DIRC-like TOF configurations.
- The tilting of the DIRC-like TOF. If the detector could be tilted by a significant angle  $\sim 20^\circ$ - $25^\circ$ , then more photons would be trapped by total internal reflection and hence detected. Due to space constraints on the forward side of *SuperB* this is only possible if the DIRC-like TOF is installed parallel and close to the forward EMC. With a tilted geometry, PMTs can be installed at the bottom of the tile as part of the Cherenkov light will go down.
- The different photocathodes of the PMT. Each photocathode has its own photo detection efficiency of the Cherenkov light as well as its own  $\sigma_{\text{chromaticity}}$ . Therefore one has to make a tradeoff between photon yield and time spread. Unless otherwise noted, we simulate a multialkali photocathode with 60 % collection efficiency.

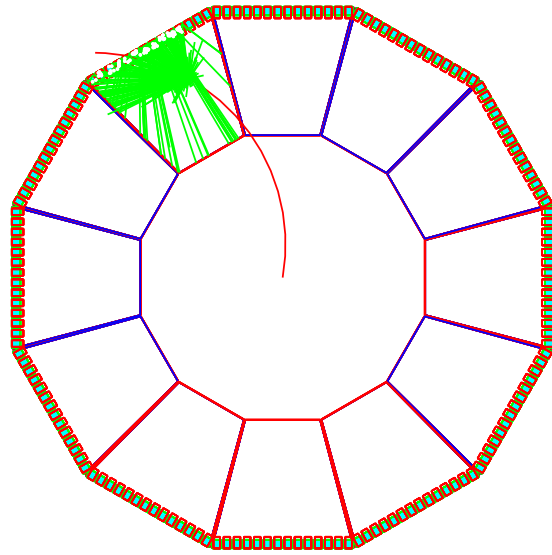


Figure 3.26:  $K^-$  with 0.8 GeV/c momentum,  $\theta = 23^\circ$ ,  $\phi = 80^\circ$  generated at the IP and propagating in the 1.5 T magnetic field.

In case of no material in front of the DIRC-like TOF detector, the momentum of the track and its  $\theta$  and  $\phi$  would completely define its intersection with the quartz tile. In reality, all charged particles will interact with material before the detector and their intersections will slightly change, but this effect is estimated to be very small [63]. Let's now study these effects one by one.

**Absorber vs. without absorber.** We generate low momentum  $K^-$  (0.8 GeV/c) which are bended by the *SuperB* magnetic field – see Figure 3.26. Therefore, the number of detected photons depends strongly on the track parameters, leading to asymmetric patterns in the 2D maps below. In case of geometries with photon absorber from the sides, the asymmetric pattern of the p.e. in the  $\theta$  -  $\phi$  plane is significant – see Figure 3.27. Removing photon absorber, the distributions look more symmetric – see Figure 3.28 – and the amount of collected light increases as expected – see Figure 3.29.

**PMT position.** Comparing the top and middle 2D histograms on Figure 3.27 shows that geometry with PMTs on the B location (GeomID=3) collects slightly less light than configuration 0. As shown above, adding a mirror allows one to recover all the lost photons and even more. If we compare the middle and bottom 2D histograms from Figure 3.28 we can see that moving PMTs from location B to C degrades the light collection even more, especially at large  $\theta$ . On Figure 3.30, one can see that the number of collected photons has longer tail for geometry 5 (PMTs at the B location) than for geometry 7 (PMTs at the C location).

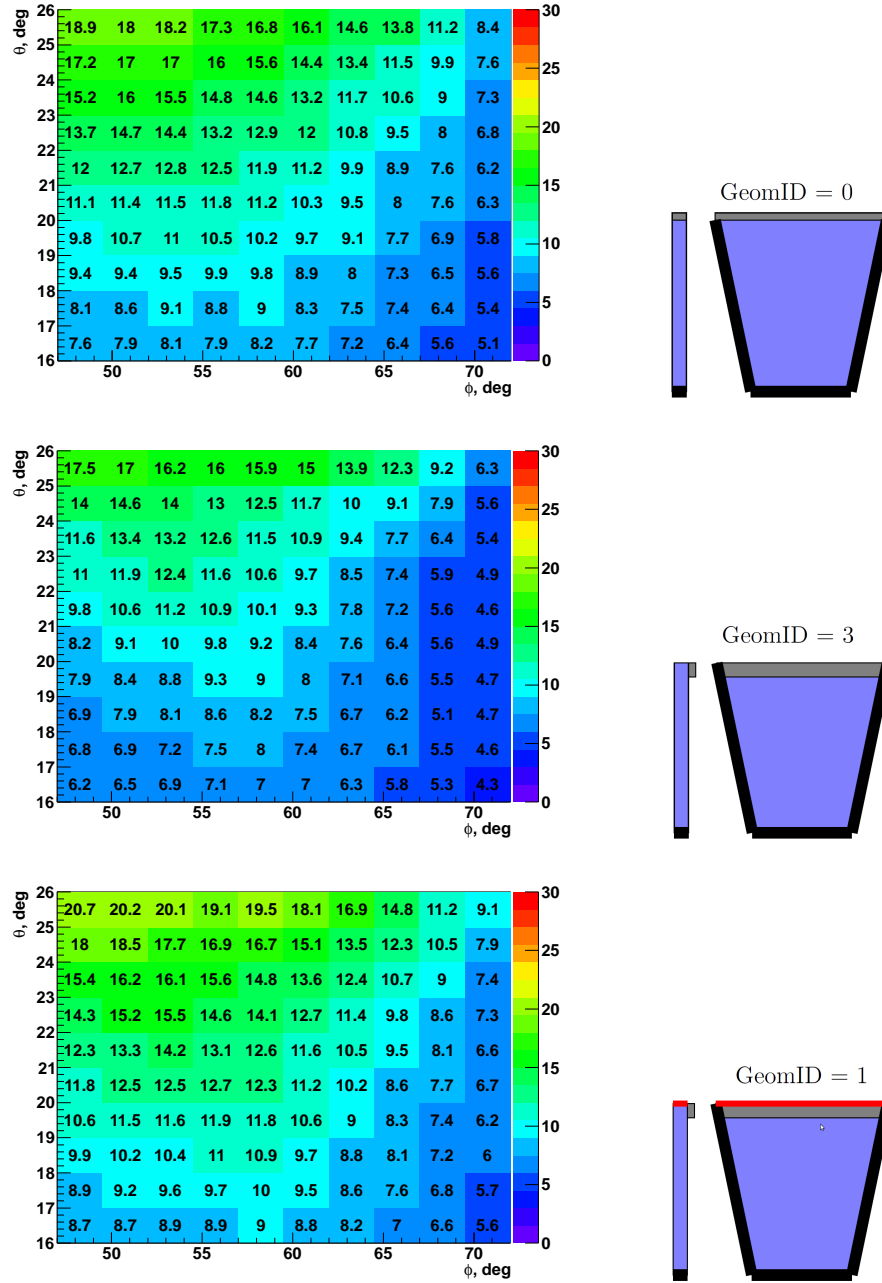


Figure 3.27: Average number of p.e. for 0.8 GeV/c kaons in the  $\theta$  vs.  $\phi$  plane for GeomID=0 (top), GeomID=3 (middle) and GeomID=1 (bottom). These three configurations have photon absorber on left, right and bottom sides, so they detect only direct photons. Comparison between top and middle 2D histograms shows a loss of photons coming from the less optimal position of the PMTs (from A to B). In order to recover photons, configuration 1 includes a mirror on the top face. As shown on the bottom map, it provides even more photons than configuration 0 due to geometrical effects (in average the 'effective' sensitive area is larger with configuration 1). For these plots and all the following we simulate a multialkali photocathode with 60 % collection efficiency and a 100 % efficient absorber.

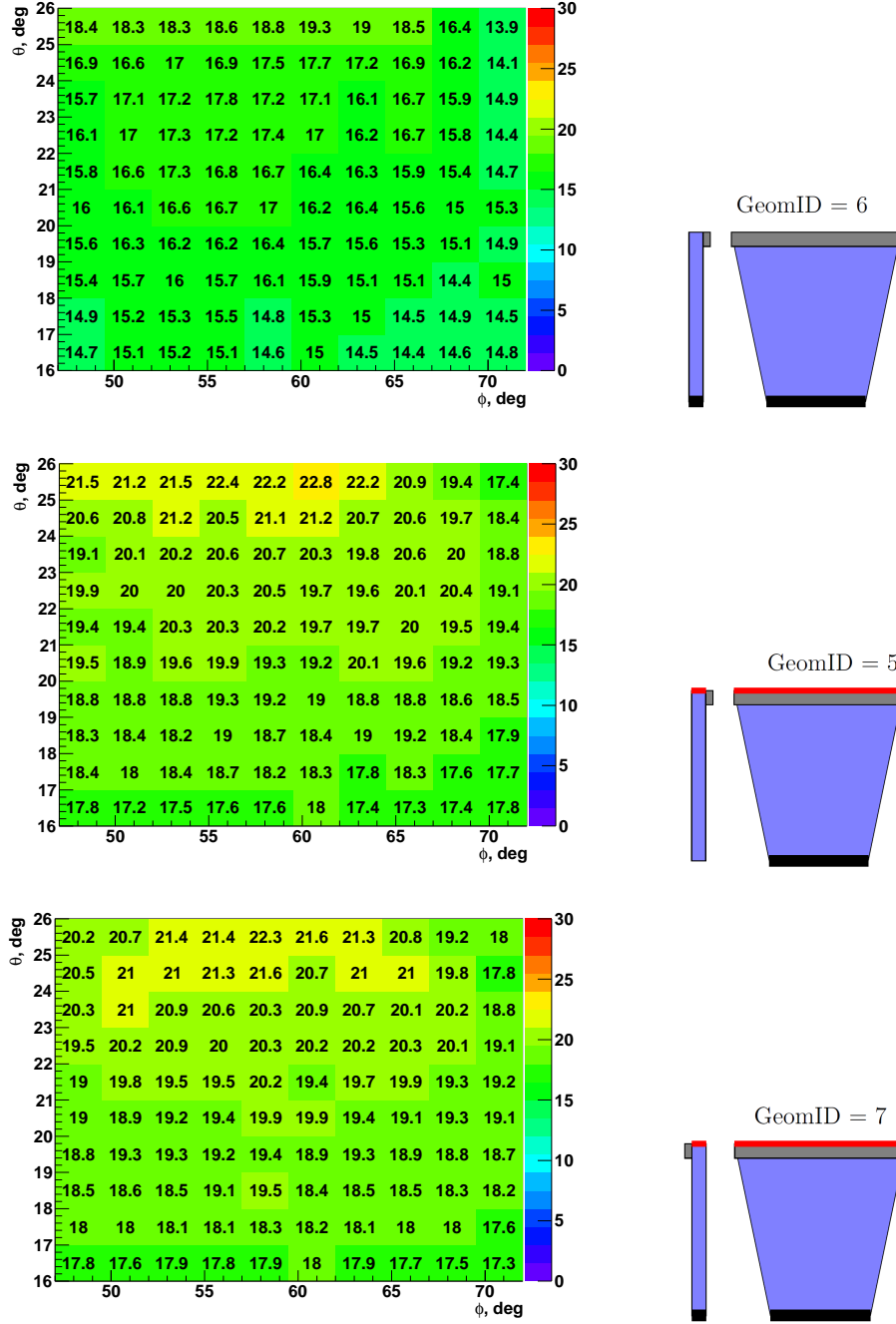


Figure 3.28: Average number of p.e. for 0.8 GeV/c kaons in the  $\theta$  vs.  $\phi$  plane for GeomID=6 (top), GeomID=5 (middle) and GeomID=7 (bottom). These three configurations have no photon absorber on the left and right sides so they detect additional photons. Comparison between top and middle 2D histograms shows an improvement in the number of p.e. coming from the mirror, just like for the screened configurations. If one compares the middle and bottom 2D histograms, one can see that moving the PMTs from position B to C slightly decreases the number of photons, in particular for large  $\theta$ .

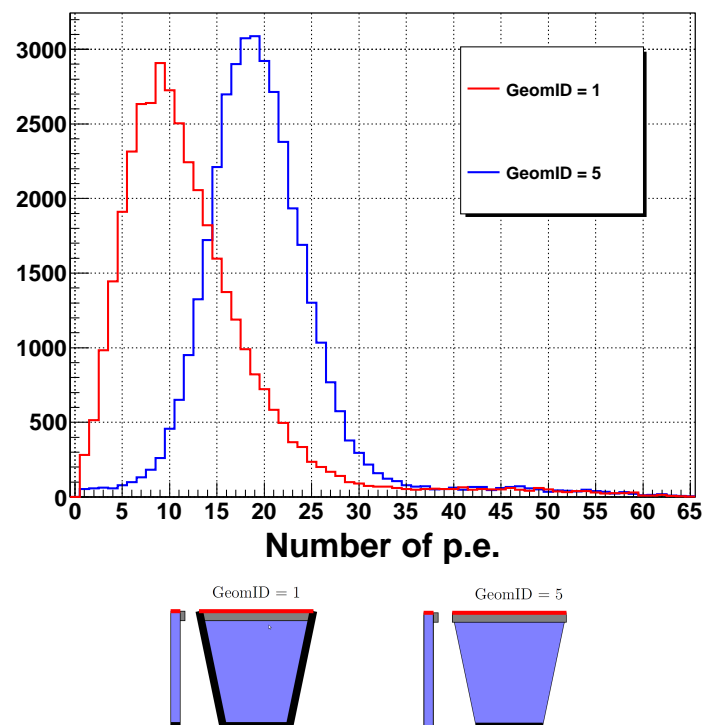


Figure 3.29: Number of p.e. for 0.8 GeV/c kaons with (red histogram) and without (blue histogram) absorber.

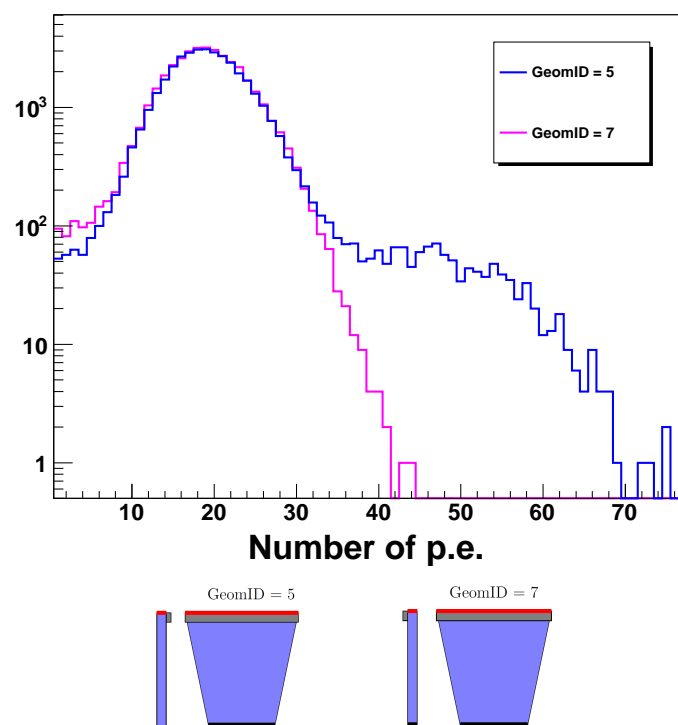


Figure 3.30: Number of p.e. for 0.8 GeV/c kaons and geometries without absorber but different positions of the PMTs: B (blue histogram) and C (magenta histogram).

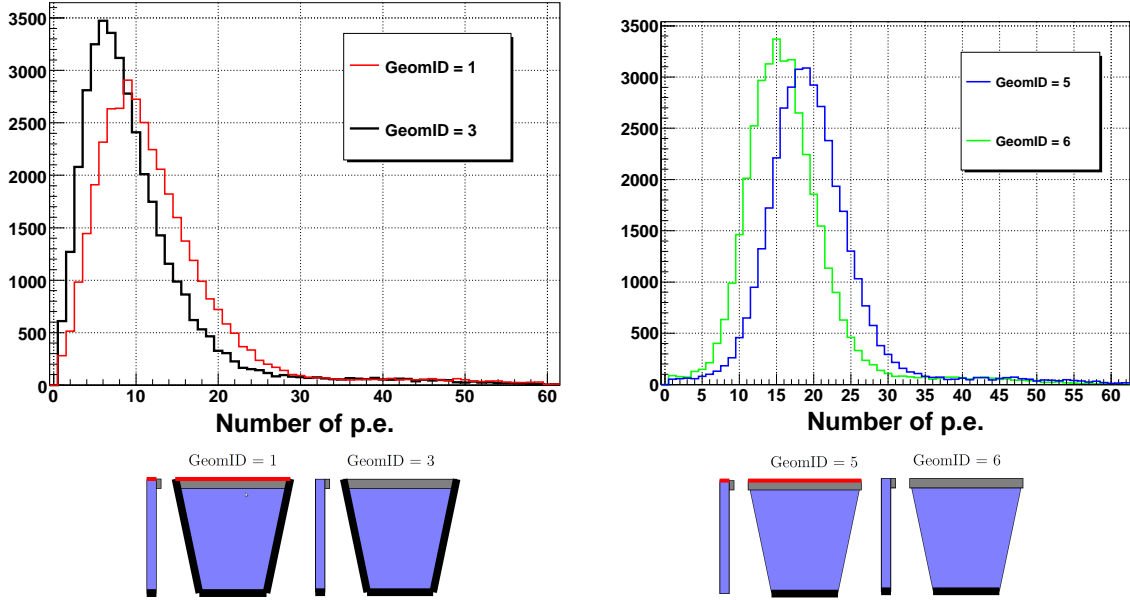


Figure 3.31: Number of p.e. for 0.8 GeV/c kaons. The effect of the mirror is shown on geometries without (Left) and with (Right) absorber. GeomIDs 3 and 6 (1 and 5) are without (with) mirror.

**Mirror.** The mirror provides a gain of 20% - 25% collected photons both for un-screened (compare GeomID=3 and GeomID=1 in Figure 3.27) and screened (compare GeomID=6 and GeomID=5 in Figure 3.28) geometries. Figure 3.31 summarizes this effect by comparing 1D distributions of the number of photo electrons.

**Tilted geometry.** This configuration is very promising at first sight as it has a lot of advantages.

- The total amount of PMTs (the dominant cost of the device) is reduced by 25% as they can be located in the inner radius of the quartz tiles.
- The DIRC-like TOF detector can be located parallel and very close to the forward EMC. In principle this would minimize the degradation of the forward EMC performances due to the additional DIRC-like TOF material. But Geant4 studies [64] have shown that the impact of the DIRC-like TOF on the  $\pi^0$  reconstruction efficiency and energy resolution of the EMC is very small. The only noticeable effect is on the low energy photon efficiency for which the distance between the DIRC-like TOF detector and the forward EMC matters.
- As can be seen on Figure 3.25, the spread of the photon arrival time for the tilted configuration is almost as good as for GeomID = 0.

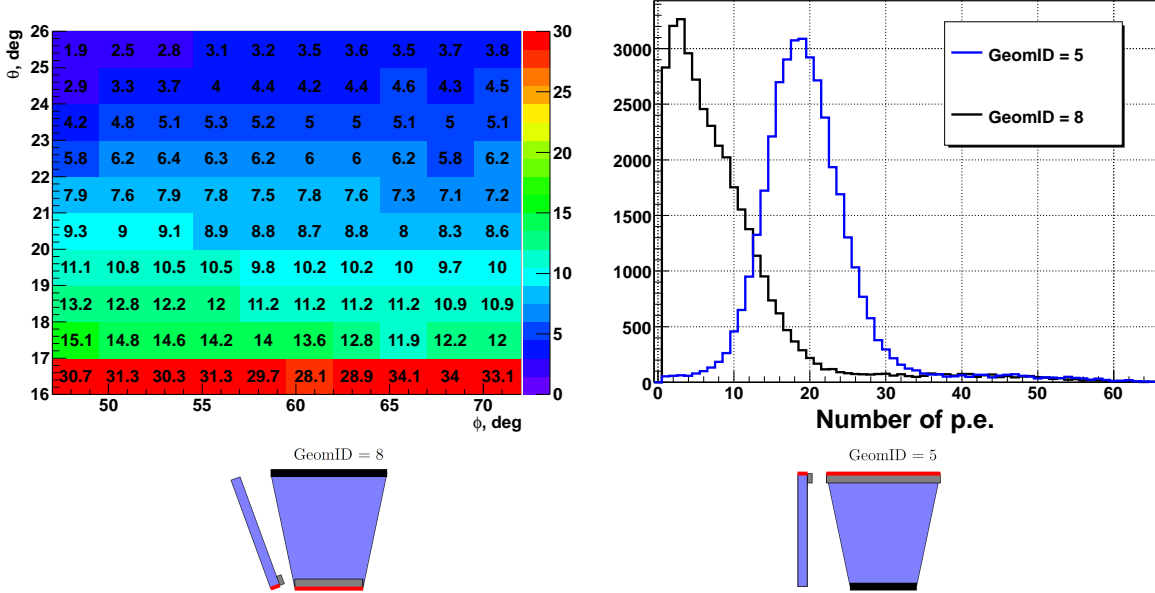


Figure 3.32: **Left:** Average number of p.e. for 0.8 GeV/c kaons in the  $\theta$  vs  $\phi$  plane for GeomID=8. **Right:** Comparison of the number of p.e. for 0.8 GeV/c kaons between GeomID=8 (tilted) and GeomID=5 (un-tilted).

But the amount of collected light is the main issue for this configuration and the main reason why it is not selected. On Figure 3.32 (left) one can see that the number of photons produced by tracks with  $\theta \approx 21^\circ$  is very small. The right side of Figure 3.32 compares the number of detected p.e. for tilted (GeomID = 8) and un-tilted geometry (GeomID = 5).

**Different photocathodes.** The histograms of the number of p.e. for different photocathodes are shown on Figure 3.33. One can see that with multialkali photocathodes, the number of detected p.e. is 20 % larger than with bialkali. This is due to the fact that the multialkali quantum efficiency extends over a wider  $\lambda$  range, especially in the low wavelength region where Cherenkov photons are preferentially produced. We show results for GaAsP and GaAs photocathodes as well. As can be seen on Figure 3.33, the PMT with GaAs photocathode does not detect much light so this type of photocathode is not suitable for the DIRC-like TOF in spite of its small  $\sigma_{chromaticity}$  see Figure 3.18. On the other hand, the GaAsP photocathode is potentially very promising as it has the best PDE for Cherenkov light spectrum and a good  $\sigma_{chromaticity}$ . Unfortunately the PMTs with GaAsP photocathodes are not commercially available yet which is the reason why our baseline solution assumes a multialkali photocathode.

**Thickness of the quartz radiator.** The variation of the average number of detected p.e. for different thicknesses of the quartz radiator and for different configurations of the DIRC-like TOF detector are shown on Figure 3.34. One can see that the increase is linear for GeomID=0, which is expected as the number of Cherenkov photons is proportional

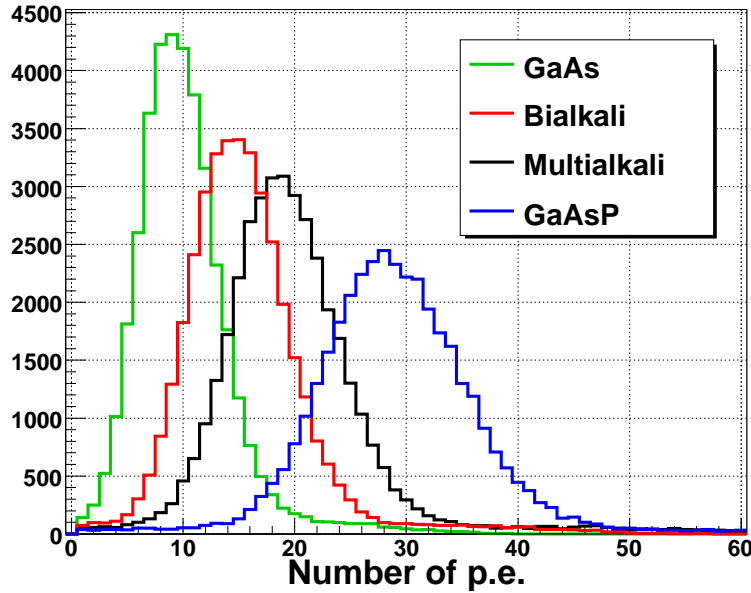


Figure 3.33: Number of detected p.e. for different photocathodes. We simulate  $K^-$  at 0.8 GeV/c and GeomID=5.

to the track path length in quartz. Yet, for GeomID=1 and 3 the variation is not linear. This effect can be understood as follows.

When photons propagate to the PMTs they bounces on the vertical faces of the quartz tile. The distance between two consecutive bounces on the same side is proportional to the thickness of the quartz radiator. Thus, it can become longer than the size of the PMT itself. In such a case, the photon could skip the PMT and reach directly the top face of the radiator. If the incident angle between the photon and that face is such that total internal reflection does not occur, the photon leaves without being detected. This explains the saturation seen at large thicknesses for GeomIDs 1 and 3. At nominal thickness (15 mm), we already saw that GeomID = 3 (no mirror, PMT on the side: position B) is slightly worse than GeomID = 0 (no mirror, PMT on the top face: position A). Yet, for smaller thicknesses, the opposite is true: this is due to geometrical effects which make the 'effective' dead space area seen by the photons smaller for PMTs on position B. Adding a mirror to the top face of the DIRC-like TOF detector allows to reflect the photon back so it gets another chance to be detected: that is why the saturation is weaker for configuration 1. Yet, not all photons reflected back are detected nor is the mirror reflectivity 100 % – see Figure 3.12 (right): it is 94 % at most. That is why the variation of the number of p.e. for the configuration with mirror is not fully linear.

Taken into account the PMT fill factor ( $\sim 70\%$ ), the maximum amount of collected light for screened geometries can be calculated:

$$N_{p.e.} = \frac{21}{20}x[\text{mm}] \quad (3.31)$$

it shown on Figure 3.34 (Magenta). Which mean that for baseline thickness (15 mm) one can collect 15 % more light.

Shaping the top face (and the mirror) or adding a small focussing wedge on the back of the tile could improve the collection light without degrading the photon timing distribution (Such piece was suggested in a talk by J. Va'vra in Orsay, 2009, slide 13: <http://agenda.infn.it> This piece would have one advantage and that is the tube axis would be aligned with a direction of magnetic field. It has to have a mirrorized surface.). However, this would make the DIRC-like TOF detector larger and more expensive. So, this option requires dedicated studies.

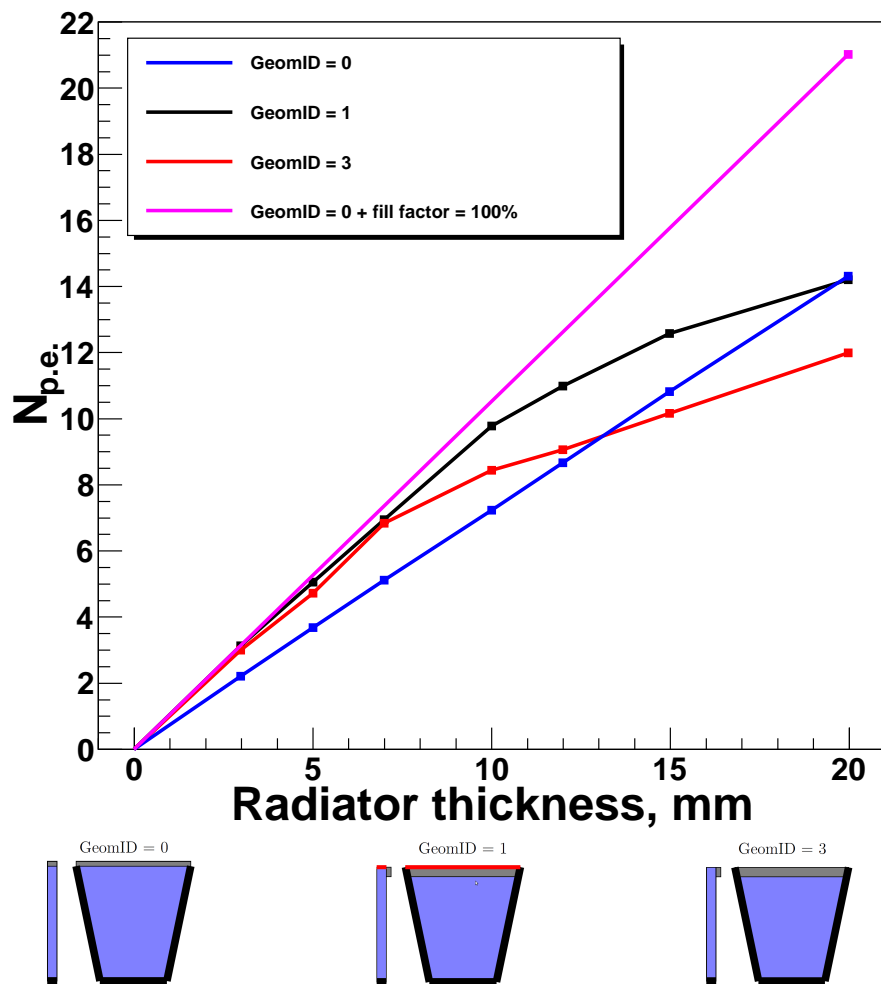


Figure 3.34: Average number of detected p.e. vs. thickness of the quartz radiator for different DIRC-like TOF geometries.

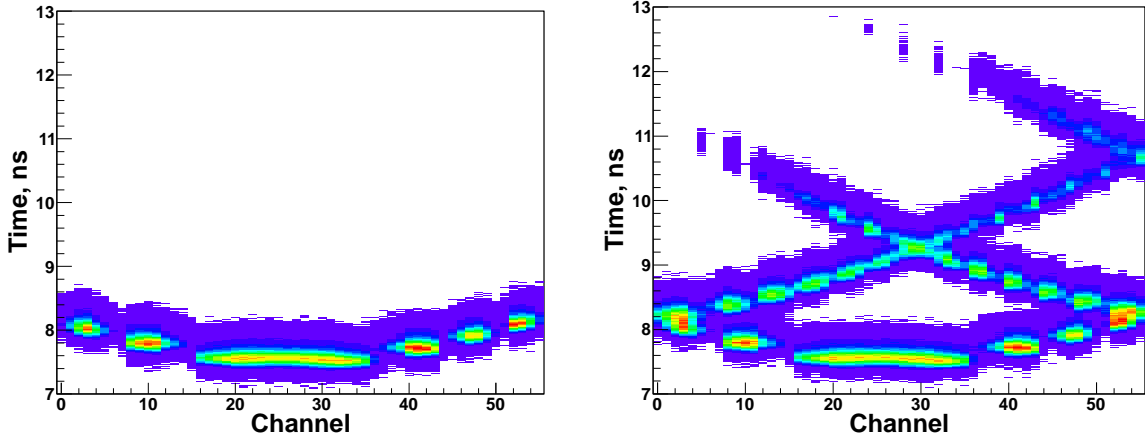


Figure 3.35: Time vs. channel 2D histograms for screened (with absorber, GeomID = 1, left plot) and unscreened (with no absorber, GeomID = 5, right plot) geometries. The pattern is more complex in the second configurations for which more photons are detected.

### 3.5.7 Comparison of time versus channel distributions for DIRC-like TOF configurations with and without photon absorber

Adding photon absorber on the left and right vertical sides of the DIRC-like TOF detector decreases the amount of collected light and makes the 2D pattern of the number of p.e. in the  $\theta$ - $\phi$  plane asymmetric. But at the same time, the corresponding timing pattern has a very simple shape which would make the reconstruction algorithm simpler. This can be seen on Figure 3.35 where the time vs. channel 2D histograms of the p.e. arrival for screened (GeomID = 1, left plot) and unscreened (GeomID = 5, right plot) geometries are shown. One can see that in the configuration without absorber, photons can arrive in the same channel at different times whereas there is almost a one-to-one correspondence between time and channel for the configurations with absorber. These ambiguities of the photon arrival time will require a more complex reconstruction algorithm.

The time window of interest for signal photons is different too as can be seen on Figure 3.35. All photons arrive within 2 ns (6 ns) for screened (unscreened) geometry. Taken into account that particle with different masses would reach the DIRC-like TOF detector within  $\sim$ 1.2 ns – see Figure 3.1 (left) – and adding 2-3 ns for convenience, one can compute the relevant time window for both configurations: 5 ns for the screened geometry and 10 ns for the unscreened one.

### 3.5.8 Recommended geometries for the DIRC-like TOF detector

In this section we are making recommendations for the geometry of the DIRC-like TOF detector by gathering all the information presented in this chapter. Three different geometries are considered to be very promising. They are:

- Geometry based on GeomID=5. This configuration of the DIRC-like TOF detector is the preferred one because of its simplicity in comparison to others. Its main characteristics are listed in Table 3.3.

Table 3.3: Details of the recommended DIRC-like TOF configuration based on GeomID=5.

Quantity	value
PMT position	B
PMT orientation	V or H
Mirror	+
Absorber	B
Tilting	-
Radiator thickness	15 mm
MCP-PMT	SL10
Number of channel per PMT	4
Total number of PMTs	168
Total number of channels	672
MCP-PMT photocathode	Multialkali
Reconstruction algorithm	complex
Time window	10 ns
$\sigma_{\text{electronics}}$	10 ps
$\sigma_{\text{TTS}}$	40 ps
$\sigma_{\text{detector}}$	80 ps
$\sigma_{\text{trk}}$	10 ps
$\sigma_{t0}$	20 ps
$N_{\text{p.e.}}$	>10
<b>Total time resolution</b>	<40 ps

The PMT orientation is not clearly defined yet. A clear answer would be given once we develop a detailed reconstruction algorithm.

- GeomID=1 with overlaps between sectors. In order to have enough light for tracks which enter the detector close to the edges, one has to make overlaps between sectors. This will increase the size and the radiation length of the detector but simplify the reconstruction algorithm. Its main characteristics are listed in Table 3.5.

Table 3.4: Details of the DIRC-like TOF configuration based on GeomID=1.

Quantity	value
PMT position	B
PMT orientation	V or H
Mirror	+
Absorber	SB
Tilting	-
Radiator thickness	15 mm
MCP-PMT	SL10
Number of channel per PMT	4
Total number of PMTs	168
Total number of channels	672
MCP-PMT photocathode	Multialkali
Reconstruction algorithm	simple
Time window	5 ns
$\sigma_{\text{electronics}}$	10 ps
$\sigma_{\text{TTS}}$	40 ps
$\sigma_{\text{detector}}$	80 ps
$\sigma_{\text{trk}}$	10 ps
$\sigma_{\text{t}0}$	20 ps
$N_{\text{p.e.}}$	>10
<b>Total time resolution</b>	<40 ps

- GeomID=0 (but without photon absorber from the left and right sides), readout by SiPM. This option is potentially very interesting because of recent and very fast development of SiPMs with good timing performances – for instance we measured about 150 ps FWHM for 1 mm<sup>2</sup>, 50  $\mu\text{m}$  HAMAMATSU MPPC, see Chapter 6.  $\sigma_{\text{detector}}$  is small for this option in comparison with GeomID = 5; that is why we can use PMTs with worse time resolution. However, ageing effects caused by background especially coming from neutrons has to be studied in details to validate or not this particular option.

Table 3.5: Details of the DIRC-like TOF configuration based on GeomID=0.

Quantity	value
PMT position	A
Absorber	B
Tilting	-
Radiator thickness	15 mm
Reconstruction algorithm	heavy
Time window	10 ns
SiPM	HAMAMATSU MPPC 1 mm <sup>2</sup> with 50 $\mu\text{m}$
Total surface to cover	810 cm <sup>2</sup>
Total number of channels	1080
$\sigma_{\text{electronics}}$	10 ps
$\sigma_{\text{TTS}}$	80 ps
$\sigma_{\text{detector}}$	30 ps
$\sigma_{\text{trk}}$	10 ps
$\sigma_{\text{t}0}$	20 ps
$N_{\text{p.e.}}$	>10
<b>Total time resolution</b>	<40 ps

## 3.6 Mechanical installation and readout electronics

### Mechanical design & integration

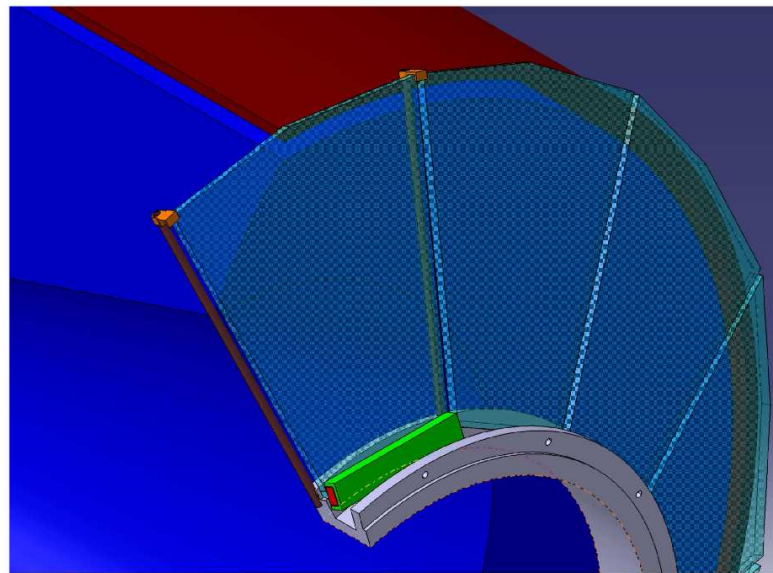
This DIRC-like TOF detector will have to fit into a very limited space between the forward end-plate of the DCH and the forward EMC. Therefore preliminary mechanical integration studies have been done by LAL engineers [65]. Their goal was to design a light support which would hold the quartz tiles, the associated electronics, the boxes which isolate the detector from the outside world and the needed services. The total weight of the detector is expected to be around 100 kg. Two main configurations have been studied:

- A DIRC-like TOF located close and parallel to the forward EMC –see Figure 3.36.
- A DIRC-like TOF located close and parallel to the DCH –see Figure 3.37.

Tilted geometry of the DIRC-like TOF detector have very low average number of the collected light (has been demonstrated with simulation). For this reason geometry where the DIRC-like TOF detector is close and parallel to the DCH considered to be baseline and so the corresponding mechanical support.

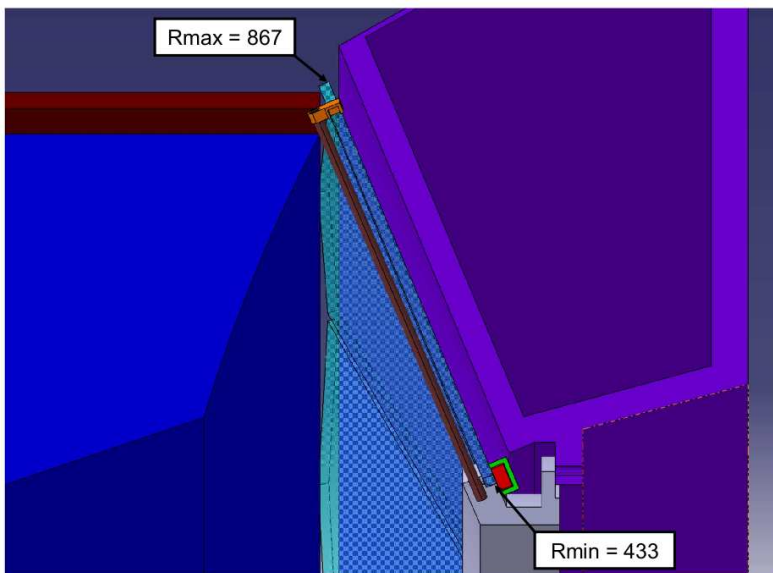
### Readout electronics

The PMTs of the DIRC-like TOF detector will be readout by the USB wavecatcher-based [66, 67] electronics. A test of the first 16-channel prototype of these electronics has been done at SLAC in Fall 2010 – see Chapter 5. The expected performances ( $\sim 10$  ps per channel) have been reached. A second 16-channel prototype has been tested at LAL in an optical test bunch, where the time resolutions of MCP-PMT and SiPM have been measured (see Chapter 6 for more details).



SuperB FPID Mechanical design and integration, Frédéric Bogard &amp; Sandry Wallon, 03/06/2010

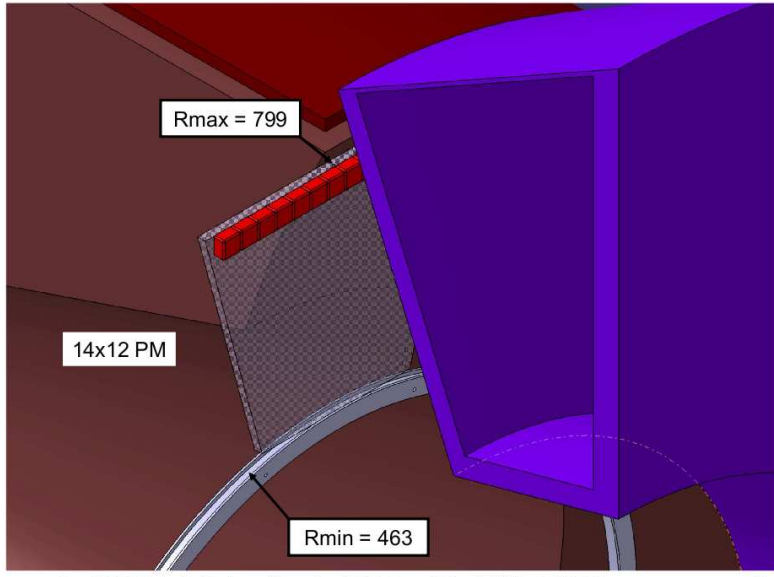
5



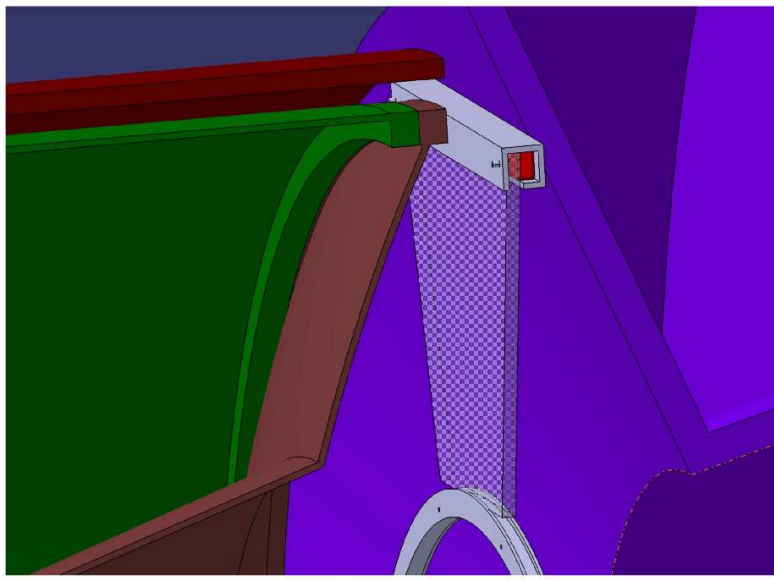
SuperB FPID Mechanical design and integration, Frédéric Bogard &amp; Sandry Wallon, 03/06/2010

7

Figure 3.36: Different views of the mechanical support of the DIRC-like TOF detector located close and parallel to the forward EMC (tilted geometry). The DCH is shown in blue color, the forward EMC is shown in lilac color, the quartz radiator volume is shown in half-transparent blue color and finally the solenoid is shown in brown color. Note: the bar boxes are not shown here.



15



17

Figure 3.37: Different views of the mechanical support of the DIRC-like TOF detector located close and parallel to the DCH (baseline geometry). The DCH is shown in blue color, the forward EMC is shown in lilac color, the quartz radiator volume is shown in half-transparent blue color and finally the solenoid is shown in brown color. Note: the bar boxes are not shown here.

# Chapter 4

## *SuperB*-related background studies

### 4.1 Introduction and overview of the *SuperB* backgrounds

This chapter contains two main parts: one about the background impact on the DIRC-like TOF, the other summarizing background studies done during the test of the 'crab waist' scheme at the upgraded DAΦNE machine in 2008-2009. The goals of the first part are the following.

- To introduce and briefly describe the backgrounds relevant for the *SuperB* machine.
- Then, to describe the full simulation package for the *SuperB* detector, named Bruno, which includes the modeling of the interaction region (IR) and which is the main tool to study the different types of backgrounds and their impact on detector performances and design.
- Finally, we describe in details the most important background sources for the DIRC-like TOF detector and their impact on the PMT lifetime and on the front-end electronics.

The Touschek background is expected to dominate the bunch lifetime at *SuperB* and to be a non-negligible source of background in the IR. For this reason it has to be well-understood. Therefore, in the second part of this chapter we show measurements of background rate caused by this effect at the DAΦNE  $\phi$ -factory and compare them with simulation.

Mitigating and keeping under control machine-related backgrounds is a challenging and very important task when designing the *SuperB* accelerator. Background levels impact several aspects of the detector design: trigger rate, radiation hardness, online configuration

(readout segmentation, electronics shaping time, data transmission speed, etc.). The main sources of background at *SuperB* are listed below, ordered by decreasing importance for DIRC-like TOF detector – as shown later in this chapter.

- Radiative Bhabha:  $e^-e^+ \rightarrow e^-e^+ \gamma$  [68, 69]. Their contribution has been estimated with Bruno.
- Touschek background [70, 71, 72] which is important for dense bunches of low-energy particles. Its impact has been estimated with Bruno.
- Elastic Bhabha:  $e^-e^+ \rightarrow e^-e^+$  [68, 69]. Its level is expected to be much lower than the two previous backgrounds and so its contribution has only been computed using analytical formulas.
- Beam gas interaction [73]. Its contribution has been estimated in Bruno at the same time than the Touschek background.
- Pair production:  $e^+e^- \rightarrow e^+e^-e^+e^-$  [74]. Simulations have shown that these particles have very low momenta and so cannot escape the SVT inner layers.

These background sources produce primary particles that can either directly hit the detector or generate electromagnetic (EM) showers which particles cross the detector and produce hits.

## 4.2 Full simulation of *SuperB*: the Bruno software

### 4.2.1 Introduction

In the present 'Technical Design Report' phase, a reliable tool simulating the detector in the IR is mandatory. First, the background rates in the subdetectors need to be carefully estimated each time the accelerator design evolves. Then, the detector optimization depends on the background levels and should be a tradeoff between performances and cost. One such full simulation tool has been developed from scratch, by the *SuperB* collaboration. Called Bruno, it is written in C++ and based on Geant4.

### 4.2.2 Geometry description

Many different file formats are available to describe High Energy Physics detectors (geometry and materials) in simulation codes. In *SuperB* the Geometry Description Markup Language (GDML) [75] was chosen due to the availability of interfaces with Geant4 and

ROOT [76]. Moreover, this format is user-friendly since it uses XML [77] structures which contents are written in plain English.

Each subsystem has its own mother volume, which houses all its components. This structure allows exchanges both ways between the official Bruno tool and standalone full simulation programs developed privately at the subsystem level. In particular, individual GDML files describing a given detector can either be produced by Bruno or included in the full simulation framework after having been produced in standalone mode.

### 4.2.3 Simulation I/O

The main backgrounds (radiative Bhabha, Touschek and beam gas scattering) have their own generators with which Bruno can interface in two ways. Either the generator code runs inside Bruno upstream of the Geant4 simulation or it runs independently and its output is stored in intermediate data files (in ASCII or ROOT format) which are then readout by Bruno. In a second step, the particle propagation and interaction with material is done by Geant4.

The information about every hit (particle type, momentum, position, time, energy deposit...) are saved in ROOT format for further processing. The Monte Carlo Truth (the genealogy of the particles producing hits in the subdetectors) is also saved, which allows one to study where the background is coming from. In addition, 'snapshots' of particles crossing the boundaries of all subdetectors mother volumes are stored event by event. This gives the possibility to read these lists later, and to use them as input for a new simulation. This is useful in case one of the detectors has changed downstream in Bruno: to study this new configuration, one does not need to track again the particles inside the upstream subdetectors. Or one can use these data in a standalone simulation.

### 4.2.4 Implementation of the DIRC-like TOF detector into Bruno

We have implemented a detailed description (dimensions and materials) of the DIRC-like TOF into the full simulation of the *SuperB* detector: mechanical support, quartz, MCP-PMTs and their associated electronics (see Figure 4.1). The DIRC-like TOF detector assembly consists of: quartz tile, MCP-PMT box, PMT window, DIRC-like TOF front-end electronics (FTOFFEE), aluminum box around the detector and finally the mechanical structure (aluminum ring located at the inner radius and which holds the quartz tiles, see Section 3.6 for more details). The dummy volume<sup>1</sup> which represents the PMT window could be used in future as a sensitive volume to detect Cherenkov light produced in quartz when this feature is implemented in Geant4. Currently, this effect is either simulated in a standalone way or computed using a parametric approach described below –

---

<sup>1</sup>This Geant4 expression means that the crossing of particles in this volume is properly simulated but that no information about the internal interactions are available.

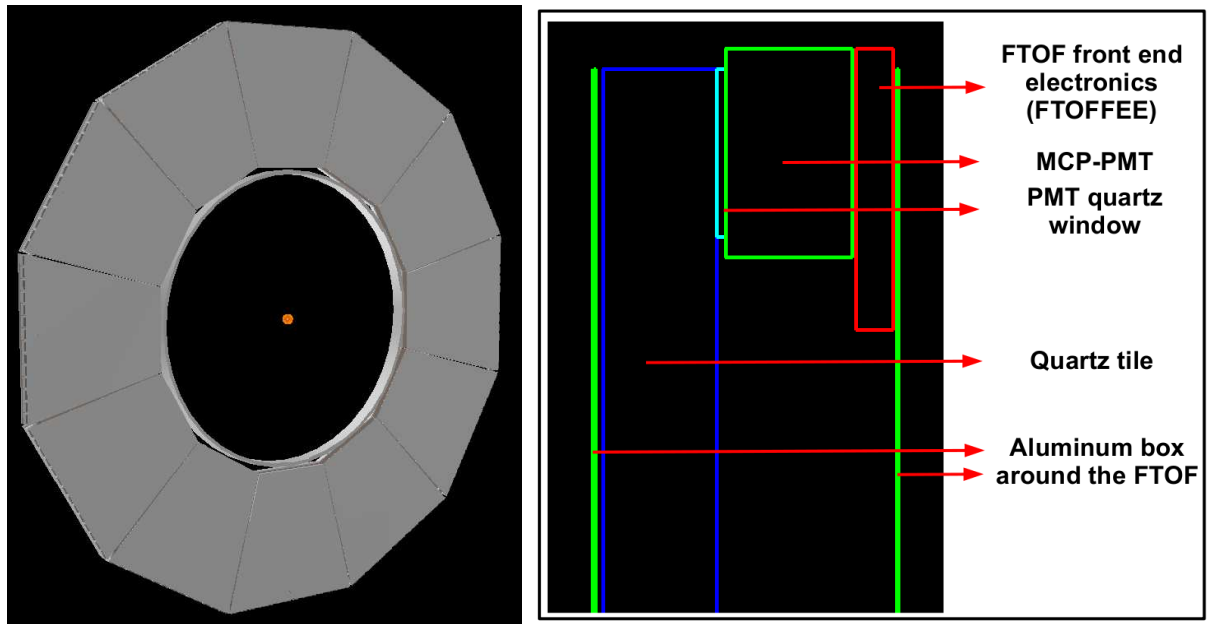


Figure 4.1: **Left:** Visualization of the GDML file produced for the DIRC-like TOF detector and which has been implemented in Bruno. One can see the 12 aluminum plates covering the quartz tiles and the internal ring which holds mechanically the whole structure. **Right:** Side view of the outer part of a DIRC-like TOF sector, showing all the material which has been implemented in Bruno. Each time a hit is produced in the quartz tile or in the front-end electronics (FTOFFEE) the corresponding information is stored.

see section 4.6.4. The properties of the simulated materials – for the moment, only two materials: quartz ( $\text{SiO}_2$ ) and aluminum – are summarized in Table 4.1. We checked that this implementation was correct by comparing their radiation lengths as computed by Geant4 with the values given in Claus Grupen book [54]: 12.3 cm for quartz and 8.9 cm for aluminum. The outermost part of the DIRC-like TOF detector (only 8 % of the total surface) has a total radiation length of 38.6 %  $X_0$  due to the MCP-PMT connected to the quartz tile. The rest of the DIRC-like TOF detector has 14.4 %  $X_0$  of radiation length. Note that the aluminum ring, which holds the DIRC-like TOF detector, is located outside of the acceptance. The total mass of the system is around 76.6 kg – the densities of quartz and aluminum are 2.2 g/cm<sup>3</sup> and 2.7 g/cm<sup>3</sup> respectively.

Table 4.1: Properties of the implemented material into the simulation.

Structure	Material	Thickness (cm)	Surface (cm <sup>2</sup> )	Mass (kg)	Rad. length (% $X_0$ )
Quartz tile	$\text{SiO}_2$ ,	1.5	$1.71 \times 10^4$	56.4	12.2 %
Al. box	aluminum	0.2	$1.71 \times 10^4$	9.2	2.2 %
MCP-PMT window	$\text{SiO}_2$	0.12	813.1	0.21	0.9 %
MCP-PMT box	aluminum	1.66	$1.27 \times 10^3$	5.7	18 %
FTOFFEE	$\text{SiO}_2$	0.5	$1.3 \times 10^3$	1.4	5.3 %
Aluminum ring	aluminum	5	276	3.7	56 %
$r_{min} = 43.5$ cm					
$r_{max} = 44.5$ cm					

### 4.3 $e^+e^-$ annihilation into anything but electron(s)-positron(s)

To see how significant background rates are, one needs to know the rates of  $e^+e^-$  annihilation into  $q\bar{q}$  and  $l^+l^-$ . The total  $e^+e^- \rightarrow$  hadrons cross section as a function of the center-of-mass energy ( $\sqrt{s}$ ) is shown on Figure 4.2. One can see peaks corresponding to resonances which sit on top of continuum production which goes down like  $1/s$ . The visible cross sections<sup>2</sup> and rates for luminosity  $10^{36} \text{ s}^{-1}\text{cm}^{-2}$  for the production of fermion pairs (apart electrons and positrons) at the center of mass energy  $\sqrt{s} = M(\Upsilon(4S))$  are shown in Table 4.2 (for more details, see [80]).

Taking into account the average track multiplicity, which is equal to  $\sim 5$  [81] in  $e^+e^-$  collisions at  $\sqrt{s} = M(\Upsilon(4S))$ , and the total visible rate of 6.54 kHz (see Table 4.2), the total track rate from  $e^+e^- \rightarrow q\bar{q}, \tau^+\tau^-, \mu^+\mu^-$  can be estimated:  $5 \times 6.54 \text{ kHz} = \sim 32.7 \text{ kHz}$

<sup>2</sup>These cross sections take into account the beam energy spread of the PEP-II accelerator and the BaBar acceptance. Hence they will have slightly different values at *SuperB*.

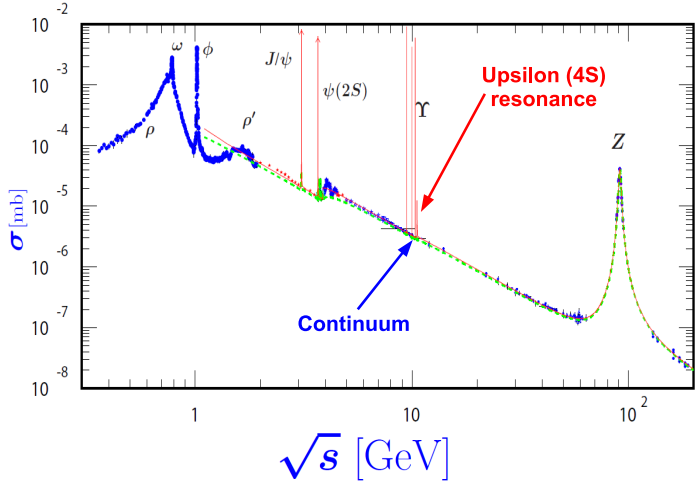


Figure 4.2: Total  $e^+e^- \rightarrow \text{hadrons}$  cross section; the plot is adapted from Ref. [78] and the PDG [79].

in the whole *SuperB* detector and about 1.54 kHz in the DIRC-like TOF (here we assume that  $\cos\theta_{CM}$  is flat-distributed).

## 4.4 $e^+e^-$ pair production

The  $e^+e^-$  pair production ( $e^+e^- \rightarrow e^+e^-e^+e^-$ ) [74] is a second order correction to the small angle Bhabha scattering. During this process, the momenta of the two incoming particles ( $e^+e^-$ ) are almost unchanged. Hence, the additional particles produced via this process have very low momenta. Due to the *SuperB* 1.5 T longitudinal magnetic field, they will not reach detectors which are far enough from the interaction point (IP). In particular, detailed Geant4-based studies show that, as expected, the DIRC-like TOF detector does not suffer from this background. However, the SVT (and especially its most internal layer L0) does: that's even the leading constraint to design this layer for the high-luminosity data taking phase.

The formula of the pair production cross section ( $\sigma_{\text{pair}}$ ) is given by [82].

$$\sigma_{\text{pair}} \sim \frac{\alpha^2 r_e^2}{\pi} \left( \frac{28}{27} \ln^3 \frac{s}{m^2} - 6.59 \ln^2 \frac{s}{m^2} - 11.8 \ln^2 \frac{s}{m^2} + 104 \right) \quad (4.1)$$

Using Eq. (4.1) one can compute  $\sigma_{\text{pair}} = 7.3$  mb, which corresponds to 7.3 GHz rate.

Table 4.2: Production cross sections at  $\sqrt{s} = M(\Upsilon(4S))$  for  $e^+e^-$  annihilation.

$e^+e^- \rightarrow$	Cross section (nb) or rate (kHz) at luminosity $10^{36} \text{ s}^{-1}\text{cm}^{-2}$
$bb$	1.05
$c\bar{c}$	1.30
$s\bar{s}$	0.35
$u\bar{u}$	1.39
$d\bar{d}$	0.35
$\tau^+\tau^-$	0.94
$\mu^+\mu^-$	1.16
total ( $q\bar{q} + \tau^+\tau^- + \mu^+\mu^-$ )	6.54

## 4.5 Elastic Bhabha background in the DIRC-like TOF detector

A schematic drawing of the elastic Bhabha process is shown on Figure 4.3 (Left). The well-known equation for leading order and spin-averaged differential cross section in the center of mass frame (CM) for this process [69] is given by:

$$\frac{d\sigma_{\text{el.}}^{CM}}{d(\cos \theta_{CM})} = \frac{\pi \alpha^2}{s} \left( u^2 \left( \frac{1}{s} + \frac{1}{t} \right)^2 + \left( \frac{t}{s} \right)^2 + \left( \frac{s}{t} \right)^2 \right) \quad (4.2)$$

where  $s$ ,  $t$ , and  $u$  are the Mandelstam variables defined below,  $\alpha$  the fine structure constant, and  $\theta_{CM}$  the Bhabha scattering angle in the center of mass frame.

$$\begin{cases} s = m_1^2 + m_2^2 + 2p_1p_2 \\ t = m_1^2 + m_3^2 - 2p_1p_3 \\ u = m_1^2 + m_4^2 - 2p_1p_4 \end{cases} \quad (4.3)$$

where  $p_1, p_2, p_3, p_4$  are the four-vectors of the particles. Using the approximation  $m_1 = m_2 = m_3 = m_4 = m_e \approx 0$  (motivated by the fact that the electron mass is small with respect to the particle momenta), one has  $s + t + u \approx 0$ . From Eq. (4.3), one can obtain  $\sigma_{\text{el.}}^{CM}$  as a function of  $\cos \theta_{CM}$ .

$$\frac{d\sigma_{\text{el.}}^{CM}}{d(\cos \theta_{CM})} = \frac{\pi \alpha^2}{s} \left( \frac{1 + (\cos \theta_{CM})^2}{2} + \frac{5 + 2 \cos \theta_{CM} + (\cos \theta_{CM})^2}{(1 - \cos \theta_{CM})^2} - \frac{(1 + \cos \theta_{CM})^2}{1 - \cos \theta_{CM}} \right) \quad (4.4)$$

$\cos \theta_{CM}$  can be computed from the polar angle in the laboratory frame  $\theta$  using the following equation:

$$\cos \theta_{CM} = \frac{\cos \theta - \beta}{1 - \beta \cos \theta} \quad (4.5)$$

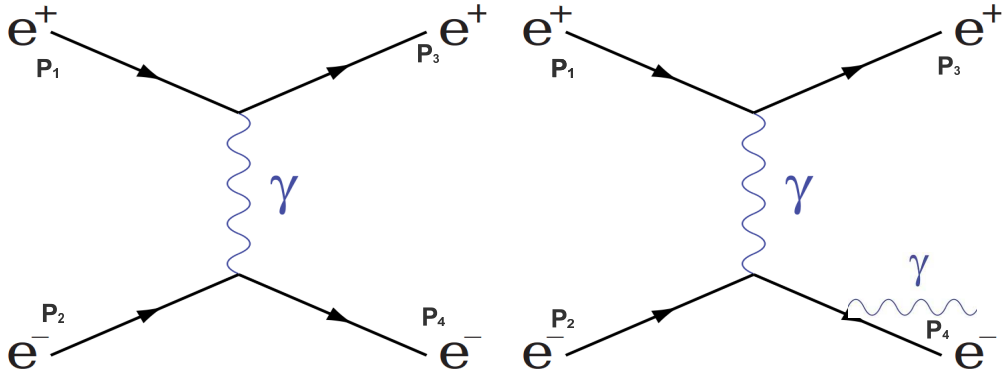


Figure 4.3: Schematic drawings of the Bhabha (left diagram) and radiative Bhabha (right diagram) processes. Time moves forward from the left side of the diagram to the right. The arrows are simply markers of particle motion. They are not the same as the arrows conventionally written into Feynman diagrams (which shows current flow of negative charged particles for fermions and positive charged particles for quarks). **Left:**  $e^- e^+ \rightarrow e^- e^+$ . **Right:**  $e^- e^+ \rightarrow e^- e^+ \gamma$  where,  $e^-$  is almost perpendicular to  $\gamma$ .

Using Eq. (4.4) and Eq. (4.5) one can compute  $\frac{d\sigma_{el.}}{d\theta}$ :

$$\frac{d\sigma_{el.}}{d\theta} = \frac{\sin \theta}{\gamma^2 (1 - \beta \cos \theta)^2} \left( \frac{d\sigma_{el.}^{CM}}{d(\cos \theta_{CM})} \right) \quad (4.6)$$

As can be seen from Eq. 4.6, the cross section becomes very large in case of very small  $\theta$  (if  $\theta \rightarrow 0$  than  $\sigma_{el.} \rightarrow \infty$ ).

The electron (positron) Bhabha rate in a given polar range  $[\theta_{min}; \theta_{max}]$  is computed by integrating the above equation:

$$\text{Rate}_{el.} = L \times \int_{\theta_{min}}^{\theta_{max}} \frac{d\sigma_{el.}}{d\theta} d\theta \quad (4.7)$$

where  $L$  is the luminosity.

Figure 4.4 shows the differential cross section of the elastic Bhabha scattering in laboratory frame ( $\frac{d\sigma_{el.}}{d\theta}$ ) as a function of scattered angle  $\theta$ . The approximate polar angle coverage of the *SuperB* detector goes from  $15^\circ$  to  $165^\circ$ . The integral (4.7) of the differential cross section over this angle range is  $\sim 7.1 \times 10^{-5}$  mb which corresponds to 71 kHz rate in whole detector and 46 kHz in the DIRC-like TOF detector for the nominal luminosity of  $10^{36} \text{ cm}^{-2} \text{ s}^{-1}$ . These rates cannot be reduced since the Bhabha electrons directly flight into the detector acceptance. These rates have to be compared with the track rates coming from the  $e^- e^+ \rightarrow q\bar{q}, \tau^+ \tau^-, \mu^+ \mu^-$  processes – see Section 4.3.

However, a Bhabha electron (positron) deflected by a small angle can hit the beam pipe not far from the IP and produce an EM shower. Hence, with a beam pipe aperture of 2 cm

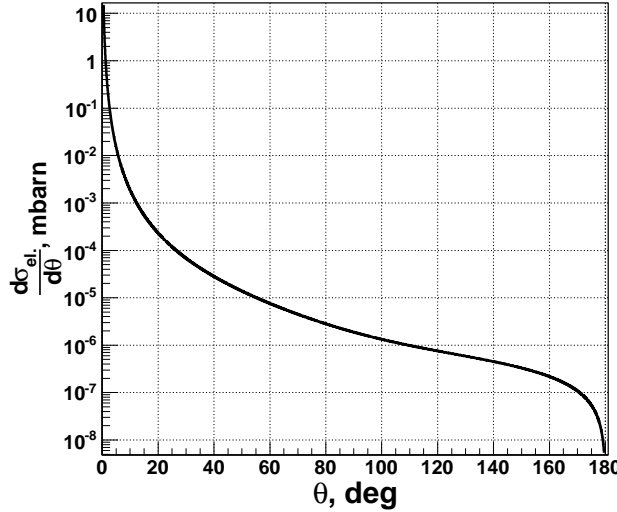


Figure 4.4: Differential cross section of the elastic Bhabha scattering in laboratory frame ( $\frac{d\sigma_{el.}}{d\theta}$ ) as a function of scattered angle  $\theta$ .

around the interaction region ( $\pm 6$  m from the IP), one can determine the corresponding minimum and maximum  $\theta$  angles –  $0.2^\circ$  and  $179.8^\circ$  – and then compute a Bhabha rate  $\sim 900$  kHz using Eq. (4.7). This rate gives the number of electrons (positrons) which will hit the beam pipe ( $\pm 6$  m from IP) every second. The actual impact of this background on the *SuperB* subsystems has to be estimated with a full Geant4-based simulation.

## 4.6 Radiative Bhabha

### 4.6.1 Introduction

Radiative Bhabha [68, 69] is the following process:  $e^-e^+ \rightarrow e^-e^+\gamma$ . This background is estimated to be dominant at *SuperB* because it has a very large cross section at small scattering angles. Its schematic drawing is shown on Figure 4.3 (Right). Due to the interaction between the electron and the positron, the  $\gamma$  can be emitted by either particle; then it propagates almost parallel to its mother particle. This effect is well-known as ‘beamstrahlung’. The theoretical approximation for the cross section of the radiative Bhabha process ( $\sigma_{red.}$ ) was obtained here [83].

$$\sigma_{red.} \approx \frac{16\alpha r_e^2}{3} \left[ \left( \ln \frac{E_{c.m.}^2}{m_e^2} - \frac{1}{2} \right) \left( \ln \frac{E}{k_{min}} - \frac{5}{8} \right) + \frac{1}{2} \left( \ln \frac{E}{k_{min}} \right)^2 - \frac{3}{8} - \frac{\pi^2}{6} \right] \quad (4.8)$$

where  $\alpha$  is the fine structure constant,  $r_e$  the classical electron radius ( $2.82 \times 10^{-15}$  m which corresponds to 79.41 mb),  $E_{c.m.}$  is the energy in center of mass frame (for *SuperB*

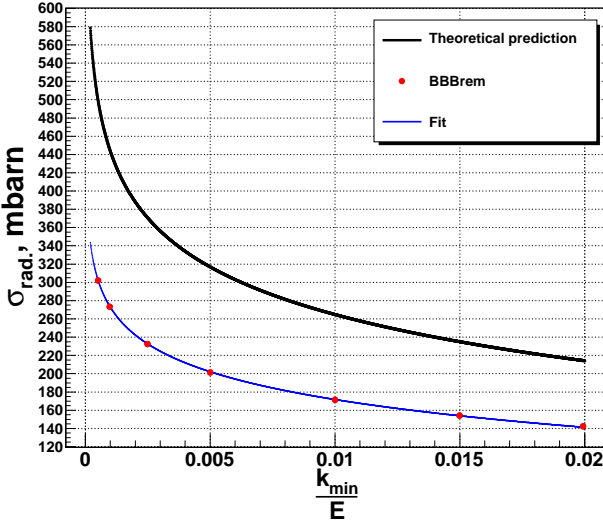


Figure 4.5: Comparison between the values of  $\sigma_{\text{red.}}$  obtained with the BBBrem radiative BhaBha generator (red dots) and the predicted values used in Eq. (4.8) (black curve). The blue curve is the fit of the values obtained with the BBBrem generator – see Eq. (4.9) and the associated text for details.

10.58 GeV which is the mass of the  $\Upsilon(4S)$  resonance),  $E$  is the energy of incoming electron or positron<sup>3</sup> and  $k_{\min}$  the minimum energy of the radiated photon. So, the ratio  $k_{\min}/E$  can be seen as the photon energy cut-off. From Eq. 4.8, one can see that for  $k_{\min} \rightarrow 0$ ,  $\sigma_{\text{red.}} \rightarrow \infty$ . In other words, the smaller the minimum photon energy, the larger the integrated cross section of this process. In reality, we cannot detect photons with very small energies which legitimates the use of a photon energy cut-off, corresponding to the minimum detectable energy.

However, experimentally [84],  $\sigma_{\text{red.}}$  was found smaller than predicted, as shown on Figure 4.5. "This reduction can be ascribed to the effect of finite bunch density" (citation from the *SuperB CDR* [7]). The BBBrem radiative BhaBha event generator [85] gives rates which match the measurements better. This generator is used by Bruno (full simulation framework of the *SuperB* detector). One can fit the integrated  $\sigma_{\text{red.}}$  values obtained with the BBBrem generator (see Figure 4.5) as a function of the photon energy cutoff. The fit result is:

$$\sigma_{\text{red.}} = \ln \frac{E}{2k_{\min}} \times 43.9 \text{ mbarn} \quad (4.9)$$

Note that this fit and Eq. 4.8 are only valid for small  $k_{\min}/E < 0.03$ .

---

<sup>3</sup>This formula estimate the cross section for one beam, hence the total is the sum for two beams.

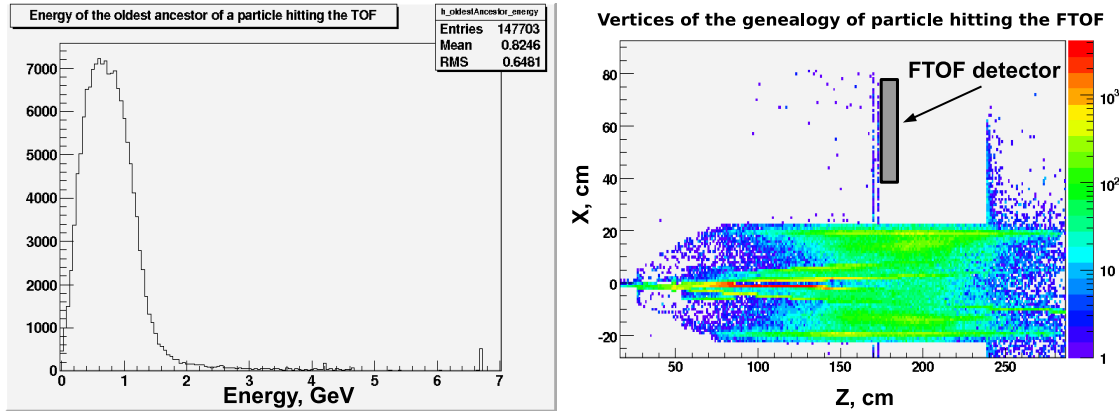


Figure 4.6: **Left:** Energy of the oldest ancestor of a particle hitting the DIRC-like TOF detector. **Right:** 'Vertex genealogy' of the particle hitting the DIRC-like TOF detector – see text for details. The hot spot around 1 m away from the IP is clearly prominent.

#### 4.6.2 Impact of the radiative Bhabha background on the DIRC-like TOF detector

After a short general description of the radiative Bhabha background, one can now describe in detail its effect on the DIRC-like TOF detector. The main source of background is coming from off-energy positrons with energies between  $\approx 0.3$  GeV and  $\approx 1.3$  GeV – see left part of Figure 4.6. The corresponding radiative Bhabha process is:  $e^+e^- \rightarrow e^-e^+(\sim 1\text{ GeV})\gamma(\sim 5\text{ GeV})$ . The high energy photons produced go straight and hit the bending magnet  $\sim 10$  m away from the IP, while the  $\sim 1$  GeV positrons get a kick from the nominal trajectory and hit the beam pipe around 1 m away from the IP. These impacts create EM showers which then affect the DIRC-like TOF detector. On the right part of Figure 4.6, one can see a 2D-map showing the locations of all intermediary vertices between the original radiative Bhabha off-energy positrons and the particles finally hitting the DIRC-like TOF – many events have been superimposed to construct this 'genealogy' distribution. One can clearly see a hot spot around 1 m away from the IP (note the logarithmic scale on the color code caption) which is where the off energy positrons hit the beam pipe. One can see as well that the accumulated hits 'draw' the profile of a cone which corresponds to the tungsten shield surrounding the beam pipe. The aim of this shield is to protect subsystems from EM-showers; its current thickness is around 3 cm.

The distribution of the types of particles hitting the DIRC-like TOF and coming from radiative Bhabha events is given by the Bruno framework: gammas – 83%, neutrons – 14% electrons, positrons – < 3%. Due to the tungsten shielding and the 1.5 T magnetic field, the charged particles from the EM showers cannot reach the DIRC-like TOF. By increasing the thickness of the shield, one could potentially reduce as well the flux of  $\gamma$ 's. The spectra of the incoming  $\gamma$ 's and neutrons are shown on Figure 4.7 while the

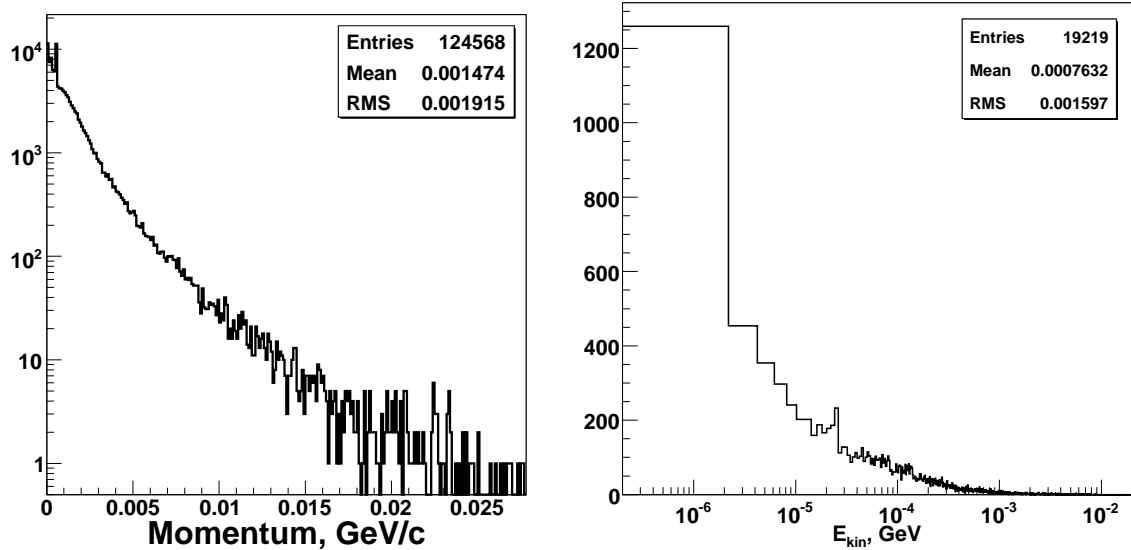


Figure 4.7: **Left:** Spectrum of the incoming gammas. The peak around 0.5 MeV correspond to gammas from annihilation; the average energy of the gammas is 1.4 MeV. **Right:** Spectrum of the incoming neutrons. These two histograms have been drawn using a total number of simulated bunch crossings of 19695.

distributions of the background hits in  $\phi$  and along the radius are shown on Figure 4.8.

We are interesting in two main quantities to quantify the impact of this background on the DIRC-like TOF.

- First, the rate of light produced by background particles inside the DIRC-like TOF detector. These background photons, which production mechanism is discussed below, have two important consequences:
  - The ageing of the MCP-PMT. Above a given value of the charge integrated by the PMT anode, the quantum efficiency (QE) of the photocathode goes down. ‘Classical’ PMTs are able to collect  $\sim 100$  C/cm<sup>2</sup> without such degradation. However, MCP-PMTs like the Hamamatsu SL-10 are much more sensitive to the integrated charge: the best result so far, which has been obtained for a squared-shape SL-10, is only 2.7 C/cm<sup>2</sup> [86].
  - The background signals could degrade the PID performances of the DIRC-like TOF detector by confusing the information coming from actual charged particles crossing the quartz tile.
- Then, the integrated dose absorbed by the DIRC-like TOF front-end electronics plus the neutron spectrum and flux. Having reliable estimates of these quantities is crucial to properly design all the components of the acquisition chain and to locate them closer or further away from the detector.

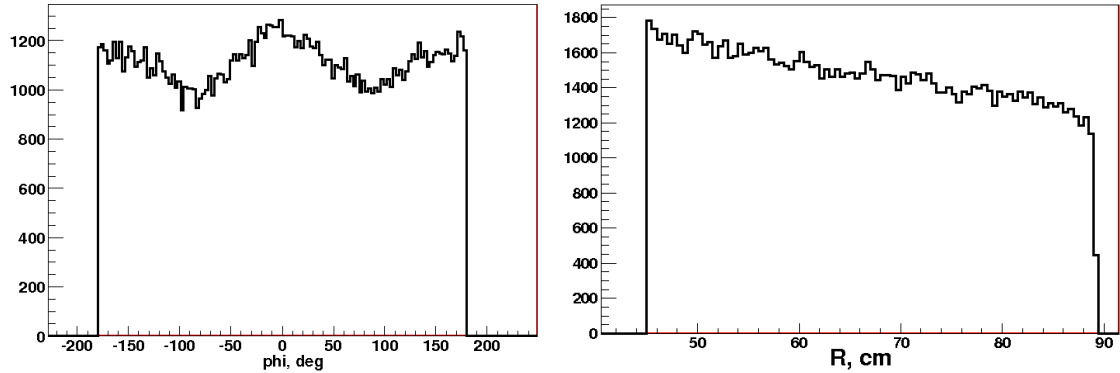


Figure 4.8: Distribution of the hits in the azimuth angle  $\phi$  (left) and along the radius  $R$  (right).

### 4.6.3 Background production of light in the DIRC-like TOF

Production of scintillation light is negligible in quartz. Therefore, light in the DIRC-like TOF detector is only produced by the Cherenkov effect. As Cherenkov light is only produced by charged tracks, neutrals ( $\gamma$ 's and neutrons) have to produce secondary particles first, which then emit light in the quartz if their momentum is above the Cherenkov threshold.

#### Production of light by gammas

We first focus on the gammas which are the dominant source of background. Their spectrum at the boundary of the DIRC-like TOF detector is shown on the left part of Figure 4.7. Given the average gamma momentum (1.4 MeV/c) and the atomic number ( $Z = 8$ ) of the Oxygen, which is the dominant atom in the quartz, the incoming gamma mainly interact with the DIRC-like TOF detector via the Compton effect (see Figure 4.9). The photoelectric effect only dominates for low momentum ( $< 70$  keV) gammas while pair production becomes important for high momentum ( $> 15 - 20$  MeV) gammas, which are very rare. However, the minimum momentum for electron to produce the Cherenkov light in medium with refractive index  $\sim 1.47$  is 0.47 MeV/c.

The equation below shows the relation between the gamma energies before ( $E_\gamma$ ) and after ( $E_{\gamma'}$ ) the Compton scattering; it depends on the angle  $\theta$  between incoming and outgoing gamma.

$$E_{\gamma'} = \frac{E_\gamma}{1 + \frac{E_\gamma}{m_e c^2} (1 - \cos \theta)} \quad (4.10)$$

where  $m_e$  is the electron mass. The difference  $E_\gamma - E_{\gamma'}$  is equal to the kinetic energy of the produced electron. Using equation Eq. (4.10), one can compute minimum energy of gamma to produce the Cherenkov light via Compton electron, which is equal to  $\sim 0.67$  MeV. The low momentum electron moves randomly in the quartz where it emits Cherenkov light almost in  $4\pi$  as shown on Figure 4.9 (Right).

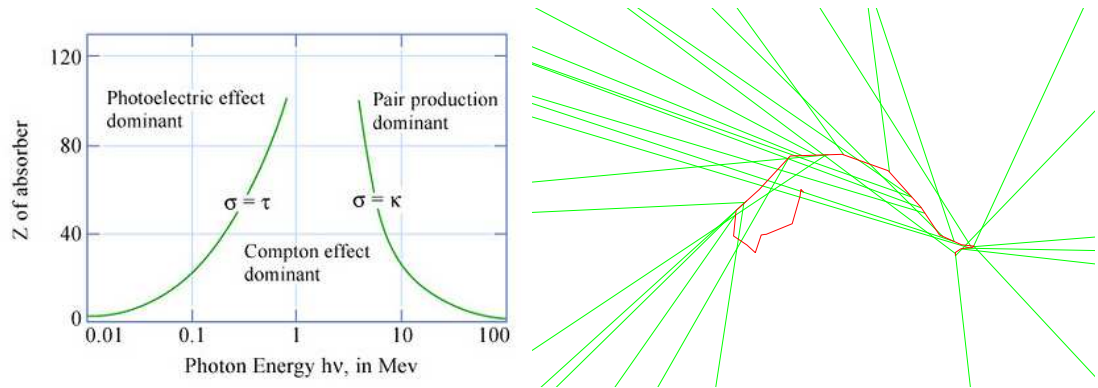


Figure 4.9: **Left:** 2D map (atomic number  $Z$  of the absorber material vs energy of the incoming photon) showing the dominant contribution to the gamma interaction process – this plot have been adapted from [54]. For the DIRC-like TOF detector, the interaction will mainly occur via Compton scattering although photoelectric effect and pair production will be present as well. **Right:** A Geant4-simulated electron with momentum 1 MeV/c (red track) propagates in the quartz and emits Cherenkov photons (green tracks). The photons are emitted in all directions due to the electron scattering, unlike for high momentum tracks.

### Production of light by neutrons

This is a more complex problem. The neutrons themselves are coming from a giant dipole resonance [87] which is a photonuclear reaction. After the neutron has been produced, it will drift in experimental hole before being thermalized and captured by a nucleus. Finally, several (1-3)  $\gamma$ 's can be emitted during the relaxation phase of the nucleus.

Figure 4.10 shows the distributions of the momenta of the secondary electrons produced in the quartz tile and the FTOFFEE<sup>4</sup>. One can see that both shapes are quite similar with very close mean momentum ( $\approx 0.6$  MeV/c). The rate of these electrons is estimated to be 44 kHz/cm<sup>2</sup> in quartz; they are the source of the background Cherenkov light.

#### 4.6.4 Method to estimate the light background rate in the DIRC-like TOF photodetectors

The best and most straightforward method would obviously be to have the simulation framework take this into account for the users. But, as we already mentionned, the physics of the Cherenkov radiation has not been implemented in Bruno yet. Consequently, one had to find other ways to estimate the amount of background light hitting the DIRC-like

<sup>4</sup>The Cherenkov light would not be produced in the FTOFFEE, however for comparison we show this plot here.

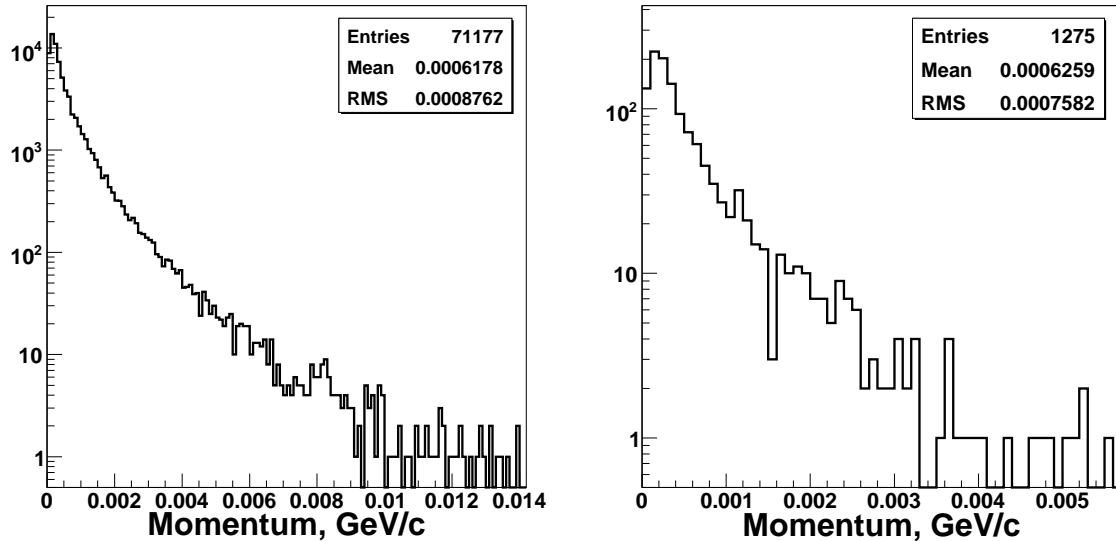


Figure 4.10: Momentum distributions of secondary electrons produced in the DIRC-like TOF quartz tiles (left) and in the FTOFFEE (right). The total number of simulated bunch crossings is 19695. The rate of these electrons is 44 kHz/cm<sup>2</sup> in quartz.

TOF MCP-PMTs.

The most general formula to estimate the number of detected p.e. can be written like this:

$$N_{d.p.e.} = \int E_g E_c N_0 \sin^2 \theta_c dx d\lambda \quad (4.11)$$

where  $x$  is the length of the track in the radiator,  $\lambda$  the photon wavelength and  $\theta_c$  the Cherenkov angle.  $E_g$  is the geometrical efficiency of the photon collection; in general, it is a function of the position and of the direction of the track.  $E_c$  is the conversion factor from photons to photoelectrons which is the product of the photocathode quantum times the PMT collection efficiency.

The problem is that the unknown parameter  $E_g$  cannot be analytically computed due to the complexity of the problem. Therefore, two alternative methods have been used in order to estimate the background rate.

- The first and most direct method is based on the experience gained on the *BABAR* DIRC [88]. The number of photoelectrons  $N_{d.p.e.}$  is given by the following equation:

$$N_{d.p.e.} = 26 \sum_i L_i [\text{cm}] \left( 1 - \frac{1}{n^2 \beta_i^2} \right) \quad (4.12)$$

where  $L_i$  and  $\beta_i$  are the length and  $\beta$  of the track for each Geant4 step  $i$  and  $n = 1.47$  is the refractive index. These parameters are available in Bruno; hence, using the

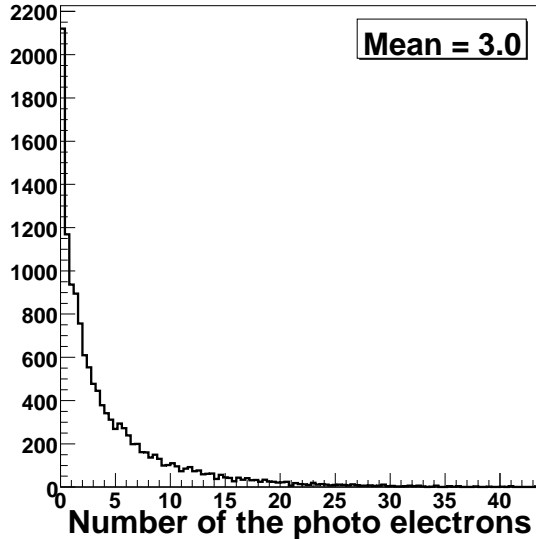


Figure 4.11: Distribution of the number of detected p.e. in the DIRC-like TOF detector per bunch crossing obtained using Eq. (4.12) and the information available in Bruno. The mean value is 3 p.e. per bunch crossing in the whole DIRC-like TOF detector.

above equation leads to the distribution of the number of p.e. in the DIRC-like TOF detector shown on Figure 4.11.

- A more precise method is to use the information from Bruno about the particles entering DIRC-like TOF mother volume and to use them as input for a standalone Geant4 simulation. The average number of background p.e. measured with this method is 1.8 per bunch crossing in the whole DIRC-like TOF detector – hence about 50% less than with the simpler method. This correspond to a background rate of 480 kHz/cm<sup>2</sup>. The distribution of the number of background p.e. hits in one DIRC-like TOF sector per bunch crossing is shown on the left side of Figure 4.12 while their timing distribution is shown on the right plot.

#### 4.6.5 Absorbed dose by the DIRC-like TOF and its front-end electronics

The radiation damage has to be studied as well. The total energy losses ( $dE/dx$ ) per bunch crossing in the whole DIRC-like TOF detector and in its FTOFFEE are shown on Figure 4.13; they are computed by Bruno. On average, the DIRC-like TOF detector and the FTOFFEE absorb 1.16 MeV and 0.0212 MeV per bunch crossing respectively. These numbers correspond to 14 Gy/year (1.4 kRad/year) in DIRC-like TOF and 10 Gy/year (1.0 kRad/year) in FTOFFEE.

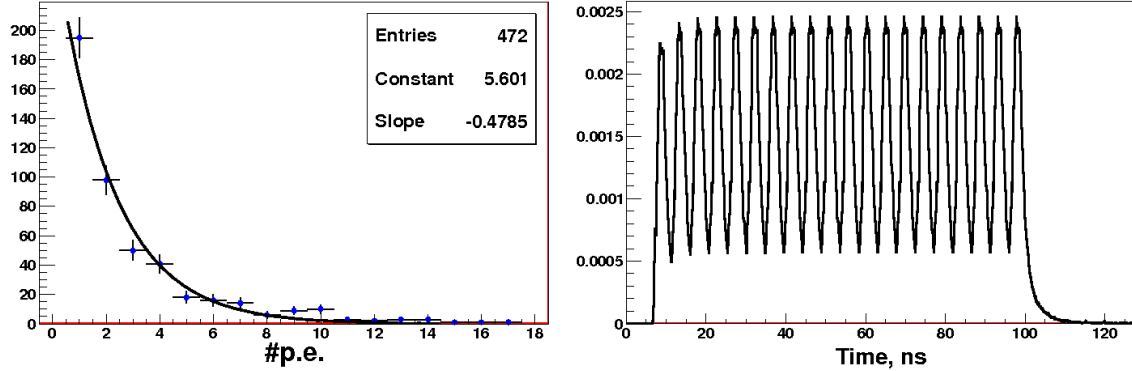


Figure 4.12: **Left:** Distribution of the number of background hits in one DIRC-like TOF sector per bunch crossing. Note zero bin is excluded in this histogram, however for computation the average number of the p.e. we take into account zero bin. **Right:** The timing of the background p.e. arriving. Note that we superimpose many bunch crossings ( $\sim 10,000$  per peak) to get clear shape of the distribution. Each peak corresponds to a new bunch crossing.

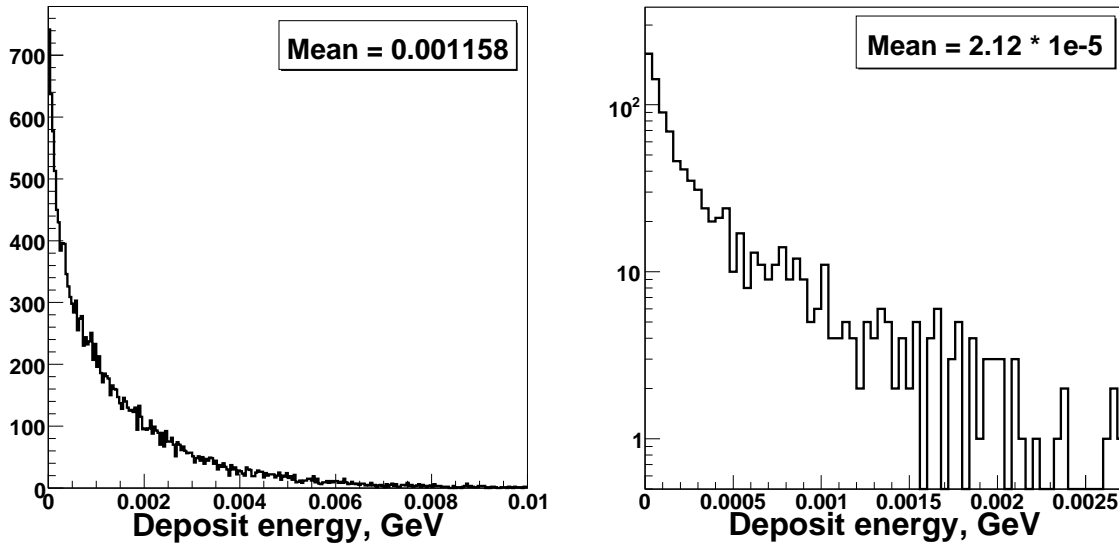


Figure 4.13: Total  $dE/dx$  per bunch crossing in the whole DIRC-like TOF detector (left) and in the FTOFFEE (right).

Another very important characteristics of the background is the flux of neutrons through the front-end electronics. From the Bruno simulation, we get  $2.4 \times 10^{11} / \text{cm}^2/\text{year}$ , which makes impossible the use of silicon photomultipliers. The spectrum of the incoming neutrons is shown on Figure 4.7.

## 4.7 Touschek effect

The following citation from J. Le Duff [89] defines nicely the Touschek effect: “*[P]articles in a circular bunch execute transverse betatron oscillation around the equilibrium orbit. Since the transverse velocities are statistically distributed, these particles can be scattered by a collision so transferring transverse momenta into longitudinal momenta. Such a change in the direction of the particle’s momentum can lead to a strong variation of its energy, due to relativistic effect; if the relative energy variation exceeds the energy acceptance of the machine the particle is lost. (...)*” Then, the off-trajectory particles hit the beam pipe and produce high multiplicity EM-showers. This effect is potentially worrisome since Touschek particles produced far away from IP can travel up to it and interact there. However, collimator’s located on both sides of the IR are used to stop these particles before they reach the detector area.

The Touschek beam lifetime ( $\tau$ ) can be estimate by using the following formula giving the particle loss per unit time [89]:

$$\frac{1}{\tau} = \frac{1}{N} \frac{dN}{dt} = \frac{r_e^2 c \lambda^3}{8\pi \gamma^2} \frac{N}{\sigma_x \sigma_y \sigma_z} D(\xi), \quad (4.13)$$

where  $N$  is the number of particles in the bunch,  $\lambda$  the momentum acceptance (typical value:  $\sim 1\%$ ),  $\sigma_{x,y,z}$  are the bunch sizes in the three directions of space,  $\gamma$  the Lorentz factor, and

$$\xi = \left( \frac{\Delta E/E}{\gamma} \right)^2 \frac{\beta_x}{\varepsilon_x} \quad (4.14)$$

is the universal function (see [7] for more details). For  $D(\xi)$ , one can use the following approximation [90], valid for  $\xi < 0.01$ :

$$D(\xi) = \sqrt{\xi} \left( \ln \left( \frac{1}{1.78\xi} \right) - \frac{3}{2} \right) \quad (4.15)$$

The Touschek effect dominates the lifetime of the off-collision beam<sup>5</sup> at *SuperB*. This is due to the very small emittances of the *SuperB* beams: 4 pm in vertical and 1.6 nm in horizontal [7, 91] axis.

A dedicated simulation has been developed by the LNF MDI group to estimate the beam lifetime and the Touschek background rate at the *SuperB* machine [92]. This simulation is used as an event generator for Bruno, which output has then been used to

---

<sup>5</sup>In case of colliding beams the intrabeam scattering dominates the lifetime of the beam.

estimate background rates and doses in the DIRC-like TOF detector. The bunches have different properties in the high energy (HER) and low energy (LER) rings which lead to different Touschek backgrounds. For this reason, we separate results for the two beams.

The incoming background particles (daughters of the Touschek particles which hit the beampipe) are mainly gammas and neutrons. In the HER: 58 %  $\gamma$ , 42 % neutrons and  $\ll 1\%$  other (electrons, positrons, muons and protons); in the LER: 94 %  $\gamma$ , 6 % neutrons and  $\ll 1\%$  other). On the top row of Figure 4.14, the spectra of the gammas which hit the DIRC-like TOF quartz tiles are shown for the HER (left histogram) and LER (right histogram) beams. The corresponding fluxes are:  $6 \times 10^7 / \text{cm}^2/\text{year}$  for the HER and  $4.6 \times 10^{10} / \text{cm}^2/\text{year}$  for the LER. The neutron spectra are shown on the bottom row of Figure 4.14; the corresponding fluxes are:  $4.2 \times 10^7 / \text{cm}^2/\text{year}$  for the HER and  $2.7 \times 10^9 / \text{cm}^2/\text{year}$  for the LER.

As already discussed in the radiative Bhabha section, the incoming gammas interact with the DIRC-like TOF detector and produce secondary electrons which then create background Cherenkov light. The spectrum and timing distribution of these secondary electrons in the DIRC-like TOF detector are shown on Figure 4.15. The corresponding fluxes are:  $3 \times 10^7 / \text{cm}^2/\text{year}$  for the HER and  $3 \times 10^{10} / \text{cm}^2/\text{year}$  for the LER.

The deposit energy per Touschek particle inside the DIRC-like TOF detector from the HER and LER beams is shown on the top row of Figure 4.16. The corresponding doses are: 0.02 Rad/year for the HER and 0.7 Rad/year for the LER. The numbers of background photo electrons per Touschek particle for HER and LER are shown on the bottom row of Figure 4.16. The corresponding p.e. rates per unit of the MCP-PMT sensitive surface are: 20.4 Hz/cm<sup>2</sup> for the HER and 2.2 kHz/cm<sup>2</sup> for the LER. To estimate the background p.e. rate, we used Eq. (4.12) which is given a reasonably accurate upper limit for such quantities.

As can be seen, the Touschek particles from the LER affect the DIRC-like TOF detector much more (2-3 orders of magnitude) than those from the HER. From Eq. (4.13) one can see that  $1/\tau$  is proportional to  $1/\gamma^4$ , which explains why the low momentum particles contribute more. However, this background is negligible in comparison to the background caused by the radiative BhaBha.

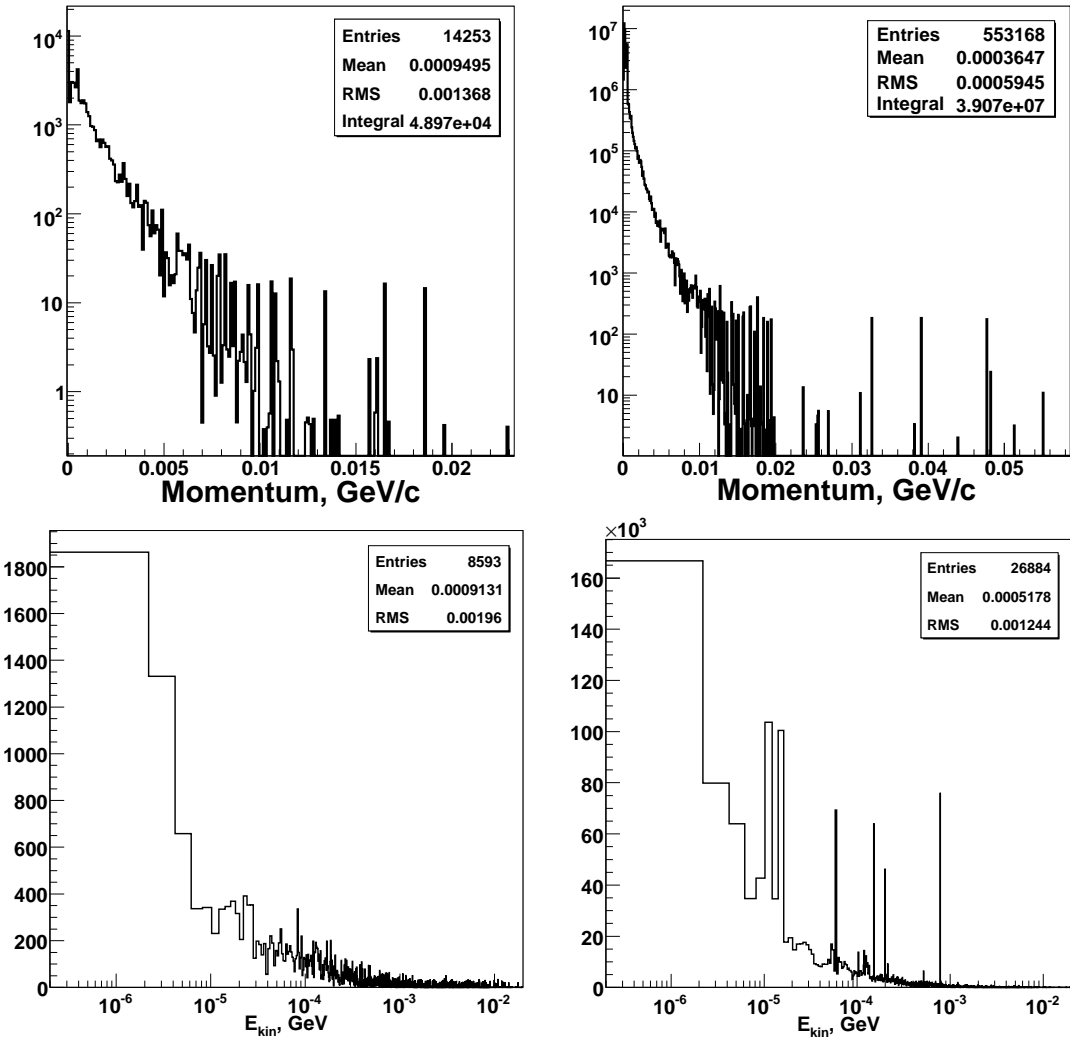


Figure 4.14: **Top row:** Spectra of the background photons produced by Touschek particles for the HER (left) and the LER (right). The 'Integral' quantity in the stats box shows the total number of photons entering the DIRC-like TOF detector per second. Knowing the surface of the DIRC-like TOF quartz tiles (see Table 4.1), one can estimate the corresponding rates: 3 Hz/cm<sup>2</sup> for the HER and 2.3 kHz/cm<sup>2</sup> for the LER. **Bottom row:** Spectra of the background neutrons produced by Touschek particles for the HER (left) and the LER (right). The corresponding fluxes are: 2.1 Hz/cm<sup>2</sup> for the HER and 135 Hz/cm<sup>2</sup> for the LER.

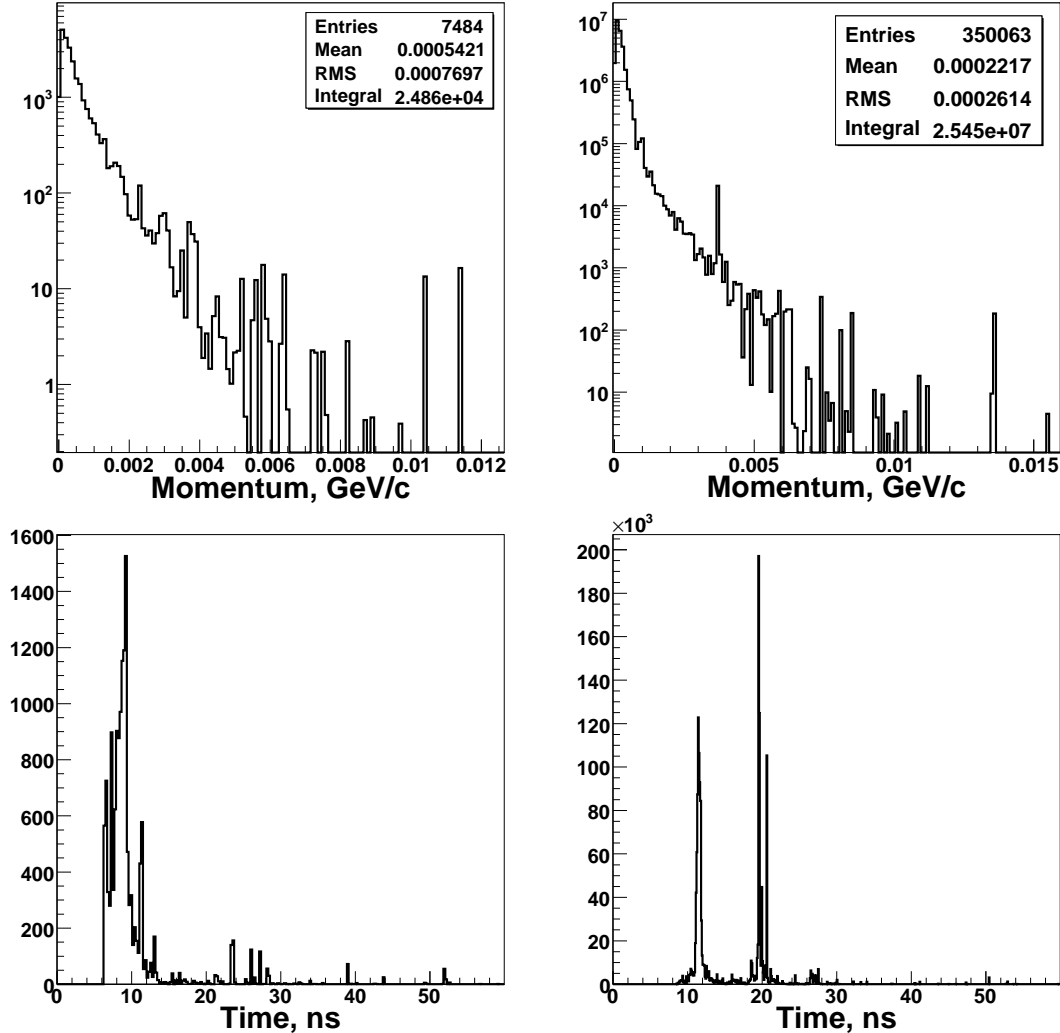
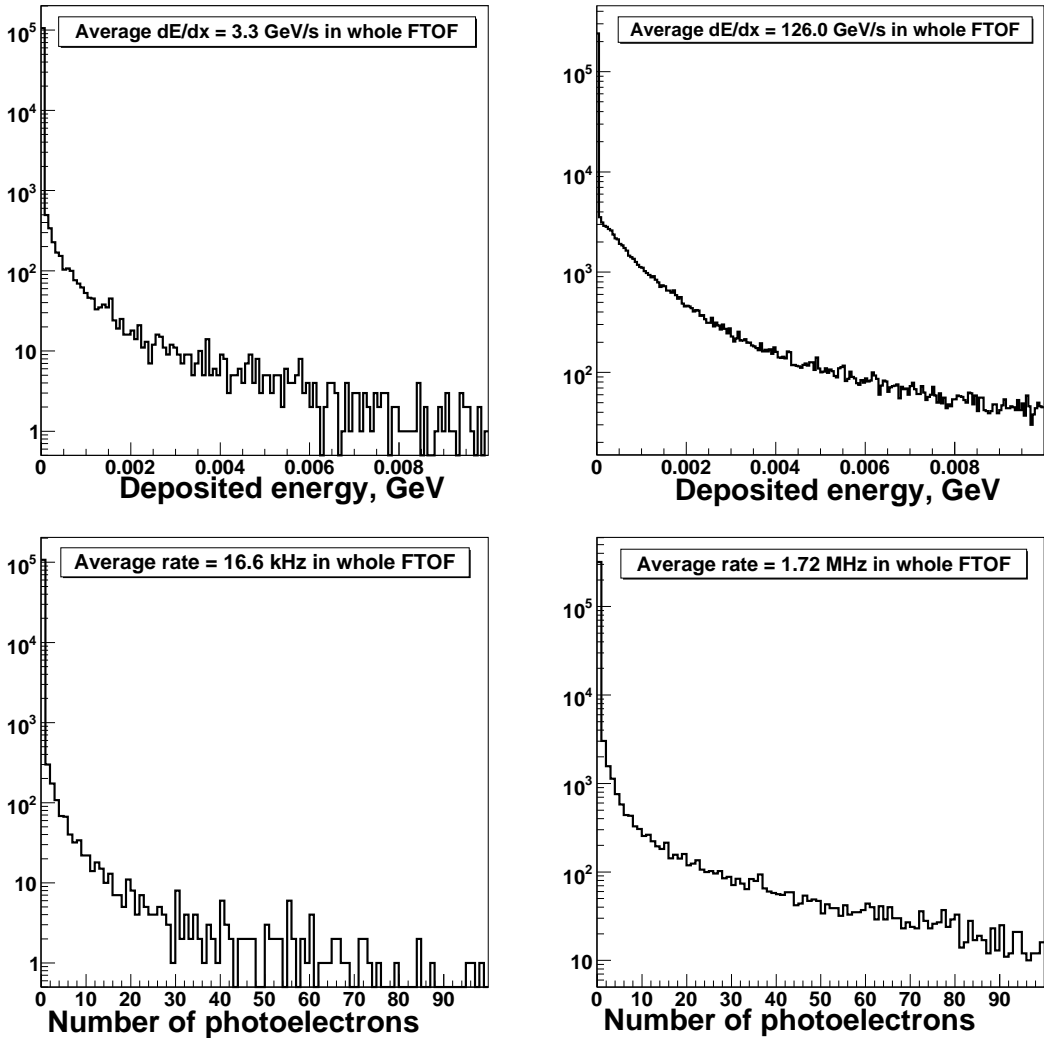


Figure 4.15: **Top row:** Spectra of the secondary electrons produced in the DIRC-like TOF quartz tiles for the HER (left histogram) and the LER (right one). The corresponding fluxes are:  $1.5 \text{ Hz/cm}^2$  for the HER and  $1.5 \text{ kHz/cm}^2$  for the LER. **Bottom row:** Timing of the secondary electrons produced in the DIRC-like TOF quartz tiles for the HER (left plot) and LER (right plot). NOTE: the Touschek particles are produced within a bunch hence they do not come from the interaction point and their time zero is arbitrary defined.



**Figure 4.16:** **Top row:** Deposited energy per Touschek particle inside the DIRC-like TOF detector for the HER (left histogram) and the LER (right histogram). The corresponding doses are: 0.02 Rad/year for the HER and 0.7 Rad/year for the LER. **Bottom row:** Number of background photo electrons per Touschek particle for the HER (left plot) and the LER (right plot). The corresponding p.e. rates per unit of the MCP-PMT sensitive surface are: 20.4 Hz/cm<sup>2</sup> for the HER and 2.2 kHz/cm<sup>2</sup> for the LER. To estimate the background p.e. rate, we use Eq. (4.12).

## 4.8 Summary of the DIRC-like TOF detector background analysis

A detailed analysis of the Bruno simulation output showed that the background from radiative Bhabha is dominant for the DIRC-like TOF detector. The source is well-localized in space and corresponds to positrons which have lost a significant part of their energy (radiated via a photon), leave the nominal trajectory of the HER beam and hit the beampipe about 1 m away from the IP. On the other hand, the outgoing high momentum gammas (4-5 GeV) fly along the beam pipe and hit the bending magnets 10 m away from the IP. Thanks to the 1.5 T magnetic field and the 3 cm thick tungsten shield around the beam pipe, the particles which reach the DIRC-like TOF detectors are almost exclusively gamma (83 %) and neutrons (14 %). Gammas produce electrons in quartz volumes of the DIRC-like TOF detector mostly via Compton scattering; these secondary charged tracks create then some Cherenkov light. The corresponding background p.e. rate is estimated to be 480 kHz/cm<sup>2</sup>. Using the fact that the maximum acceptable integrated anode charge for SL-10 is 2.5 C/cm<sup>2</sup> [86] and assuming 5 years of nominal data taking, one can draw a plot which shows the maximum acceptable p.e. rate as a function of the MCP-PMT gain – see Figure 4.17.

The absorbed dose by the FTOFFEE is estimated to be 10 Gy/year (1 kRad/year) while the corresponding neutron flux is  $2.4 \times 10^{11} / \text{cm}^2/\text{year}$ . This implies that SiPMs cannot be used, due to a significant increase of the dark count rate in these conditions. A report about radiation damage of pixelated photon detectors – including SiPMs – by neutron irradiation can be found here [93].

The DIRC-like TOF event size and data rate can be estimated as well, taking into account the first level (hardware) trigger rate (150 kHz), the DIRC-like TOF readout time window width (100 ns) and the hit size (64 bit which include time and charge measurements). The event size is then about 0.3 kByte and the data rate  $\sim 0.4 \text{ GBit/s}$ .

For these computations we are using the numbers listed in Table 4.3.

Table 4.3: List of the constants used in this summary section to compute parameters relevant for the radiative Bhabha background.

Variable	Name	Value
Snowmass year	$t_{\text{Snowmass}}$	$2.0 \times 10^7 \text{ s}$
Crossing bunch frequency	$w_{\text{bunch crossing}}$	209 MHz
Data taking duration	$t_{\text{Data taking}}$	5 Snowmass years
MCP-PMT	SL-10 (4 channel)	
Total number of PMT	$N_{\text{PMT}}$	168
Effective area per PMT	$S_{\text{Effective}}$	$2.2 \times 2.2 \text{ cm}^2$
Photocathode	Multialkali	
Collection efficiency		60% (see [86])

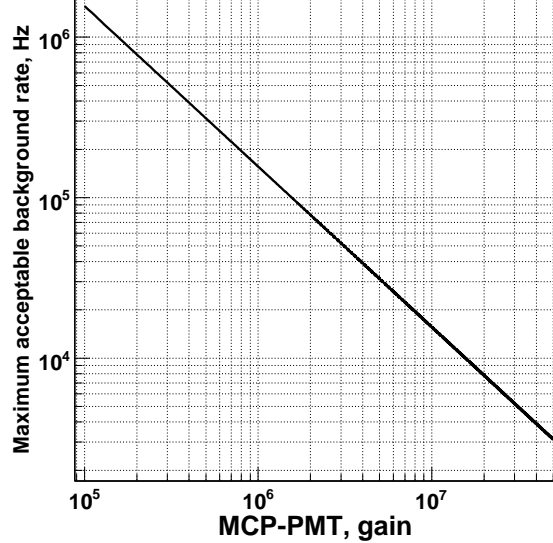


Figure 4.17: Maximum acceptable p.e. rate /cm<sup>2</sup>/s as a function of MCP-PMT gain to keep the integrated charge below 2.5 C after 5 years of running at nominal luminosity.

The background caused by the Touschek effect in the DIRC-like TOF detector is negligible with respect to the background coming from radiative Bhabha. However, due to the very small beam emittances at *SuperB*, the Touschek effect dominates the off-collision beam lifetime. For this reason, we perform studies of the Touschek background at the upgraded DAΦNE  $e^- e^+$  collider [94], where the “crab-waist” scheme designed for *SuperB* has been successfully tested in 2008-2009 [10].

## 4.9 Studying of the Touschek background at DAΦNE $e^- e^+$ collider

In 2007-2008, the LNF Accelerator Division modified the DAΦNE interaction region in order to test the new "crab waist" scheme [10, 95, 96], proposed to allow the *SuperB* machine to reach its ambitious luminosity goals while keeping power and background at a reasonable level. The main goal of this upgrade was to compare the luminosity increase with the simulation predictions. In addition, it was used to validate the simulation of the Touschek and beam-gas backgrounds which can potentially impact the next generation  $B$ -factory. This was done by comparing rates measured experimentally with the simulation predictions. I took part in this analysis at the beginning of my PhD thesis, using the data collected in 2008 and 2009 and a dedicated Geant-based simulation code I wrote for this task.

### 4.9.1 Upgrading the DAΦNE $\phi$ -factory

DAΦNE is a  $\phi$  meson factory which allows precise studies of kaon physics. Two 510 MeV electron and positron beams collide at the  $\phi$  energy. This resonance then decays by a majority in kaon pairs. A comparison of the interaction region (one arm) before and after the upgrade is shown on Figure 4.18. In particular, the upgraded DAΦNE's interaction region has two beampipes to produce collisions at a 50 mrad crossing angle and two sextupoles which induce the crab waist effect.

Various apparatus have been used to measure the luminosity of the new machine. The main one is made of two calorimeters installed on both sides of the IP and which counts the measured rate of Bhabha scattering events ( $e^+e^- \rightarrow e^+e^-$ ). This physics process is convenient for luminosity measurement because of its very clean experimental signature (two energetic back-to-back tracks coincident in time) which makes easier the signal selection and the background rejection. The measured rates are converted into an absolute luminosity by using a scaling factor provided by a dedicated full simulation of the apparatus. In addition to this luminometer, low-angle photon detectors have been installed few meters away from the IP: sensitive to the background fluctuations (the background rates exceeds significantly the luminosity-driven one, in case of the off-collision beams and so measuring the counting rate gives access to the background level), they can also be used to follow variations of the luminosity in real time – but not for absolute luminosity measurements because of the difficult separation between signal events and background.

The main parts of the detector are built, tested and installed in the DAΦNE IR by the LUMI team [95], are shown in Figure 4.19: the Bhabha calorimeters, the low-angle photon monitors and the gas electron multipliers (GEMs) which aimed at providing tracking information to the charged particles crossing the calorimeter modules but which could not be used for technical reasons during the data taking periods. There are two

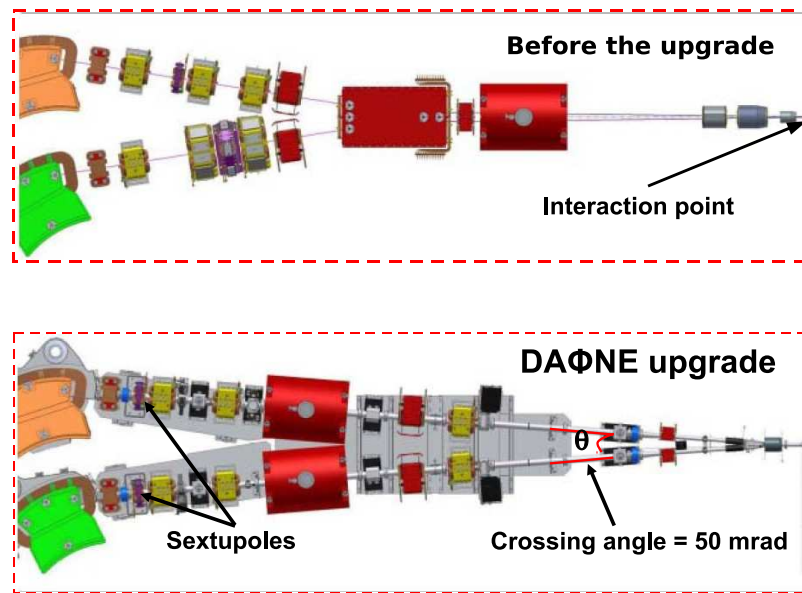


Figure 4.18: **Top:** DAΦNE’s interaction region before the upgrade. **Bottom:** Upgraded DAΦNE’s interaction region. We can see two beampipes instead of one before: in the new design, the electrons and positrons collide with a 50 mrad crossing angle. The back arrows on the left indicate the sextupoles inducing the crab waist effect and which are located about 9 meters away from the IP on both sides.

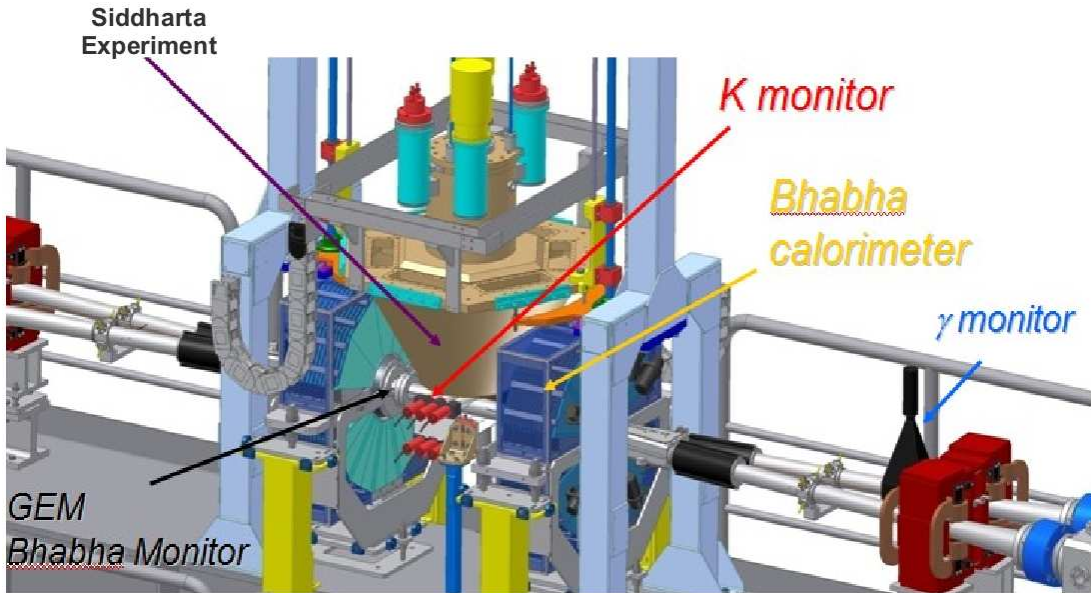


Figure 4.19: The various LUMI detectors installed in the DAΦNE interaction region: Bhabha calorimeters, GEM detectors (not used as they could not be installed in their nominal location due to conflict with the background shield of the independent Siddharta detector, located at the IP) and  $\gamma$  monitors (two of them located symmetrically from both sides of IP).

identical detectors of each type, installed at symmetric locations on both sides of the IP. Siddharta [97] is an independent detector which was taking data parallel to the test of the modified DAΦNE IR.

The calorimeters reconstruct the energy of the charged tracks produced in Bhabha scattering events. They have cylindrical shape and placed along the beampipe. Each calorimeter arm is made of 12 sectors of trapezoidal shape, which cover each  $30^\circ$  in azimuth; it is divided into 2 modules, one above the beampipe, and the other below. Each sector is a sandwich of 12 scintillating plastic tiles and 11 lead layers, 1 cm thick (the total depth corresponds to about  $12.5 X_0$ ). It is located at a distance of 32.5 cm on both sides of the IR and covers angular region between 18 and 27 degrees in theta. The calorimeter segmentation is a compromise between the need to know the track angle (Bhabha scattering events produce back-to-back tracks) and the number of independent DAQ channels. The calorimeters are protected from the background by lead walls which explain why additional detectors dedicated to the background monitoring are needed.

Finally, two photon detectors are located  $\sim 160$  cm away from the IP and on the way of the photons produced by low-angle radiative Bhabha events. They are made of four scintillating  $PbWO_4$  crystals. The sizes of each crystal is  $3 \times 3 \times 11\text{ cm}^3$  with a radiation length per unit length of about  $X_0 = 0.92$  cm. Each of the 4 crystals is wrapped in

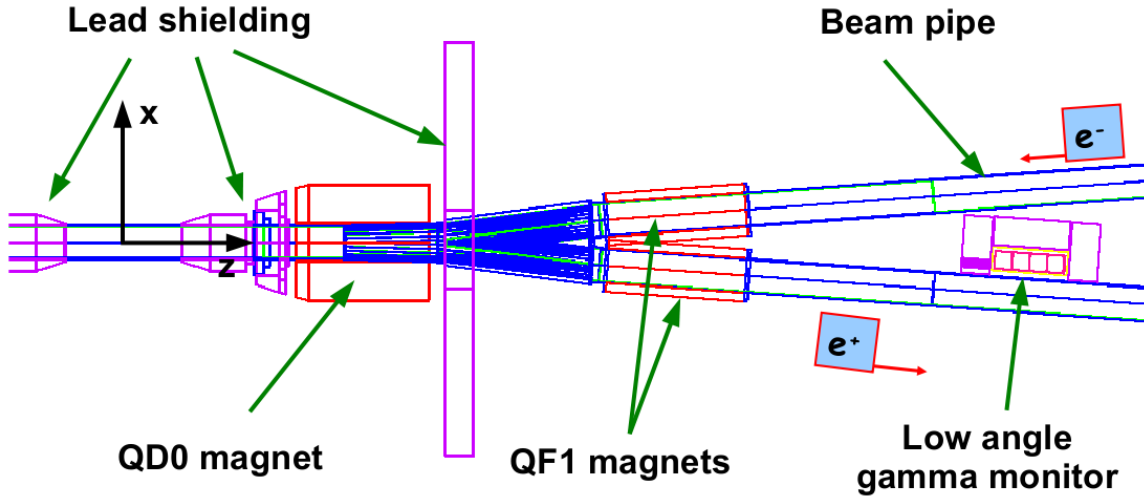


Figure 4.20: Geometry and material description of the interaction region implemented in Geant4. The simulation includes the lead shielding, the QD0 and QF1 quadrupoles, the low-angle gamma monitors and the beampipe.

reflective material in order to collect more light and readout by a Hamamatsu R7600 PMT. The primary role of these detectors is to detect photons emitted at low angle by radiative Bhabhas. This provides an additional relative luminosity measurement, independent from that performed with the calorimeters. Moreover, because the high rate at which low angle radiative Bhabhas events occur, it has been used to monitor the instantaneous variations of the luminosity.

#### 4.9.2 Geant4 simulation of the modified DAΦNE interaction region

A simulation predicting the rate and the energy of the Touschek background particles, as well as their position where they leave the beampipe, has been developed by the DAΦNE collider team [71]. It cannot be used directly for a comparison with real data since it does not include the interaction between these particles and the various materials present in the interaction region (not simulated), nor the response of the detectors. For these reasons we developed a Geant4 simulation based of the IR. The final goal is to predict the background particle rate and the energy distribution. The geometry of the interaction region implemented in Geant4 is shown on Figure 4.20. One can note that we did not include<sup>6</sup> into the simulation the calorimeters nor the GEMs since they are surrounded by thick protecting lead tiles and hence do not contribute to the electromagnetic showers

<sup>6</sup>However all elements have been included into the Geant3 simulation which has been used to estimate geometrical acceptance of the luminometer. This information is crucial for the luminosity measurements.

### Implementation of the magnetic field into Geant4 sim.

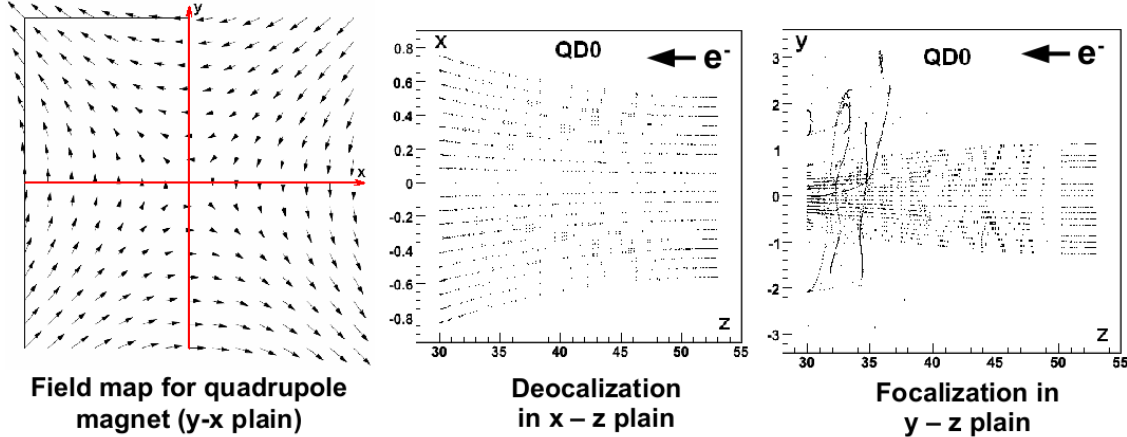


Figure 4.21: **Left:** Field map for the QD0 quadrupole magnet (see Eq. (4.16)). **Middle:** Defocalization in the  $z-x$  plane of the electrons which propagate toward the  $-z$  direction. **Right:** Focalization of the electrons in the  $z-y$  plane.

created by the Touschek particles outside this shielding and which propagate until the low-angle photon detectors. The components included in the Geant4 simulation are the following: the lead shielding around the IP (proper geometry plus accurate material description), the QD0 and QF1 quadrupoles, the low angle gamma monitors and the beampipe. We include as well a detailed description of the magnetic field

- for QD0:

$$\begin{cases} B_x[\text{kG}](y) = -2.938[\text{kG/cm}] \times y[\text{cm}] \\ B_y[\text{kG}](x) = -2.938[\text{kG/cm}] \times x[\text{cm}] \\ B_z = 0 \end{cases} \quad (4.16)$$

- and for QF1:

$$\begin{cases} B_x[\text{kG}](y) = 1.25[\text{kG/cm}] \times y[\text{cm}] \\ B_y[\text{kG}](x) = 1.25[\text{kG/cm}] \times x[\text{cm}] \\ B_z = 0 \end{cases} \quad (4.17)$$

with  $x$  and  $y$  being the coordinates in the transverse plane.

A typical field map for the QD0 quadrupole magnet is shown on Figure 4.21 (Left). To check the correctness of the magnetic field implementation in Geant, we performed a test. First we generate electrons with nominal and located on the nominal orbit (the center of the beampipe in the  $x-y$  plane): they follow the nominal trajectory while crossing the IR. By design, the QD0 magnet field should defocalize the electron beam in

## Low angle gamma monitor

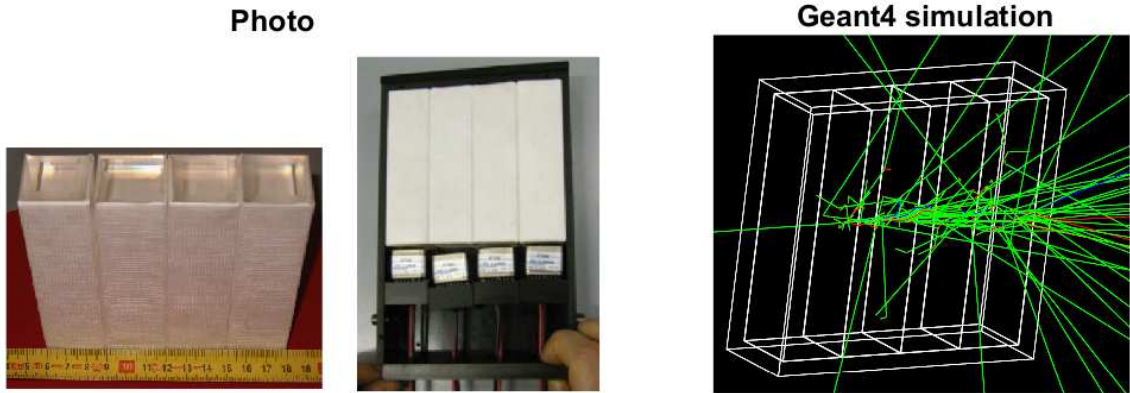


Figure 4.22: **Left:** Picture of the 4 PbWO<sub>4</sub> crystals. Each of them is wrapped into a reflective coating (in order to collect more light) and readout by a Hamamatsu R7600 PMT show on the middle picture. **Right:** The corresponding simulation of the gamma monitor; the 50 MeV gamma entering the volume and producing an EM-shower.

the  $z - x$  plane and focalize it in the  $z - y$  plane – as the electrons propagate toward the  $-z$  direction. These effects were observed in simulated data, as shown on the middle and right plots of Figure 4.21.

On Figure 4.22 one can see the picture of the PbWO<sub>4</sub> photon detectors which have been used for background studies and their implementation into the simulation. We did not simulate scintillation photons but rather reconstruct energy deposits in the four crystals.

### 4.9.3 Touschek generator

As already mentioned, a simulation of the Touschek background particles has been developed by the DAFNE collider team [71]. It predicts position and momentum (at the point when lost particles interact with the beampipe) of the particles which leave their stable trajectory due to the Touschek effect. On Figure 4.23, the outputs from this simulations are shown. This information has been used as input to the Geant4 standalone simulation of the DAΦNE interaction region we mentioned in the previous section. One can see that many particles hit the beampipe at  $z$  around  $\pm 160$  cm from the IP where the photon monitors are indeed installed. Note: this simulation has been done for the electron ring. However, since the electron and positron rings are ‘symmetrical’, the corresponding positron distributions would be the same for the  $x$ ,  $y$ ,  $P_x$  and  $P_y$  variables, and opposite for  $z$  and  $P_z$ .

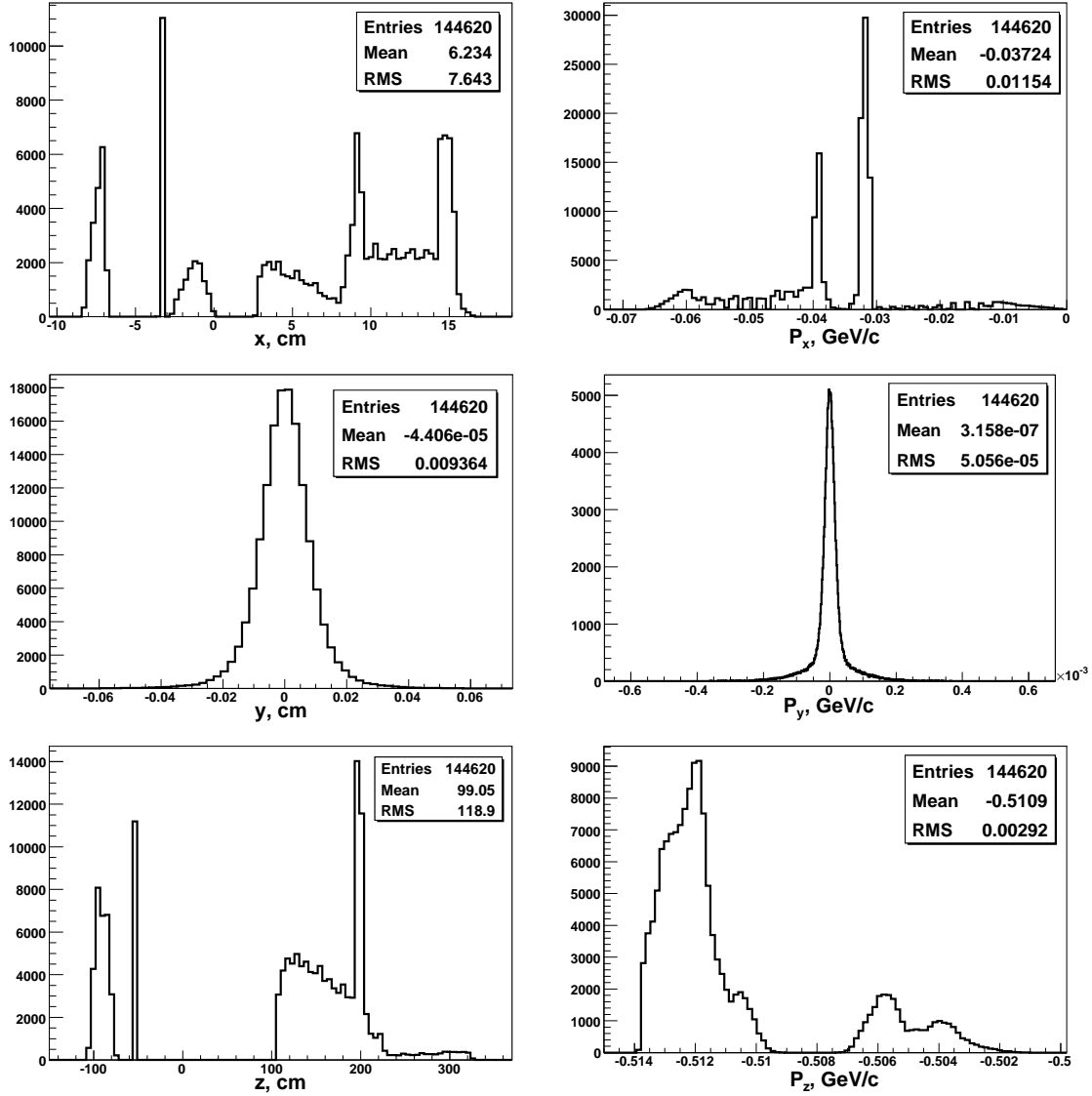


Figure 4.23: **Left column:** Histograms of the  $x$  (top),  $y$  (middle) and  $z$  (bottom) positions where the Touschek particles hit the beampipe. **Right column:**  $P_x$  (top),  $P_y$  (middle) and  $P_z$  (bottom) momentum coordinates at the location where the Touschek particles hit the beampipe.

#### 4.9.4 Calibration of the low-angle photon detectors

The gamma monitors have been calibrated by using their spectra which are shown on Figure 4.24 from the top. These measurements were done during the runs with colliding beams. One can see the sharp drop on the spectrums indicated with magenta dashed line (channel = 40 for electrons and 67 for positrons). This drop corresponds to a deposited energy by the radiative Rhabha gamma emitted with the maximum possible energy  $\sim 500$  MeV<sup>7</sup>. From the simulation (see Figure 4.24 from the bottom) we know that 500 MeV gamma in average deposit 440 MeV. Taking into account parameters of the ADC (the range is from 0.0 V to 0.5 V and total number of channels: 256) the calibration for electron and positron photon monitor respectively can be obtained:

$$E[\text{MeV}] = (5.3 \pm 0.4) \times \text{Amplitude}[\text{mV}] \quad (4.18)$$

$$E[\text{MeV}] = (4.9 \pm 0.7) \times \text{Amplitude}[\text{mV}] \quad (4.19)$$

#### 4.9.5 Background rate measurement and comparison with simulation

Assuming that the Touschek background is dominant for off-collision beams, its level can be estimated by measuring the rate in the photon monitors during this particular beam conditions. The black triangles in Figure 4.25 show the simulated variation of the gamma monitor rate versus threshold (in MeV), as obtained in simulation. As already pointed in the previous section, the experimental setup makes the spectrum end around 440 MeV which is below the beam energy (510 MeV). Blue (red) bullets show the actual rates measured by the gamma monitor sensitive to photons emitted by positrons (electrons) for a few thresholds. In order to allow a direct comparison with the simulation, these numbers have been corrected to take into account the coupling between the beams. Although the agreement between simulation and measurements is not perfect, both sets of numbers appear to be in the right ballpark – the actual rates also depend on various machine conditions which are not easy to reproduce nor to quantify.

---

<sup>7</sup>Obtained with bhwide radiative Bhabha generator

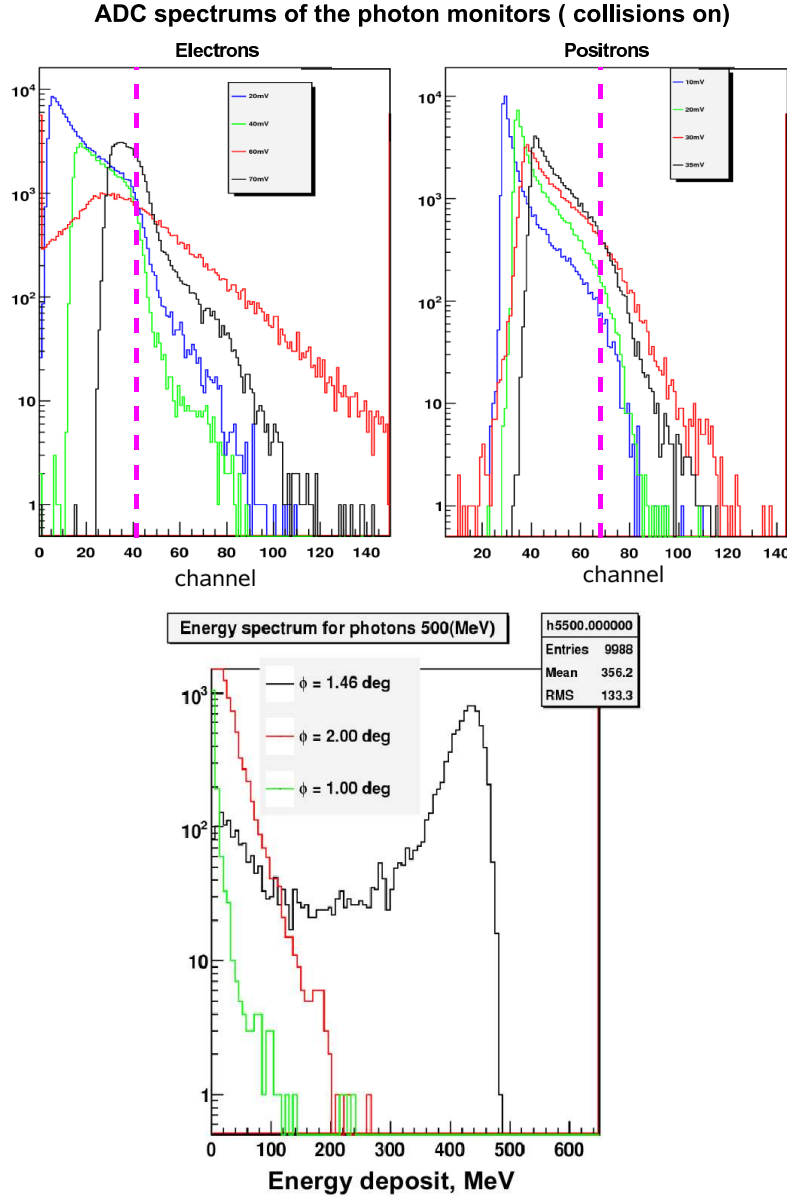


Figure 4.24: **Top:** ADC spectra of the electron (left) and positron (Right) low angle photon monitors. The histograms correspond to measurements done with different discriminator thresholds. For electrons the thresholds are equal to: 20 mV (blue histogram), 40 mV (green), 60 mV (red) and 70 mV (black). Note that measurements with a 60 mV threshold have not been taken into account. For positrons the thresholds are equal to: 10 mV in blue, 20 mV in green, 30 mV in red and 35 mV in black. **Bottom:** Simulated distributions of the energy deposited in the low angle photon monitor by 500 MeV gamma generated at the IP (0,0,0) with different  $\phi$  angles ( $1.46^\circ$  in black,  $2.0^\circ$  in red,  $1.0^\circ$  in green).

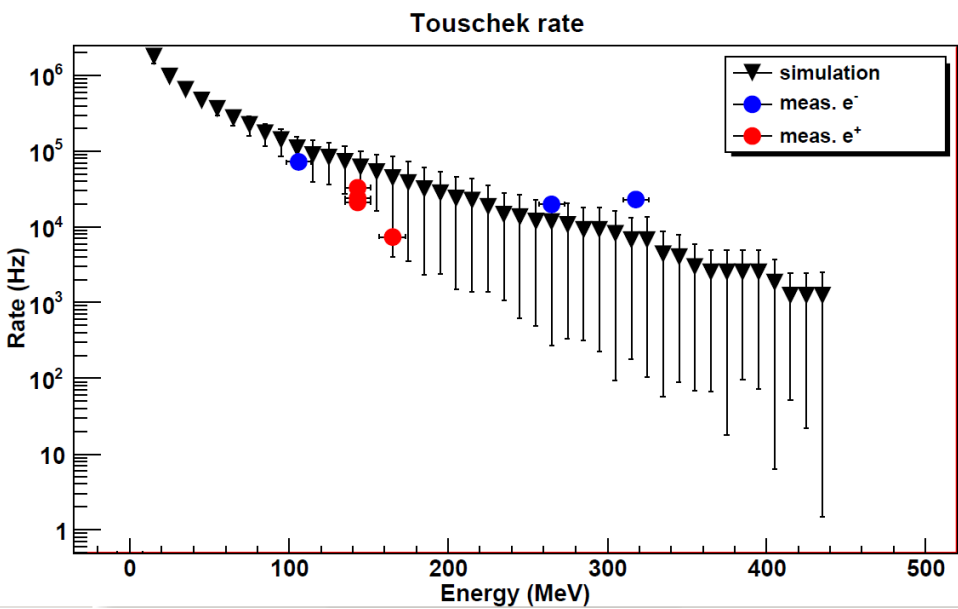


Figure 4.25: Comparison between simulated (black triangles) and measured (blue dots for the electron beam, red ones for positrons) rates in the gamma monitors. The rates extracted from data have been corrected to take into account the beams coupling in order to allow a direct comparison with the simulation.

# Chapter 5

## Test of the DIRC-like TOF prototype at SLAC CRT

In this chapter we describe the test of a DIRC-like TOF prototype performed at SLAC Cosmic Ray Telescope (CRT) from Fall 2010 to Spring 2011. We start by the main goals of the experiment; then, we describe the prototype itself and the associated ultrafast readout electronics developed at LAL: the WaveCatcher. A detailed description of the CRT follows the DIRC-like TOF prototype one. Then we describe the full simulation of the DIRC-like TOF prototype, including the PMT response, and what we learn from it. Finally, we present the measurements and compare them with the simulation.

The main goals of the CRT experiment are:

- a proof of principles of the DIRC-like TOF concept.
- to test the performances of an electronics crate containing 8 USB WaveCatcher (USBWC) 2-channel boards [66, 67].
- to estimate the time resolution per channel of the prototype.

### 5.1 Experimental setup

The DIRC-like TOF prototype has been assembled at SLAC CRT in Fall 2010. The prototype is readout by dedicated USBWC electronics through amplifiers and filters. The experimental setup is shown in Figure 5.1: schematics (top drawing) and picture of the actual device (bottom). The DIRC-like TOF prototype is working in coincidence with a quartz start counter located under it which provides  $t_0$ -time of the system. It is located inside the CRT which is used to obtain a clean sample of cosmic muons and to measure the track to about 1.5 mrad accuracy. In particular it allows us to restrict strongly

the muon polar angle around  $90^\circ$  – vertical tracks provide the cleanest measurements of the prototype performances. During the 6 months of data taking, the CRT collected  $\sim 2.5 \times 10^6$  muons. Each time there is a coincidence between the quartz start counter and at least one channel of the prototype, all 16 channels are readout and the whole waveforms stored.

### 5.1.1 Cosmic Ray Telescope

#### Description of the apparatus

The CRT facility [98] has been built at SLAC National Accelerator Laboratory about a decade ago to test new Cherenkov detectors: the first focusing DIRC prototypes [19] and now the *SuperB* FDIRC [21]. The CRT is also used to test new ideas like pixelated TOF detectors [99, 100, 101, 102] or the DIRC-like TOF prototype. Figure 5.2 shows a side view of the CRT. Its main components are the following:

- The quartz start counter (QSC).

The arrival time of the cosmic muon is given by the quartz start counter. It is made of two quartz bars ( $29.3 \times 4.2 \times 1.5 \text{ cm}^3$  each), coupled to a 4 pixel Photonis MCP-PMT – pixel number 3 provides the QSC trigger to the DIRC-like TOF prototype. The QSC is tilted by  $43^\circ$  from the horizontal plane to use the direct Cherenkov light produced by almost vertical tracks. Its resolution was measured to be 42 ps in a test beam [104, 105, 22] and 73 ps with cosmic muons [102].

- Two trigger counters (T1, T2).

The CRT includes two large ( $60.1 \times 121.9 \text{ cm}^2$ ) trigger counters. They are made of 30.48 cm-wide pieces of plastic scintillators glued together along their long edges and readout by Photonis Quantacon PMTs located at each corner. The coincidence between  $T1 \times T2 \times QSC$  is the general trigger of the CRT. About 12,000 events are collect per day.

- Four stack counters (S4, S3, S2, S1).

These detectors provide indirect information about the muon momenta. They consist of  $\sim 30$  cm thick iron plates with plastic scintillators in between, each readout by four PMTs located on the corners – see Figure 5.3 (Left). The stack counters have  $10\times$  amplifiers to achieve a good sensitivity to small signals. On Figure 5.3 (Right) the muon range in iron is shown as a function of momentum. The more a muon penetrates inside the stack counters, the higher its momentum. For example, by requiring a signal in the S1 detector muons with momentum bigger than  $1.6 \text{ GeV}/c$  are selected. The composition of the 'CRT muon' sample (i.e. the muons which make the CRT trigger:  $T1 \times T2 \times QSC$ ) is shown in the Table 5.1.

- Two hodoscopes: Hodoscope1 (bottom), Hodoscope2 (top) – see Figure 5.4.

The hodoscopes have an area of  $51 \times 106.9 \text{ cm}^2$  each. They are providing two points

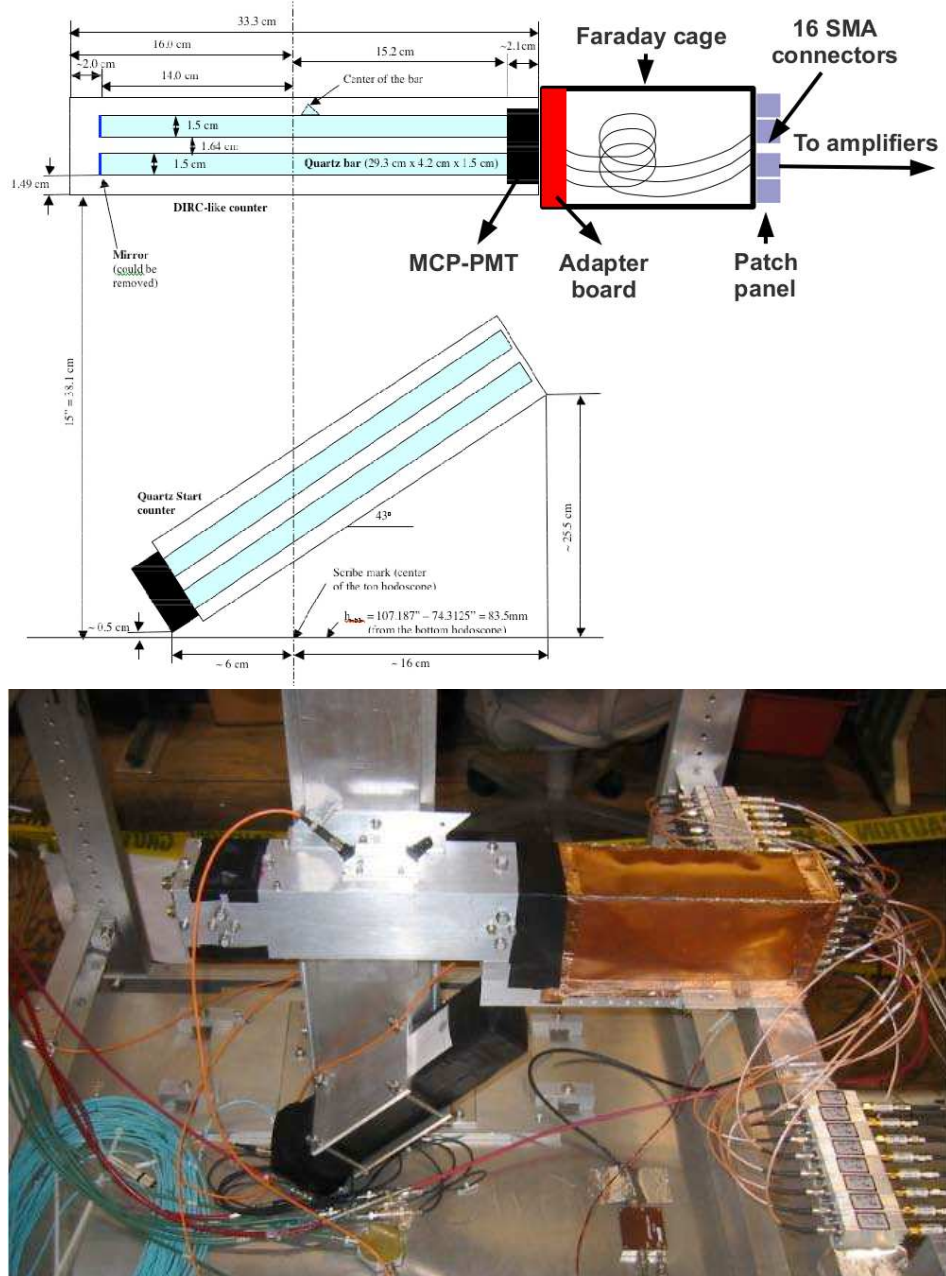


Figure 5.1: **Top:** The DIRC-like TOF prototype is made of two quartz bars on top of each other (blue rectangles in the top part of the drawing) in which cosmic muons produce Cherenkov light. The photons propagate through total internal reflection until a MCP-PMT (black box on the right of the bars). The signals produced by the 16 PMT channels are readout by an USBWC electronics crate protected from electromagnetic noise by a Faraday cage. The prototype is working in coincidence with a quartz start counter located under it (the tilted device in the bottom part of the schematics) which provides a fast trigger when a muon crosses it. **Bottom:** Corresponding picture of the experimental setup. The DIRC-like TOF prototype is inside the aluminum box visible on the left; right to it, there is the Faraday cage (orange box). There are 16 PMT outputs, each connected to an USBWC electronics channel – see text for details. Under the DIRC-like TOF prototype, one can see the tilted quartz start counter.

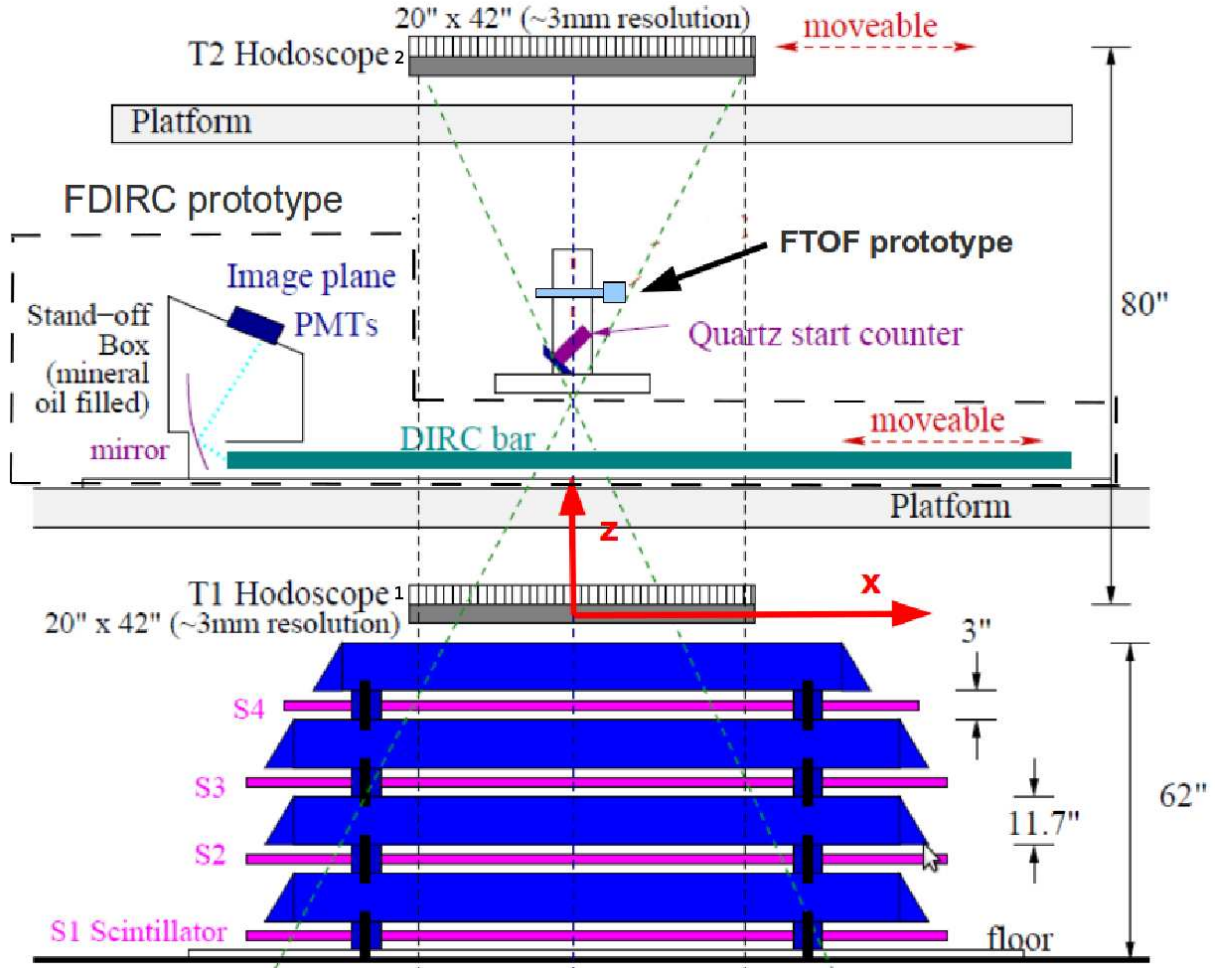


Figure 5.2: CRT side view adapted from Ref. [103]. The CRT has two large ( $60.1 \times 121.9 \text{ cm}^2$ ) trigger counters called T2 (above the top platform) and T1 (below the bottom platform). The arrival time of the cosmic muon is given by the quartz start counter (QSC) which precision is around 73 ps. Four stack counters (S4, S3, S2, S1) provide information about muon momentum: for example, requiring a signal in the S1 detector selects muons with momentum bigger than 1.6 GeV/c. Two  $51 \times 106.9 \text{ cm}^2$  hodoscopes (top: Hodoscope2; bottom: Hodoscope1) are located close to the trigger counters. Their spatial resolution (about 0.29 cm) allows one to measure muon angles with a precision of 1.1 mrad. The coincidence  $\text{T1} \times \text{T2} \times \text{QSC}$  makes the CRT trigger: around 12,000 CRT events are collected per day. The origin of the coordinate system used in this chapter is located in the center of the bottom hodoscope; the z-axis is pointing upwards while the x-axis goes from left to right (in the direction opposite to the FDIRC stand-off box, located on the left side of the drawing). Finally, the y-axis is chosen to complete the right-handed coordinate system.

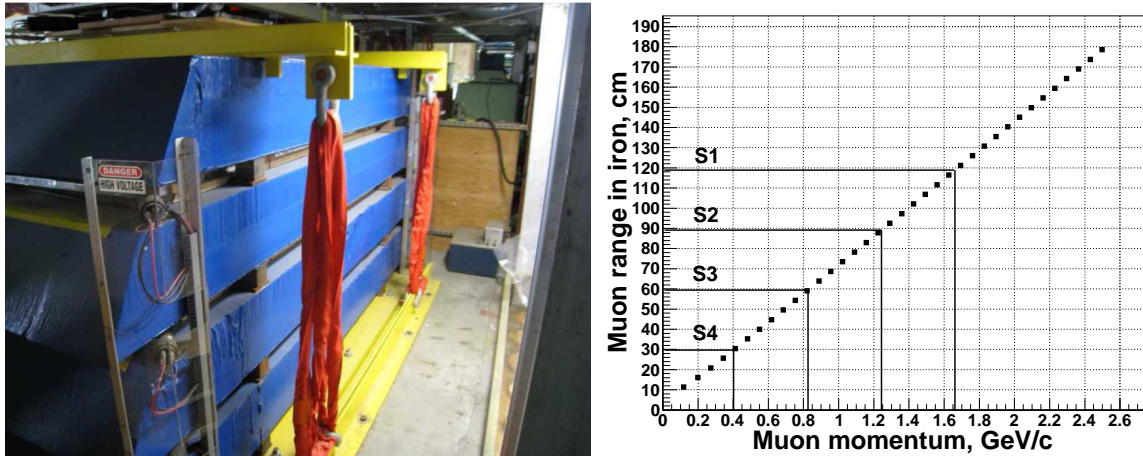


Figure 5.3: **Left:** Picture of the CRT stack counters. They are made of  $\sim 30$  cm thick iron plates and plastic scintillators in between, readout by four PMT located on the corners. **Right:** Plot of muon range in iron as a function of momentum, adapted from a Geant4 simulation performed by the KEK-to-Kamioka long-baseline neutrino experiment [106].

on the muon trajectory (assumed to be a straight line), hence allowing to compute its direction. Each hodoscope consists of two parts (each made of two overlapping layers) measuring the  $x$  and  $y$  coordinates independently. The hodoscope fingers are 3 cm wide; thanks to the overlap between layers, the effective granularity of this system decreases from 3 to 1 cm – see Figure 5.4 (Right). This means that the RMS of the hit distribution is equal to  $1.0 \text{ cm}/\sqrt{12} = 0.29 \text{ cm}$ . Taken into account the distance between the top and bottom hodoscopes (263.4 cm), the angle resolution is:  $(0.29 \text{ cm})/(263.4 \text{ cm}) \sim 1.1 \text{ mrad}$ .

Finally, the origin of the coordinate system used in this chapter is located in the center of the bottom hodoscope; the z-axis is pointing upwards while the x-axis goes in the direction opposite to the FDIRC stand-off box. And the y-axis is chosen to complete the right-handed coordinate system – see Figure 5.2 for details.

### Muon reconstruction

The muon reconstruction is done using the two hodoscopes. The trajectory of the muon is assumed to be a straight line, which is an approximation because of multiple scattering in the 5 1.5 cm thick quartz bars (the 2 of the DIRC-like TOF prototype, 2 in the QSC and 1 in the FDIRC prototype not used for our test). Each hodoscope finger is connected on one side to a PMT which is readout by a TDC.

Let us describe briefly the muon reconstruction algorithm which has been developed to analyze the CRT test. In order to reduce the number of background hits per finger we set the time window for signal between 20 and 60 ns (the start time is given by the QSC). Then we count the number of fired channels in each hodoscope part ( $x$  and  $y$ ). Three

Table 5.1: Composition of the 'CRT muons' (i.e. the muons which make the CRT trigger: T1×T2×QSC). The 'reco.' column gives results for the CRT muons which trajectories are reconstructed in the hodoscopes. In the 'cuts' column we require in addition that the reconstructed muon track crosses the QSC.

Stack counter	Momentum (GeV/c)	Momentum ID	Fraction (%) all	Fraction (%) reco.	Fraction (%) reco. + cuts
-	< 0.4	0	22.9	8.6	3.9
S4	0.4 - 0.8	1	11.3	6.6	4.6
S3	0.8 - 1.2	2	9.6	5.6	4.3
S2	1.2 - 1.6	3	11.0	6.2	5.0
S1	> 1.6	4	45.2	25.0	21.2
Total eff.			100	52.0	39.0
Rate/day			~11760	~6115	~4586
Rate/day with mom. > 1.6			~5316	~2940	~2493

different cases can happen.

1. The number of hits is one.
2. The number of hits is two but the fingers overlap.
3. The number of hits is more than one but the fingers do not overlap.

In order to reconstruct a cosmic muon, all four hodoscope parts have to satisfy condition 1 or 2; taking into account the effective width of the finger (1 cm) and its position the track coordinate can be calculated. Events which belong to case 3 are rejected as the muon trajectory cannot be reconstructed.

The  $y$  vs.  $x$  muon hit coordinates in top and bottom hodoscopes are shown in Figure 5.5. One can see that muon hits are uniformly distributed on the top hodoscope while they mostly appear in the center of Hodoscope1. This is because the CRT trigger includes the QSC which is located close to the bottom hodoscope.

The distributions of the coordinates of the muon intersections with the QSC are shown on Figure 5.6. Their measured boundaries match very well the shape of the QSC projection on the  $x - y$  plane. Efficiency of CRT muon reconstruction is about 52% – see Table 5.1 – but if we require additional cuts on the muon intersection with the QSC (namely  $-8.6 < x_{\text{intersection QSC}} < 12.4$  and  $-1.6 < y_{\text{intersection QSC}} < 2.59$ ), the muon reconstruction efficiency goes down to 39%. Figure 5.7 shows the fraction of selected muons vs. momentum ID for different samples. The tighter the selection cuts, the more the sample contains high momentum muons.

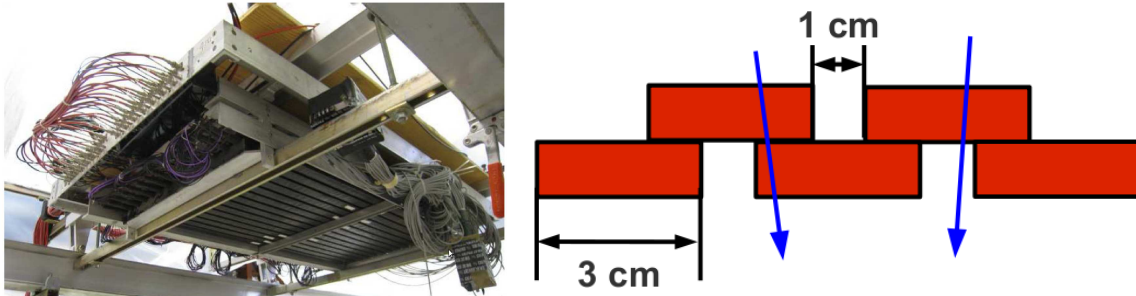


Figure 5.4: **Left:** Photo of the top hodoscope (T2). **Right:** Schematic sectional view of two hodoscope layers measuring a given coordinate. The red boxes are detector fingers and blue arrows are muons. The overlap between fingers makes the effective granularity of this detector equal to 1 cm.

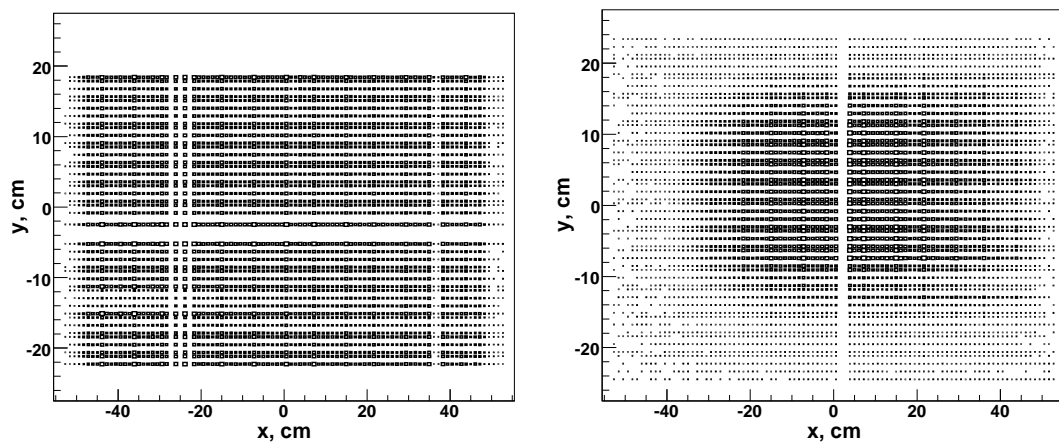


Figure 5.5:  $y$  vs.  $x$  muon hit coordinates in top (left) and bottom (right) hodoscopes. White bands correspond to dead channels. All muons fire the QSC which is located close to the bottom hodoscope. This is why the right distribution is not uniform.

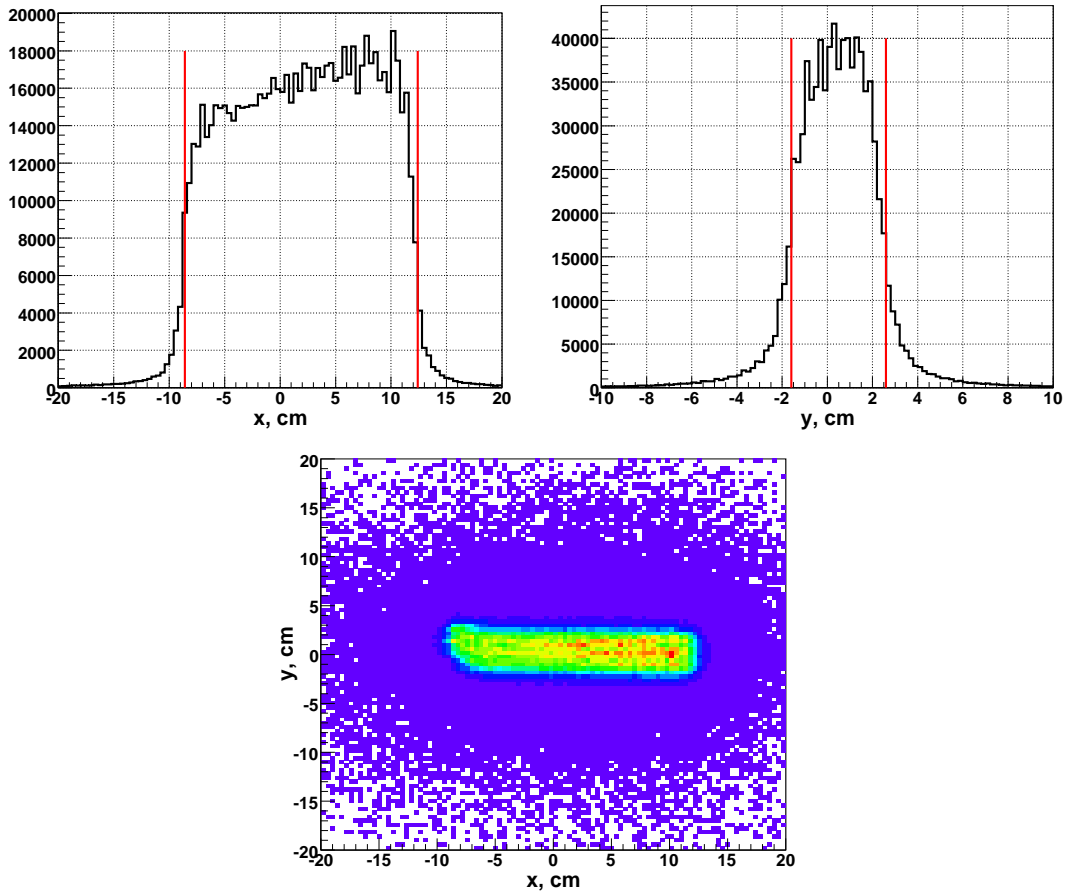


Figure 5.6: Coordinates of the muon intersection with the QSC. **Top left:**  $x$  distribution. **Top right:**  $y$  distribution. **Bottom:**  $y$  vs.  $x$  distribution. The red vertical lines on the top plots mark the measured boundaries of the QSC. The distances between them are 21 cm in  $x$  and 4.2 cm in  $y$  which are consistent with the size of the QSC projection on the  $x - y$  plane.

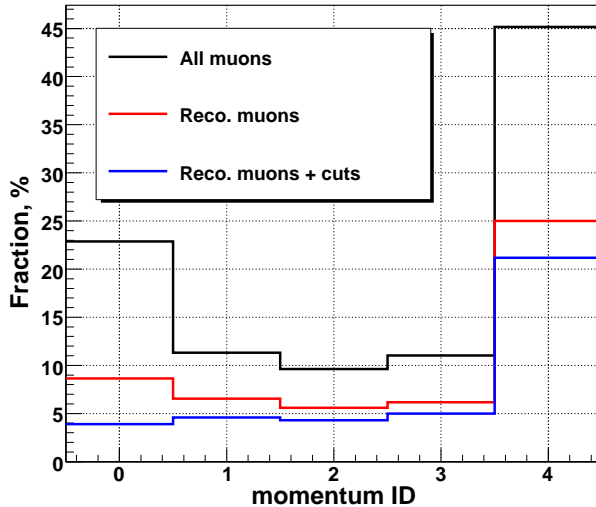


Figure 5.7: Fraction of selected CRT muons vs. momentum ID (see Table 5.1 for the definition of this quantity) for three different muon samples: no reconstruction (black histogram), reconstructed muons (red histogram) and reconstructed muons intersecting the QSC (blue histogram).

### 5.1.2 DIRC-like TOF prototype

#### Setup.

The two quartz bars ( $29.2\text{ cm} \times 4.2\text{ cm} \times 1.5\text{ cm}$ ) are connected on one side to a Photonis 10-micron holes MCP-PMT (serial number: 85014) with a 6 mm stepped face, as shown on Figure 5.14. There are aluminum mirrors attached to the opposite sides of the bars which are held by small dots of epoxy and greased to the quartz surface. The mirrors could be removed, if desired and they are not used in the following. The whole setup is located into an aluminum box. The front view of the DIRC-like TOF prototype is shown in Figure 5.9 (Left).

The drawing of the PMT high voltage (HV) divider is shown on Figure 5.10 (Left). The PMT is operating at -2.7 kV which corresponds to a gain of  $7 \times 10^5$  according to a calibration curve obtained at SLAC – see Figure 5.10 (Right). This high gain makes possible the detection of single photons. This tube has a cathode-to-MCP distance of only 0.85 mm, which means that the TTS distribution does not have a long tail. TTS measurement for a similar stepped face MCP-PMT was done by Jerry Va'vra: he got a TTS of  $\sim 37$  ps [100].

16 independent channels are defined from the  $8 \times 8$ -pixel matrix of the PMT using the scheme presented in Figure 5.9 (Right). The top three pixels of a given column are connected together to form one channel. Going down, the next two pixels are grounded and the bottom three form another channel. The same pattern is reproduced on all 8

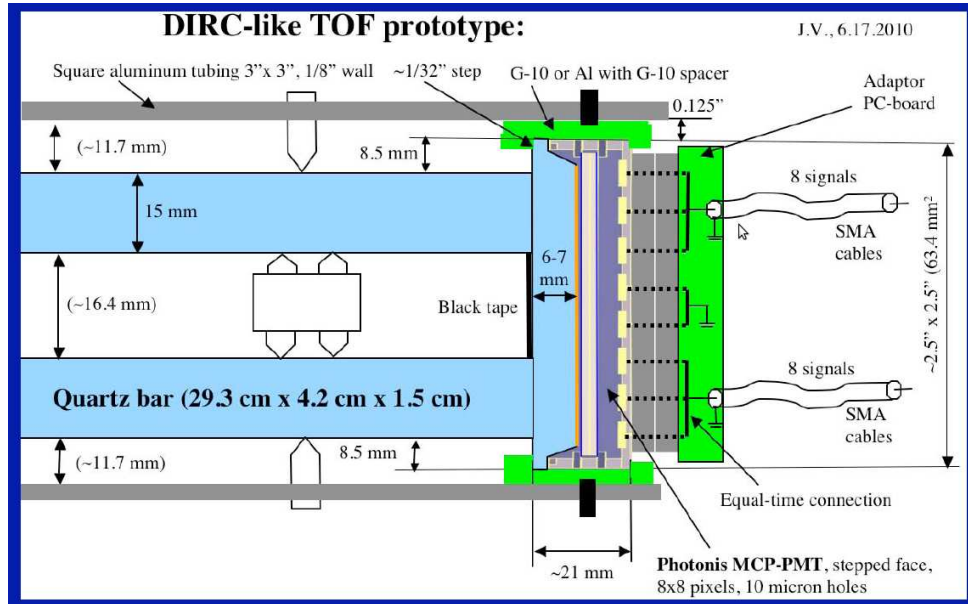


Figure 5.8: FTOF prototype side view showing the quartz bars (in blue), the quartz window, the Photonis MCP-PMT and the cables going to the USBWC electronics.

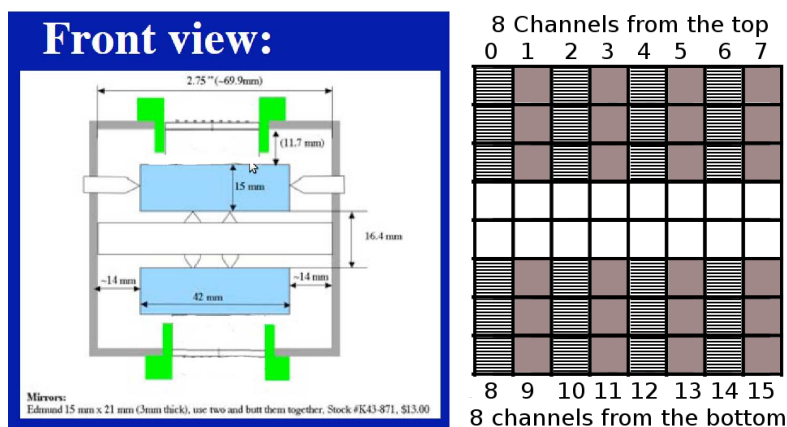


Figure 5.9: **Left:** DIRC-like TOF prototype front view. **Right:** Schematic view of the 16 MCP-PMT pixels (8 on the top bar, 8 on the bottom bar).

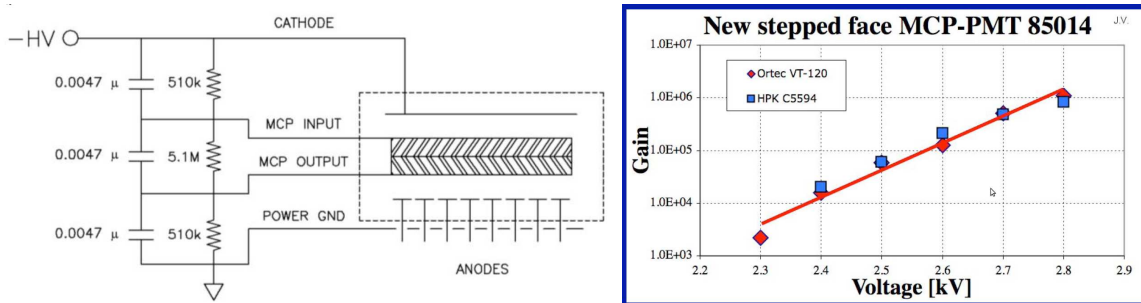


Figure 5.10: **Left:** High voltage divider circuit for the Photonis MCP-PMT. **Right:** Gain of this MCP-PMT vs. high voltage [100].

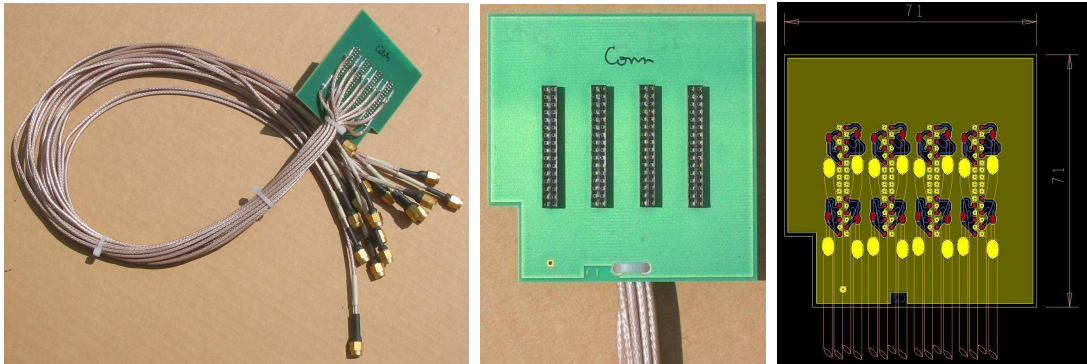


Figure 5.11: Pictures and schematics of the LAL-made adapter board which makes the 16 channels from the  $8 \times 8$  pixel matrix of the MCP-PMT. Within this board, all lengths between MCP-PMT anodes which make one channel and corresponding cable inputs are corrected to have the same length: 14.7 mm. This removes additional time jitter when connecting pixels together.

columns and allows the top and bottom channels to be clearly separated. In order to remove additional time jitter, all lines between the MCP-PMT anodes which make one channel and the cable inputs need to have the exact same length. This requirement was achieved using an adaptor board developed at LAL and shown in Figure 5.11. Within this board, the lengths are corrected: they all measure 14.7 mm.

Each channel is connected to a 1 GHz bandwidth MITEQ amplifier with a 36 dB gain (for more details, see Table 5.2), followed by a 530 MHz bandwidth filter (see Table 5.3) and finally to an USBWC channel. Events are saved to disk each time there is a coincidence between the quartz start counter and one of the USBWC channels (which common threshold is set to 20 mV). Each of the 16 waveforms has a length of 256 points separated in time by 312.5 ps. The light leakage from one bar to the other was reduced by adding black tape on the MCP-PMT window between the contact surfaces of the two bars.

Table 5.2: MITEQ amplifier

Model	AM-1687-1000
Input and output connector	SMA
Frequency Minimum	1 MHz
Frequency Maximum	1 GHz
Electrical Specifications	
Gain Minimum	36 dB
Gain Flatness	$\pm 0.75$ dB
Noise Figure	3.3 dB
Voltage 1 (Nominal)	15 V
Current 1 (Nominal)	150 mA
Impedance	50 Ohms
Datasheet	see Ref. [107]

Table 5.3: Low Pass Filter VLF-530.

Producer	Mini-Circuits
Model	VLF-530
Operating Temperature	-55 °C to 100 °C
Input and output connector	SMA
Passband (loss < 1 dB)	530 MHz
Cutoff frequency (loss 3 dB)	700 MHz
Stop band (loss > 20 dB)	820 – 5500 MHz
Stop band (loss > 40 dB)	1050 – 3200 MHz
Datasheet	see Ref. [108]

### Suppression of electromagnetic noise and cross-talk.

To reduce the electromagnetic noise coming from the outside world, one had to enclose the MCP-PMT and the adapter board in a Faraday cage. The waveform produced by a single p.e. and measured using a HPK 1.5 GHz bandwidth amplifier C5594 is shown on Figure 5.12 (Left) together with another channel showing a cross-talk signal plus pulse. The amplitude of the cross-talk is around 5-8% of the single p.e. signal amplitude. The cross-talk and pulse ringing was reduced by inserting a low pass filter (530 MHz bandwidth) after the amplifier. One can compare the cross-talk levels without (middle oscilloscope screenshot) and with (right screenshot) filter in Figure 5.12.

### Laser connection to calibrate the DIRC-like TOF prototype.

In order to test the DIRC-like TOF prototype, a laser beam ( $\lambda = 635$  nm) was used – see Figure 5.13. The laser fiber ends with a lens, which produces a parallel beam. In order to inject photons into the quartz bar, a glass prism has been used. Its two short faces are sanded while the bottom face is polished and glued to the center of the bar. The sanded surfaces scatter light in all directions, ensuring a good coverage of all channels. Mylar sheets, inserted at the laser end, allow to decrease the photon flux to the single photon

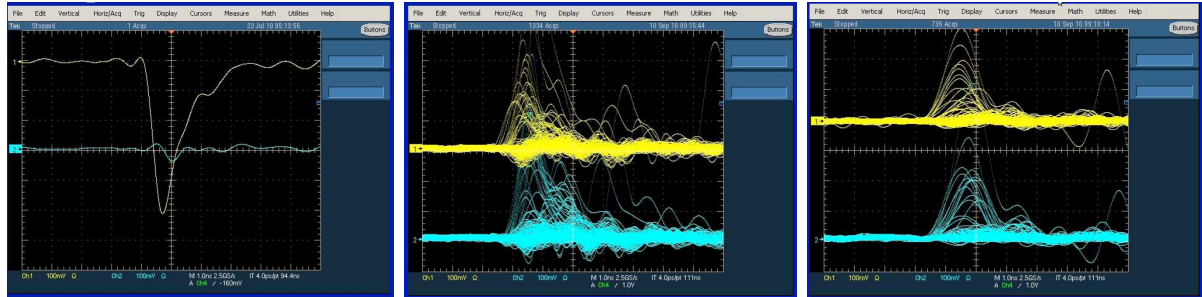


Figure 5.12: Oscilloscope screenshots illustrating cross-talk ringing effects in the MCP-PMT channels. **Left:** Single p.e. pulses, cross-talk and pulse ringing. **Middle:** Superposition of several events showing cross-talk effect without low pass filter. **Right:** Similar screenshot showing the attenuation of cross-talk after adding the low pass filter with 530 MHz bandwidth.

level in the whole PMT.

### 5.1.3 Readout electronics and data acquisition software

The readout electronics called USB WaveCatcher (USBWC) developed at LAL and CEA/IRFU has been used for the test of the DIRC-like TOF prototype. In Figure 5.15, pictures of the 16-channel USBWC crate are shown. Progress on development of electronics and data acquisition software can be followed by looking at status reports presented during consecutive *SuperB* workshops [109, 110, 111, 112, 113, 114].

The whole system consists of eight 2-channel USBWC V5 boards [66] plus one Controller (clock and control) board. Its block diagram is shown on Figure 5.16. The patch panel is providing the interface between the MCP-PMT inside the Faraday cage and the external coaxial cables. Each of the 16-channels is connected to a 36-dB, 1-GHz bandwidth amplifier, followed by a 530-MHz low pass filter and finally the analog inputs of an USBWC board. The Controller board distributes 8 very well-synchronized clocks to the USBWC boards via coaxial cables. Both the USBWC and the Controller boards have Trig in and Trig out ports to exchange trigger signals both ways. Pixel number 3 of the QSC defines an external trigger for all 8 USBWC boards through the control board. When this signal is received, if any of the USBWC has a valid signal on one of its channels, all analog memories are stopped and their contents are read out. A valid signal is defined as a waveform with amplitude above a given threshold, which can be chosen arbitrarily via the USBWC graphic user interface – we set it to 20 mV for the CRT test. If at least one channel is found to contain a signal, all 16 waveforms are readout and stored into the disk of the data acquisition (DAQ) PC via USB.

The clock and control board – see Figure 5.17 (Top) – houses the following components.

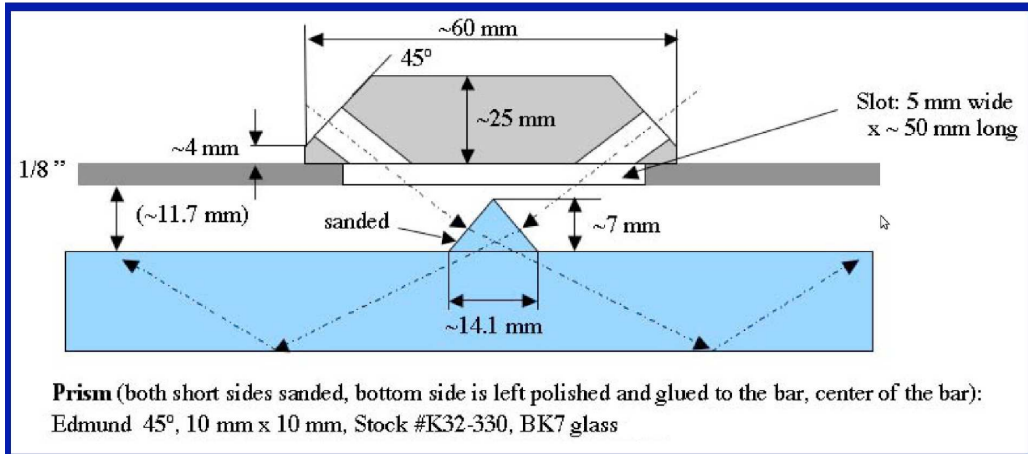


Figure 5.13: Drawing of the setup used to calibrate the DIRC-like TOF prototype with a laser. On the top one can see the plug for the laser fiber. The fiber ends with a lens, which produces a parallel photon beam. In order to inject photons into the quartz bar, a glass prism has been used. Its two short faces are sanded while the bottom face is polished and glued to the center of the bar. The sanded surfaces scatter light in all directions, ensuring a good coverage of all channels. Mylar sheets allow to decrease the photon flux to the single photon level in the whole PMT.

- Trigger input/output which requires/sends NIM signals.
- Pulse output – mainly used for debugging.
- Cyclone FPGA which controls the board and sends event data to the DAQ.
- 480 Mbits/s USB interface chip for the DAQ and  $\mu$  USB connector (ensuring communication with the PC and power supply in standalone mode).
- Zero jitter clock buffer which distributes 8 clocks (very well synchronized) to the USBWC boards.
- 200 MHz reference clock.
- 8 clock outputs.
- 8 trigger inputs and 8 trigger outputs. They permit communication between the controller and USBWC boards.
- +5 V power Jack plug, used to bring the main power to the board when it is used in a crate – a PC cannot provide power to many boards in parallel through USB.

The 2-channel USBWC V5 board – see Figure 5.17 (Bottom) – has a very low power consumption ( $\approx 2.5$  W). It houses the following components.

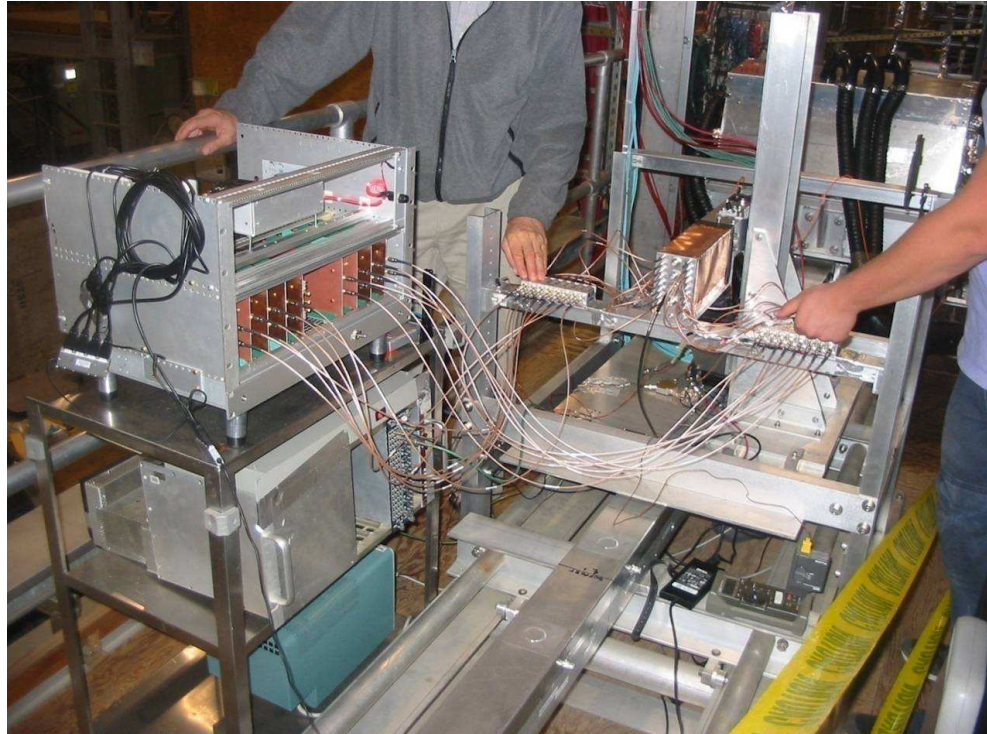


Figure 5.14: Photo of the experimental setup. DIRC-like TOF prototype from the right and readout electronics from the left.

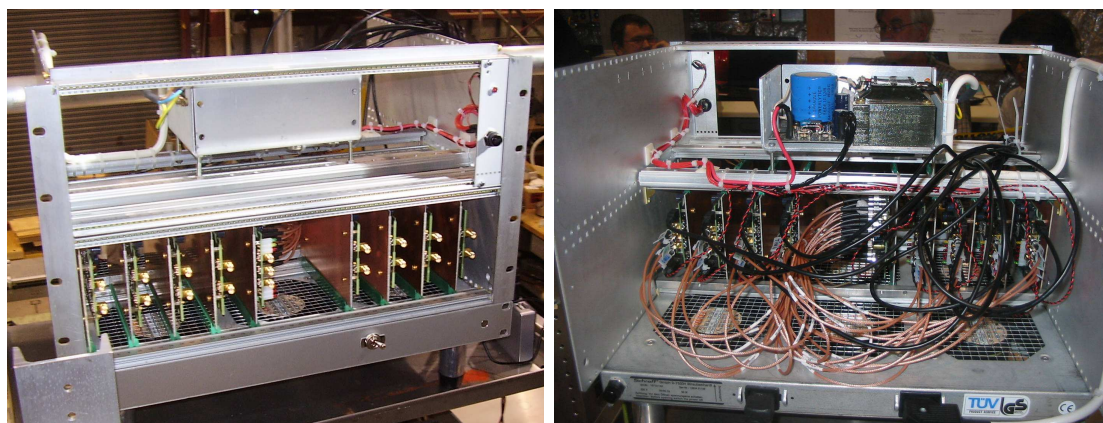


Figure 5.15: Pictures of the 16-channel USBWC crate. On the front view (left picture), one can see nine boards: from left to right four USBWC boards, the clock and control board and the other four USBWC boards. On the back view (right picture), the USB (black) and clock & trigger (orange) cables are visible. The crate power supply is located on top.

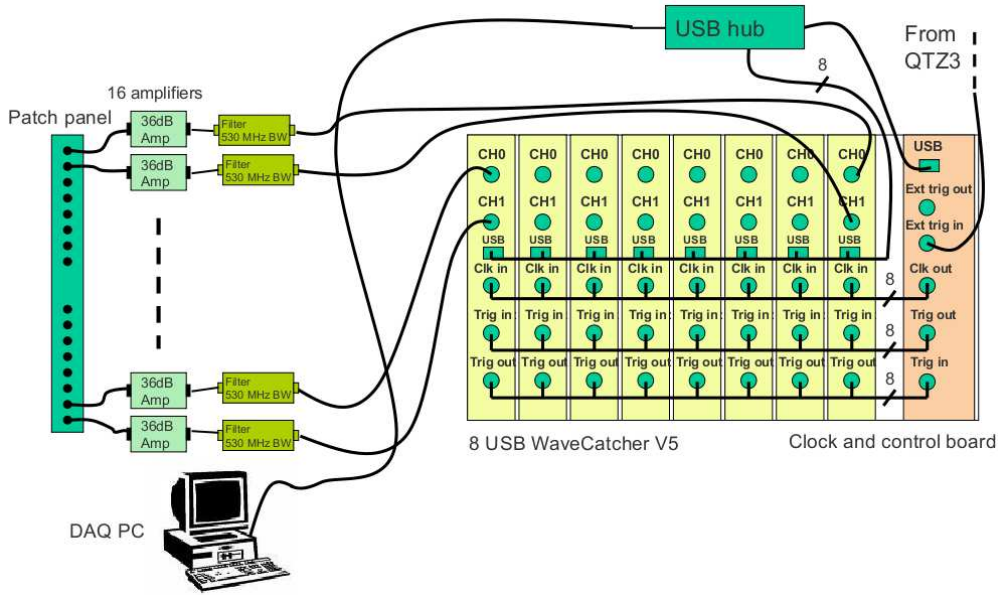


Figure 5.16: Electronics setup: The patch panel (green box on the left) is making the interface between the MCP-PMT inside the Faraday cage (not shown here) and the external electronics. Each of the 16-channels is connected to a 36 dB, 1 GHz bandwidth amplifier, followed by a 530 MHz low pass filter and finally the analog inputs of an USBWC board. The clock and control board (right-most board) distributes 8 very well-synchronized clocks to the USBWC boards via the clock out port ('Clk out' on the drawing). Both the USBWC boards and the clock and control board have 'Trig in' and 'Trig out' ports to exchange trigger signals both ways. Pixel number 3 of the QSC (labelled 'QTZ3' on the drawing) defines an external trigger for all 8 USBWC boards through the control board. When this signal is received, all analog memories are stopped and their contents are scanned to look for a signal. A signal is defined as a waveform with amplitude above a given threshold, which can be chosen arbitrary via the USBWC graphic user interface – we set it to 20 mV for the CRT test. If at least one channel is found to contain a signal, all 16 waveforms are readout and stored into the disk of the DAQ PC via USB.

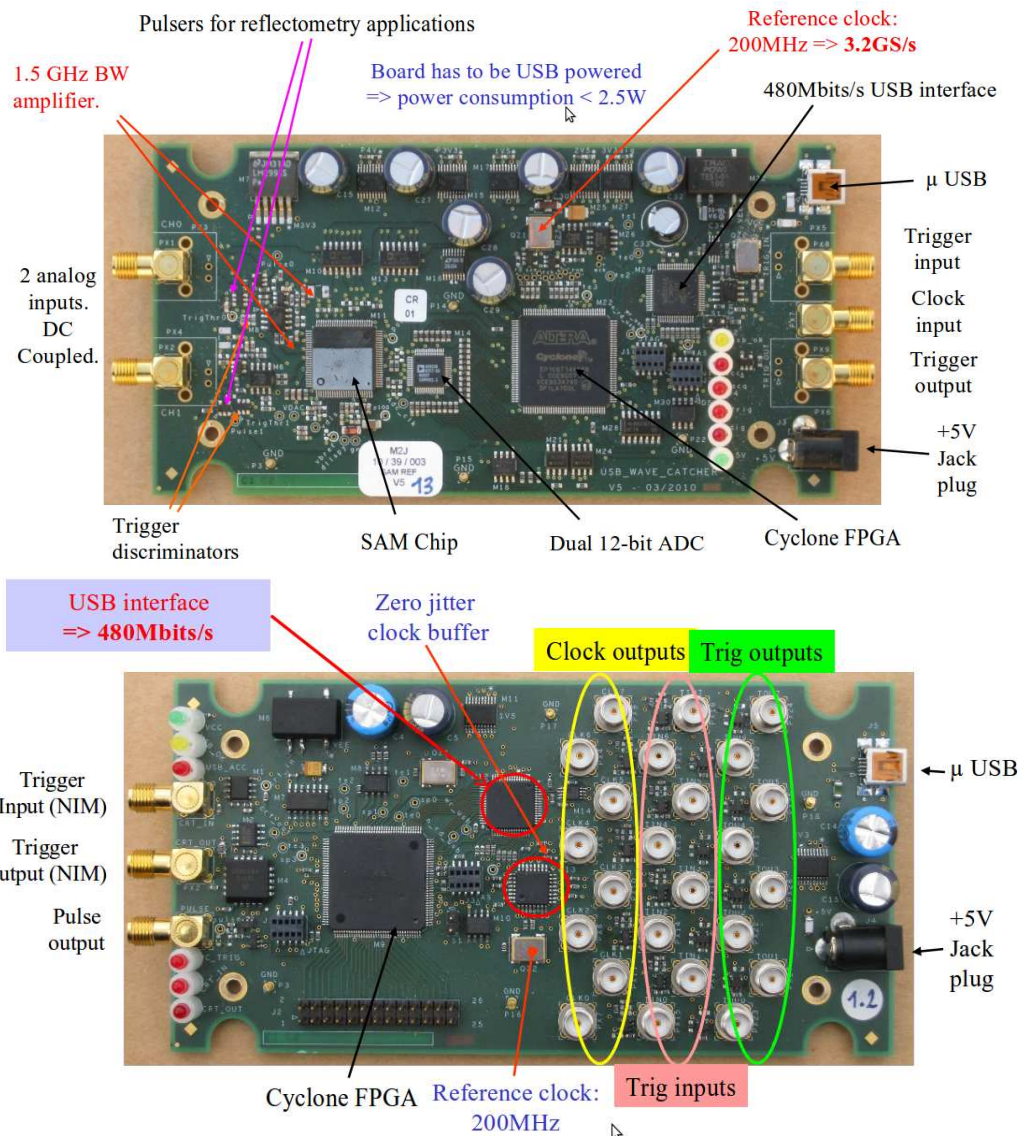


Figure 5.17: **Top:** Clock and control board. **Bottom:** USBWC board V5. See text for details.

- 2 analog inputs, DC coupled by 1.5 GHz bandwidth amplifiers.
- 2 trigger discriminators: by choosing a suitable amplitude threshold, noise can be rejected.
- 2 pulsers for reflectrometry applications (for instance calibration and monitoring of the timing delays in the system).
- 200 MHz reference clock.
- SAM chip [115]. This analog memory is the main component of the board. Its area is about  $11 \text{ mm}^2$ ; it integrates 60,000 transistors and houses two channels with  $16 \times 16 = 256$  memory storage cells each. The analog memory contains the samples of the waveform taken at different instants of time. The distance in time between two consecutive samples is defined by the delay between memory cells. Fortunately, thanks to the innovative design of the memory, these delays are almost insensitive to temperature variations, but they have anyway to be calibrated. This calibration is performed with a simple 70 MHz sine wave. During one period of the clock, 16 delays of a delay line are crossed by the write pointer. Hence one can reach a sampling rate  $16 \times 200 \text{ MHz} = 3.2 \text{ GS/s}$ .
- 12-bit ADC which houses two channels. Its main purpose is to perform the analog-to-digital conversion of the selected waveforms.
- Cyclone FPGA which performs data acquisition and data transmission through USB interface.
- 480 Mbits/s USB interface and  $\mu$  USB connector.
- Trigger input and output, which requires/sends NIM signals.
- Clock input which reads the signal distributed by the clock and control board.
- +5 V power Jack plug.

A dedicated software to configure the USBWC crate and to steer the DAQ has been developed in LAL. Screenshots of the associated graphic user interface (GUI) written in CVI/LabWindows are shown in Figure 5.19. The panels are oscilloscope-like and permit displaying all 16 waveforms. The main panel allows to setup the DAQ and the live display by acting on the following parameters.

- RUN: the run type is specified here. Three options are possible: single (acquisition of events one by one for debugging); finite (choice required to store events on disk) or continuous (same as finite but events are not written on disk).
- DISPLAY: on/off live visualization of events (turning the display off increases the DAQ speed); choice between superposition of waveforms and average; display of the Fast Fourier Transformation (FFT) of the waveforms.

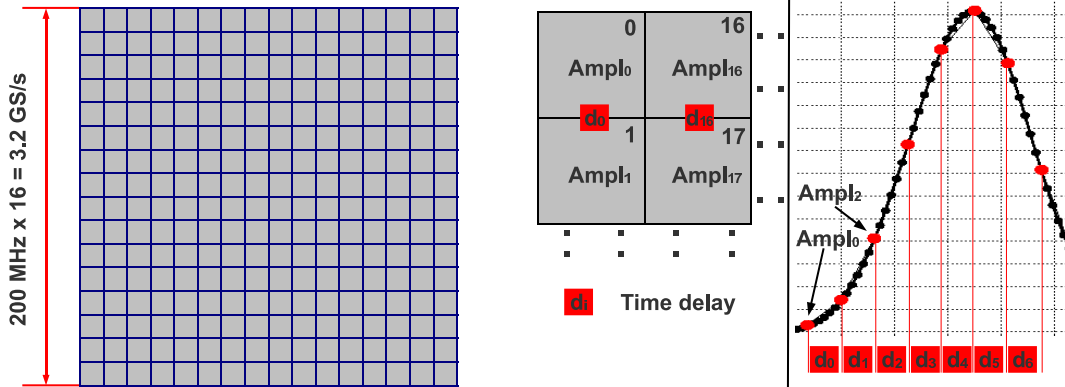


Figure 5.18: **Left:** Schematic view of the  $16 \times 16$  analog memory. **Right:** The waveform recorded by the analog memory. One cell contains the amplitude of the waveform at a given time  $t_0$ . Next closest cell contains the amplitude at time  $t_0 + d_0$ , where  $d_0$  is a servo-controlled time delay between these two cells.

- Pulse Output to setup output signals (Pulse/clock and pulse internal/external).
- TRIGGER DELAY by up to 255 samples.
- SAMPLING: the sampling rate ranges from 400 MHz to 3200 MHz which correspond to 640 ns and 80 ns waveform time window respectively.
- TRIGGER TYPE. The possible choices are: software, normal, auto, internal, external and CRT trigger. For the CRT test, we use the CRT mode which requires an external trigger and at least one USBWC channel firing.
- POSITION: this defines the relative positions of the waveforms in the display window on the right side of the panel. Possible choices are: equidistant (waveforms displayed one below the other with the same vertical spacing between them), merged (superposition of the 16 waveforms), by board (same as equidistant with shorter vertical gap between channels from the same board), and user defined.

Additional information like which channels are active and the event rate are displayed as well on this panel.

There are 8 independent board panels, each dedicated to two channels. In each of them, different parameters can be set channel by channel.

- THRESHOLD: sets the trigger threshold (20 mV in our case).
- Edge: defines whether the trigger is applied on the rising edge or on the falling edge of the signal.

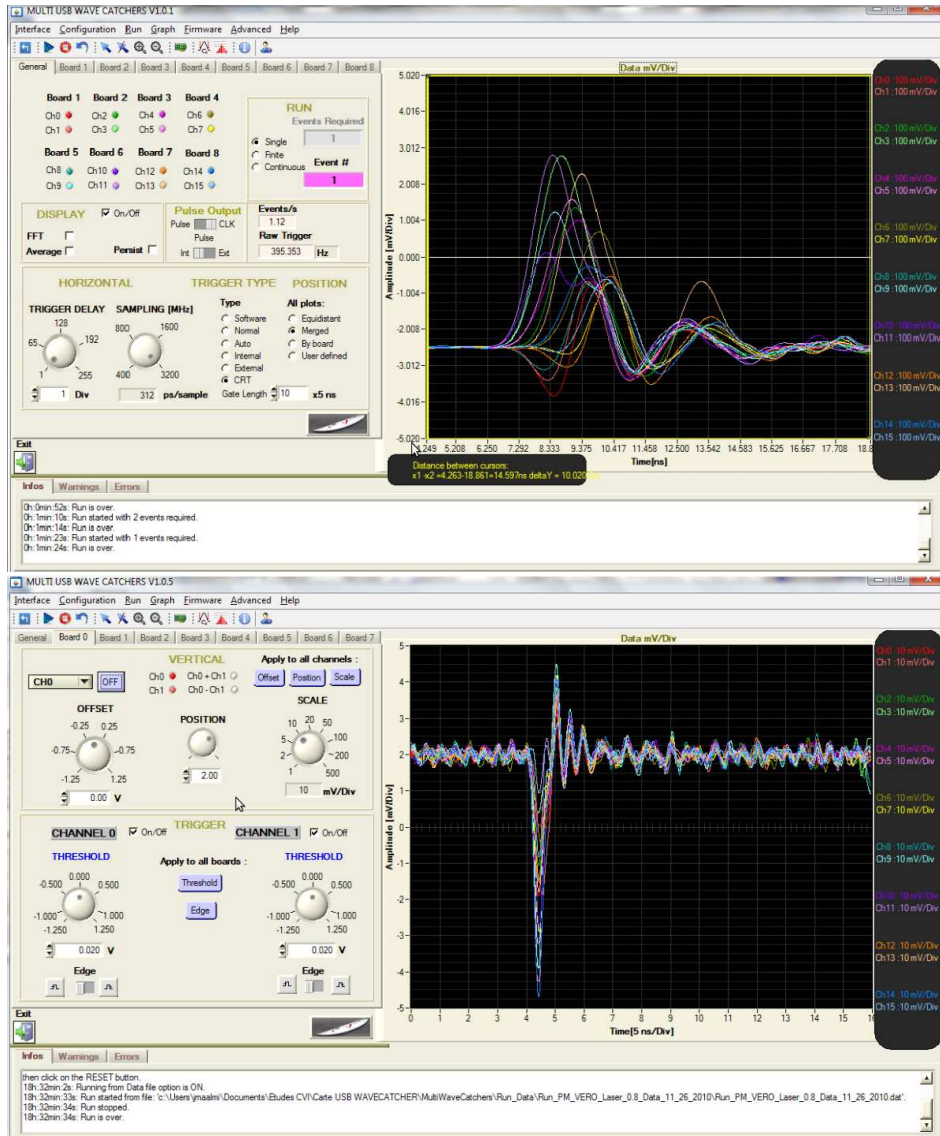


Figure 5.19: Displays of the 'multi USBWC' software developed in LAL to steer the USBWC crate. The top display shows the main panel while the bottom one shows an example of the panel used to configure a particular board. See text for details.

- **OFFSET:** the DC offset of the input channel. The full amplitude range of the ADC goes from -1.25 to 1.25 V. Depending on the level of the input channel, a proper constant DC offset is applied to preserve the signal shape.
- **POSITION:** defines the vertical offset on the display.
- **SCALE:** defines the vertical scale on the display.

All software output (general information, warnings and errors) are saved in a logfile. The raw waveform data plus some quantities computed online (charge, amplitude and timing) are written in ASCII format to disk. Each file contains 500 events which correspond to 2-3 hours of data taking. This is a tradeoff between the number of files and their individual size: in this way only a small amount of data would be lost in case of writing error. Data are stored on a PC sitting close to the DIRC-like TOF prototype in the SLAC CRT building. They are transferred remotely to LAL through the dropbox @software [116] without the need of any intervention on site. Flushing out regularly the DAQ PC disk makes sure that no data would be lost in case of hardware crash.

## 5.2 Waveform analysis

In this section we describe the analysis of the waveforms stored during the DIRC-like TOF prototype data taking. The analysis of each waveform starts with a third-order spline interpolation. It provides  $N_{sp} = 5$  additional equidistant points (then joined by straight lines to define the signal amplitude at any time) between two consecutive USBWC values – the time distance between two consecutive points is approximately 50 ps. This choice is a bit conservative as detailed simulation studies – see section 5.4.1 – have shown that the final time precision is almost independent from  $N_{sp}$ . As a raw waveform contains 256 points, the spline interpolation provides us with a total of  $256 + 255 \times 5 = 1531$  values. Many parameters are computed for each waveform; the most relevant are the following – see Figure 5.20 for a graphical definition.

- The amplitude of the signal, taken from the first peak exceeding a 20 mV threshold.
- The signal time corresponding to a constant fraction of 50% from the amplitude:  $cft_{50}$ .
- The signal charge ( $Q_{kn}$ ), proportional to the integral of the waveform between bins  $k$  and  $n$ . It can be computed using the following formula:

$$Q_{kn}[\text{in C}] = \sum_{i=k}^n \Delta Q(t_i) = \sum_{i=k}^n \frac{U(t_i)}{R} \Delta t = K \frac{\Delta t[\text{in ps}]}{R[\text{in Ohm}]} \sum_{i=k}^n U(t_i)[\text{in V}] \quad (5.1)$$

where  $\Delta t = 52.1$  ps is the time distance between two consecutive digitized points,  $R$  is the input impedance of the USBWC equal to 50 Ohm,  $U(t_i)$  is the amplitude of

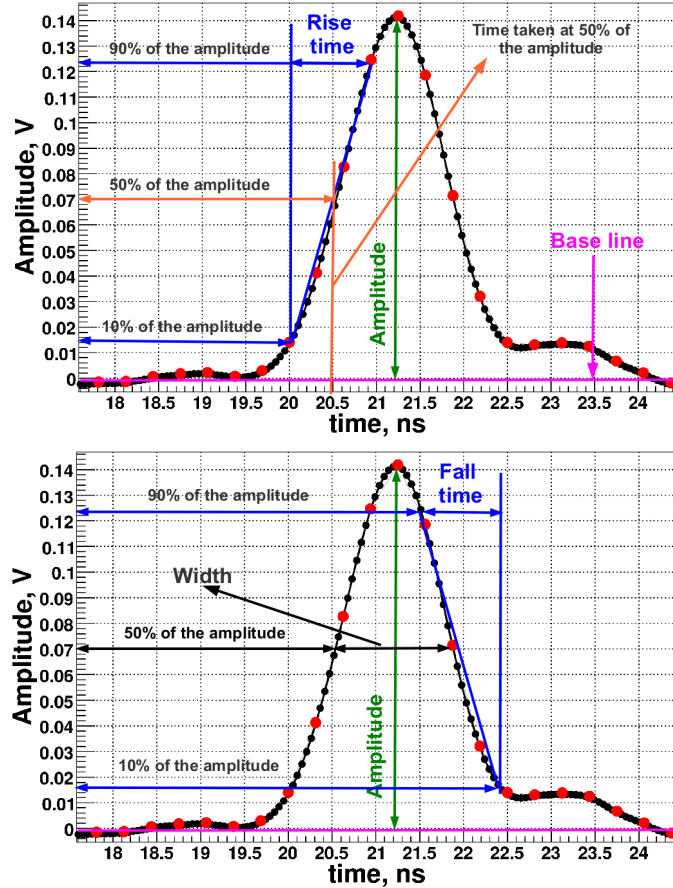


Figure 5.20: Definition of the main parameters computed for each waveform (this example of signal is extracted from the laser run described in the following section). The two plots show the same signal which has been duplicated for clarity reasons: some quantities are defined on the top plot while others are defined on the bottom one. Red points correspond to real measured values of the amplitude with USBWC electronics. One can see five additional equidistant black points in between two consecutive red dots; these values are obtained with a third order spline interpolation. This makes the time distance between two closest values of the amplitude equal to  $\Delta t = 312.5/6 \approx 52.1$  ps. **Top:** First we calculate the baseline amplitude (magenta line) by averaging the 6 first real measurements (red dots); this allows us to minimize the time smearing due to baseline fluctuations. Then we subtract this baseline from all points to make the amplitude pedestal always equal to 0. The amplitude of the signal (shown in green) is defined as the first local maximum of the waveform exceeding a 20 mV threshold. The constant fraction time is a time taken at given fraction of the amplitude from the rising or fallen edge of the signal (cft or  $cft^f$  respectively). On the figure one can see in orange the time taken at 50% of the amplitude:  $cft_{50}$ . The rise time (shown in blue) is defined as  $cft_{90} - cft_{10}$ . **Bottom:** The fall time (shown in blue) is defined as  $cft_{10}^f - cft_{90}^f$ . The width of the signal (shown in black) is given by  $cft_{50}^f - cft_{50}$ .

the signal at time =  $t_i$ . In practice, we measure the charge of the whole waveform: for this reason,  $t_{k=0} = 0$  and  $t_{n=1530} = 80$  ns.  $K$  is a dimensionless normalization constant equal to  $10^{-12}$ .

More sophisticated algorithms could be used to compute the integral under the waveform, hence improving the precision of the charge measurement. However, this variable was mainly used for rough estimations of the number of p.e. and not for the waveform selection. Instead, the amplitude was the main discriminant variable.

- The signal rise time, defined as the difference  $cft_{90}-cft_{10}$  taken at rising edge of the waveform.
- The signal fall time, defined as the difference  $cft_{10}^f-cft_{90}^f$  taken at falling edge of the waveform.
- The signal width, defined as the difference  $cft_{50}^f - cft_{50}$  taken at falling and rising edges of the waveform respectively.
- A shape classification number (shapeID) used to identify clean waveforms suitable for time measurements. We define four categories of waveforms – see Figure 5.21 and text below for details.
  - 'Crosstalk-like': signals which start with a negative edge (shapeID = 0).
  - 'Singlepeak-like': signals which start with a positive edge and only have one peak (shapeID = 1).
  - 'Multipeak-like': signals which start with a positive edge and present at least 2 peaks (shapeID = 2).
  - Other shapes (shapeID = -1).

We now describe the shape analyzer algorithm used to determine the shapeID variable. This algorithm has three input parameters shown on Figure 5.21.

- The signal threshold (SP threshold) = 20 mV: this parameter defines the minimum positive amplitude a signal should have to be analyzed. The amplitude of the first local maximum after threshold crossing defines the amplitude of the signal. The time  $cat_{20mV}$  which corresponds to the crossing of this constant amplitude will be used in the following.
- The crosstalk threshold (CT threshold) = -7 mV: this parameter defines the minimum negative amplitude for a signal to be identified as Crosstalk-like. The time ( $cat_{-7mV}$ ) which corresponds to this constant amplitude will be used as well.
- The multipeak fraction = 0.8: it is defined in the following equation.

$$\text{Multipeak fraction} = \frac{\Delta A}{\text{Amplitude}} \quad (5.2)$$

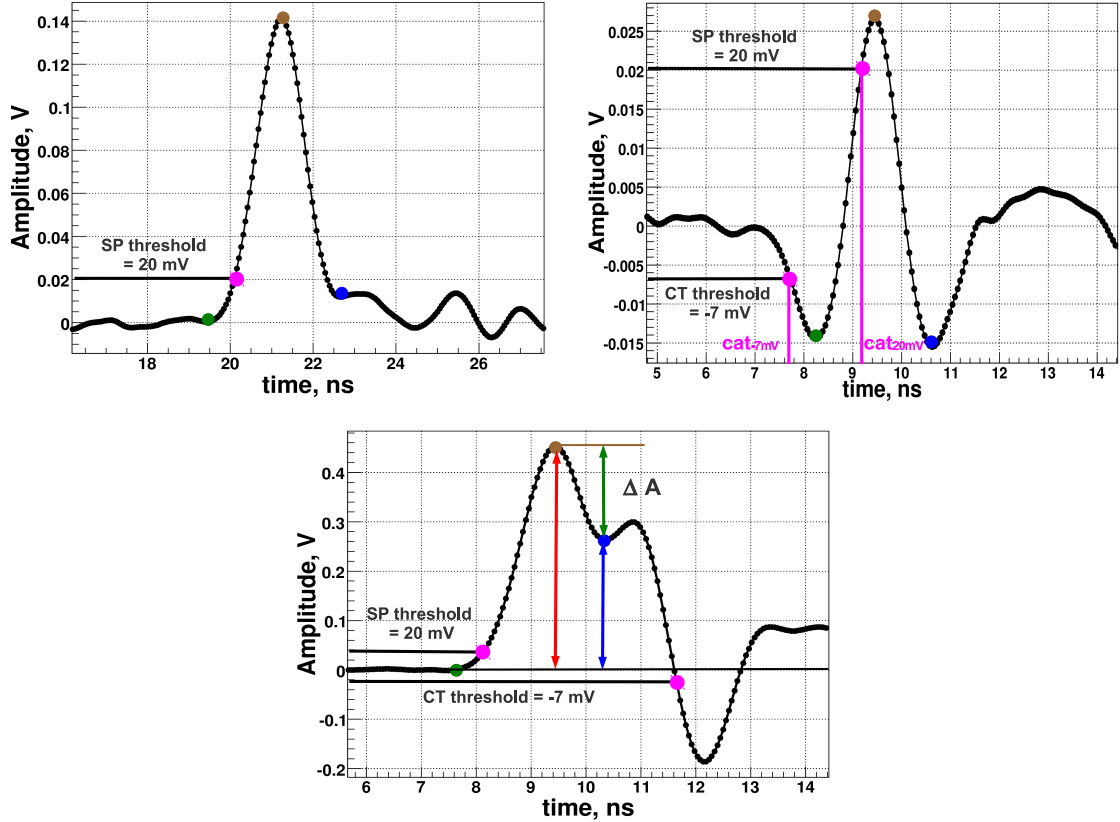


Figure 5.21: Examples of the three main signal shape categories. **Top left:** Singlepeak-like. **Top right:** Crosstalk-like. **Bottom:** Multipeak-like. In all plots, the brown dot shows the first peak exceeding the 20 mV threshold; the green (blue) dot marks the change of sign of the waveform derivative on the left (right) side – in short LDC (RDC) – of the peak. The magenta dots show the times at which the 20 mV and -7 mV thresholds are crossed – labelled cat<sub>20mV</sub> and cat<sub>-7mV</sub> respectively. One can note that for Singlepeak-like and Multipeak-like signals, cat<sub>20mV</sub> < cat<sub>-7mV</sub> while for Crosstalk-like waveforms, cat<sub>20mV</sub> > cat<sub>-7mV</sub>. We use this criterion in the shape analyzer algorithm described in the text.

where  $\Delta A$  is the amplitude difference between the first peak and the RDC location – see the caption of Figure 5.21 for the definition of this acronym. This variable is used to select Multipeak-like waveform shapes.

The amplitude of the first peak is the main parameter of the shape analyzer algorithm. Two cases are possible:

1. It is not defined. Then only the total charge can be determined; the shapeID is set to -1 and all other parameters to unphysical values.
2. The amplitude can be determined. Then we search for the positions of the derivative sign changes on the left (LDC) and right (RDC) sides of that amplitude – see the green and blue points in Figure 5.21.
  - (a) If the LDC and RDC values exist, the waveform can be classified in one of the following three categories.
    - i.  $\text{cat}_{-7\text{mV}} < \text{cat}_{20\text{mV}}$ : Crosstalk-like, shapeID = 0
    - ii.  $\text{cat}_{20\text{mV}} < \text{cat}_{-7\text{mV}}$  or  $\text{cat}_{-7\text{mV}}$  has unphysical value
      - A. Multipeak fraction  $> 0.8$ : Singlepeak-like, shapeID = 1
      - B. Multipeak fraction  $\leq 0.8$ : Multipeak-like, shapeID = 2
  - (b) If they do not, shapeID is set to -1 as well.

Singlepeak-like and crosstalk-like signals have their own typical rise time and width values. These quantities can be used to identify these categories and hence to test the shape analyzer algorithm. The corresponding distributions are shown in Figure 5.22 for all waveforms (black histograms), waveforms identified as singlepeak-like (red histograms) and as crosstalk-like (blue histograms). The typical values of these parameters are well-separated for the two categories of waveforms: 0.95/0.45 ns for the rise time and 1.35/0.85 ns for the width respectively.

Waveforms with normal rise time and width ( $\approx 0.95$  ns and  $\approx 1.35$  ns respectively) can have crosstalk before the p.e. signal and so are identified by shape analyzer as crosstalk-like. This population can be seen as a small secondary blue peak on the two histograms of Figure 5.22. These 'hybrid' signals are anyway not very good for timing measurement; so their rejection is a good feature of our algorithm.

In order to complete description of the waveform analysis below we describe double threshold timing algorithm. This algorithm uses two time measurements taken at two chosen constant thresholds (threshold1 and threshold2) of amplitude, hence two points  $\{\text{threshold1}; \text{time}_1 = \text{cat}_{\text{threshold1}}\}$  and  $\{\text{threshold1}; \text{time}_2 = \text{cat}_{\text{threshold1}}\}$  can be obtained. These points will define straight line and its intersection with baseline amplitude which give time measurements see Figure 5.23 for graphical interpretation.

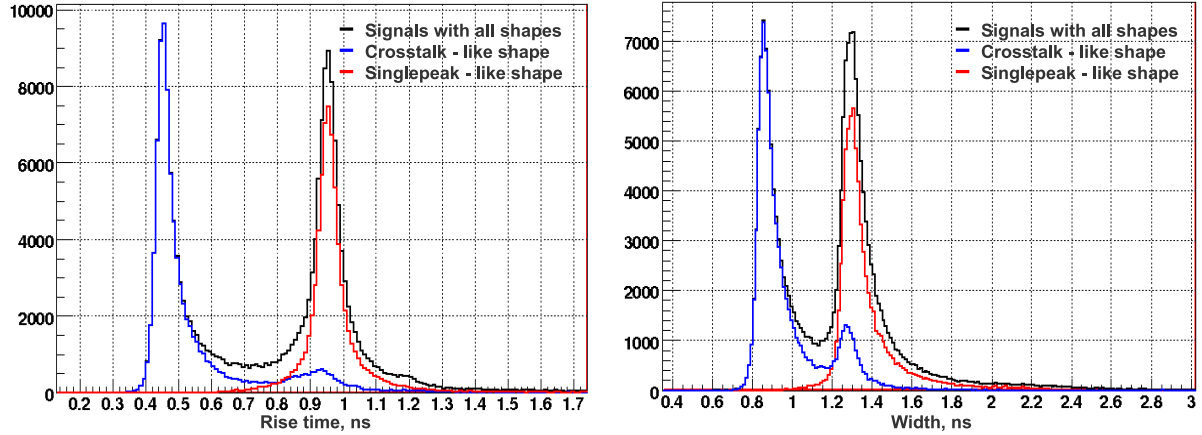


Figure 5.22: **Left:** Histograms of the rise time (in ns) for all signals (black), singlepeak-like (red) and crosstalk-like (blue) waveforms. **Right:** Histograms of the width (in ns) for all signals (black), singlepeak-like (red) and crosstalk-like (blue) waveforms. For both variables, the separation between the two categories of waveforms is clear. The shape analyzer algorithm is classifying them well.

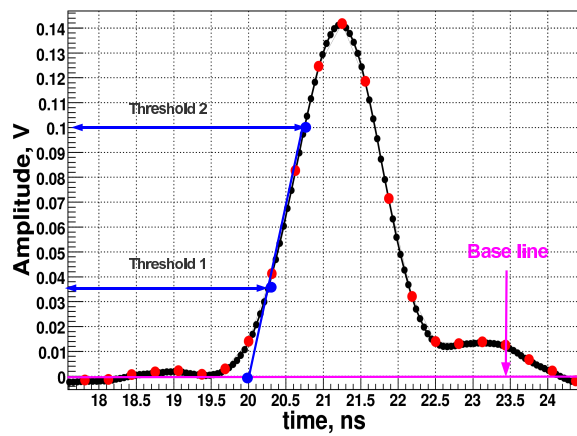


Figure 5.23: Double threshold timing algorithm (see text for details).

### 5.3 Laser tests of the DIRC-like TOF prototype

To calibrate the DIRC-like TOF prototype, a laser with  $\lambda = 635$  nm has been used. The photon flux was attenuated to the single photon level in the whole PMT. Channel number 15 was replaced by the output trigger from laser for time reference. The stored waveforms are analyzed offline. From this analysis we extract the signal time, its amplitude and charge plus additional information about its shape. For more information about the waveform analysis, see section 5.2.

The event display on Figure 5.24 show the amplitude of the signal versus time for all 16 channels. One can see a single p.e. signal in channel 5 and the trigger signal in channel 15. As expected, the time jitter between the laser trigger and the signal in a given channel is quite large due to differences in photon path lengths in quartz – photons enter the bar with very different directions and many paths can reach the same PMT channel. Two examples of these jitters are shown on Figure 5.25; fits with a Gaussian give an RMS of  $\sim 250$  ps and  $\sim 220$  ps respectively. Laser light enters the DIRC-like TOF detector from the top bar, hence it should only illuminate top channels 0-7. But photons can travel to the bottom channels 8-15 through the 6 mm thick MCP-PMT window – see Figure 5.26 (Left). This effect is estimated to be at the 10-15% level.

With the laser run, we obtain information about the PMT response on single photo electron. In addition to the expected signal, we observe the two following known phenomenas:

- Charge sharing.

The photon detection process in a MCP-PMT is shown on Figure 5.27 (Top). The incident photon hits the photocathode and produces a p.e. which is then accelerated by the  $\Delta U_1$  potential before entering the micro channel plate (MCP). Inside the pore under high voltage ( $\Delta U_2$ ), the incident electron creates an avalanche of secondary electrons through secondary emission – see Figure 5.27 (Bottom). Hence, the signal is amplified by a factor around  $10^6$ . Finally, the electron cloud drifts under the voltage difference  $\Delta U_3$  and goes to a channel where the output signal is created. Usually the spatial distance between two channels is smaller than the size of the electron cloud and part of the charge can go into neighbor channels which create a small signal called charge sharing. The average charge sharing shape and amplitude distribution (extracted from the laser run) are shown on Figure 5.28 (Middle).

- Cross-talk.

Each time a single p.e. signal appears on one channel, small signals are induced in all other channels with approximately the same common amplitude (proportional to but much lower than the physical signal): this phenomenon is known as cross-talk. Its average shape and amplitude are shown on Figure 5.28 (Bottom).

Figure 5.28 shows the average shapes and amplitude distributions for the three main categories of signals observed during the laser run. From top to bottom: single p.e., charge

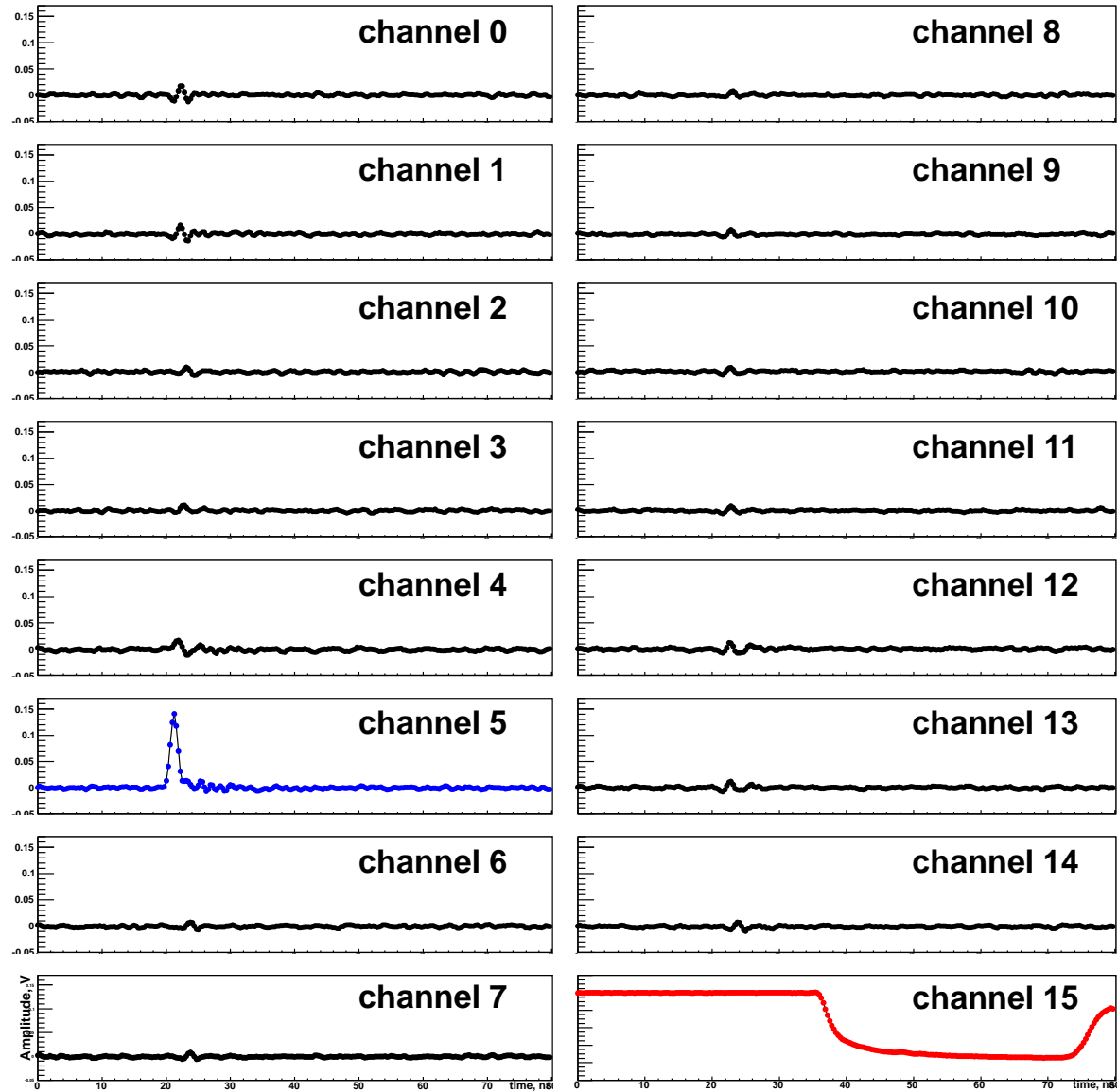


Figure 5.24: Example of event from the laser run. The amplitude of the signal vs. time is plotted for all 16 channels. One can see a single p.e. signal in channel 5 and the trigger signal in channel 15.

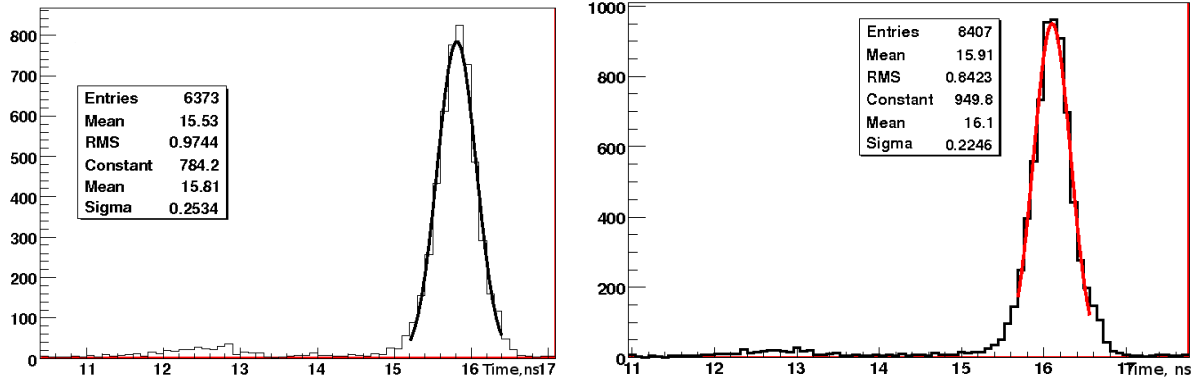


Figure 5.25: **Left:** Distribution of  $t_{15} - t_2$ , where  $t_{15}$  is the time of the laser trigger (plugged into channel 15) and  $t_2$  is the time of the signal in the channel 2. Fits with a Gaussian gives a RMS of  $\sim 250$  ps. **Right:** Distribution of  $t_{15} - t_3$ ; the Gaussian fit gives a RMS of  $\sim 220$  ps. In both plots a small accumulation of events is visible about 3 ns before the main peak. It is due to photons starting in a direction opposite to the PMT and which are reflected by the mirror located at the other end of the bar.

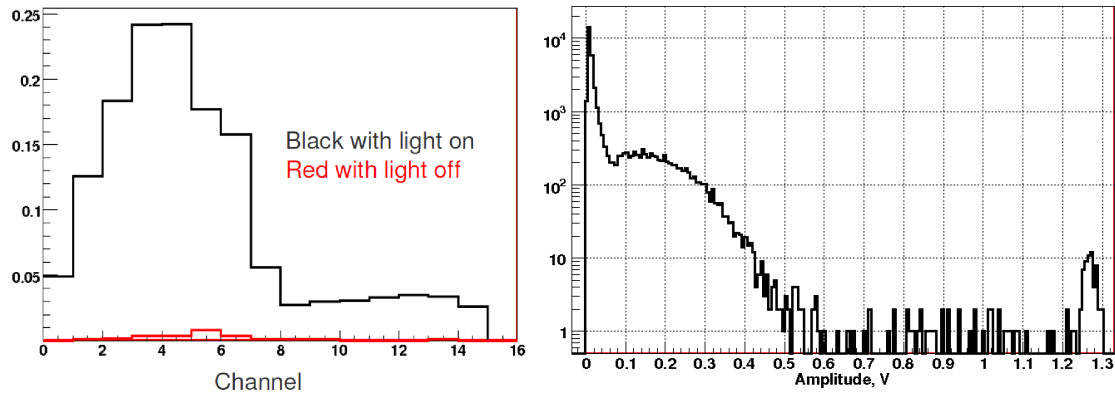


Figure 5.26: **Left:** Probability for a channel to fire with laser light on (black histogram) and off (red histogram). One can see that channels from 0 to 7 see a signal more often because the laser light enters in the top bar. However, channels on the bottom bar (8-15) are not totally silent due to the light leakage from top to bottom through the MCP-PMT 6 mm thick window. **Right:** Distribution of the maximum positive amplitude in channel 3 for the laser run. To construct this plot we did not apply any selection cut, which means that this histogram is the integrated spectrum of all possible waveforms: single photon, charge sharing or cross-talk (see later in the text for details) and even multiple photons or noise. The first narrow peak contains charge sharing, cross-talk and noise events only, while the next wide bump corresponds to single p.e. signals. The scattered events at large amplitude (1.3 V this is the upper limit of the ADCs in the USBWC electronics) are noise as well.

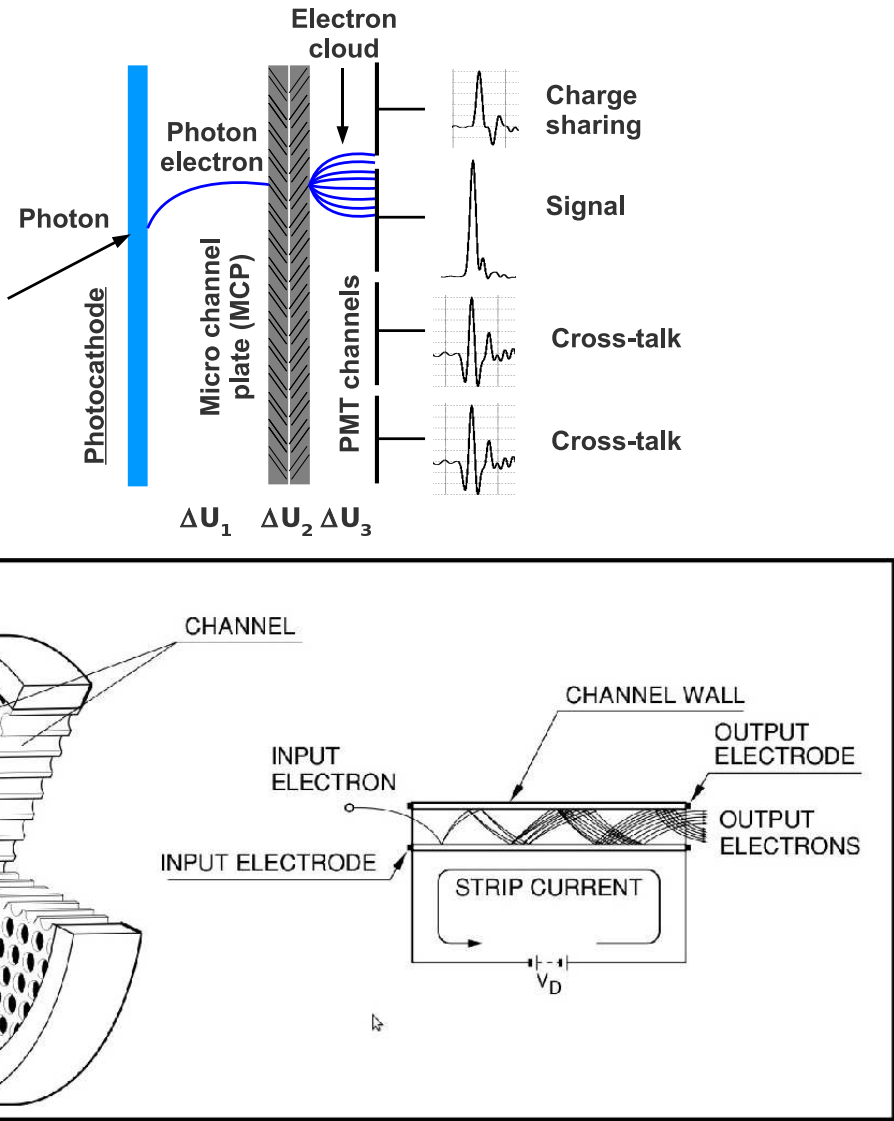


Figure 5.27: **Top:** MCP-PMT working schema – see text for details. **Bottom:** Micro channel plate on the left and zoom on a pore on the right. The p.e. which enters the pore in which high voltage is applied, creates an avalanche of secondary electrons through secondary emission. In one MCP a gain of about  $10^3$  can be achieved; therefore, with two consecutive MCPs one can reach a gain of about  $10^6$ . This high signal amplification makes possible to see single photons. In addition, due the small size of the pore  $\sim 10 \times 400 \mu\text{m}^2$  a MCP-PMT has very good timing properties because the electron cloud remains compact. The bottom picture has been adapted from Ref. [57].

sharing and cross-talk. The single p.e. information is computed as follows. A 60 mV amplitude threshold is applied to select real single p.e. events. All selected waveforms are scaled so that their amplitude is equal to one and shifted to have their peaks coincide in time. The top left curve is the average of these transformed waveforms. For the two other types of signals, the procedure is very similar. Each time a single p.e. signal is found, we look at the neighbor channels which signals are either charge sharing or cross-talk. The latter category is identified by its first peak which is negative; if the first peak is positive, the signal is called charge sharing. Then all signals are scaled, shifted and averaged to produce the bottom two left plots. As expected the amplitudes of the charge sharing and cross-talk signals are much lower than for single p.e. – note the difference in the x-axis range between the top right histogram and the bottom two.

Before moving to the analysis of data from cosmic muons, it is interesting to look at events from the laser run in which two neighbor channels show signals high enough to be from real photo electrons. As the photon flux is very small, one of the two channels fires because of charge sharing. As these two signals are due to the same photon, they should be very close in time. One example is shown in Figure 5.29: the RMS of the time difference between channels 1 and 2  $t_1 - t_2$  is 35 ps. Hence, the channel resolution is  $(35 \text{ ps})/\sqrt{2} = \sim 25 \text{ ps}$  which is less than the intrinsic time resolution of the MCP-PMT itself ( $\Delta U_3 \sim 37 \text{ ps}$ ). Indeed, in the PMT, the charge sharing effect appears downstream of the p.e. acceleration by the  $\Delta U_1$  HV and the first MCP (see Figure 5.27) which are the dominant TTS sources. It is well-known that small signal-to-noise ( $S/N$ ) ratios degrade the time resolution. In case of charge sharing, the amplitudes are often small (see Figure 5.28) hence the  $S/N$  ratios are small too. With a high enough statistics allowing to cut hard on the amplitudes, one would see the intrinsic time resolution of the electronics which is about 10 ps.

This last study gives us two main informations. First, one should not make time differences between neighbor channels to compute the timing performances of the DIRC-like TOF prototype as the result could be to good due to the contribution of events with charge sharing. Second, we measured the USBWC electronics resolution to be better than 25 ps – we already knew from independent studies that it is much better but it is good to have an indirect confirmation of its performances. This effect could potentially be used to monitor constant delays in the real DIRC-like TOF detector.

Finally, turning the laser off allows us to measure the RMS of the noise: about 1.3 mV in all channels. This value is used in the full simulation of the DIRC-like TOF prototype to make it closer to reality.

## 5.4 Full simulation of the DIRC-like TOF prototype

The main goals of this full simulation are the following: to verify our understanding of the system, to estimate the different contributions to the time resolution of the device and

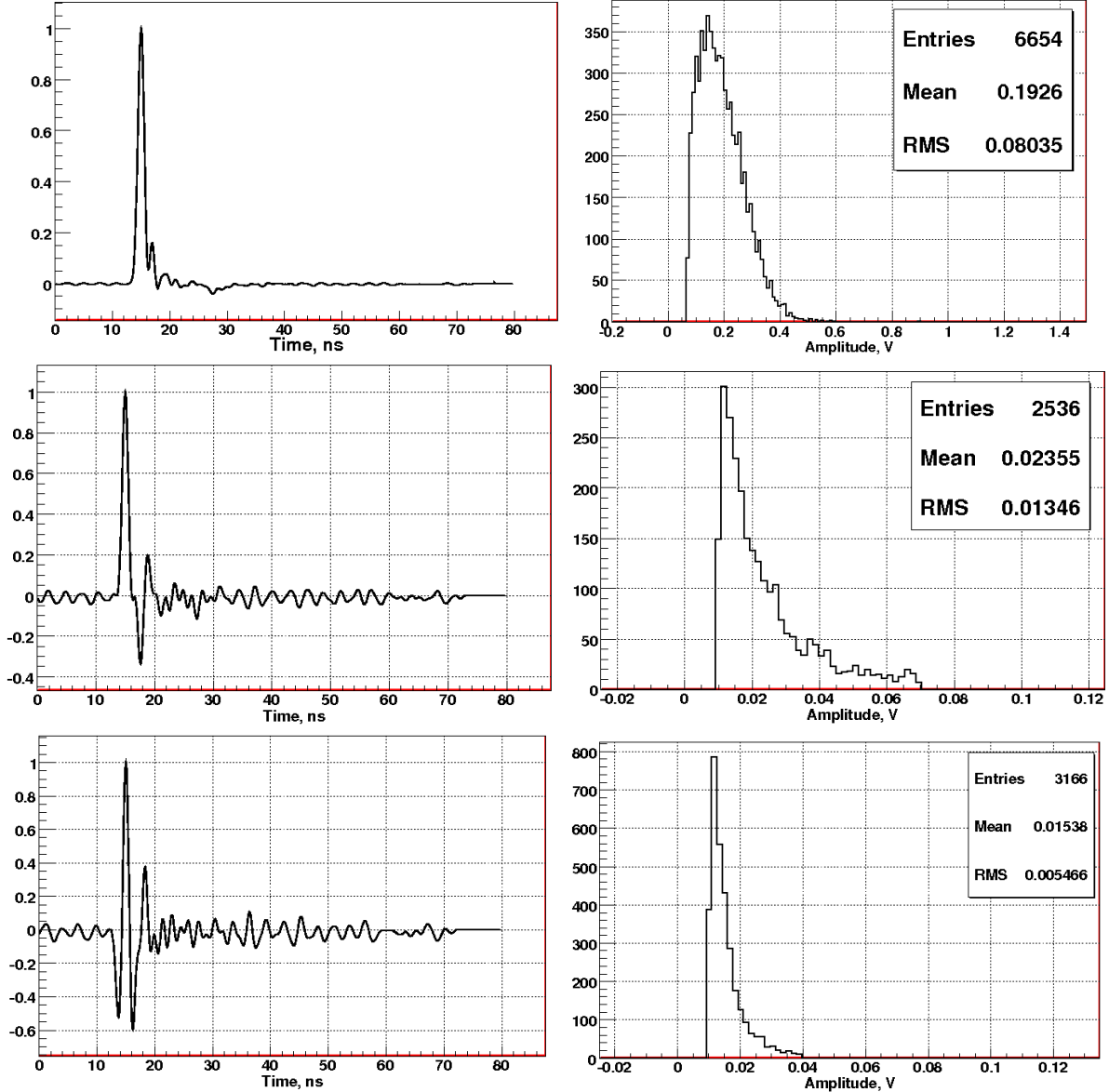


Figure 5.28: Average shapes and amplitude distributions for the three main categories of signals observed during the laser run. From top to bottom: single p.e., charge sharing and cross-talk. The text describes how these average waveforms and amplitude distributions have been computed.

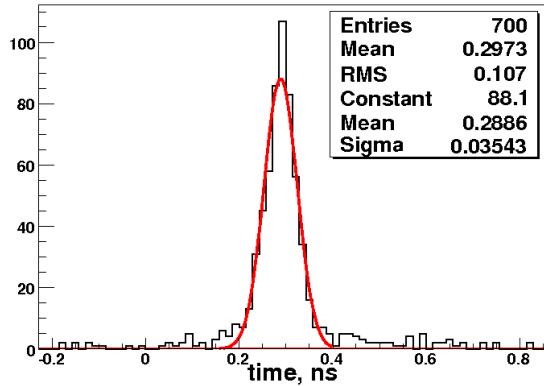


Figure 5.29: Time difference between channels 2 and 1 for laser run. To build this distribution we require amplitude of both signals be greater than 30 mV and number of channels with signals equal 2. The flux of the photons is very small so if two neighbor channels fire most probably one of them is charge sharing, the time jitter between them has to be very small. Form the Gauss fit we obtain RMS around 35 ps which is consistent with what we expect.

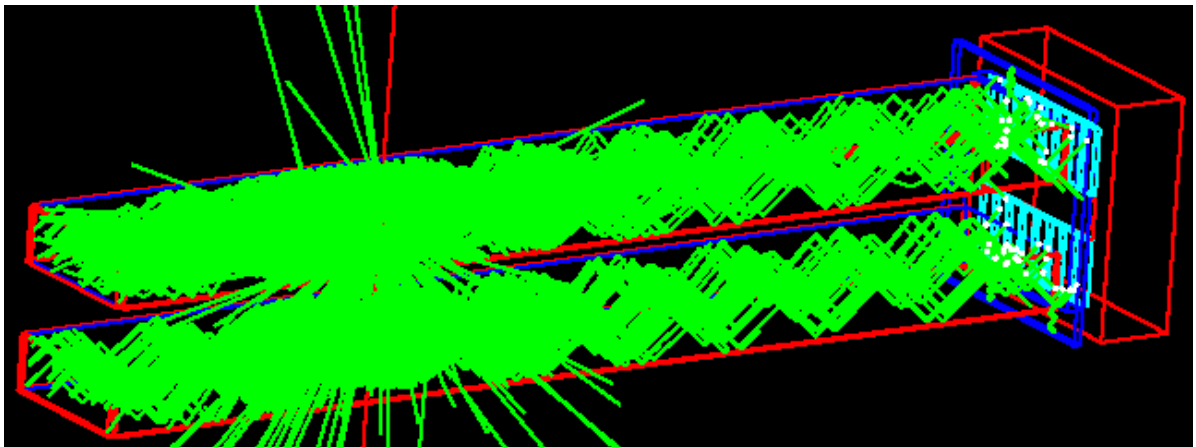


Figure 5.30: Geant4 simulation of the DIRC-like TOF prototype. Muons with momentum 1.5 GeV/c cross the two quartz bars and produce Cherenkov light. Part of these photons are trapped by total internal reflection inside the bars and propagate until the PMT. To get a clear picture, a special configuration of the DIRC-like TOF prototype with absorbers on the vertical faces of the bars (absent in reality) has been simulated. Hence only a subset of photons (those with only reflections on the horizontal faces) can propagate until the PMT and be detected. White dots mark the impact points of the photons which touch the sensitive volume of the photon detector.

finally to help demonstrating the validity of the DIRC-like TOF detector. The whole chain (detector geometry, PMT, electronics and cosmic muon generator) has been simulated.

- A fast muon generator – see section 5.4.2.
- The production and propagation of the Cherenkov light inside the quartz bars is done in Geant4 see Figure 5.30. The optical properties of the quartz (absorption length, polishing quality and dispersion) are the same as in the simulation of the DIRC-like TOF detector see Chapter 3.
- 16 PMT channels of size  $6 \times 18 \text{ mm}^2$  each – see Figure 5.31 (Left).
- The quantum efficiency of the Bialkali photocathode – see Figure 5.31 (Right).
- The p.e. collection efficiency: 70.0%.
- The Transit Time Spread of the MCP-PMT (TTS): 37 ps per photo electron.
- the electronics resolution: 10 ps per channel.
- Two algorithms can be used to compute the p.e. time of arrival:
  1. either the measured time in a given channel corresponds to the true time of the first detected photo electron, smeared by the TTS and the electronics resolution. This algorithm is labeled 'G4Sim + first p.e.' in the following – including the figure captions.
  2. or it is computed using the same waveform analysis algorithm as for the real measurements – see section 5.2 – after a dedicated simulation of the PMT response described in the next section. This algorithm is labeled 'G4Sim + wavef. sim.'

One can expect the second algorithm to be more realistic and hence closer to the real data. Yet, the first algorithm is very fast and can be used to crosscheck the results from the second one. Therefore timing plots will often compare the two approaches in the following.

After this general overview of the full simulation, the next two sections give more details about the simulation of the waveform and PMT response and about the muon generator.

### 5.4.1 Waveform and PMT response simulation

A dedicated simulation of the waveform has been developed in order to study its impact on the time resolution. In the following, we will call waveform simulator this software.

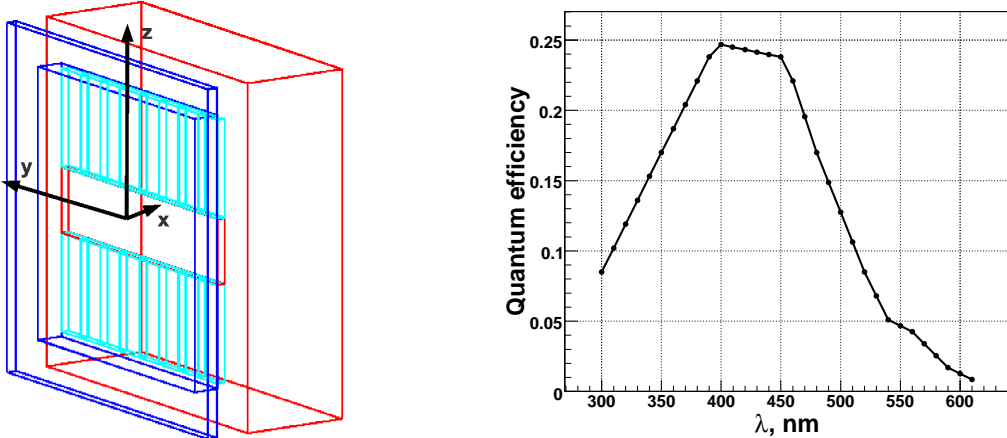


Figure 5.31: **Left:** Picture of the Geant4-simulated MCP-PMT with 16 channels ( $6 \times 18 \text{ mm}^2$  each) shown in light blue color. The stepped face of the MCP-PMT window has been simulated as well (boxes shown in dark blue color) in order to include optical crosstalk between top and bottom channels. The red box represents the body of the MCP-PMT. **Right:** Simulated quantum efficiency of the Bialkali photocathode as a function of the wavelength; this curve is given P.Hinks, Burle Co.

### General description.

A test run made with a 635 nm laser tuned to emit a low flux of photons provided information on the single p.e. detector response, which was then used to simulate the waveforms (single photo electron, charge sharing and cross-talk). The templates for the waveforms are the average shapes of the signals recorded during this laser run – see Figure 5.28 (Left). Their amplitudes are randomly drawn from the distributions shown on Figure 5.28 (Right). The number of p.e. per channel and their arrival times (smeared by 37 ps, which correspond to the TTS of the PMT) are taken from the Geant4 simulation. In case of multiple photo electrons, the total waveform is the sum of all individual waveforms properly shifted in time. Finally, white noise with a 1.3 mV RMS (the level measured with the real system) is added to the generated signal.

Additional signal shapes were implemented into the simulation: triangle shape, Gaussian function and sinusoid, as shown on Figure 5.32. The triangle and sine waveforms were mainly used for debugging and tuning the waveform simulator. Standalone trigger signals (for instance coming from a pulse generator) which usually have big amplitude, rise time and width, were parameterized with Gaussian shapes.

### Calibration of the waveform simulator (estimation of $\sigma_{S/N \rightarrow \infty}$ ).

To calibrate the waveform simulator, we perform measurements of the time difference between two high pulses similar to the signals used at LAL to characterize the USBWC electronics. Each of them is parametrized as a Gaussian with amplitude = 0.8 V and rise time = 2.5 ns. There is no additional time jitter between them and the RMS of

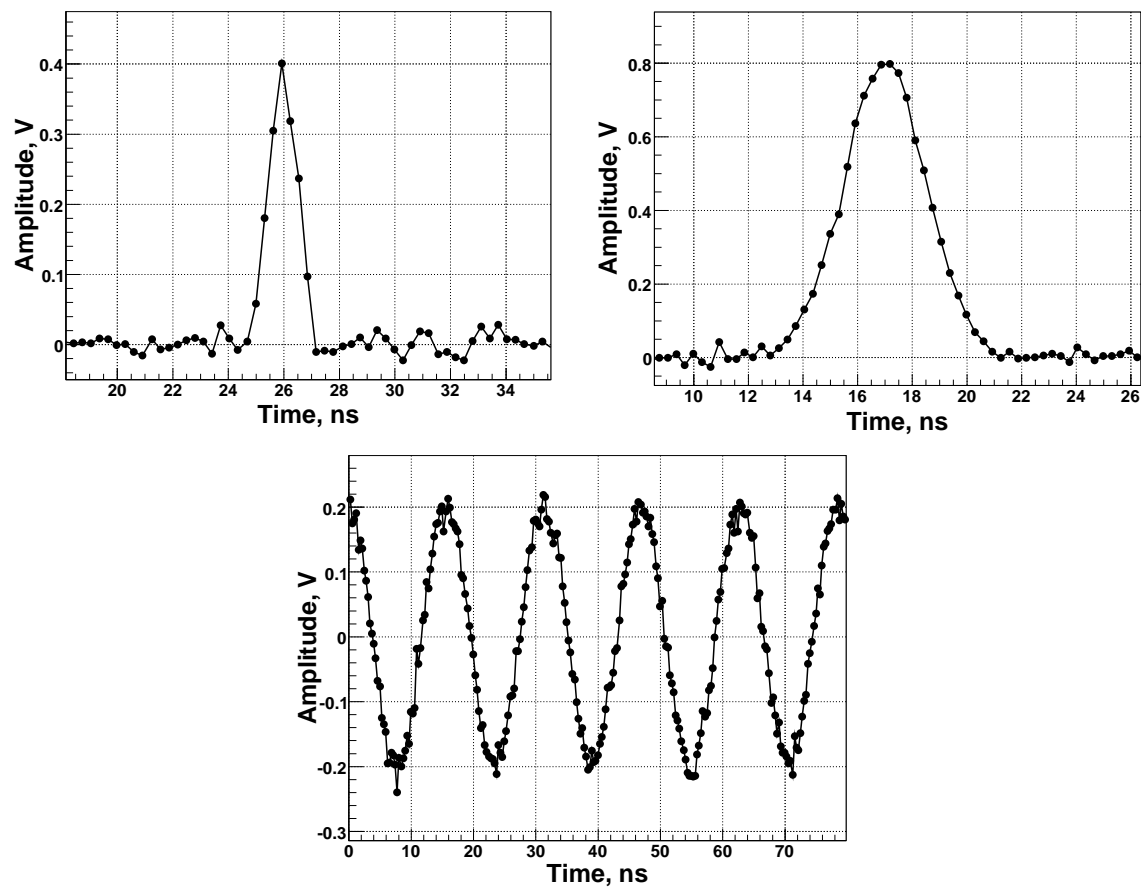


Figure 5.32: Different simulated waveform shapes: triangle (top left), Gaussian (top right) and sinusoid (bottom). Their shapes are slightly distorted by the additional white noise.

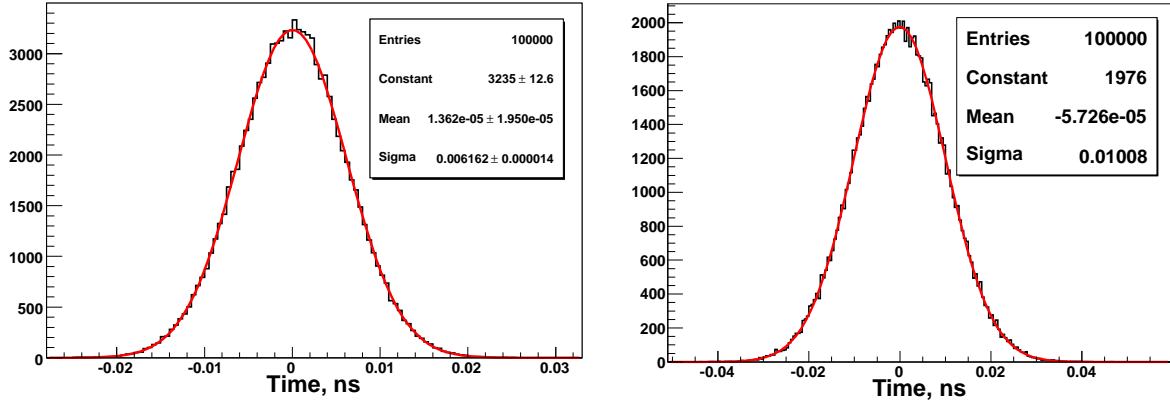


Figure 5.33: Time jitter between two pulses (similar to those used to characterize US-BWC boards), each of them parametrized as a Gaussian with amplitude = 0.8 V, rise time = 2.5 ns and RMS of the noise equal to 1.3 mV. The timing of each signal is measured by the constant fraction algorithm used with real data. **Left:** The RMS of this histogram corresponds to  $\sigma_{\text{waveform}} = 6$  ps. Note that we did not include any additional time jitter. **Right:** The contribution  $\sigma_{S/N \rightarrow \infty} = 8$  ps has been added to the simulation. One can see that the RMS of this new distribution matches the precision of the USBWC electronics: 10 ps.

the noise is equal to 1.3 mV. The histogram of this time difference has a RMS of about 6 ps, as shown on Figure 5.33) (Left). This RMS correspond to  $\sigma_{\text{waveform}}$  (as defined in Chapter 3.3:  $\sigma_{\text{electronics}} = \sigma_{\text{waveform}} \oplus \sigma_{S/N \rightarrow \infty}$ ). To match the real measurement ( $\sigma_{\text{electronics}} \sim 10$  ps see the right part of Figure 5.33), the  $\sigma_{S/N \rightarrow \infty}$  term is found to be 8 ps; this contribution has to be included in the simulation.

### Results of the waveform simulator standalone studies.

Various effects have been studied using the waveform simulator.

- First, the impact of the  $S/N$  ratio and signal rise time on  $\sigma_{\text{waveform}}$  – here, the  $S/N$  ratio is defined as the ratio between the amplitude of the signal and the RMS of the noise. For this purpose we generate two signals aligned in time, compute their timings using the waveform analyzer and finally look at the distribution of their differences. The first signal is simulated as a single p.e. waveform with variable  $S/N$  ratio, while the second is a pulse parametrized as a Gaussian with amplitude = 0.8 V and rise time = 2.5 ns. Figure 5.34 (Left, black line) shows that  $\sigma_{\text{waveform}}$  is rising quickly when the  $S/N$  ratio becomes small whereas it reaches a plateau of a few ps at very high  $S/N$  ratio.

The single p.e. waveform has a given rise time ( $\sim 0.95$  ns). Therefore, in order to study the effect of the rise time on  $\sigma_{\text{waveform}}$ , we use Gaussian shapes. Indeed, the first peak of the single p.e. waveform – which dominates the computation of the

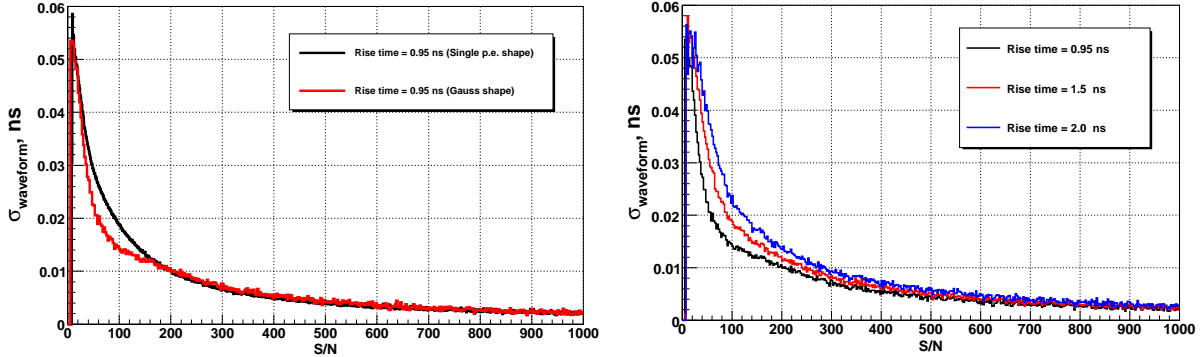


Figure 5.34: **Left:** Simulated  $\sigma_{\text{waveform}}$  vs.  $S/N$  for single p.e. signal (shown in black) and Gaussian (shown in red) with rise time equal to 0.95 ns. In both cases, the trigger signal is parametrized as a Gaussian with amplitude = 0.8 V and rise time = 2.5 ns. We can see that at high  $S/N$  ratios ( $>200$ ) the two waveforms give same results. **Right:** Simulated  $\sigma_{\text{waveform}}$  vs.  $S/N$  for Gaussian signals with different rise times. One can see that signals with bigger rise time have larger  $\sigma_{\text{waveform}}$  for same  $S/N$  ratio.

signal time in the waveform analyzer – looks Gaussian in Figure 5.40. Moreover, the left plot of Figure 5.34 shows that replacing the real signal by a Gaussian of same rise time ( $\sigma = 0.56$  ns which corresponds to a rise time of  $\sim 0.95$  ns), gives a similar timing resolution ( $\sigma_{\text{waveform}}$ ): at  $S/N$  ratios lower than  $\sim 200$ , the differences in shape make the Gaussian results slightly better. Above that level, the computed  $\sigma_{\text{waveform}}$ 's are almost identical. Simulated  $\sigma_{\text{waveform}}$  versus  $S/N$  ratio for Gaussian signals with different rise times are shown on the right side of Figure 5.34. One can see that signals with bigger rise times have larger  $\sigma_{\text{waveform}}$  for same  $S/N$  ratio.

On Figure 5.35 (Top), a fit of  $\sigma_{\text{waveform}}$  versus  $S/N$  ratio is shown for a Gaussian shape of rise time 2.0 ns. The fit function is the following:

$$\sigma_{\text{waveform}} = \frac{C_1}{(S/N)^{C_2}} \quad (5.3)$$

Parameters  $C_1$  and  $C_2$  have been studied for different rise times (see the bottom plots in Figure 5.35). One can see that  $C_2$  remains constant, while  $C_1$  linearly increases with the rise time:  $C_1 = (\text{Rise time})[\text{ns}] + 1.16$ .

Finally the general formula for  $\sigma_{\text{waveform}}$  as a function of  $S/N$  ratio and rise time can be written:

$$\begin{cases} \sigma_{\text{waveform}}[\text{ns}] = \frac{(\text{Rise time})[\text{ns}] + 1.16}{S/N} & \text{for} \\ S/N > 150 \\ (\text{Rise time}) > 0.8 \text{ ns} \end{cases} \quad (5.4)$$

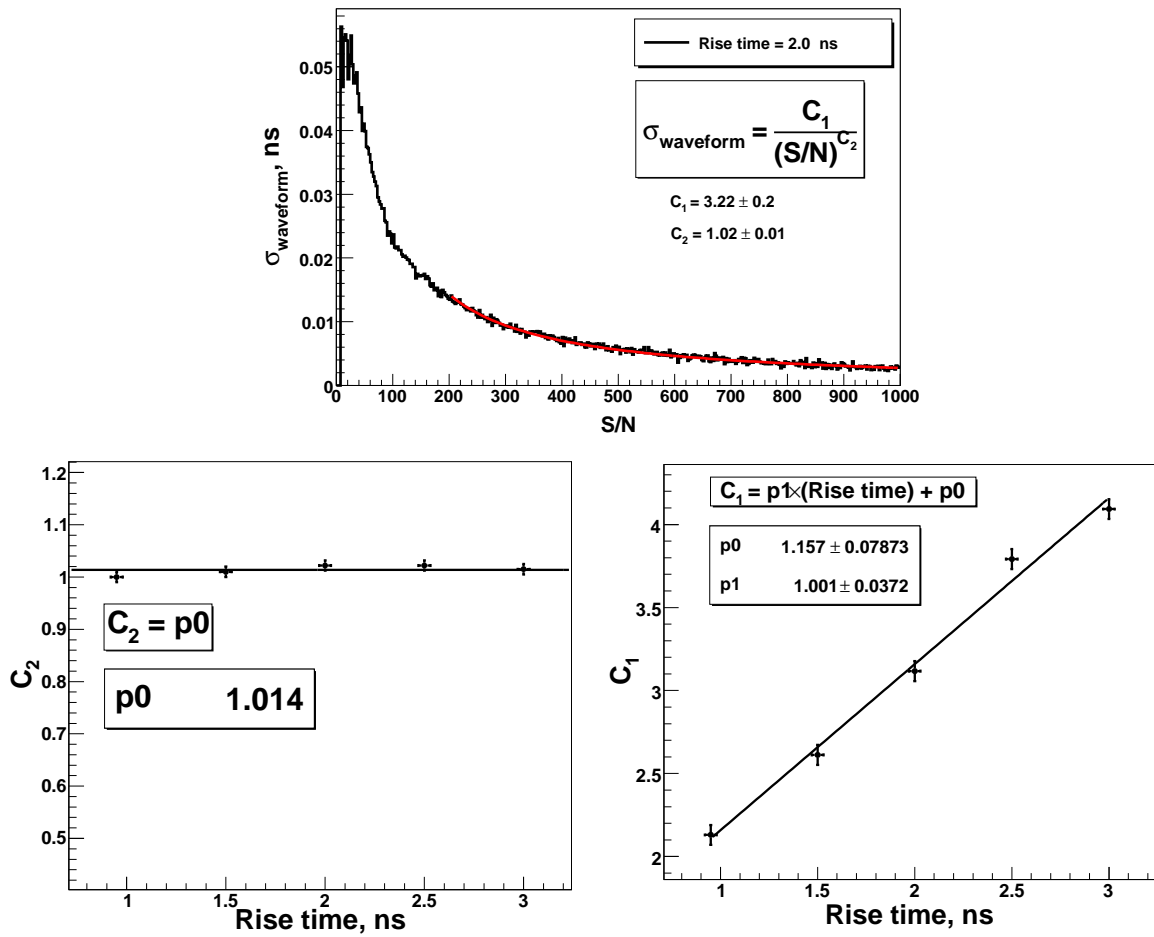


Figure 5.35: **Top:**  $\sigma_{\text{waveform}}$  vs.  $S/N$  ratio for a Gaussian signal with rise time = 2 ns. The red line corresponds to a fit (see Eq. 5.3). **Bottom left:** Value of the fit parameter  $C_2$  for different rise times. This parameter is almost constant and equal to  $\sim 1.0$ . **Bottom right:** Value of the fit parameter  $C_1$  for different rise times. It linearly increases with the rise time.

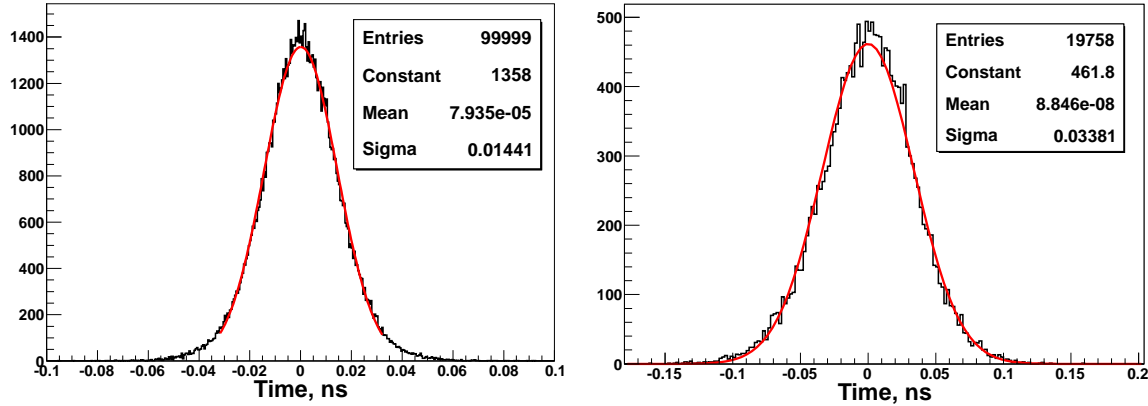


Figure 5.36: **Left:** Simulation of the intrinsic time jitter between two MCP-PMT signals from single photo electron. The RMS of this distribution is equal to 14 ps. **Right:** Simulated intrinsic time jitter between the single p.e. signal from and its charge sharing in another MCP-PMT channel. The RMS of this timing distribution is equal to 34 ps which is in very good agreement with measured value (35 ps) with laser run (see Figure 5.29). In both cases, the simulation includes the contribution  $\sigma_{S/N \rightarrow \infty} = 8$  ps.

- The second effect studied is the estimation of the intrinsic time jitter between two MCP-PMT signals from single photo electron. This is important because the time difference between signals from single p.e. is used in the following to estimate the time resolution of the DIRC-like TOF prototype. Figure 5.36 (Left) shows that it is equal to 14 ps which is negligible.
- Then, we estimate the intrinsic time jitter between the single p.e. signal from and its charge sharing in another MCP-PMT channel because this effect was measured during the laser run. This simulation provides an important test for waveform simulator. The simulated distribution is shown on Figure 5.29 (Right). Its RMS is equal to 34 ps which is in very good agreement with the measured value obtained in the laser run: 35 ps, see Figure 5.29.
- We also studied the effect on  $\sigma_{\text{waveform}}$  of multiple p.e. in a given channel. Indeed, as shown later, the simulation of cosmic muons crossing the DIRC-like TOF prototype predicts around 5 p.e. per channel in the configuration with no absorber between the bars and the MCP-PMT. This was confirmed when looking at the first data from the prototype. Most of these p.e. will hit the PMT within 1 ns which is equal to the signal rise time. This means that the front rising edge of the waveform (which is used for the timing measurements) is distorted. Moreover, the constant fraction time algorithm requires an accurate determination of the signal amplitude, which in case of multiple p.e. will be larger and shifted in time. Hence, the constant fraction voltage level for time measurements is wrongly measured.

To quantify this effect, we simulate a single p.e. signal in two channels with no

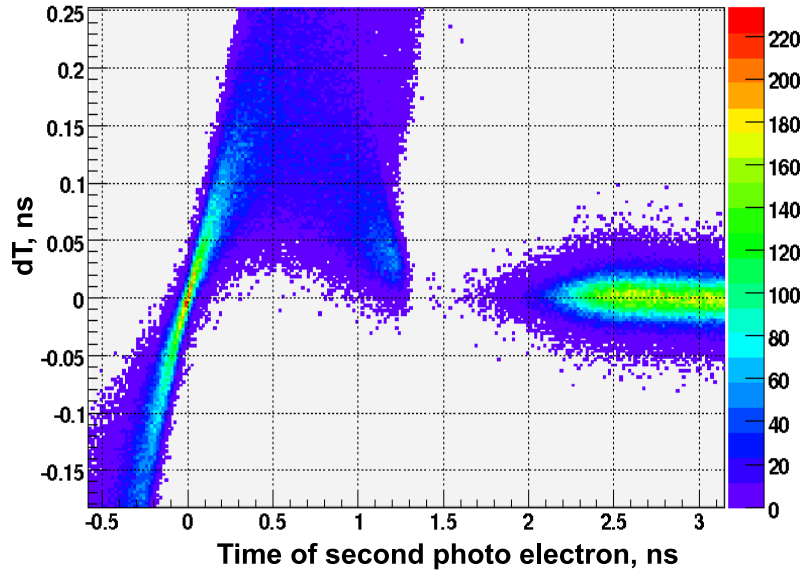


Figure 5.37: Time difference between two MCP-PMT channels: one signal is a single p.e. waveform while the other is the sum of two such waveforms shifted in time. The x-axis shows the delay between the two p.e. in the same channel. See the corresponding text for details about the rich structure of this 2D-plot.

time jitter between them; we add to the second one another single p.e. signal delayed in time. The measured time difference between these two signals is shown on Figure 5.37 as a function of the time of the delayed photo electron. One can see that both the mean and the RMS of the time difference distribution at given delay change dramatically. For small delays (up to 200 ps), the RMS stays almost constant while the mean value changes rapidly. Then, the RMS increases significantly in the region where the delay is between 200 ps and 900 ps. This effect disappears if the delayed p.e. arrive later than 2 ns, which is expected given that the waveform width is around that value: the two single p.e. waveforms are then 'independent'. One can conclude from this study that this effect is very important and will contribute to the time resolution of the MCP-PMT. The fact that there is almost no event plotted when the delay between p.e. is around 1.5 ns is a feature of the waveform analyzer which rejects most of these signals as 'multipeak-like'.

- Then we focus on the contribution to  $\sigma_{\text{waveform}}$  coming from crosstalk signals. As previously explained, the crosstalk has a small amplitude (5 %) with respect to the single p.e. signal. This means that this effect should not be very important. However, the crosstalk coming from one p.e. will affect all channels; hence, its effect is proportional to the total number of p.e. and can become important in case of large amount of collected light. We perform a study similar to the previous one but in this new simulation the delayed signal is a crosstalk waveform instead of a single

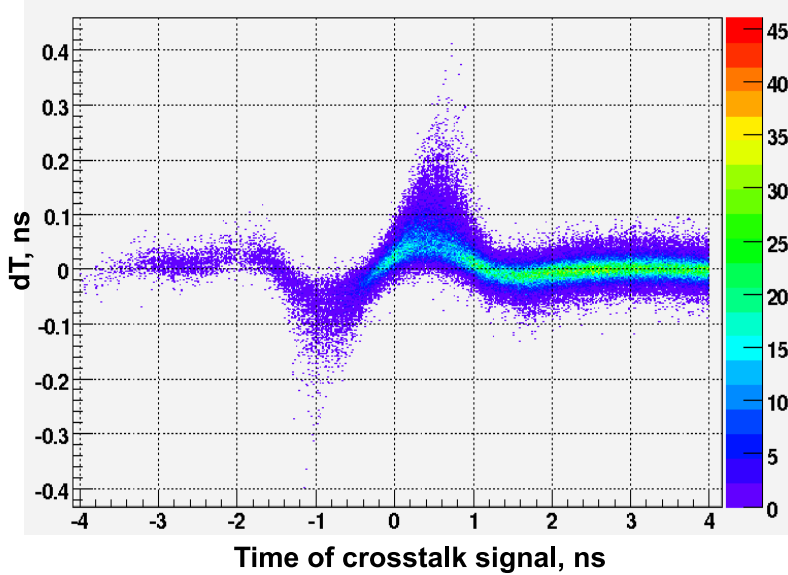


Figure 5.38: 2D histogram of time difference between two signals (one from single p.e. and the other one from single p.e. plus delayed crosstalk signal) versus the time delay of the crosstalk signal; see text for details.

photo electron: Figure 5.38 shows the resulting 2D histogram. One can see an effect when the delay is shorter than 1 ns but it is rather small. Most of the signals are classified as 'crosstalk-like' by the waveform analyzer when the delay is negative, that is when the crosstalk precedes the single photo electron.

- The waveform simulator was used to select the best timing algorithm. Three such algorithms (described in section 5.2) have been tested using the following procedure: single p.e. waveforms (with amplitude varying according to the distribution measured during the laser run, just like in all waveform simulations) are simulated; noise is then added; finally, the timing of the signal is measured and subtracted from the time of the usual trigger signal (Gaussian signal with amplitude 0.8 V and rise time 2.5 ns). Figure 5.39 shows a comparison between the performances of the three algorithms. On the left column, 2D histograms of the time difference versus single p.e. signal amplitude are plotted; on the right side, the corresponding projected time difference histograms are shown.

1. Time taken at leading edge at constant amplitude threshold – see Figure 5.39 (Top) as well known as Fixed threshold method.

This is the most robust and simple algorithm but its precision is bad: the RMS of the time difference distribution is  $\sim 200$  ps. Moreover, the mean time difference depends on the waveform amplitude. By measuring simultaneously the time and the amplitude one could apply some correction and improve the

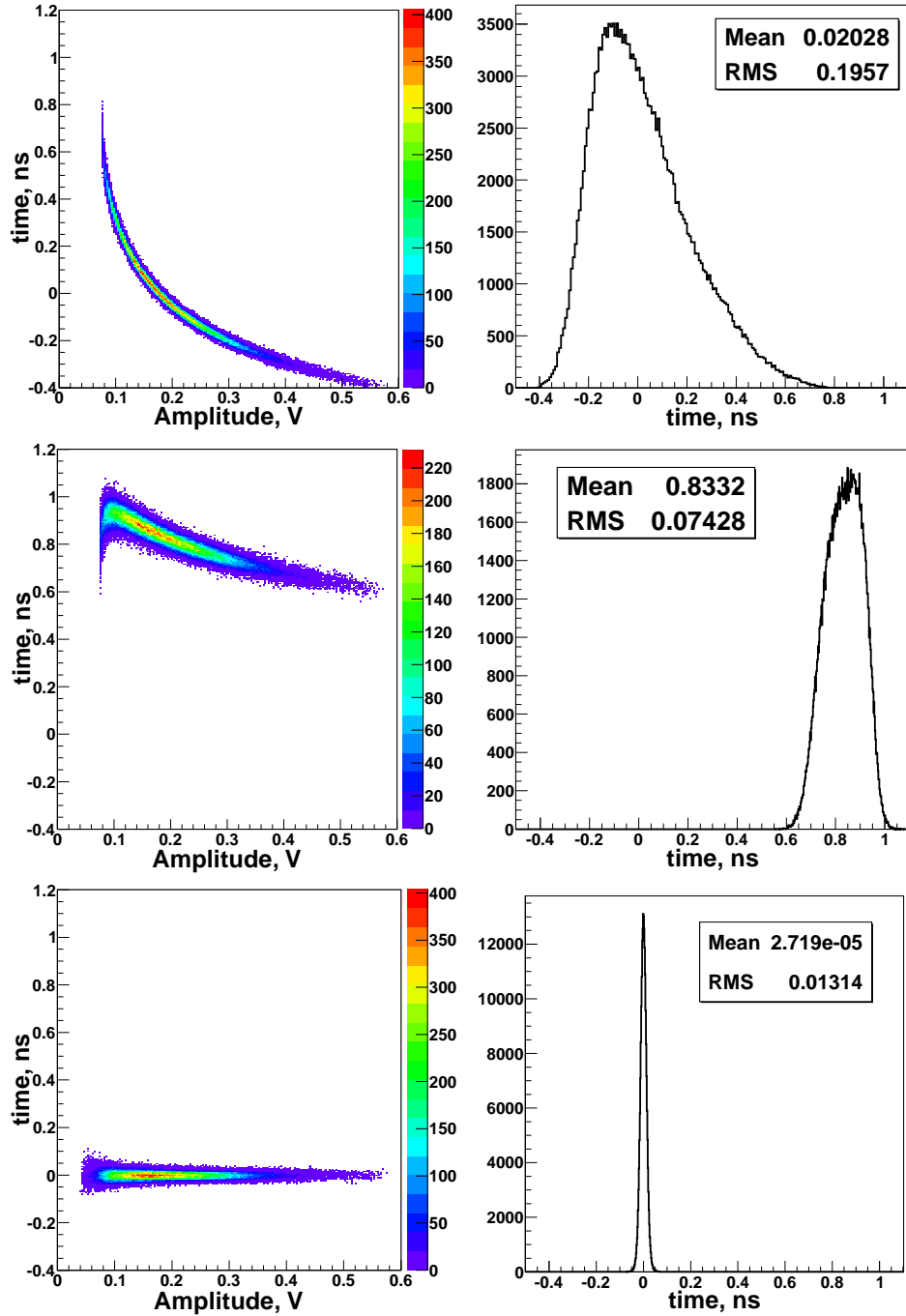


Figure 5.39: Comparison of the performances of the three timing algorithms. **Top:** Constant amplitude threshold algorithm. **Middle:** Double threshold timing algorithm. **Bottom:** Constant fraction from amplitude threshold algorithm. On the left, 2D histograms showing how the time difference 'trigger minus single p.e.' changes as a function of the waveform amplitude. On the right, the projected time difference histograms are displayed. See text for a detailed description of the main features visible in these plots.

timing resolution. Yet, the third algorithm is so much better than this one; hence, this idea was not implemented.

2. Double threshold timing algorithm – see Figure 5.39 (Middle).

This algorithm shows a better resolution than the constant amplitude threshold one but the time difference distribution is still very large ( $\sim 70$  ps). Here as well the mean time difference depends on the single p.e. waveform amplitude and corrections could in principle be applied.

3. Time taken at leading edge at constant fraction from amplitude threshold – see Figure 5.39 (Bottom) as well known as Constant fraction discriminator (CFD) method.

This timing algorithm is by far the most precise (RMS  $\sim 10$  ps) and the mean measured time difference is independent from the signal amplitude. Therefore this algorithm was selected for the analysis of the DIRC-like TOF prototype data.

- Once the timing algorithm has been chosen, one can find the constant fraction value (CF, the only parameter of this method) which gives the best timing resolution. We know from Eq. (5.4) that the smaller the rise time, the better the time resolution. Using the first derivative of the average single p.e. signal, the best CF can be computed – see Figure 5.40 (Left). It corresponds to the amplitude fraction for which the first derivative is maximum: the rise time in this point has the largest slope. To validate this choice, simulations of  $\sigma_{\text{waveform}}$  at various CF values were performed: see Figure 5.40 (Right). One can see that this study gives the expected result: the best CF value is  $\sim 0.5$ .
- And finally we use the waveform simulator to monitor the performance of the timing algorithm for different numbers of spline points ( $N_{SP}$ ). Figure 5.41 (Left) shows  $\sigma_{\text{waveform}}$  versus  $N_{SP}$ : the resolution is almost constant for  $N_{SP} > 0$ . Even for  $N_{SP} = 0$ ,  $\sigma_{\text{waveform}}$  is only about 12 ps which is very small. For the CRT experiment we chose  $N_{SP} = 5$  but in the future we will probably use no spline at all as the timing algorithm CPU requirement scales linearly with  $N_{SP}$  as shown on Figure 5.41 (Right). The USBWC electronics has a sampling frequency good enough for our purpose.

### 5.4.2 Cosmic muon generator

In order to include a realistic distribution of the cosmic muons into the full simulation of the DIRC-like TOF prototype, a cosmic muon generator has been developed. The zenith angular ( $\theta$ ) distribution of the cosmic muons is parametrized like  $(\cos \theta)^{1.85}$  [117] while the azimuthal angle  $\phi$  is flat-distributed between  $[-\pi; \pi]$ . Muons reconstructed by the CRT (see Figure 5.42) have specific distributions which are computed by including into the simulation the triggers, the QSC and the DIRC-like TOF prototype itself. The muon tracks are assumed to be straight lines. Figure 5.43 shows how the cosmic muon

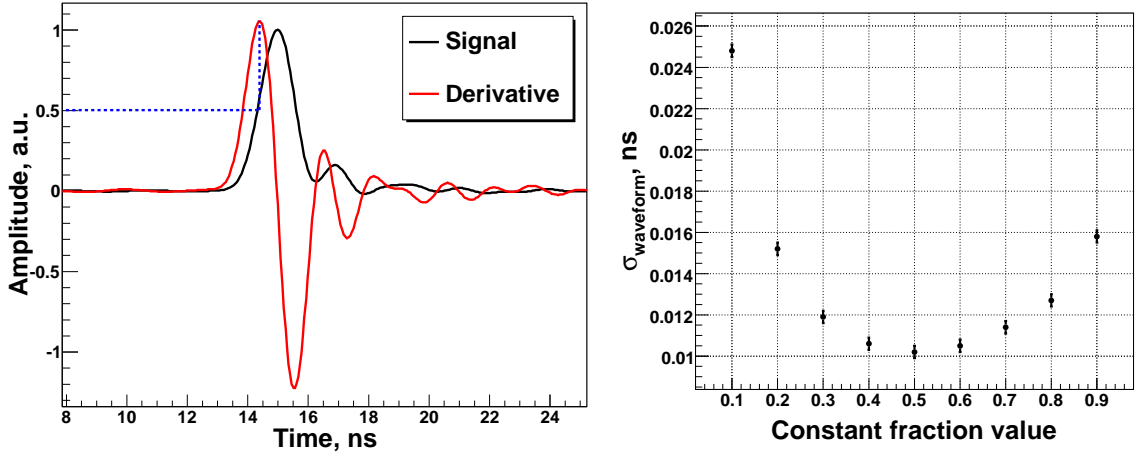


Figure 5.40: **Left:** The average shape of the single p.e. waveform (in black, normalized to have a maximum amplitude equal to one) and its first derivative (in red). The blue dashed line shows the maximum of the derivative; the corresponding amplitude fraction is about 0.5 which explains why this value is the best possible choice. **Right:**  $\sigma_{\text{waveform}}$  as a function of the constant fraction is shown. One can see that the minimum indeed corresponds to 0.5, the expected value.

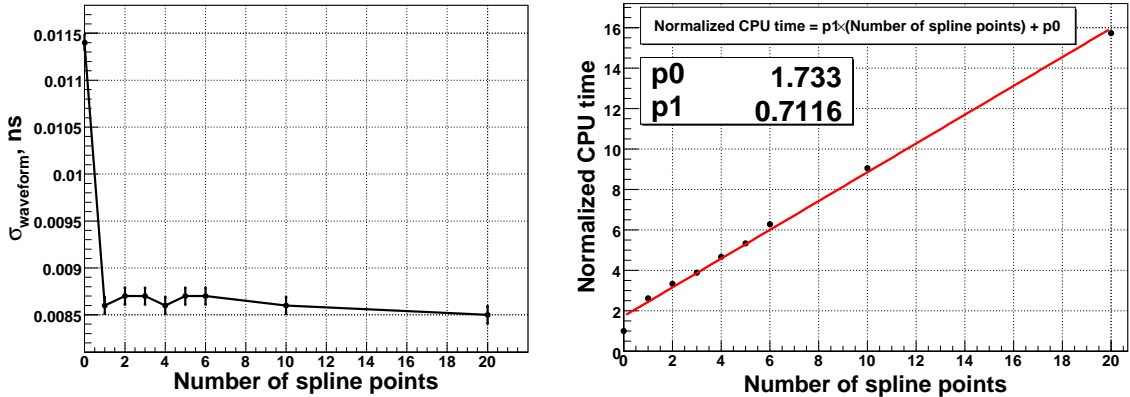


Figure 5.41: **Left:**  $\sigma_{\text{waveform}}$  as a function of the number of spline points: the resolution is almost independent from  $N_{SP}$ . **Right:** Normalized CPU time vs.  $N_{SP}$ : the CPU time increases linearly with  $N_{SP}$ . One can conclude from these two plots that spline interpolation is not needed and that not using it would make the timing algorithm faster.

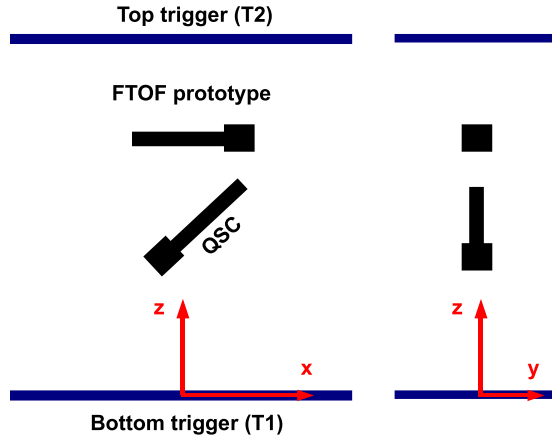


Figure 5.42: Drawing of the components of the CRT relevant for the cosmic muon generator: two triggers (T2 and T1) located on top of one another; in between them, the DIRC-like TOF prototype and the quartz start counter (QSC). Requiring coincidences between these different elements impacts the angle and position distributions of the cosmic muons.

distributions change when CRT elements and the DIRC-like TOF prototype are required to fire. In these plots, the colors correspond to different trigger requirements. In all the simulations the cosmic muon momentum is fixed to 1.5 GeV/c – tests have shown that varying the momentum does not change the timing results significantly.

### 5.4.3 Simulation results

The full simulation of the DIRC-like TOF prototype was mainly used to study two topics.

- The timing distribution of photons in a given MCP-PMT channel and the timing resolution one can expect when comparing the photon timing in two different channels.
- The effect on the timing resolution of the number of photo electron.

#### The timing distribution of the photons in a given channel.

We first simulate muons with momentum, initial position and direction fixed and look at the timing distribution of the detected Cherenkov photons. At this stage we do not simulate the MCP-PMT and therefore we use the true timing given by Geant4. Figure 5.44 (Left) shows one example of the photon arrival 2D pattern in the top quartz bar – for that particular figure, muons hit the bar perpendicularly and in its center. The vertical axis

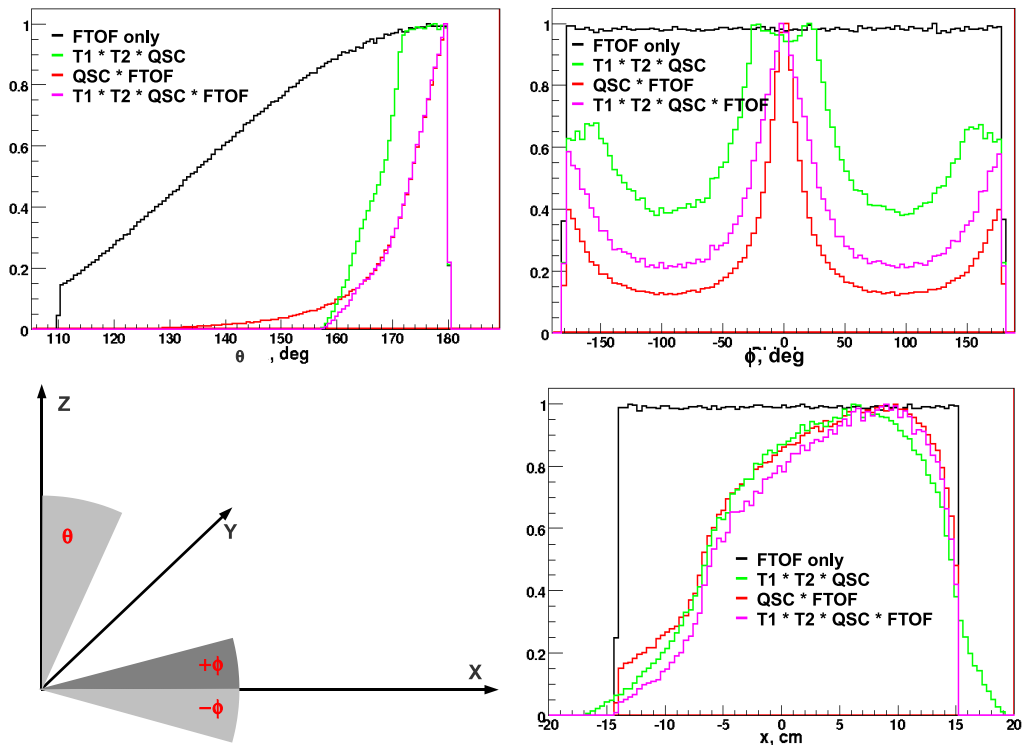


Figure 5.43: Definition of the  $\theta$ ,  $\phi$  angles (bottom left). Simulated angles  $\theta$ ,  $\phi$  (top two plots) and  $x$  coordinate (bottom right plot) of the muons intersecting the DIRC-like TOF prototype. Different colors correspond to different trigger requirements.

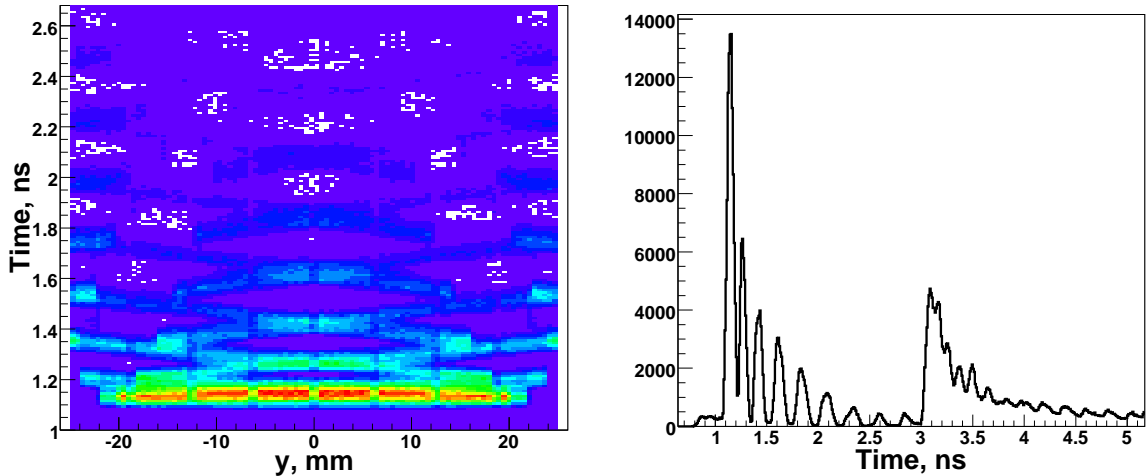


Figure 5.44: We generate muons which hit the DIRC-like TOF prototype top bar in its center and perpendicular to its surface. For this particular study, we do not include any effect coming from the PMT (TTS, waveform) and we plot all photons which hit the PMT channels. **Left:** 2D histogram showing the time of the detected Cherenkov photons on the PMT plane versus their  $y$  positions – note that the color code scale is linear. **Right:** Corresponding time distribution of the Cherenkov photons in MCP-PMT channel 3. Photons from the same peak are referred to as belonging to the same ‘population’ in the following.

gives the p.e. detected time ( $t = 0$  ns) while the horizontal axis provides its position along the  $y$  axis – along which the MCP-PMT channels are located, as shown on Figure 5.31; we recall that our TOF-based detector is a 2D device: it uses both the photon timing and position for PID. One can see that for a given  $y$  position the photons arrive at many different times which correspond to different photon path lengths in the quartz bar. The time distribution of the photons in a given MCP-PMT channel is shown on Figure 5.44 (Right). The peak structure reflects the fact that only a fraction of the paths can lead to this particular channel and that the corresponding propagation time increases with the number of reflections on the bar sides. The RMS of each peak is around 20-30 ps which is smaller than the TTS of the PMT ( $\sim 37$  ps): adding the PMT resolution will smear that ideal picture. The second largest bump around 3 ns corresponds to the photons which have been reflected on the face opposite to the PMT. In the following, photons from a given timing peak will be said to belong to the same ‘population’.

A convenient method to estimate the time resolution per channel is to look at the RMS of the time difference between two channels. Figure 5.45 shows two examples of such time differences: the first two lines show the individual channel timing histograms while the last line shows the corresponding time difference plots. Looking at these two histograms, one can clearly see a narrow component on top of a wide structure. The narrow component corresponds to time differences between photons from the dominant

populations, usually those associated with the shortest path lengths, while the wide structure is due to time differences between photons from different populations. In order to extract timing resolution information from these plots, one fits them with the sum of two Gaussian functions, one narrow and the other one wide.

One can see that the time difference distribution of muons with  $\phi = 180^\circ$  and  $\theta = 175^\circ$  (see the right side of Figure 5.45) is very wide: there is almost no narrow component visible. Indeed, for this particular combination of track parameters, the Cherenkov photons which are internally reflected in the bars follow long and complicated path lengths prior to reaching the MCP-PMT. More direct photons (going toward the PMT) are transmitted and leave the bars undetected as shown on Figure 5.46 (Left). This effect is only for muons which enter the DIRC-like TOF prototype with 'bad angles' ( $\phi \geq 90^\circ$  or  $\phi < -90^\circ$ ) for which direct photons are not trapped by total internal reflection. Hence, the only photons which hit the PMT have very bad timing and cannot be used for time resolution measurements. On Figure 5.46 (Right), the  $\phi$  distribution of the muons triggering both the CRT and DIRC-like TOF prototype is shown. The black arrows indicate the region of 'good' muons producing direct Cherenkov photons which will be detected. In the analysis presented later in this chapter, this cut is applied to the cosmic muons.

Summary Table 5.4 shows the fitted parameters ( $\sigma_{n/w}$  and  $fr_{n/w}$ ) for the narrow and wide components of time difference histograms obtained in simulation with different muon parameters. The muons with 'good angles' have narrow components with RMS around  $60 \pm 15$  ps; those with 'bad angles' show much wider distributions which make them not suitable for accurate timing measurements. The mean values of these timing histograms depend obviously on the muon track parameters (position and direction). Therefore, integrating over these variables – mandatory in data due to the limited statistics – will produce wider timing difference histograms. That is indeed what we will show in the next section which deals with the CRT data analysis.

### **Number of p.e. and its impact on timing resolution.**

Our full simulation provides estimation of the number of p.e. per channel per cosmic muon. It is around 5 (see left histogram in Figure 5.47), hence about 80 per PMT, which is a lot for one such device running at high gain. Consequently, three main effects are degrading the timing resolution.

- Most of the p.e. arrive in a given channel within the rise time of the first signal – see the right part of Figure 5.47. This affects the leading edge of the waveform and its amplitude, hence the time measurement as already shown by the waveform simulator: see Figure 5.37.
- Each p.e. will create a crosstalk signal on all others channels which, as we know, degrade the time resolution – see Figure 5.38.

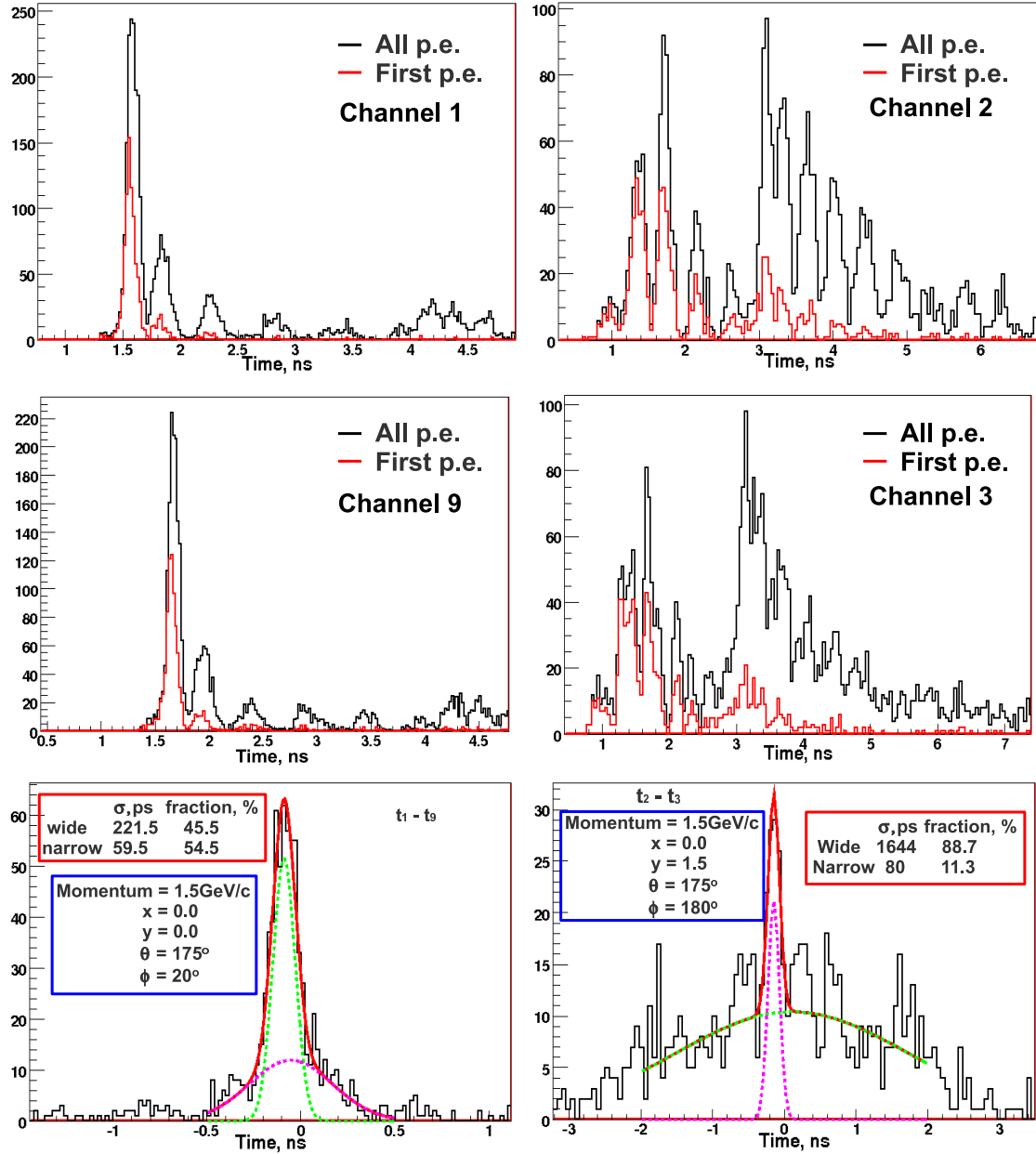


Figure 5.45: Two examples of analysis based on timing differences between two MCP-PMT channels. **Left column:** Muons intersect the DIRC-like TOF prototype in the center ( $x = y = 0$ ) with  $\theta = 175^\circ$  and  $\phi = 20^\circ$ . **Right column:** The muon track parameters are:  $x = 0$ ;  $y = 1.5$  cm;  $\theta = 175^\circ$ ;  $\phi = 180^\circ$ . The top four plots show p.e. timing distributions in given channels; the red (black) histogram includes only the first photon (all photons). The bottom two plots show the corresponding time differences (using the first photon only) fitted by the sum of two Gaussian functions. The RMS of the narrow Gaussian gives information about the time resolution per channel when the individual timing histograms show a clear dominant first peak (left case) whereas it is useless when the situation is more complex (right case). The wide Gaussian function is meant to describe the timing differences of photons which belong to the other populations.

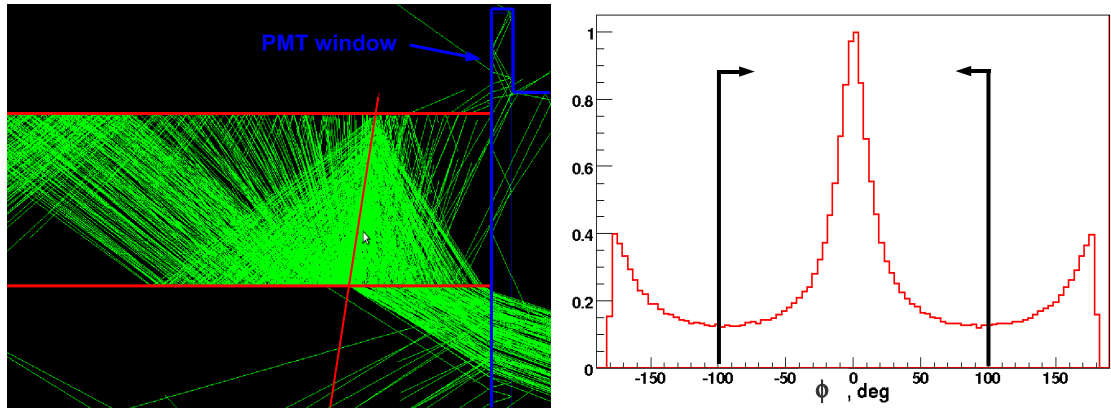


Figure 5.46: **Left:** Example of a muon with 'bad angle' ( $\phi = 180^\circ$  and  $\theta = 175^\circ$ ) entering the quartz bar. The direct Cherenkov photons leave the bar; hence, they are not detected. **Right:** The  $\phi$  distribution of the muons selected by the CRT and crossing the DIRC-like TOF prototype. Black arrows indicate the  $\phi$  range in which muons produce detectable direct light. This cut is applied later in the analysis of the DIRC-like TOF prototype data.

Table 5.4: Double Gaussian fits of time difference histograms between two channels for different sets of muon track parameters (momentum, position,  $\theta$ , and  $\phi$ ). The quartz bars extend in the horizontal plane from  $\approx -14.5$  cm to  $\approx 14.5$  cm (side of the PMT) in  $x$ , and from  $\approx -2.5$  cm to  $\approx 2.5$  cm. The few examples analyzed here allow one to understand how the muon direction affects the time difference resolution. For instance, the last two lines show bad time performances in case of muons with 'bad angles', flying 'away' from the PMT. On the other hand, the width and fraction of the narrow Gaussian are quite stable for muons with 'good angles', pointing toward the PMT. One can also note that the further the muon from the PMT (decreasing  $x$ ), the larger  $\sigma_n$ : there are more optical paths for the photons.

channels	x, cm	y, cm	$\theta^\circ$	$\phi^\circ$	$\sigma_w$ , ps	$fr_w$ , %	$\sigma_n$ , ps	$fr_n$ , %
$t_1 - t_9$	0	0	175	20	221	46	60	54
$t_2 - t_3$	0	0	175	20	211	51	56	49
	8	0	180	0	200	34	68	66
	8	0	175	-10	165	36	55	64
	8	1.5	180	0	300	28	79	72
	14	0	170	0	—	0	45	100
	14	0	170	90	—	0	52	100
$t_2 - t_3$	0	-1.5	175	180	1644	88	80	12
	14	0	170	180	$\infty$	40	492	60

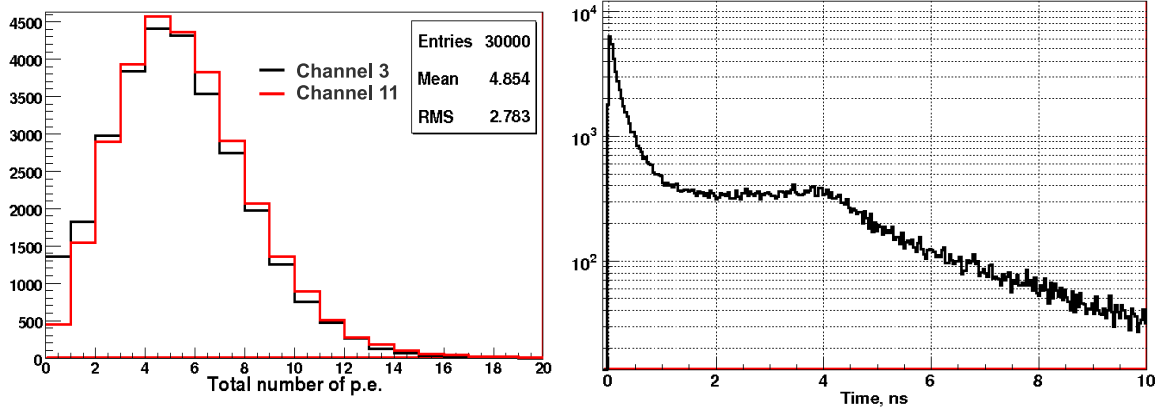


Figure 5.47: **Left:** Simulated number of p.e. per cosmic muon in channels 3 (black histogram) and 11 (red histogram). The average is around 5 in both cases. **Right:** Histogram of the photon arrival time in channel 3 in which only the second, third, etc. photons are included. The time origin corresponds to the arrival of the first photon. Note the logarithmic scale: when there are more than 1 p.e. in a given channel, the following hits are very likely to arrive within the initial PMT rise time, hence impacting the shape of the waveform signal and making the determination of the p.e. arrival time less accurate.

The number of incoming photons can be decreased by adding a photon absorber layer between the quartz bars and the PMT. To study the impact of the absorber on the time resolution, we use the full simulation. The level of attenuation can be described by a single parameter, the attenuation power (AP). We assume that the absorber AP is the same for all wavelengths. The transmission efficiency (TE) describes the total p.e. detection efficiency.

$$\text{Transmission efficiency} = \text{Attenuation power} \times \text{Collection efficiency} \quad (5.5)$$

As we know, the collection efficiency is 0.7 for the particular MCP-PMT at SLAC. The attenuation power can be chosen arbitrarily by changing the thickness of the photon absorber layer.

Two examples of simulated time differences between channels 2-13 and channels 3-11 for different TE are shown on Figure 5.48. Two main effects are visible when the transmission efficiency increases.

- The tails decrease while the width of the peak increases. This is expected as the absorber makes the arrival time of the first photon more 'random': they are more likely to come from different populations whereas in the case without absorber the first peak is enhanced. Fitting these timing distributions with our usual double Gaussian model the narrow and wide components vary accordingly, as shown in Figure 5.49 (Left).

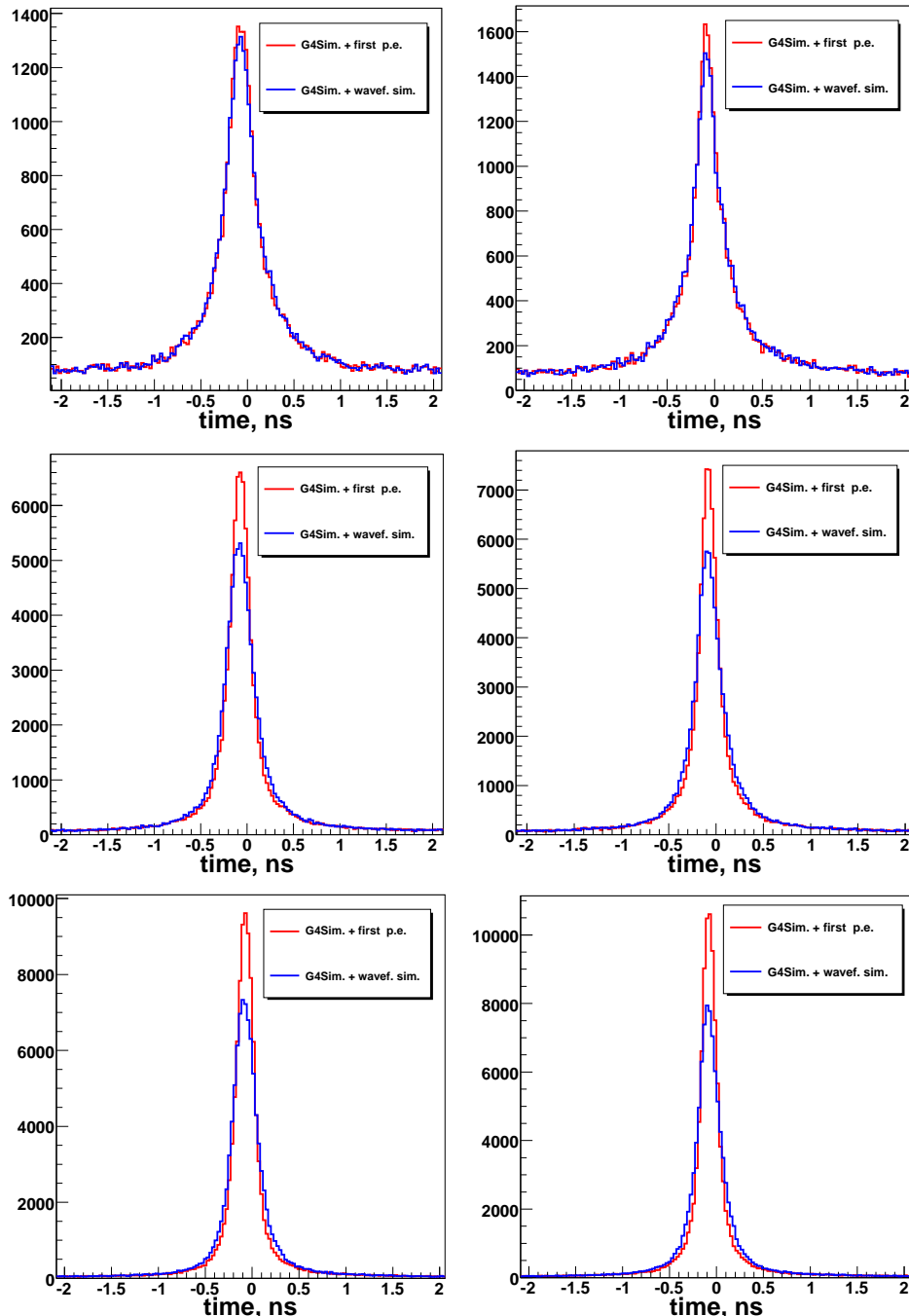


Figure 5.48: Simulated time differences between channels 2 and 13 (left column) and channels 3 and 11 (right column) for three different transmission efficiencies: from top to bottom,  $TE = 0.07$  (thick absorber), 0.4, 0.7 (no absorber at all) respectively. On each plot, the histograms correspond to the two available simulations: time of the first p.e. taken from Geant4 and smeared by the PMT TTS (the simple simulation, red histogram) or simulation of the waveform for each p.e. + waveform analyzer (more realistic, blue histogram). The smaller the  $TE$ , the more the red and blue histograms are in agreement: there is at most one p.e. per channel. Moreover the peak gets wider and the tails higher as the (first) photon which crosses the absorber can come from any population: the first peak is not favored anymore.

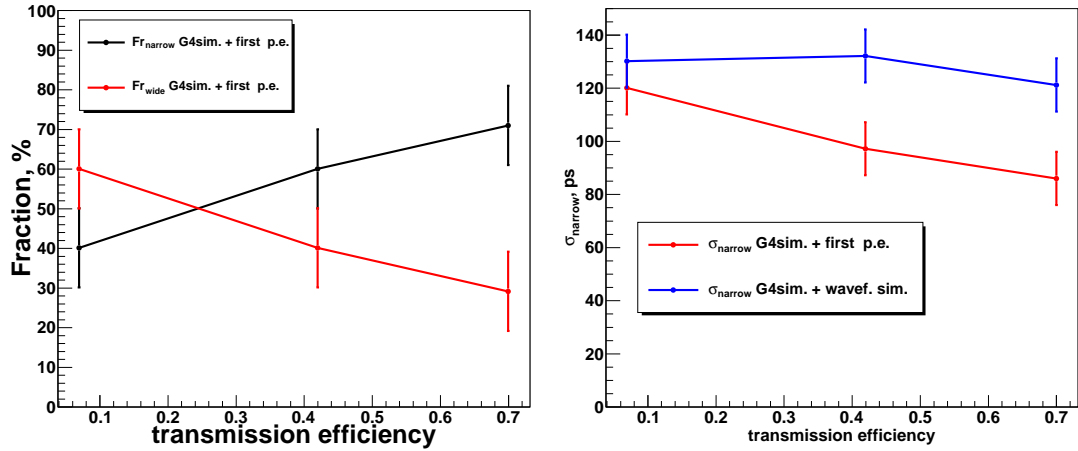


Figure 5.49: **Left:** The fraction of the narrow and wide components of the time difference distribution is shown. One can notice increasing/decreasing the narrow/wide component with increasing the transmission efficiency. **Right:** The RMS of the narrow component of the time difference distribution for two timing algorithms.

- Figure 5.49 (Right) shows how the RMS of the narrow component changes with increasing TE. It is almost constant for the more realistic waveform simulation (blue curve) while it goes down significantly for the simpler simulation (red curve). This is an important difference between the two methods. As shown later,  $\sigma_{\text{narrow}}$  goes up with TE which shows that the waveform simulation is better although not complete. Indeed, it only includes effects coming from the multiple photo electrons: due to the complexity of the problem, we did not succeed in finding a proper way to include into the simulation the charge sharing and crosstalk. As we will see from measurements, crosstalk and charge sharing are dominant sources of timing inaccuracy in case of high flux of photons.

## 5.5 Measurements

In this section we will present measurement of the DIRC-like TOF prototype time resolution. We start with the description of the two separate data acquisition systems (DAQ): one for the CRT and the other for the prototype. Then, we describe the different data taking periods which correspond to different running conditions. And finally we show the measurements and compare them with simulation.

### 5.5.1 CRT and USBWC DAQs merging

The CRT and USBWC DAQs are separated due to technical reasons. The CRT raw data are stored in ASCII format in filenames with extension 'dst2'. Each file contains 1,000 events with information from TDCs and ADCs. The USBWC raw data are stored in ASCII files as well, with filename extension 'dat'. Each file contains 500 events with waveforms from all 16 channels. Both DAQs have their own PCs. Each time they record an event both PCs store its Unix time<sup>1</sup>. These time marks are used in a second step to merge the common events. Usually, a PC clock drifts by a couple of seconds per day which would impact the synchronization of the two systems. For this reason, Unix times are constantly updated from a common NTP server [118]. The monitoring of this time synchronization for the USBWC DAQ PC is shown on Figure 5.50.

On Figure 5.51 the distribution of the minimum time difference between USBWC and CRT events is shown – for each USBWC event, one looks for the CRT event closest in time. One can see a big peak close to zero (note the logarithmic  $y$  scale) which corresponds to real events seen in both detectors. On each side, the histogram shows exponential tails which correspond to random coincidences. Finally the lack of coincidences with time differences slightly positive is due to a veto applied at the CRT level. Indeed, once the CRT gets a trigger it takes around 1 s to read all the TDCs and ADCs. During this dead time the USBWC electronics does not accept any event.

The minimum Unix time difference between USBWC and CRT events versus time is shown on Figure 5.52 (Left) for a period of about two months, which is used in the following to measure the DIRC-like TOF prototype timing accuracy. One can see that the most probable difference is drifting in time. In order to take this variation into account, we select events which are within  $\pm 0.2$  s from this value, updated every four hours. Figure 5.52 (Right) shows the time difference for the events which have been found coincident (called 'merged events' in the following) using the algorithm we just described. Looking at these two pictures, one can see that the time difference was fluctuating more during the first week. This was due to the USBWC DAQ PC clock which, for some unknown reason, needed that time to get properly synchronized with the NTP server. Once it got locked, these variations disappeared and never came back.

---

<sup>1</sup>It measured in second and started at the Unix epoch which is the time 00:00:00 UTC on 1 January 1970.

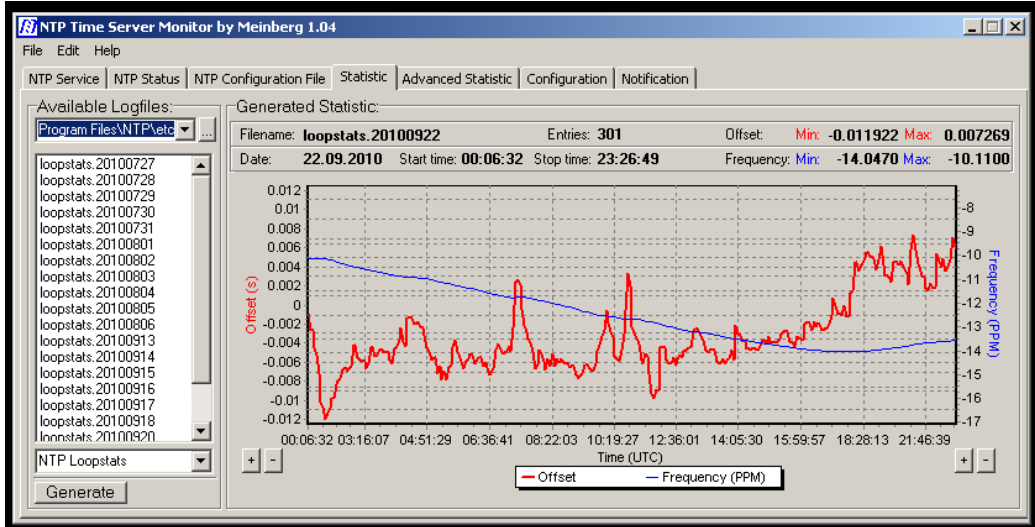


Figure 5.50: Screenshot of the NTP time server monitor for the USBWC DAQ laptop. The red line corresponds to the time offset between the PC clock and the NTP server. One can see that the accuracy is on the order of 0.01 s over a day. This precision is good enough to perform the DAQ merging step.

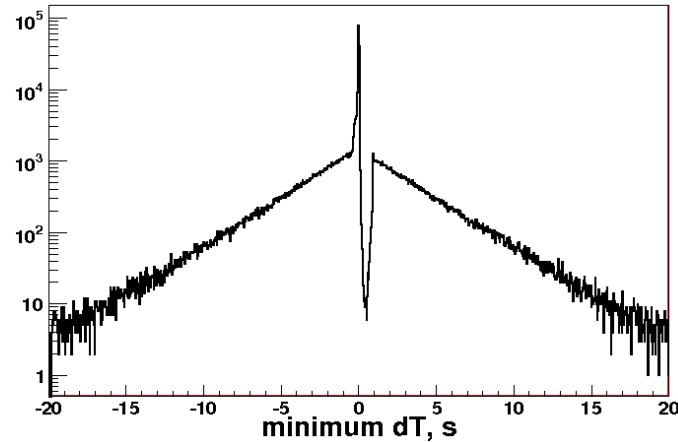


Figure 5.51: Example of histogram showing the minimum time difference between CRT and USBWC events.

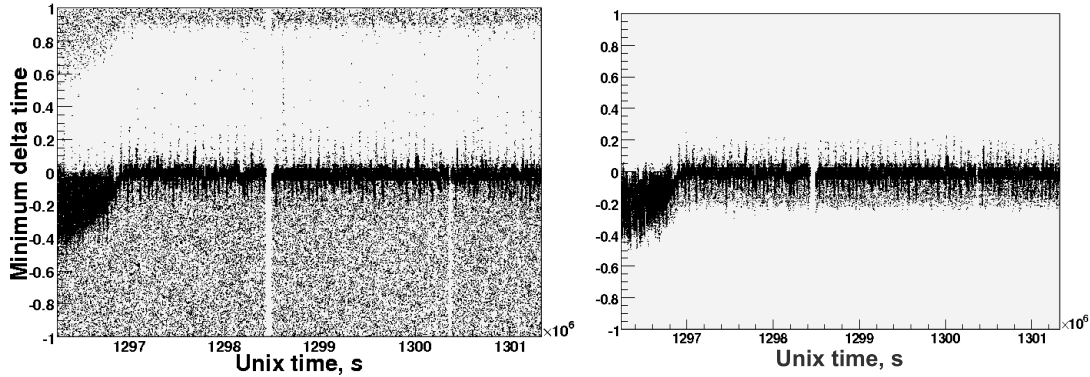


Figure 5.52: Evolution of the minimum Unix time difference between USBWC and CRT versus time over a two month period – see text for details.

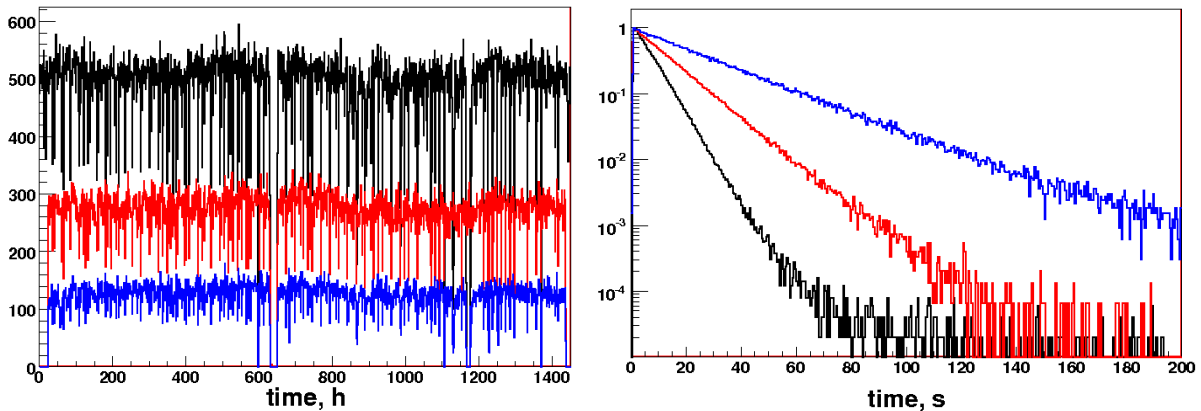


Figure 5.53: Event rate per hour (left) and distance in time between consecutive events (right) for CRT (black), USBWC (red) and merged (blue) events.

Figure 5.53 (Left) shows the event rate per hour for CRT events (in black), USBWC events (in red) and merged events (in blue) respectively. On the right side one can see histograms of the distance in time between two consecutive events (with the same color conventions). All three distributions appear to be roughly exponential.

The coordinates of the muon intersections with the horizontal plane located in the middle of the two DIRC-like TOF prototype bars are shown on the top row of Figure 5.54 for merged events (red) and all CRT events (black). One can see that merged events have narrower distributions (especially in  $y$ ), which shows that the merging procedure is selecting a particular area on this plane. As shown on the 2D map below, merged events cluster in the expected location of the prototype, indicated by the red box. This geometrical cut will be used later to select events suitable for timing measurements.

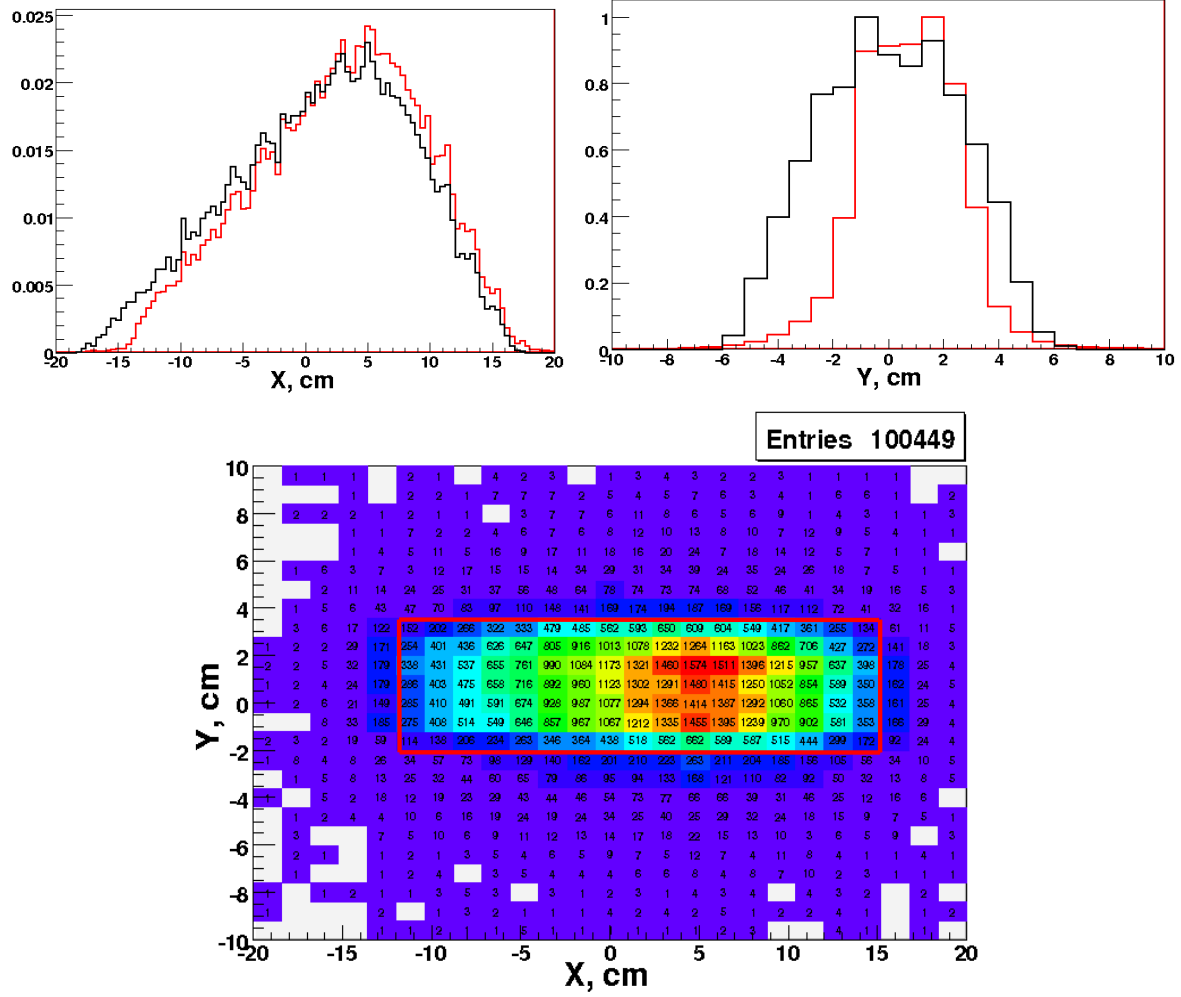


Figure 5.54: In order to crosscheck the merging procedure between USBWC and CRT events, one can look at the coordinates of the muon intersections with the horizontal plane located in the middle of the two DIRC-like TOF prototype bars. Tracks associated with merged events should cross this plane in the area where the prototype is located. This is indeed what the two top histograms and the bottom 2D-map show. **Top left:** Distribution of the  $x$  intersection coordinate for tracks from merged (red histogram) and all CRT (black histogram) events. **Top right:** Distribution of the  $y$  intersection coordinate; its FWHM is equal to 4.2 cm which corresponds to the  $y$  dimension of the quartz bars. **Bottom:**  $y$  vs.  $x$  coordinates of the intersection points for tracks from merged events. The boundaries of the quartz bars are shown in red.

### 5.5.2 Summary of data taking

During 7 months of data taking the CRT collected  $\sim 2.5 \times 10^6$  cosmic muons. The data taking period can be divided into 6 main runs. The details of the different runs are given in Table 5.5.

- RUN1

This run was dedicated to commission the DIRC-like TOF prototype together with its electronics and the dedicated software which was being developed at that time. During this run, we discovered a feature related to the USB reading. The problem was that from time to time a board was losing its synchronization, probably because of buffers becoming full. Then, events written to file by the USBWC acquisition software were containing waveforms from different physical events which made them useless. This effect was found by noticing wide tails ( $\pm 5$  ns) in the time difference histograms between two channels. As the problem was rare, it was permanently fixed by purging all USB buffers every 500 events (about every two hours) and each time when the USB interface reported an error.

- RUN2

For this run we used a new version of the software ensuring event synchronization between the different boards. This was the only difference with respect to RUN1. During this run, we measured the time resolution of the DIRC-like TOF prototype for high photon flux. The main conclusions from this run were:

1. the MCP-PMT was saturating due to high photon flux while running at high gain.
2. charge sharing and crosstalk from the many photons detected were affecting significantly the time resolution of the DIRC-like TOF prototype, which made impossible the measurement of the real time resolution in case of single photo electrons.

Hence we decided to decrease the Cherenkov photon flux.

- RUN3

By inserting two 0.005" Mylar sheets between the quartz bar exit faces and the MCP-PMT, the photon flux was reduced by a factor five – hence the transmission efficiency became 0.14 instead of 0.7. This short run was then dedicated to commissioning the upgraded DIRC-like TOF prototype.

- RUN4

For this run we upgraded the USBWC DAQ laptop to make the running more stable. MCP-PMT channel 15 was replaced with the signal coming from pad number 3 of the MCP-PMT connected to the QSC. And finally we included a veto coming from the CRT to the USBWC DAQ – see previous section for details. During this nominal

run we measured the time resolution of the upgraded DIRC-like TOF prototype for low photon flux.

- RUN5

During this run we used the same setup as for RUN4, but the CRT hodoscopes were not fully functioning.

Table 5.5: Short description of the different runs.

	RUN1
Run number	RUN1
Total run time, h	1432
Total number of entries USBWC	575164
GMT time START run :	5.10.2010 00:02:39
GMT time END run :	3.12.2010 16:10:34
Note	Commissioning
	RUN2
Run number	RUN2
Total run time, h	719
Total number of entries USBWC	305677
GMT time START run :	7.12.2010 18:41:29
GMT time END run :	6.01.2011 17:56:36
Note	New USBWC software
	RUN3
Run number	RUN3
Total run time, h	428
Total number of entries USBWC	163265
GMT time START run :	06.01.2011 18:36:31
GMT time END run :	24.01.2011 15:01:31
Note	Photon absorber added
	RUN4
Run number	RUN4
Total run time, h	1414
Total number of entries USBWC	378347
GMT time START run :	28.01.2011 18:21:19
GMT time END run :	28.03.2011 16:37:34
Note	Best run
	RUN5
Run number	RUN5
Total run time, h	767
Total number of entries USBWC	198971
GMT time START run :	28.03.2011 16:37:58
GMT time END run :	29.04.2011 15:58:44
Note	Hodoscope problem

### 5.5.3 Comparison between runs without and with photon absorber

Here we compare the USBWC data taken without and with photon absorber between the quartz exit faces and the MCP-PMT. However, measurements of the time resolution will be presented later.

Examples of typical events for RUN2 and RUN4 are shown on Figure 5.55 and 5.56 respectively. The RUN2 event – taken without absorber – shows a lot of p.e. signals in all channels while the RUN4 event is more quiet. Moreover the amplitudes of the signals are smaller in RUN4 but their shapes are less distorted and hence more suitable for timing measurements. In both pictures the color of the waveform indicates the type of signal: blue for singlepeak-like black for crosstalk and multipeak-like, red for the QSC signal.

These behaviors are in fact general, as shown in the following. First, Figure 5.57 (Left) compares the number of firing USBWC channels for different configurations: the blue histogram labelled 'Old setup' corresponds to RUN2 while the black one ('New setup') is for RUN4. The red histogram shows the result of the laser run and is used as reference for the single photon mode. Without absorber, most (if not all) channels fire simultaneously and the peak at 16 channels indicates that the MCP-PMT was probably not working properly because of high photon flux and high gain. With absorber the distribution looks more physical; yet, more photons are detected in average than during the laser run. On the right side of Figure 5.57, the rise time distributions of the same three configurations are compared. The histograms for the laser run and the new setup are quite close in the peak region ( $\approx 0.95$  ns) with slightly longer tails in the latter case. For the old setup, the rise time is significantly higher ( $\approx 1.1$  ns) and the tails extend much more, two other indications of the large number of photons per event.

These observations imply that the signal shape should be different without or with absorber. This can indeed be checked on Figure 5.58. Both plots show the superposition of all singlepeak-like waveforms in USBWC channel 3 for events in which that channel fires. These waveforms have been aligned in time (coincident time for the maximum amplitude of the first peak) and normalized by their amplitude. The left (right) plot is for the laser run (RUN2). As anticipated, waveforms recorded in the configuration without absorber vary a lot and present more prominent secondary peaks due to charge sharing and crosstalk. The leading edge of the signal is also fluctuating more, which impacts the timing measurements even when the constant fraction timing algorithm is used.

### 5.5.4 Measurements of the DIRC-like TOF prototype time resolution

Finally, we present our measurements of the time resolution of the DIRC-like TOF prototype. First, we show the measurements done using RUN4 data: these are the cleanest

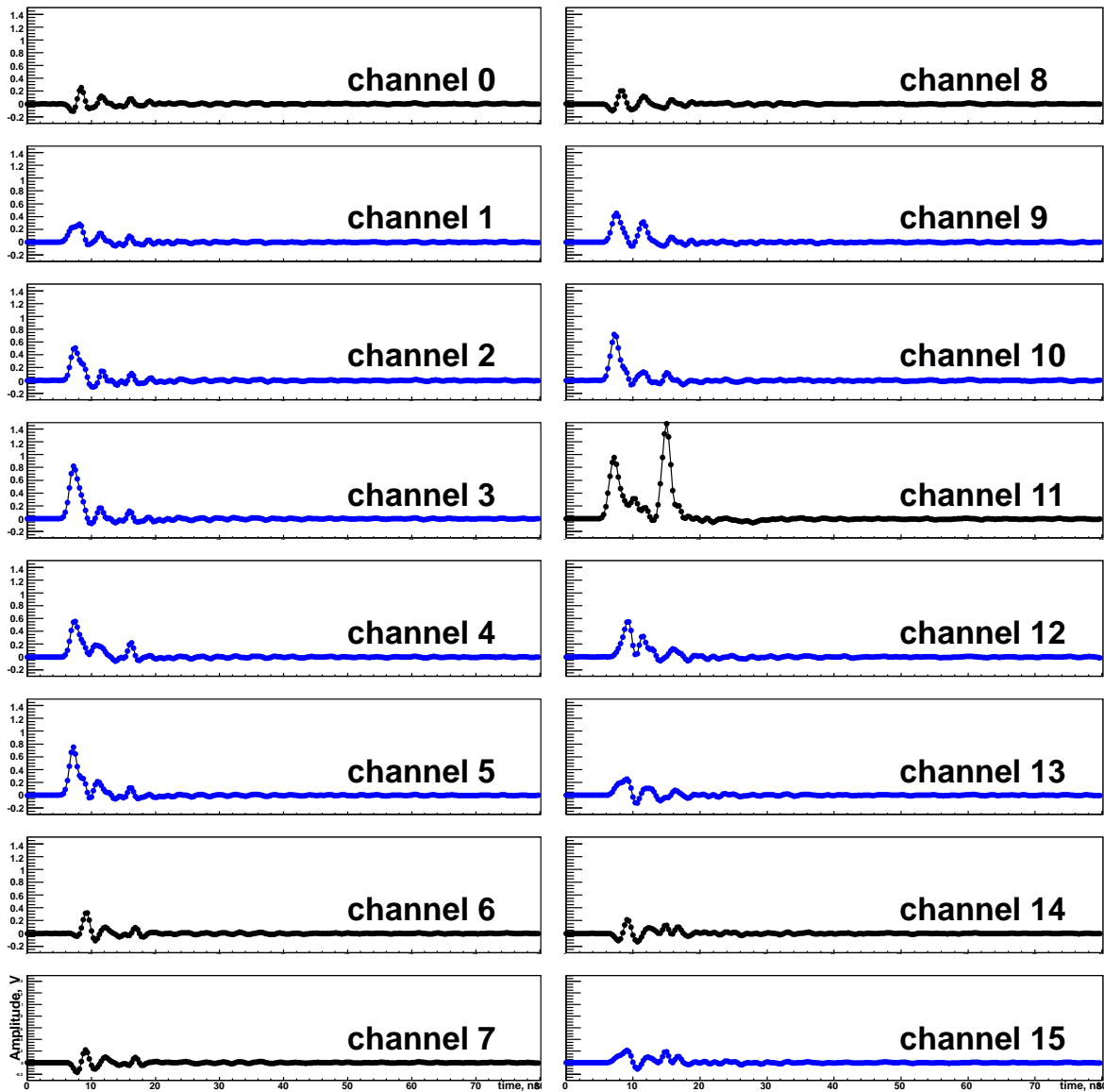


Figure 5.55: Typical event for RUN2, used as input to the waveform analyzer. Singlepeak-like waveforms (used for timing measurements) are shown in blue; crosstalk and multipeak-like signals are in black.

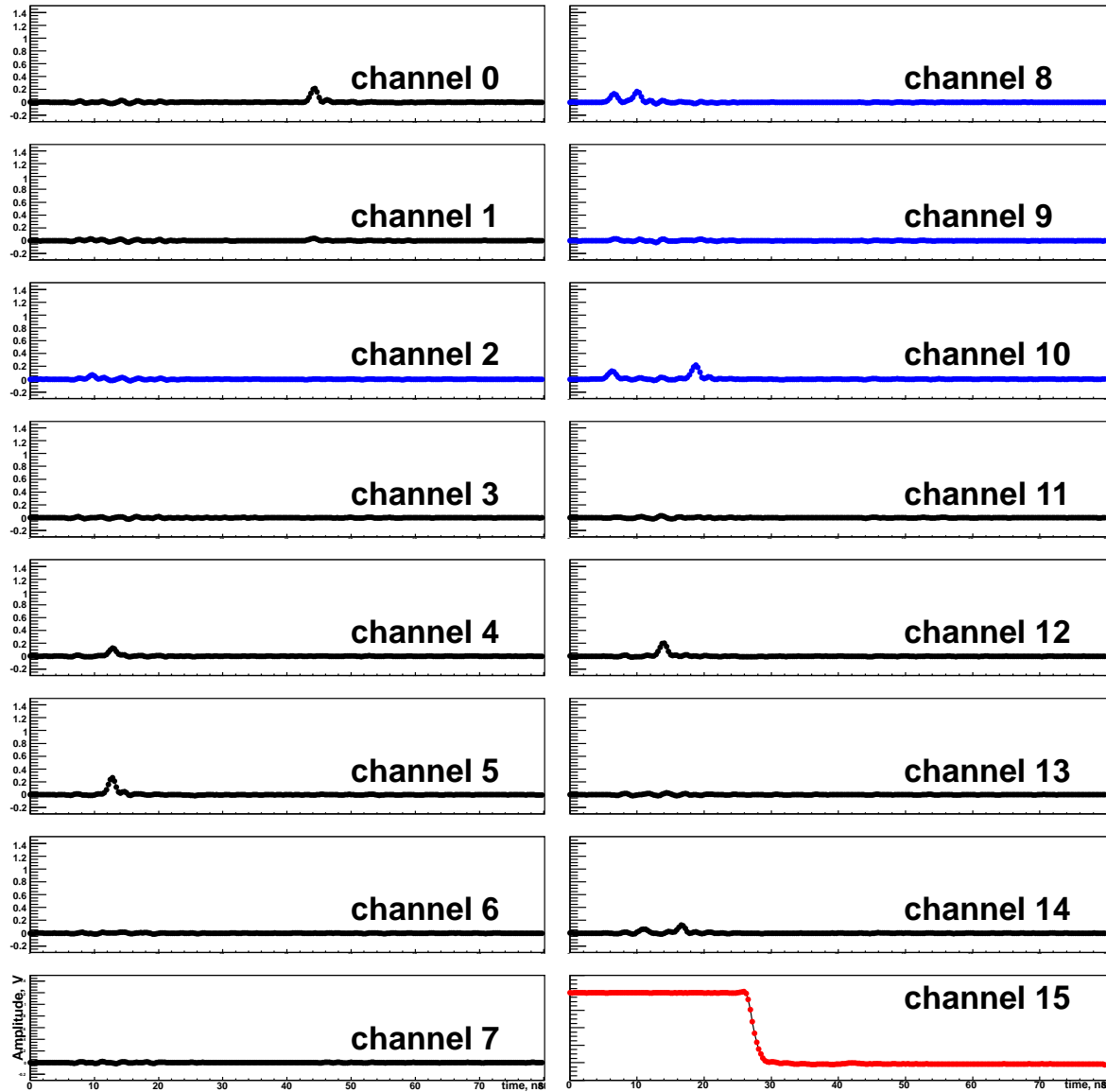


Figure 5.56: Typical event for RUN4, used as input to the waveform analyzer. Singlepeak-like waveforms (used for timing measurements) are shown in blue; crosstalk and multipeak-like signals are in black; the red signal comes from the QSC pad number 3.

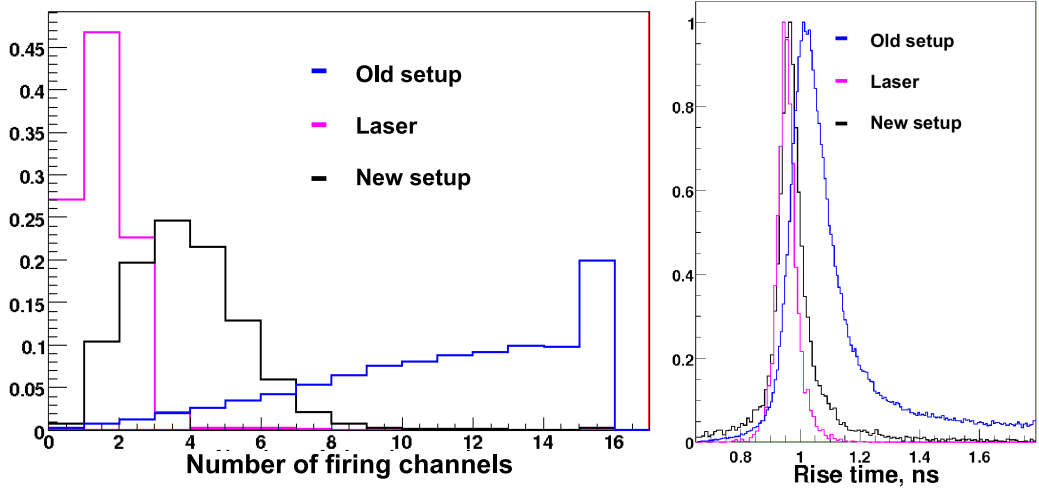


Figure 5.57: **Left:** Number of firing channels for different configurations: laser run (magenta), old setup without photon absorber (blue) and new setup with absorber (black). **Right:** Histograms of the signal rise time for the same configurations. See text for details.

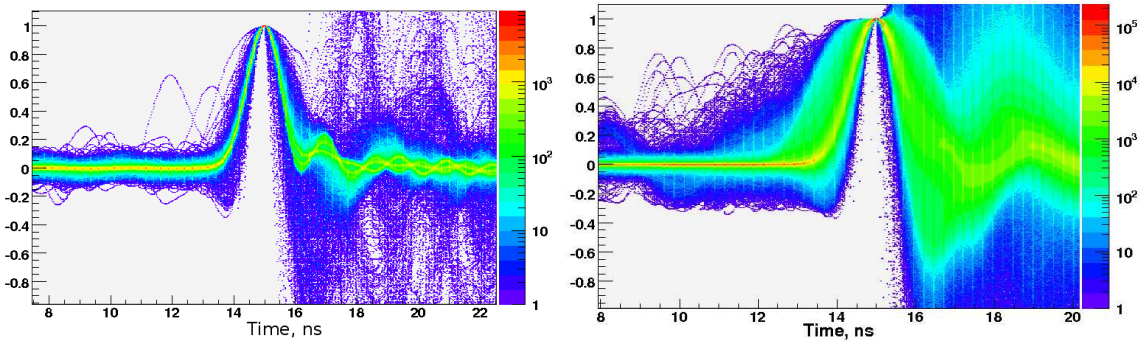


Figure 5.58: 2D (amplitude vs. time) histograms showing the 'stability' of the waveform in a given firing channel. **Left:** laser run. **Right:** RUN2. See text for details.

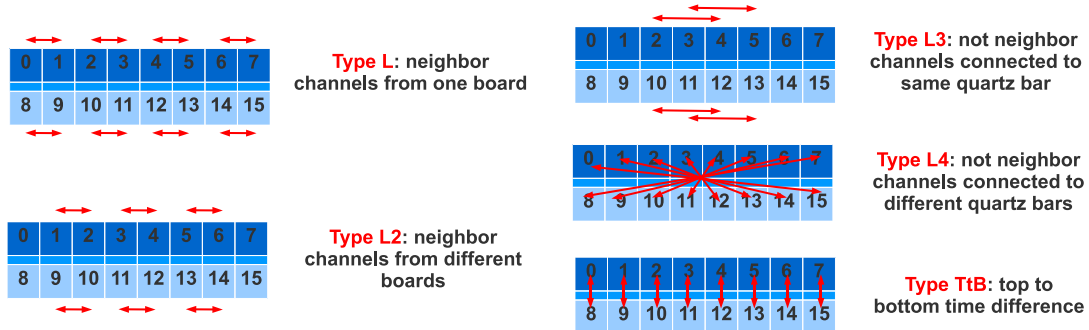


Figure 5.59: Different type of the time differences.

for timing measurements thanks to the photon absorber which decreased significantly the number of p.e. per event. Then we show similar results for RUN2 (data taken without absorber). As already explained, we do not know precisely when muons arrive. Hence, to measure the time resolution we construct time differences between two USBWC channels. Different types of time differences have been studied: see Figure 5.59 for a graphical view of all the configurations tested in the following.

- **Type L**

Time differences between neighbor channels from the same USBWC board. The main purpose of these time differences is to look at charge sharing effect on the time resolution – see section 5.3.

- **Type L2**

Time differences between neighbor channels from different USBWC boards. This type is complimentary to the L type and is also sensitive to charge sharing. It can also help identifying a loss of synchronization between different USBWC boards.

- **Type L3**

Time differences between not neighbor channels which are close to each other and connected to the same quartz bar. Since these channels are not neighbor, we remove effect from charge sharing.

- **Type L4**

Time differences between channels far from each other and connected to different quartz bars.

- **Type TtB**

Time differences between channels located one on top of each other. Since the top and bottom parts of the DIRC-like TOF prototypes are identical, the p.e. time

distributions would be very similar for almost vertical muon tracks which could potentially lead to 'cleaner' time difference histograms.

For the analysis of the RUN4 data we use the following sets of cuts:

- Cuts applied on the waveforms
  - Time measurement required (a sanity check: in 99.9% of the cases, the time measurements exists).
  - The waveform is singlepeak-like.
  - Its amplitude exceeds 80 mV.
  - The number of firing channels in the event is at most 5 to reduce effects coming from crosstalk.
- Cuts applied on muon tracks
  - The muon track is properly reconstructed in the CRT (see Section 5.1.1).
  - The track crosses the QSC and the DIRC-like TOF prototype. Using the  $x$  and  $y$  coordinates of the intersection of the track with QSC and DIRC-like TOF 'scoring' planes, these two requirements translate into the following conditions:  
 $-9 < x_{QSC} < 13 \ \&\& -2 < y_{QSC} < 3;$   
 $-14 < x_{FTOF} < 15 \ \&\& -2 < y_{FTOF} < 3.5.$

### RUN4, time differences between not neighbor channels (L3, L4 and TtB types).

Figures 5.60 (L3 type), 5.61 (L4 type), 5.62 (TtB type) compare time difference measurements with simulation for different pairs of channels. One can see a good overall agreement between data and simulation which validates our measurements and reflects our detailed understanding of the DIRC-like TOF prototype.

As already explained – see Section 5.4.3 – all these distributions contain narrow and wide components on top of a flat pedestal. We remind that the wide component appears when times of p.e. coming from different populations are subtracted. Hence its RMS is very big and can not be used to estimate the time resolution of the DIRC-like TOF prototype. Instead, we have to use the narrow component for this measurement. On Figure 5.63 two examples of double Gaussian fit of time differences measured with RUN4 data are shown. One can see that the width of narrow component  $\sigma_{\text{narrow}}$  is around 110 ps.  $\sigma_{\text{narrow}}$  includes many contributions:

$$\frac{\sigma_{\text{narrow}}}{\sqrt{2}} = [\sigma_{\text{detector}} \oplus \sigma_{\text{TTS}} \oplus \sigma_{\text{electronics}}] \oplus \sigma_{\text{muon}} \quad (5.6)$$

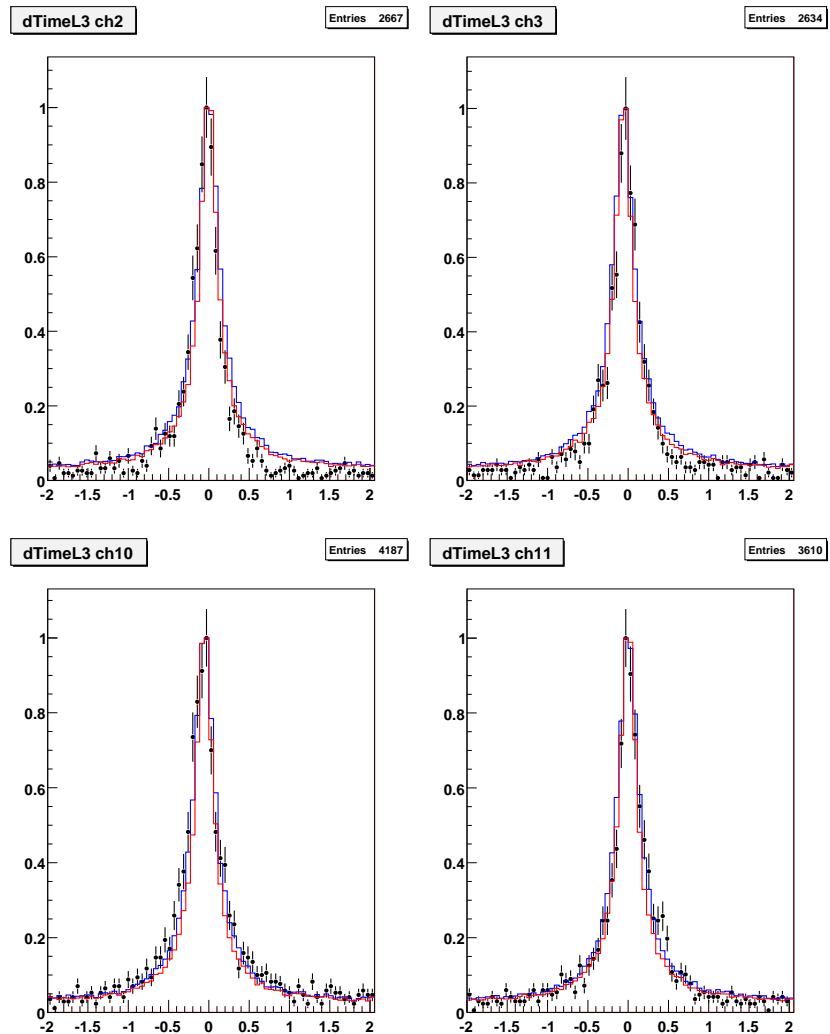


Figure 5.60: Time differences (in ns) for various combinations of channels from type L3. The black dots are the measurements while the two solid histograms are the corresponding results of the Geant4 simulations already described earlier in this chapter – in red, the simple simulation in which the true Geant4 times are just smeared by the MCP-PMT TTS; in blue, the full waveform simulation analyzed in the same way than the data by the waveform analyzer software. These measurements are done using RUN4 data (absorber added to control the flux of Cherenkov photons). **Top:**  $t_2 - t_4$  (Left),  $t_3 - t_5$  (Right). **Bottom:**  $t_{10} - t_{12}$  (Left),  $t_{11} - t_{13}$  (Right). Both the data and simulation histograms are scaled to have their maximum values equal to 1.

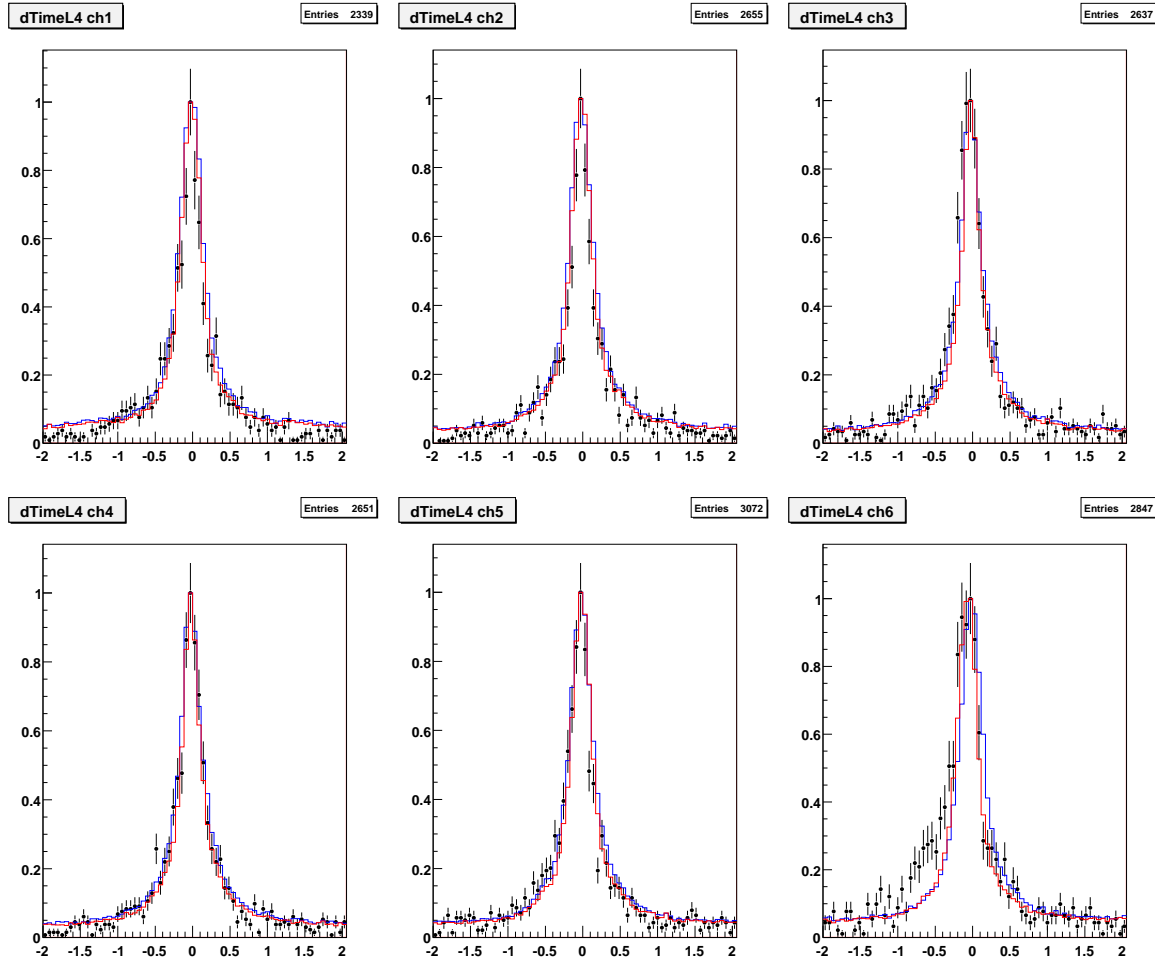


Figure 5.61: Time differences (in ns) for various combinations of channels from type L4. The black dots are the measurements while the two solid histograms are the corresponding results of the Geant4 simulations already described earlier in this chapter – in red, the simple simulation in which the true Geant4 times are just smeared by the MCP-PMT TTS; in blue, the full waveform simulation analyzed in the same way than the data by the waveform analyzer software. These measurements are done using RUN4 data (absorber added to control the flux of Cherenkov photons). **Top:**  $t_1 - t_{14}$  (Left),  $t_2 - t_{13}$  (Middle)  $t_3 - t_{12}$  (Right). **Bottom:**  $t_4 - t_{11}$  (Left),  $t_5 - t_{10}$  (Middle)  $t_6 - t_9$  (Right). Both the data and simulation histograms are scaled to have their maximum values equal to 1.

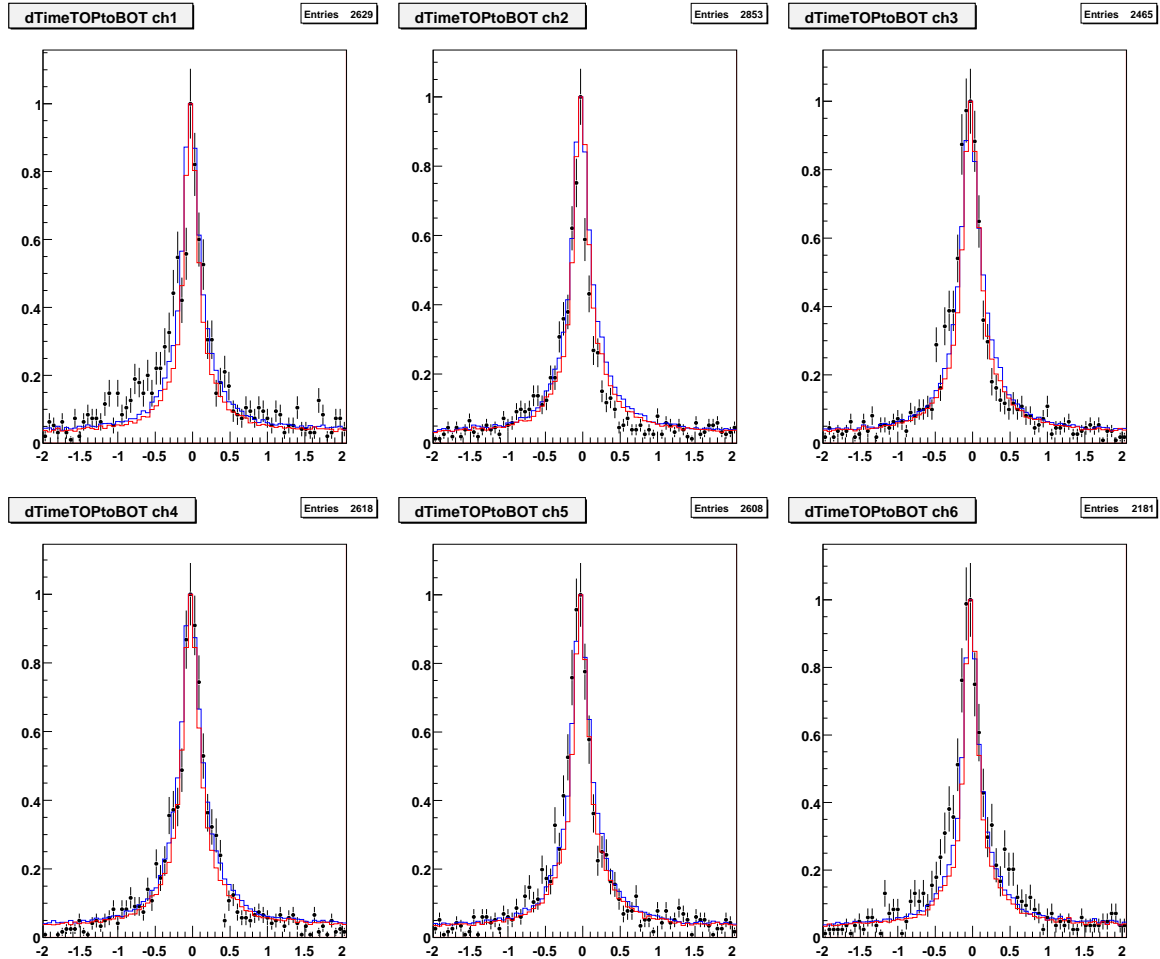


Figure 5.62: Time differences (in ns) for various combinations of channels from type TtB. The black dots are the measurements while the two solid histograms are the corresponding results of the Geant4 simulations already described earlier in this chapter – in red, the simple simulation in which the true Geant4 times are just smeared by the MCP-PMT TTS; in blue, the full waveform simulation analyzed in the same way than the data by the waveform analyzer software. These measurements are done using RUN4 data (absorber added to control the flux of Cherenkov photons). **Top:**  $t_1 - t_9$  (Left),  $t_2 - t_{10}$  (Middle)  $t_3 - t_{11}$  (Right). **Bottom:**  $t_4 - t_{12}$  (Left),  $t_5 - t_{13}$  (Middle)  $t_6 - t_{14}$  (Right). Both the data and simulation histograms are scaled to have their maximum values equal to 1.

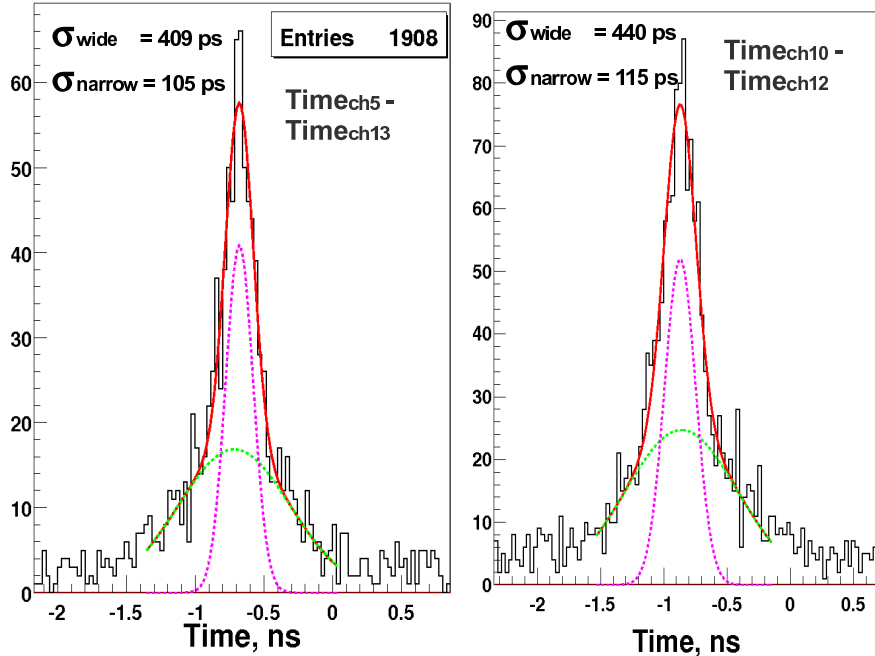


Figure 5.63: Double Gaussian fit (red curve) of measured time differences between channels in RUN4 data (low flux of Cherenkov photons). These distributions have narrow (magenta curve) and wide (green curve) components. **Left:**  $t_5 - t_{13}$  (TtB type); the fitted values are  $\sigma_{\text{narrow}} = 105$  ps and  $\sigma_{\text{wide}} = 409$  ps. **Right:**  $t_{10} - t_{12}$  (L3 type); the fitted values are  $\sigma_{\text{narrow}} = 115$  ps and  $\sigma_{\text{wide}} = 449$  ps.

where the factor  $\sqrt{2}$  comes from the assumption that  $\sigma_{\text{narrow}}$  is the quadratic sum of two independent and identical channel timing resolutions. For DIRC-like TOF detectors,  $\sigma_{\text{detector}}$  is irreducible – see Section 3.3 for details. The term  $\sigma_{\text{muon}}$  appears because we do not take into account event by event the muon track parameters when computing time differences between channels. It is foreseen to include this effect in a future reanalysis of the DIRC-like TOF prototype data.

From Eq. 5.6 and  $\sigma_{\text{narrow}} = 110$  ps we can compute that  $\sigma_{\text{detector}} \oplus \sigma_{\text{muon}} = 70$  ps hence  $\sigma_{\text{detector}} < 70$  ps for the DIRC-like TOF prototype. Unfortunately, we can not make direct comparison of  $\sigma_{\text{detector}}$  for the DIRC-like TOF prototype and the DIRC-like TOF detector because of their different geometries.

### RUN4, cuts on the muon direction

As we know from simulation, muons with 'bad' angles are not suitable for precise timing measurements as the Cherenkov photons they emit are detected in the MCP-PMT over a wide timing range. So these tracks contribute to the long tails of the time difference distributions. Using CRT information one can cut on the track  $\phi$  angle

to decrease this flat pedestal as well as the width of the narrow component in the time distributions. Examples of measurements with this additional cut – see Figure 5.46 – are shown on Figure 5.64. Again, we can see a good agreement between data and simulation. As expected, the constant pedestal is reduced such as the width of narrow component  $\sim 90$  ps which gives a new upper limit for  $\sigma_{\text{detector}} < 55$  ps.

From the full simulation of the DIRC-like TOF detector we know that  $\sigma_{\text{detector}} = 30$  ps for geometry GeomID = 0. Position of the photon detector for this configuration is the same as for the DIRC-like TOF prototype such are the properties of the quartz. Hence these two setups should have approximately the same  $\sigma_{\text{detector}}$ . Using  $\sigma_{\text{electronics}} = 10$  ps and  $\sigma_{\text{TTS}} = 37$  ps: one can then estimate  $\sigma_{\mu\text{on}} = 45$  ps. This computation seems to indicate that  $\sigma_{\mu\text{on}}$  is a dominant contribution to the narrow component width. It will be studied in more details when the data are reanalyzed.

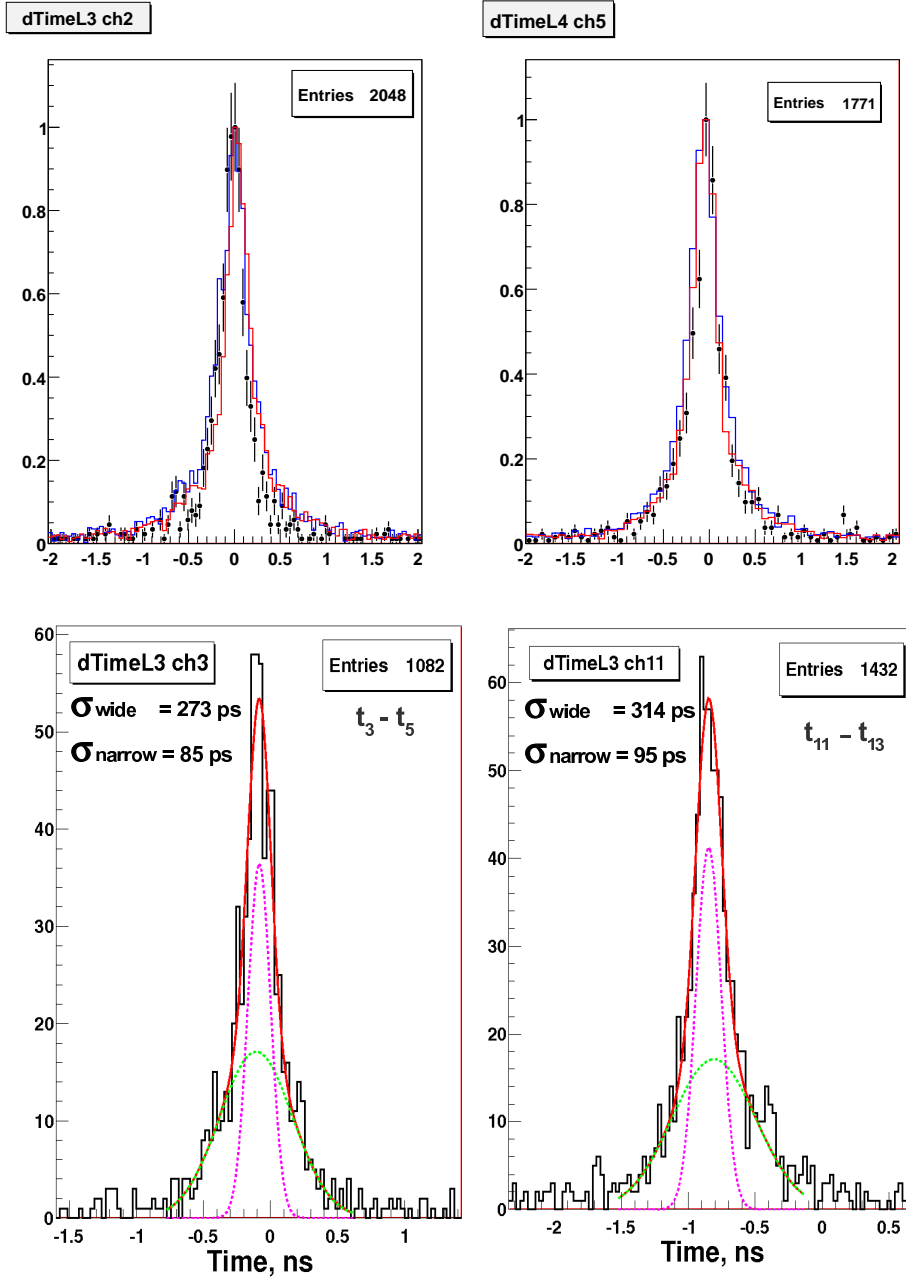


Figure 5.64: **Top:** Comparison between data and simulations for two time differences after cutting on the muon track  $\phi$  angle. The left plot corresponds to the difference  $t_2 - t_4$  (L3 type) while the right one shows  $t_5 - t_{10}$  (L4 type). **Bottom:** Two examples of double Gaussian fits:  $t_3 - t_5$  (L3 type, left plot) and  $t_{11} - t_{13}$  (L3 type, right plot).

### RUN4, time difference between neighbor channels

From laser run (single photon mode, see Section 5.3 for more details) we know that the measured time difference between neighbor channels is very narrow – around 35 ps, see Figure 5.29. The resulting histogram is too narrow because it contains a component coming from the measurement of the time difference between a p.e. and its own charge sharing signal in the neighbor channel. This effect would artificially reduce the width of the narrow component. This makes time resolution measurements of the DIRC-like TOF prototype using these pairs of channels wrong. This is dangerous because the timing resolution of the device would be overestimated. One can see on Figure 5.65 (L type) and Figure 5.66 (L2 type) some differences between data and simulations which indicate this problem.

### RUN2, time difference between NOT neighbor channels

Finally we present measurements done with RUN2 data. As previously described, the Cherenkov flux was high in this run because the photon absorber had not been inserted yet. Consequently, we use different sets of cuts for this particular analysis.

- Cuts applied on the waveforms
  - Time measurement required.
  - The waveform is singlepeak-like.
  - Its amplitude exceeds 80 mV.
  - Rise time between 0.9 ns and 1.2 ns. The distribution of the signal rise times in RUN2 has a mean value shifted with respect to the laser run and very long tails (see Figure 5.57). Events with distorted leading edge which are bad for timing measurements often have a rise time different from the typical values found in single p.e. mode. Therefore, cutting on this variable allows one to reduce the fraction of such events in the selected data.
- Cuts applied on muon track
  - The muon track is properly reconstructed in the CRT.
  - The track crosses the QSC and the DIRC-like TOF prototype. Using the  $x$  and  $y$  coordinates of the intersection of the track with QSC and DIRC-like TOF ‘scoring’ planes, these two requirements translate into the following conditions:  
 $-9 < x_{QSC} < 13 \ \&\& -2 < y_{QSC} < 3;$   
 $-14 < x_{FTOF} < 15 \ \&\& -2 < y_{FTOF} < 3.5.$

Figures 5.67 (L3 type), 5.68 (L4 type) and 5.69 (TtB type) show data-simulation comparisons for all pairs of channels already studied in RUN4. Contrary to the previous

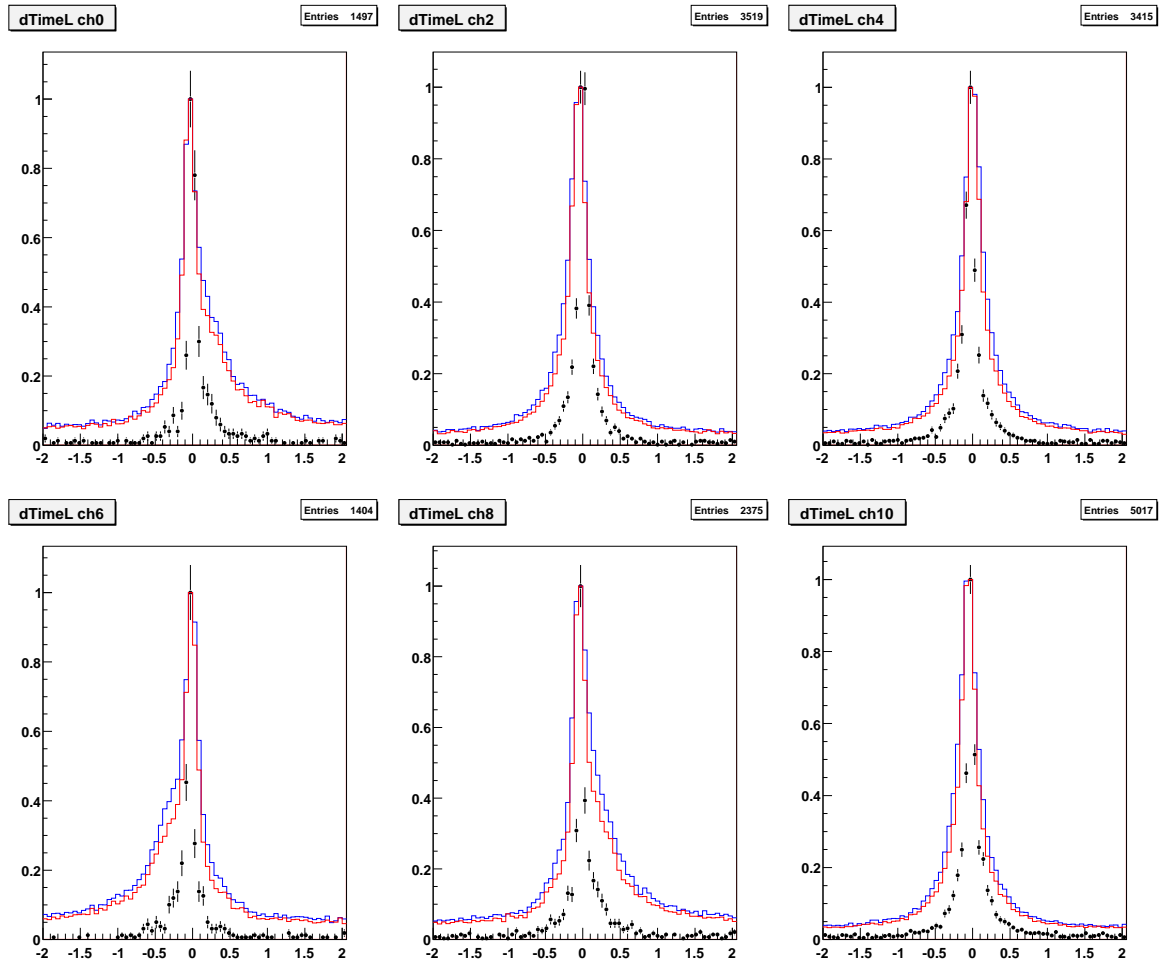


Figure 5.65: Time differences (in ns) for various combinations of channels from type L. The black dots are the measurements while the two solid histograms are the corresponding results of the Geant4 simulations already described earlier in this chapter – in red, the simple simulation in which the true Geant4 times are just smeared by the MCP-PMT TTS; in blue, the full waveform simulation analyzed in the same way than the data by the waveform analyzer software. These measurements are done using RUN4 data (absorber added to control the flux of Cherenkov photons). **TOP:**  $t_0 - t_1$  (Left),  $t_2 - t_3$  (Middle),  $t_4 - t_5$  (Right). **Bottom:**  $t_6 - t_7$  (Left),  $t_8 - t_9$  (Middle)  $t_{10} - t_{11}$  (Left). Both the data and simulation histograms are scaled to have their maximum values equal to 1.

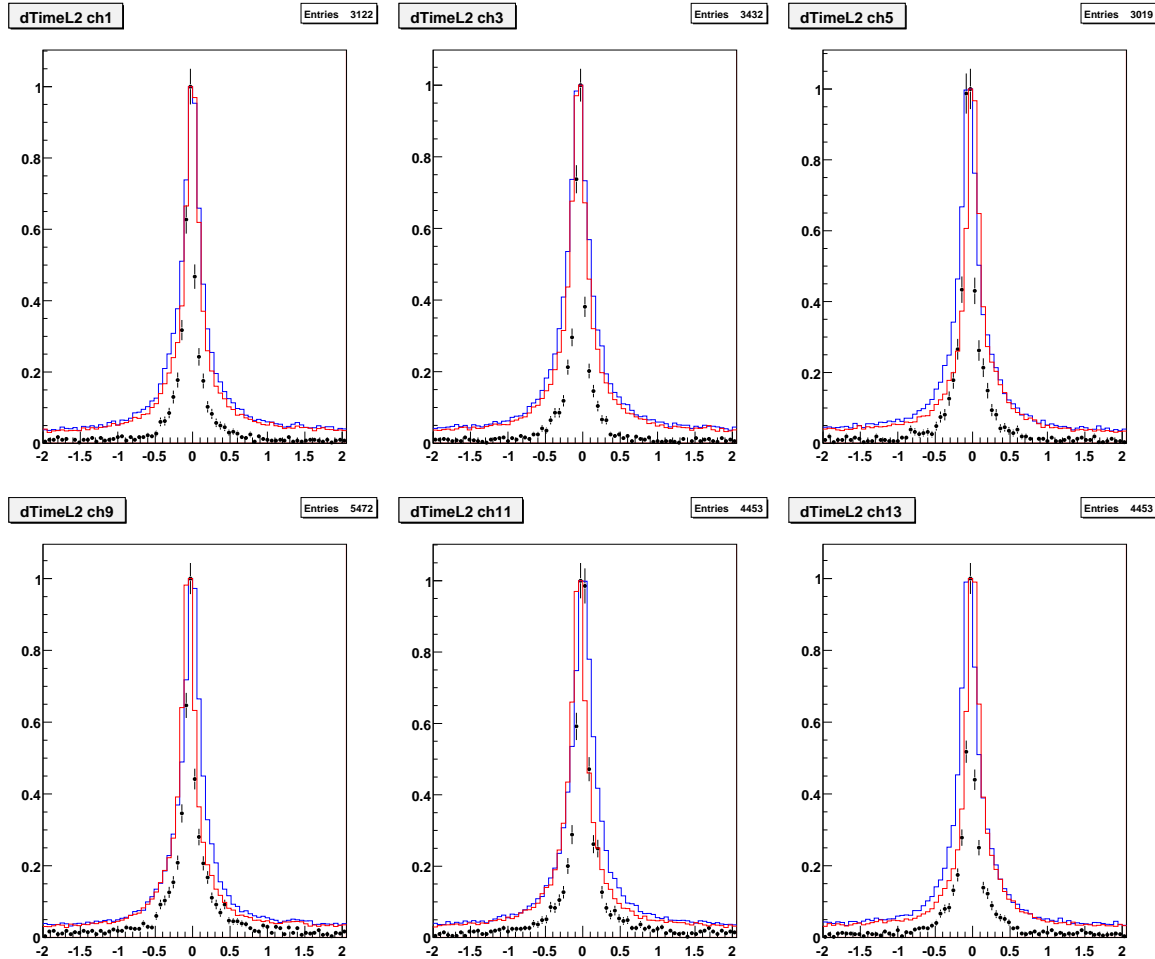


Figure 5.66: Time differences (in ns) for various combinations of channels from type L2. The black dots are the measurements while the two solid histograms are the corresponding results of the Geant4 simulations already described earlier in this chapter – in red, the simple simulation in which the true Geant4 times are just smeared by the MCP-PMT TTS; in blue, the full waveform simulation analyzed in the same way than the data by the waveform analyzer software. These measurements are done using RUN4 data (absorber added to control the flux of Cherenkov photons). **TOP:**  $t_1 - t_2$  (Left),  $t_3 - t_4$  (Middle),  $t_5 - t_6$  (Right). **Bottom:**  $t_9 - t_{10}$  (Left),  $t_{11} - t_{12}$  (Middle),  $t_{13} - t_{14}$  (Right). Both the data and simulation histograms are scaled to have their maximum values equal to 1.

results significant disagreements are visible in all plots: the data show wider peaks and much stronger tails. These differences come from charge sharing, crosstalk and complex MCP-PMT effects due to running at high gain with high photon yield and which are not simulated.

On Figure 5.70, double Gaussian fits of two particular pairs of channels (L3 type) are shown. The average RMS of the narrow component is  $\sim 175$  ps, about 50% more than with the cleaner RUN4 data.

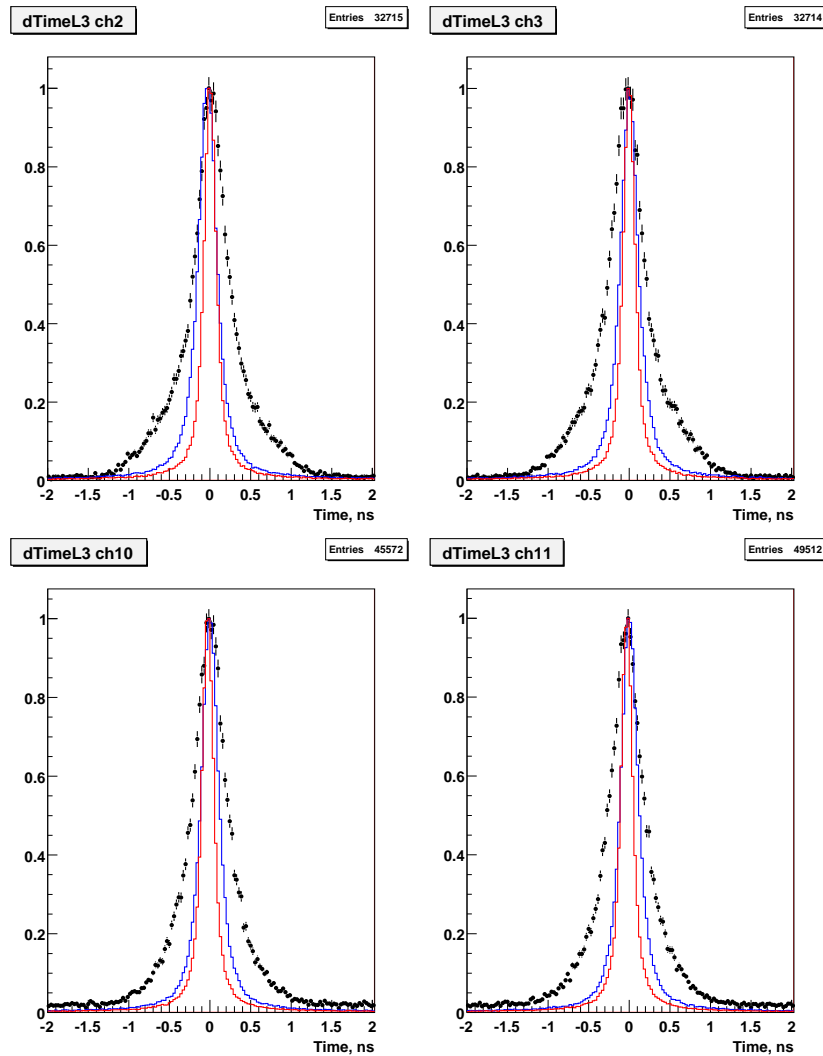


Figure 5.67: Time differences (in ns) for various combinations of channels from type L3. The black dots are the measurements while the two solid histograms are the corresponding results of the Geant4 simulations already described earlier in this chapter – in red, the simple simulation in which the true Geant4 times are just smeared by the MCP-PMT TTS; in blue, the full waveform simulation analyzed in the same way than the data by the waveform analyzer software. These measurements are done using RUN2 data (high flux of Cherenkov photons). **Top:**  $t_2 - t_4$  (Left),  $t_3 - t_5$  (Right). **Bottom:**  $t_{10} - t_{12}$  (Left),  $t_{11} - t_{13}$  (Right). Both the data and simulation histograms are scaled to have their maximum values equal to 1.

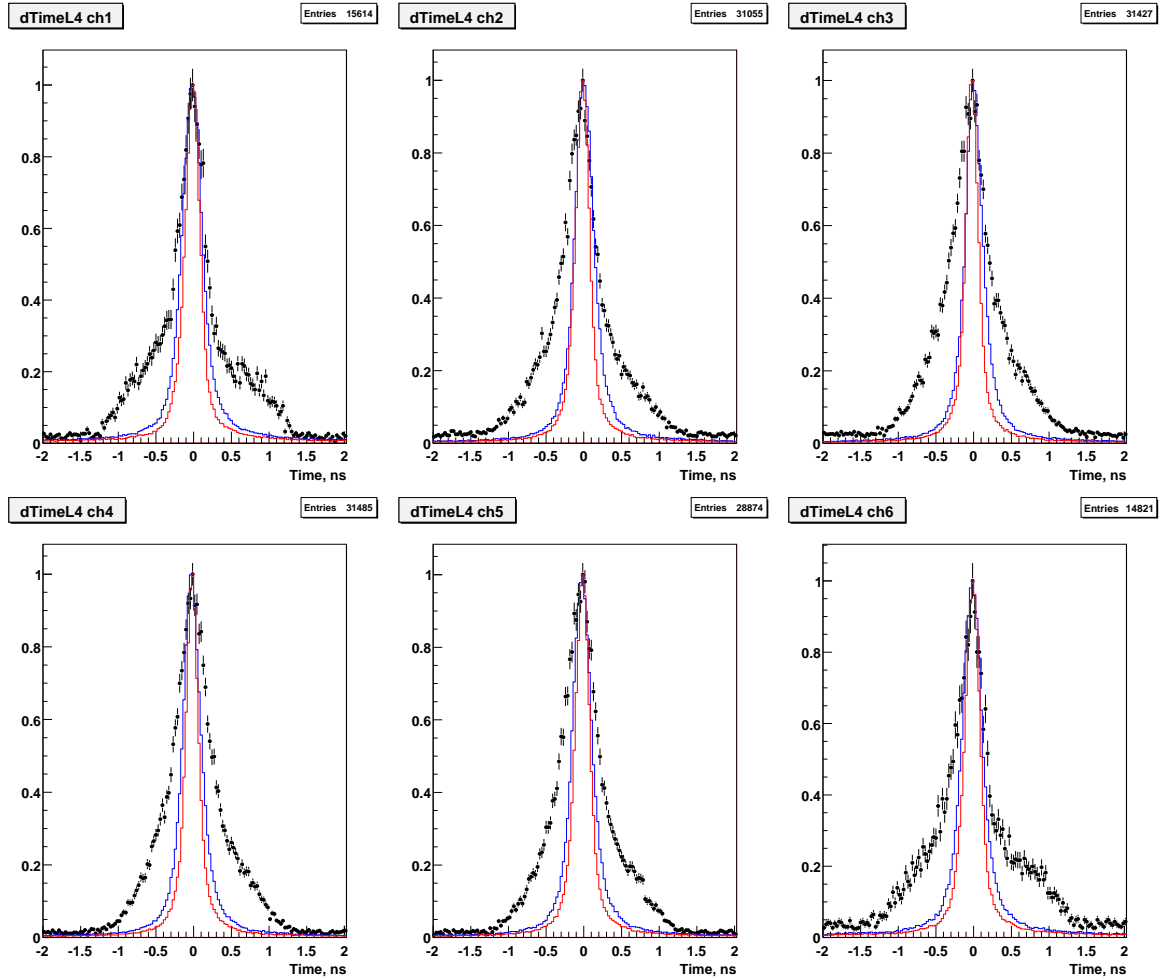


Figure 5.68: Time differences (in ns) for various combinations of channels from type L4. The black dots are the measurements while the two solid histograms are the corresponding results of the Geant4 simulations already described earlier in this chapter – in red, the simple simulation in which the true Geant4 times are just smeared by the MCP-PMT TTS; in blue, the full waveform simulation analyzed in the same way than the data by the waveform analyzer software. These measurements are done using RUN2 data (high flux of Cherenkov photons). **TOP:**  $t_1 - t_{14}$  (Left),  $t_2 - t_{13}$  (Middle),  $t_3 - t_{12}$  (Right). **Bottom:**  $t_4 - t_{11}$  (Left),  $t_5 - t_{10}$  (Middle),  $t_6 - t_9$  (Right). Both the data and simulation histograms are scaled to have their maximum values equal to 1.

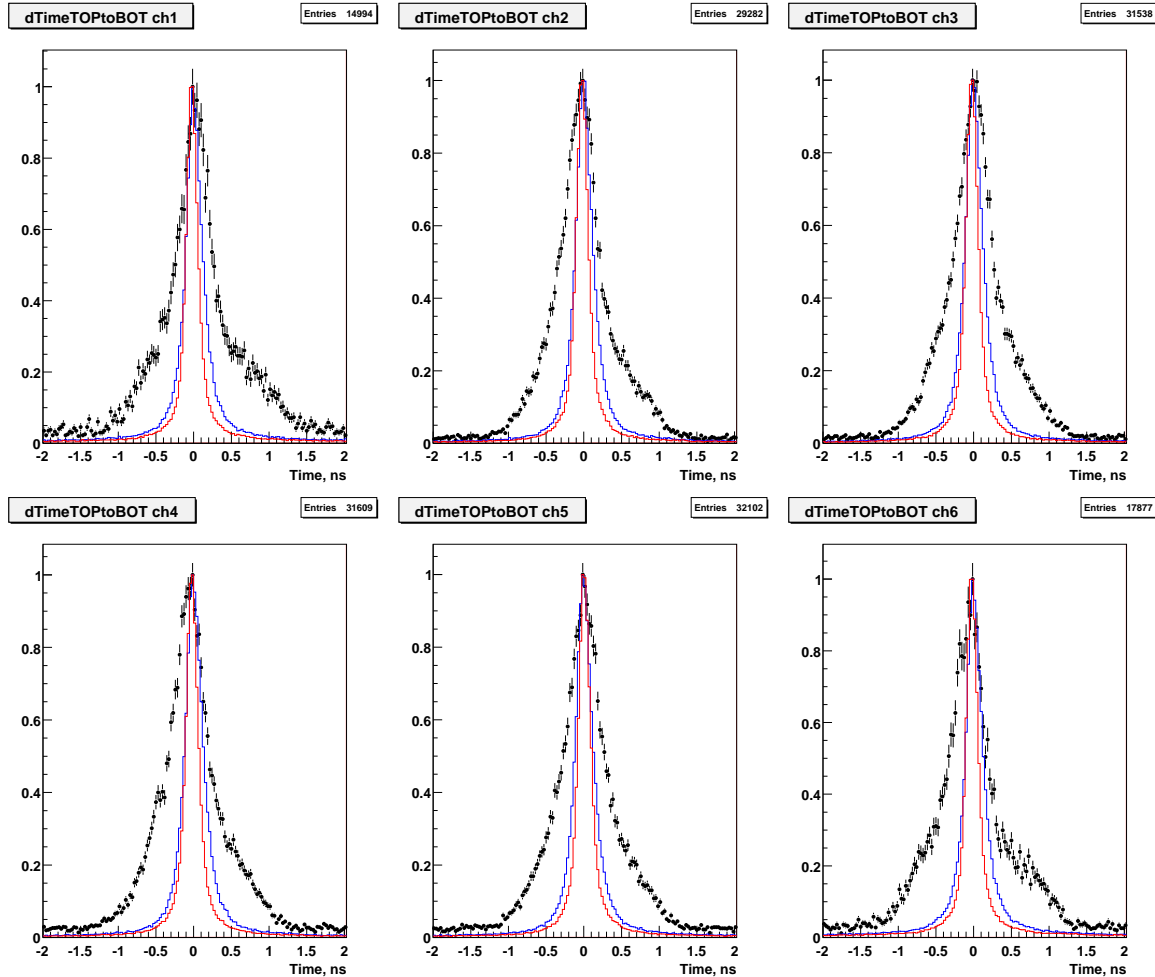


Figure 5.69: Time differences (in ns) for various combinations of channels from type TtB. The black dots are the measurements while the two solid histograms are the corresponding results of the Geant4 simulations already described earlier in this chapter – in red, the simple simulation in which the true Geant4 times are just smeared by the MCP-PMT TTS; in blue, the full waveform simulation analyzed in the same way than the data by the waveform analyzer software. These measurements are done using RUN2 data (high flux of Cherenkov photons). **TOP:**  $t_1 - t_9$  (Left),  $t_2 - t_{10}$  (Middle),  $t_3 - t_{11}$  (Right). **Bottom:**  $t_4 - t_{12}$  (Left),  $t_5 - t_{13}$  (Middle),  $t_6 - t_{14}$  (Right). Both the data and simulation histograms are scaled to have their maximum values equal to 1.

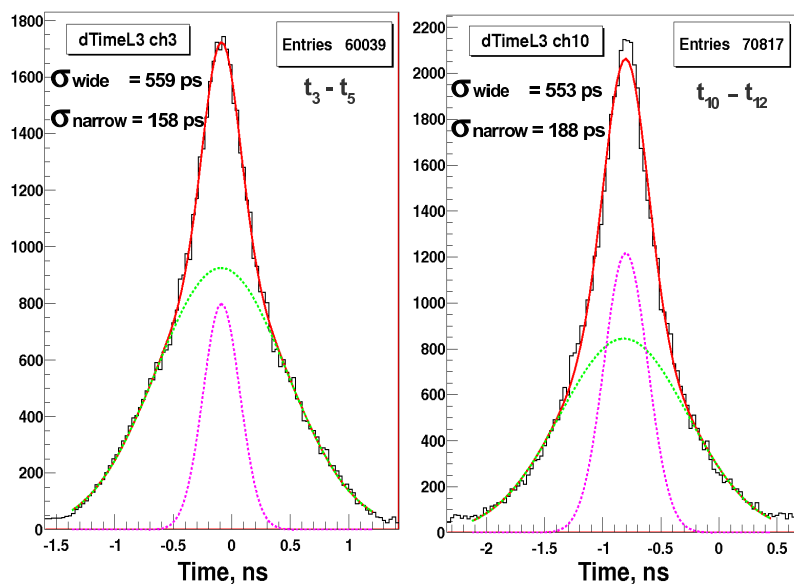


Figure 5.70: Double Gaussian fits of time difference histograms for two pairs of channels (L3 type). **Left:**  $t_3 - t_5$ . **Right:**  $t_{10} - t_{12}$ . The narrow (wide) component is drawn with a magenta (light green) dashed line while the red curve shows the sum of the two. The black histogram represents the data.

## 5.6 Conclusions

The test of the DIRC-like TOF prototype at SLAC CRT was successfully completed. Thanks to a precise simulation of the apparatus good detector setup and good electronics, the following results have been achieved.

- The good agreement between measurements and simulation shows that we understand the prototype well and that we do not miss any significant contribution to the timing resolution. In particular, we reproduce the narrow and wide components of the time difference distributions. This makes us confident that our full simulation of the *SuperB* DIRC-like TOF (which uses the same tools: physics and material properties) gives us access to the main characteristics of this device. This achievement was very important to convince the *SuperB* 'forward task force' that our proposal for a forward PID detector was worth being selected.
- For the first time a crate containing 8 USB WaveCatcher (USBWC) 2-channel boards was used to take data. Measurements have shown that the single board performances (timing accuracy of 10 ps per channel) have been maintained in the whole crate. This is the first step towards the use of USBWC-based electronics for the *SuperB* DIRC-like TOF and probably many other applications. The next step will be to test a 16-channel USBWC board.
- The time resolution of the DIRC-like TOF prototype has been computed:  $\sigma_{\text{narrow}}/\sqrt{2} = \sim 80$  ps per photo electron. Figure 5.71 compares data and simulation by showing how the RMS of the narrow component changes as a function of the transmission efficiency of the device. One can notice that the fit results only agree at low photon flux. In case of hight photon flux, contributions from multiple photo electrons, charge sharing and crosstalk become dominant.

With the SLAC CRT test we also gained experience which will be useful to develop the *SuperB* DIRC-like TOF detector.

- In case of low photon flux (single photon per whole PMT) one can measure very narrow time differences between neighbor channels (< 35 ps) due to charge sharing. This effect can be used to monitor the performances of the electronics.
- The constant fraction timing algorithm gives the best performances. The best constant fraction value is around 0.5 for the signal shapes delivered by the MCP-PMT used for this test. A similar optimization will have to be performed for the next prototype.
- Spline interpolation of the waveform does not improve significantly the time resolution; in addition, this increases the time of data analysis. Anyway, it would have been very difficult to implement spline interpolation in a FPGA. Our tests show that a simple linear interpolation should give good results.

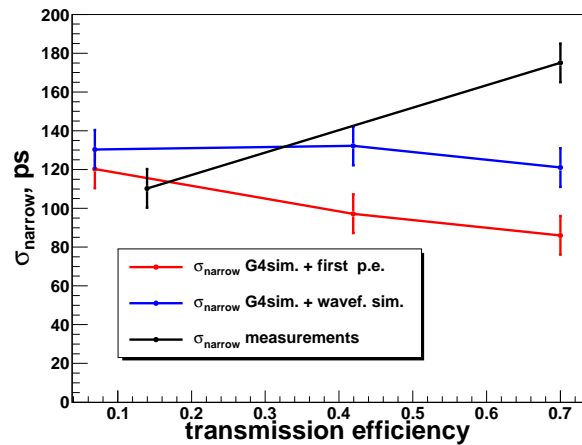


Figure 5.71: Comparison of the RMS of the narrow component between measurements and simulations as a function of transmission efficiency.

- The S/N ratio of the output signal (PMT + amplifier) has to be greater than 150-200 in order to reduce significantly  $\sigma_{\text{waveform}}$ .
- The rise time of the signal is not a very important parameter when the S/N ratio is big enough (more than 150).

# Chapter 6

## Selection of a photodetector for DIRC-like TOF detector

In this Chapter we present results of the timing measurement of the MCP-PMT and SiPM. We start from description of the experimental setup and tools which have been used to measure the time resolution. Then we show results of measurements done with Burle Planacon (XP85012) MCP-PMT, Hamamatsu SL10 MCP-PMT and finally with various different SiPM.

### 6.1 Introduction

Main parts of the DIRC-like TOF detector are the quartz radiator, which radiates Cherenkov photons and the photon detectors which detects these photons. In Chapter 3 two configurations which use MCP-PMT [57] and SiPM [61, 119] photon detectors are described. We performed characterization of these devices at LAL, to determined which kind of detector is the best candidate for DIRC-like TOF.

### 6.2 Experimental setup

First let us define the coordinate system: z is in the direction of the photon beam, y goes up vertically and x points in the direction to make right handed coordinate system. The experimental setup shown on Figure 6.1 is composed of:

- Climatic chamber.

All the measurements to characterize the photon detectors were performed inside a climatic chamber (labeled 'Dark box' in the figure) that assures a high stability

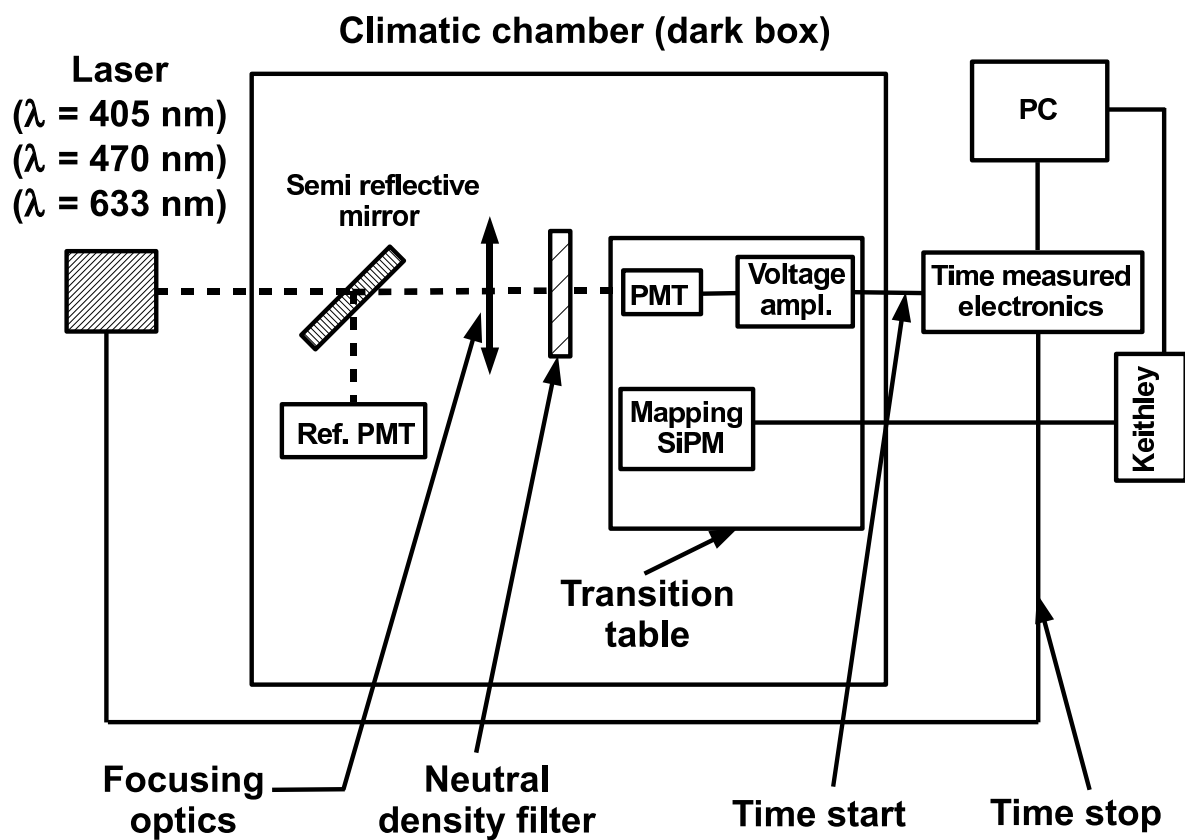


Figure 6.1: Experimental setup for the characterization of the photodetectors at LAL. Its main parts are: the pulsed laser (with  $\lambda = 405 \text{ nm}$ ,  $\lambda = 470 \text{ nm}$  and  $\lambda = 633 \text{ nm}$ ), the climatic chamber with temperature variation around  $\pm 0.1 \text{ }^{\circ}\text{C}$  and very high obscurity, transition table controlled from the PC, reference photodetector for flux measurements and mapping SiPM for beam profile measurements and finally readout electronics.



Figure 6.2: Photos of the experimental setup: dark box (top left), Pilas laser diodes and its control box (top right), Wavepro 750ZI LeCroy digital oscilloscope (bottom left) and USB wave catcher electronics with 8 ps time precision.

( $\pm 0.1$  °C) of the temperature and very high obscurity level. The temperature is monitored with 5 Pt100 sensors mounted inside the chamber and read by an acquisition unit (Keithley 2700). The stability of the temperature is controlled in order to avoid any variation of the SiPM properties.

- **Laser.**

Photon pulses from Pilas laser diodes were sent via an optical fiber to the semi-reflective mirror located inside the climatic chamber. The photon beam is then splitted into two beams: one goes to the reference photomultiplier tube, while another enlights the studied photodetector. Three different laser diodes (405, 467 and 635 nm) were driven at a repetition rate of 500 kHz. The light intensity was controlled with neutral density filters placed between the semi-reflective mirror output and the studied photodetector. The spectral width of the laser pulses does not exceed 3 nm and, depending on the laser diode head, the pulse timing width (FWHM) is between 48 ps for 80% from maximum power and 76 ps for 40% from maximum power (datasheet of the laser). On Figure 6.3 the time profile of the 467 nm laser is shown. The measurement has been done using streak camera at LAL. The FWHM, which is equal to  $2.35 \times \sigma$  is  $\sim 52$  ps is in agreement with the datasheet value. One can notice the 200 ps width tail (see Figure 6.3) which goes from 300 ps up to 500 ps (same tail show up on the datasheet figures). It will contribute to the time resolution measurements.

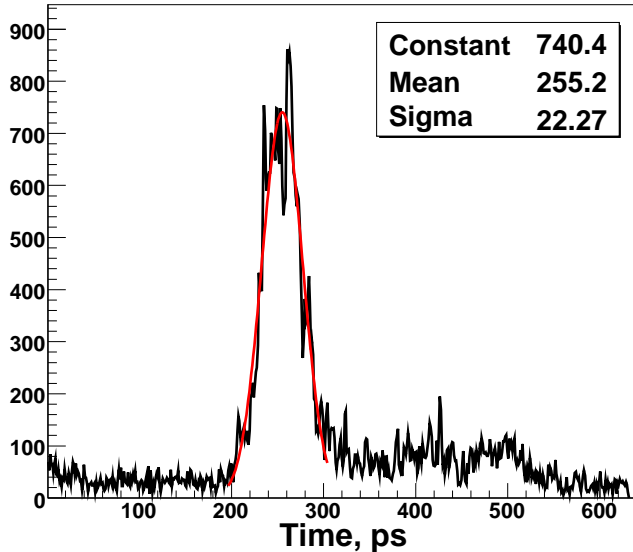


Figure 6.3: The timing profile of the photon beam provided by Pilas laser diodes ( $\lambda = 467$  nm) at 80% from maximum power with 10 Hz repetition rate. Measurements performed with streak camera at LAL.

- Reference photodetector.

The main purpose of the Hamamatsu R7400U-01 calibrated photodetector is to monitor stability with time of the laser intensity.

- Transition table (M-413 Linear Transition Stage).

The minimum incremental (decremental) motion is  $6 \mu\text{m}$  which also define its position resolution. The transition table has been used for various purposes: surface scanning of the MCP-PMT, precise alignment of the laser beam and the detector, photon beam profile and size measurements.

- Mapping SiPM.

For beam profile measurements, we use the Hamamatsu  $1 \text{ mm}^2$  S13362-11-50 SiPM. An example of the measurement of the beam transverse profile without focussing optics is shown on Figure 6.4 (Left). The transition table (driven by the Labview program) with attached mapping SiPM was used to move it in front of the beam. For each point the average output current, which is proportional to the incoming number of photons, had been measured by the Keithley 2700 during 2 s. One can see that the equal intensity spot (within 10 % deviation) has shape of a circle with the radius around 2 cm.

- Time measurement electronics.

For our studies we use three devices to measure parameters of the output signal.

- Wavepro 750ZI LeCroy digital oscilloscope (40 GSamples/s, 4GHz of analog

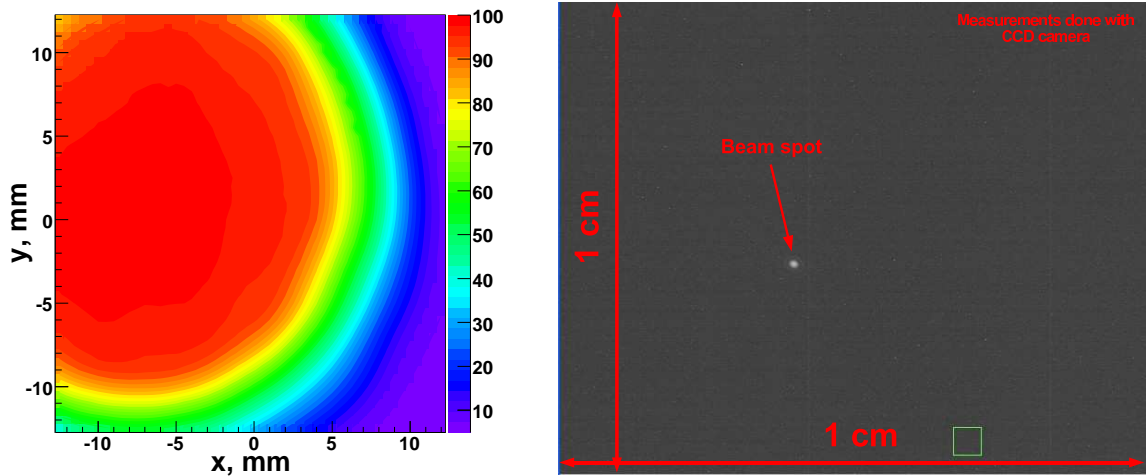


Figure 6.4: **Left:** The intensity of the photon pulse in transverse ( $y$  vs.  $x$ ) plane, measured with use of the mapping SiPM and the transition table. One can see that the equal intensity (within 10 % deviation) spot has the shape of the circle with radius around 2 cm. **Right:** The focussed photon pulse in transverse ( $y$  vs.  $x$ ) plane. Its size is around  $0.2 \times 0.2 \text{ mm}^2$ .

bandwidth)

- Two channel 3.3 GSamples/s WaveCatcher ASIC-based waveform digitizer developed at LAL [66].
- Electronics crate containing 8 USB WaveCatcher 2-channel boards (16-channel in total) controlled by the clock and control board. Progress on development of electronics and data acquisition software can be followed by looking at status reports presented during consecutive *SuperB* workshops [109, 110, 111, 112, 113, 114]. One has to mention that voltage amplifiers (with 20 dB, which mean 10 times voltage amplification, 450 MHz bandwidth 'LMH6552 from National Semiconductors') have been permanently attached to all input channels in order to detect small signals.
- Focussing optics.  
For the detail study of a given MCP-PMT channel one needs to have much smaller beam spot. For this reason system of focusing, defocusing lenses and collimators has been used. The distances, number and location of the lenses and collimators are driven by needs of the experiment. Smallest beam size we obtained is around  $0.2 \times 0.2 \text{ mm}^2$  measured with CCD camera (see Figure 6.4 from the right).

## 6.3 Measurements

After detailed description of the experimental setup we present results of the measurements of the single photon time resolution (SPTR) using the constant fraction time algorithm (see Chapter 5.2 for more details).

The laser driver provides output synchronization signal, which we call laser trigger. The time jitter of the laser trigger is around 3 ps, this precision is far enough for our measurements since it is very small in comparison with the pulse width and resolution of the studied photodetectors. It provides time start ( $t_{start}$ ), while the signal from photodetector gives time stop ( $t_{stop}$ ). We define the resolution as the RMS of the  $t_{stop} - t_{start}$  distribution.

### 6.3.1 Burle MCP-PMT

This is a MCP-PMT with a pixelated anode (64 channels) with a pixel size  $5.9 \times 5.9 \text{ mm}^2$ . Main characteristic of the Planacon MCP-PMT are listed in Table 6.1. To reduce number of readout channels, we group together 4 neighbor anodes, in such a way we get  $4 \times 4$  output channels.

Table 6.1: Planacon MCP-PMT photon detector (XP85012)

Model	XP85012
Window material	UV-Glass, Schott 8337B or equivalent
Photocathode	Bialkali
MCP pore diameter	$25 \mu\text{m}$
MCP pore length to diameter ration	40:1
Initial anode structure	$8 \times 8$ array, $5.9/6.5 \text{ mm}$ (size/pitch)
Active area	$53 \times 53 \text{ mm}^2$
Open-area-ratio	80 %

We performed measurements with the very low intensity photon flux ( $\sim$  one photon per pulse) pointing in the center of the channel using LeCroy oscilloscope and 16-Channels USBWC crate. In order to align the MCP-PMT with respect to the photon beam we use the transition table. Since the softwares which drive USBWC and transition table are separated, we use a time mark to match position of the photodetector with data from USBWC. First we make a scan in  $x$  direction (see Figure 6.5) and then in  $y$ . In such a way we determine the centers of the MCP-PMT channels with respect to the photon beam. Note that to perform the alignment we use high flux of photons and low gain ( $\sim 10^5$ ) of the MCP-PMT. In order to reduce the beam size, we insert a colimator before the MCP-PMT window with hole around 2 mm in diameter. This colimator has been located 3-5 mm from the photodetector, so the size of the beam which enter the MCP-PMT is around same size as the hole itself.

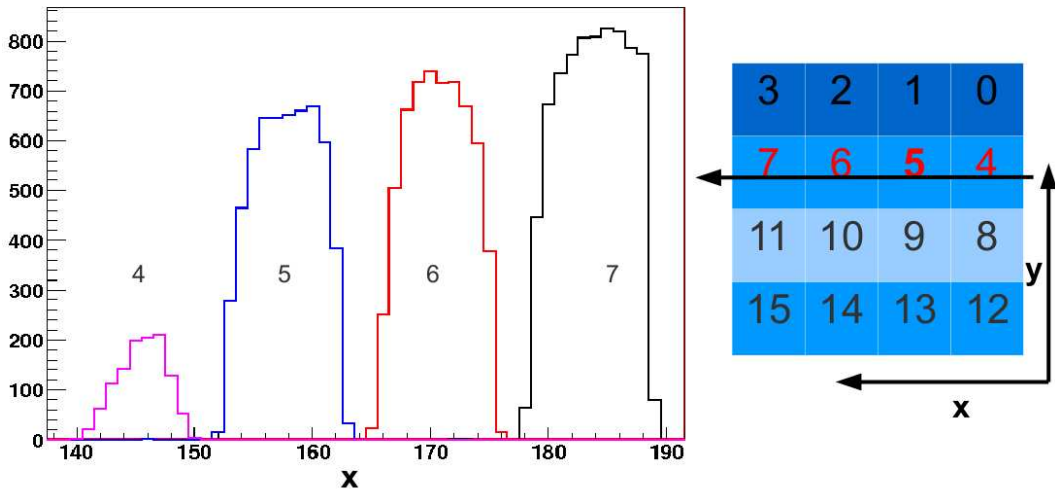


Figure 6.5: **Left:** Number of signals with amplitude bigger than 30 mV threshold for different channels as a function of  $x$  position of the Burle XP85012 MCP-PMT with respect to the photon beam in mm. Note we did not normalize the histograms by the laser intensity (which drifts in time). **Right:** The MCP-PMT channel map, the arrow shows scanning direction. Enlighten channel are shown in red.

Before doing the timing measurements, we perform a gain calibration of the device shown on Figure 6.6. One can see that at high voltage equal to -2.3 kV the MCP-PMT gain is around  $4.5 \times 10^5$ . At same gain we measure the time resolution for single photo electron (see Figure 6.7 and the caption for more details). The RMS of 50 ps has been obtained with LeCroy oscilloscope.

We perform also some more studies of the signals itself. On the Figure 6.8 (Top) the rise time and width of the signals are shown. One can see that these parameters are well defined and have 0.72 ns the rise time and 1.2 ns the width. The rising edge of the signals is very important for timing measurements. For this reason we study how the time of the signal depends from its rise time. But we did not find the correlation between them (see Figure 6.8 from the bottom).

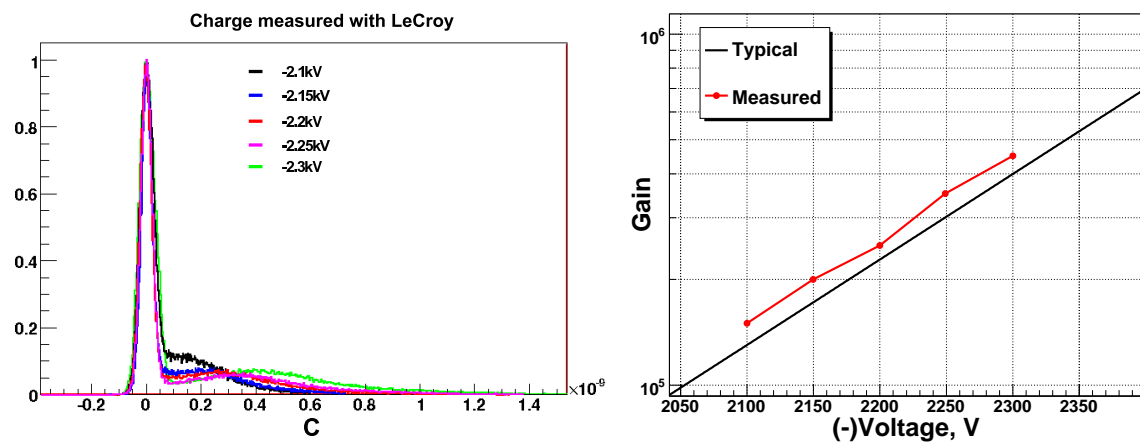


Figure 6.6: **Left:** Charge from the Burle XP85012 MCP-PMT measured with LeCroy oscilloscope at different voltages. **Right:** Gain as a function of high voltage for typical XP85012 MCP-PMT and measured for our device.

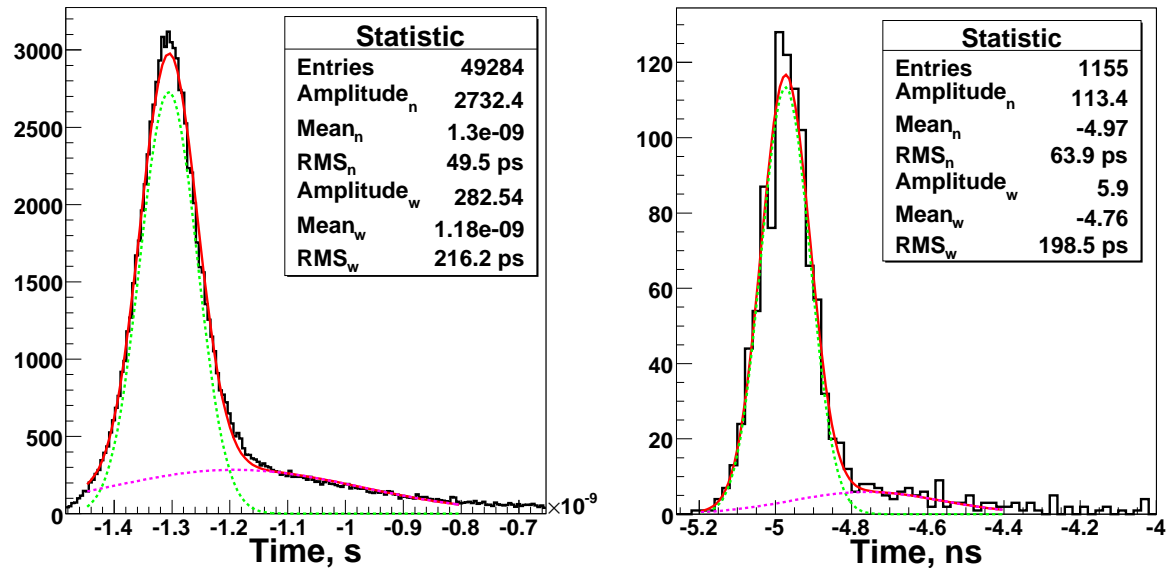


Figure 6.7: **Left:** The black histogram corresponds to the time difference between the trigger and signal from channel 10 of the XP85012 MCP-PMT (LeCroy oscilloscope). Measurements done with 36 dB ( $\sim 63$  times voltage amplification) MITEQ amplifier (for more details see [107]). The histogram has been fitted with sum of two Gaussian (wide and narrow). The green dashed curve corresponds to a narrow Gaussian, the magenta dashed curve represents wide Gaussian while red solid line is their sum. The wide component is caused by the recoil electron from the first MCP, which is delayed in time. One can see that the RMS of the narrow component is around 50 ps. **Right:** Same measurements done with 16-channel USBWC electronics. As we can see that narrow component is around 64 ps. Note we did not use same amplifier for this measurement (the amplification was 6 times less). Which explains the difference in measured time resolution.

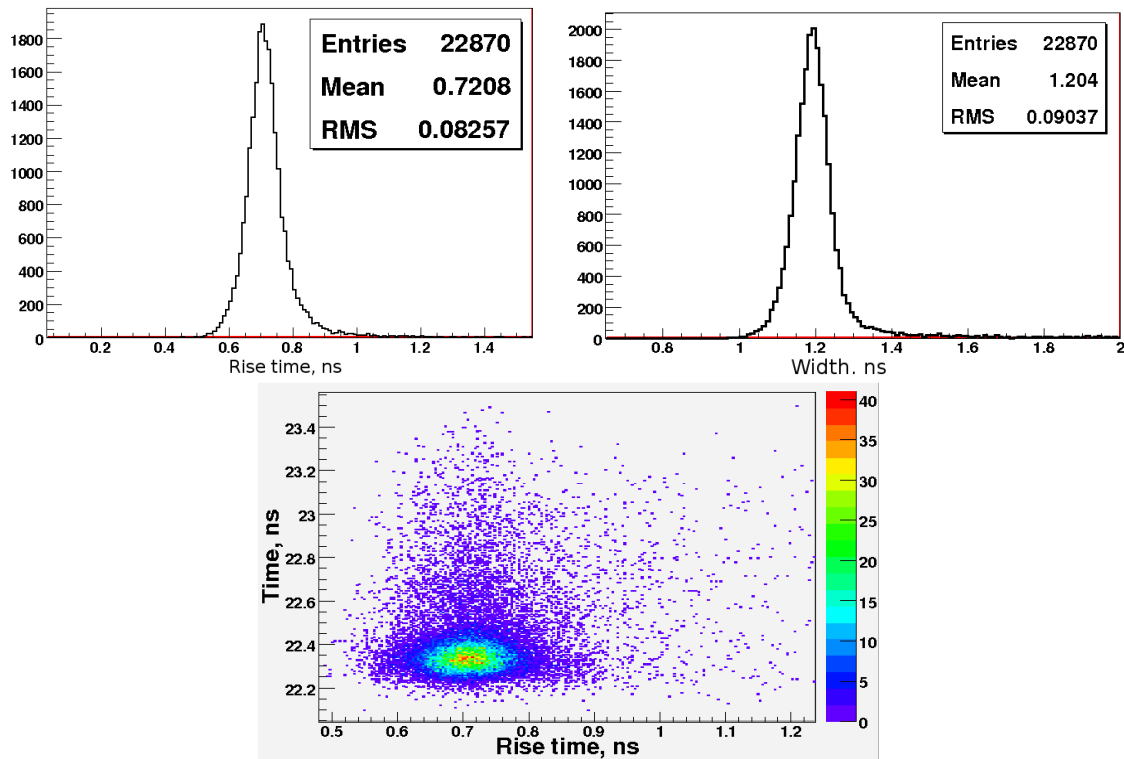


Figure 6.8: **Top:** XP85012 signal rise time ( $\sim 0.7$  ns) is on the left and width ( $\sim 1.2$  ns) is on the right (measured with 16-channels USBWC electronics) at  $4.5 \times 10^5$  gain. **Bottom:** The correlation between the time of the signal and its rise time (measured with LeCroy oscilloscope). One can see that these variables do not correlate.

### 6.3.2 Hamamatsu MCP-PMT

Next studied device is Hamamatsu SL-10 MCP-PMT with 4 channels (see Table 6.2 for more details). On Figure 6.9 the time difference between the signal from SL10 and the laser trigger is shown. We run the MCP-PMT at very high gain  $\sim 10^6$ . Measurements with 16-channel USBWC are in agreement with LeCroy oscilloscope. The time resolution of this device is around 32 ps (RMS of the narrow component). One have to mention that the number of events with single p.e. is only 60 %, which makes the time resolution better than it is. The measurements in single photon condition give 37 ps.

Table 6.2: Hamamatsu SL-10 MCP-PMT with 4 channels

Model	SL-10
Window material	borosilicate glass
Photocathode	Bialkali
MCP pore diameter	$10 \mu\text{m}$
MCP pore length to diameter ration	40:1
Initial anode structure	4 channels, $22 \times 5.5 \text{ mm}^2$ size
Active area	$22 \times 22 \text{ mm}^2$
Open-area-ratio	70 %

### 6.3.3 SiPM

Finally we show results of the S PTR for  $1 \times 1 \text{ mm}^2$  SiPM (see [120] for more details). Devices from Hamamatsu Photonics (MPPC), Sensl (SPM) and AdvanSiD (ASD, produced by F.B.K) were characterized in the same experimental conditions. The characteristics of these detectors are listed in Table 6.3. The readout chain of the SiPM signal consist of a 500 MHz MITEQ voltage amplifier (gain = 350) with an input impedance of  $50 \Omega$ . The amplifier output connected via a 3 m SMA cable to the LeCroy oscilloscope or two channel USBWC. The timing resolution was studied by measuring the time difference between the SiPM amplified signal and the laser trigger. We are not going to describe the working principles of the SiPM since it is done in numerous books and articles – see for example the book by C. Grupen and B. Shwartz 'Particle detectors' [54]. To operate the SiPM one needs to know its breakdown voltage ( $V_{BD}$ ), the voltage at which it works in Geiger mode. The summary plot, which shows the time resolution (FWHM) for different SiPM as a function of over voltage ( $V_{bias} - V_{BD}$ ) is shown on Figure 6.10. The ASD-SiPM1S-M-50 detector shows the best time resolution  $\sigma = 64 \text{ ps}$  (RMS) for over voltage bigger than 2 V. One can see that the S PTR decreases with increasing the over voltage. Two effects contributes to improving of the time resolution: first, the signal to noise ratio increases with over voltage, second, the time of the avalanche development is faster which potentially may decrease the avalanche spreading and as the consequence improve the time resolution.

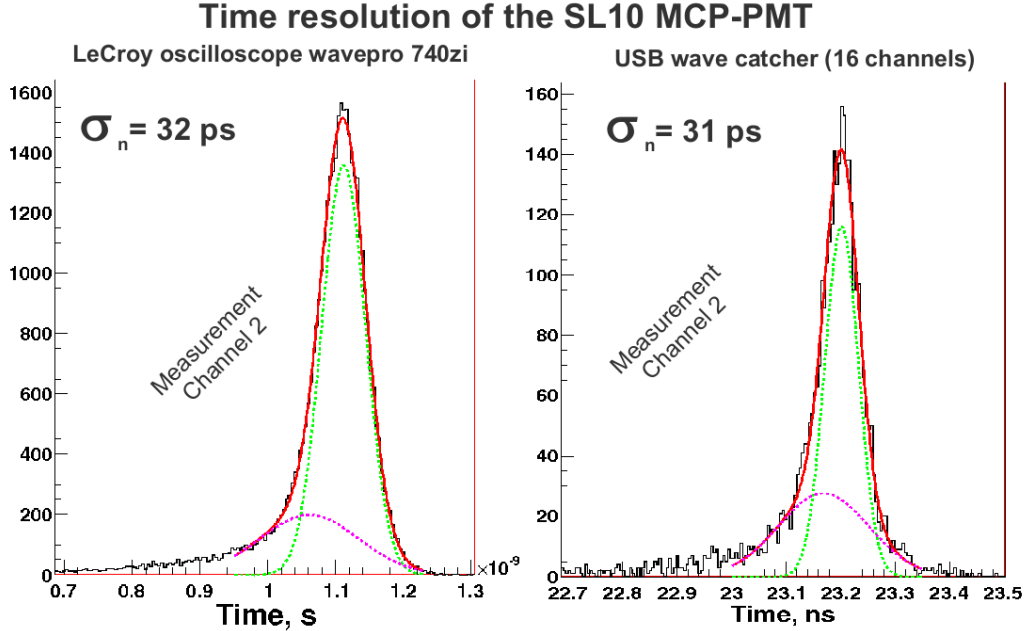


Figure 6.9: The black histogram corresponds to the time difference between signal from channel 2 of the SL10 MCP-PMT and the laser trigger. The measurements done with LeCroy oscilloscope(16-channel USBWC) is shown on the left(right). The timing histogram has been fitted with sum of two Gaussian (wide and narrow). The green dashed curve corresponds to a narrow Gaussian, magenta dashed curve represents wide Gaussian and red solid line is their sum. One can see that the RMS of the narrow components for both measurements is around 32 ps.

Table 6.3: Characteristics of the tested SiPMs

Producer	Ref. SiPM	pixel size ( $\mu\text{m}$ )	$V_{BD}$ , V at 20°C
AdvanSid	ASD-SiPM1S-M-50	$50 \times 50$	29
HAMAMATSU	S10262-11-25	$25 \times 25$	69.2
HAMAMATSU	S10262-11-50	$50 \times 50$	68.3
HAMAMATSU	S10262-11-100	$100 \times 100$	68.7
HAMAMATSU	10-50S-BK-4S	$50 \times 50$	69.1
HAMAMATSU	10-100S-FS	$100 \times 100$	69.1
Sensl	SPM1020X13	$20 \times 20$	27

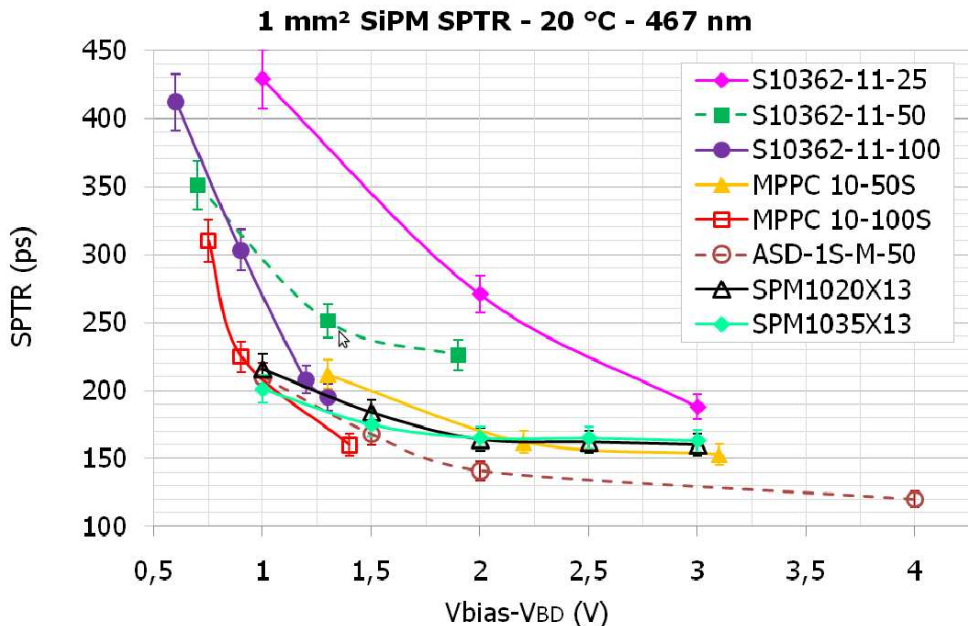


Figure 6.10: Time resolution (FWHM) for different SiPM as a function of over voltage. One can see that the S PTR decreases with increasing of over voltage.

## 6.4 Conclusions

We performed studies of the timing properties of the different photodetectors, which can be used for the DIRC-like TOF detector.

The ASD-SiPM1S-M-50 SiPM has 64 ps time resolution (for a single photon), which is good enough for the DIRC-like TOF detector. However, the high neutron flux, which is estimated to be  $10^{11} \text{ cm}^{-2}$  per year makes impossible to use that device and SiPM in general since it dramatically increases their dark count rate.

The Burle MCP-PMT shows a good time resolution (50 ps), but its total acceptable integrated anode charge is around (0.3 C) which 10 times less then what is needed in *SuperB*.

The Hamamatsu SL-10 MCP-PMT has the best time resolution that we had been measured ( $\sim 37$  ps for single photon) in addition its life time match the needs of the *SuperB* ( $\sim 3$  C) which makes SL10 the best candidate for the DIRC-like TOF detector.



# Chapter 7

## Conclusions

Research and development activities on an innovative particle identification detector, named DIRC-like TOF and designed for the *SuperB* experiment, are presented in this PhD thesis. The optimal geometry for this device has been selected using a full Geant4-based simulation and by taking into account the constraints associated with the integration of the DIRC-like TOF in the *SuperB* detector: mechanical integration in a limited space on the forward side, background levels, etc. In addition, its time resolution has been estimated by identifying the main contributions to this quantity and by computing them separately. These studies are summarized in Table 7.1: a 30 ps time resolution per track can be achieved, allowing a  $\pi/K$  separation up to 3 GeV/c given the 2 m flight path of the particles in the *SuperB* configuration.

Table 7.1: Main contributions to the total time resolution of the DIRC-like TOF.

Quantity	value
$\sigma_{\text{electronics}}$	10 ps
$\sigma_{\text{TTS}}$	40 ps per photo electron
$\sigma_{\text{detector}}$	80 ps
$\sigma_{\text{trk}}$	10 ps
$\sigma_{t0}$	20 ps
$N_{\text{p.e.}}$	>10 photo electrons per track
<b>Total time resolution per track</b>	<40 ps

Different types of background and their effect on the DIRC-like TOF performances have been studied using a full simulation of the *SuperB* interaction region which includes the detector. The optical properties of the DIRC-like TOF radiator volume has not been implemented yet in the global simulation framework. Therefore, a standalone Geant4-based code was developed and used to simulate this key step, using as input the data of the particles reaching the DIRC-like TOF envelope in the *SuperB* simulation.

We find that radiative Bhabha processes dominate the DIRC-like TOF background:

the corresponding estimated rate per MCP-PMT channel is  $\sim 0.5$  MHz. This high background rate is not expected to impact much the particle identification performances of the detector; however, it limits the lifetime of the baseline photon detectors – see below – which suffer from aging effect when their integrated charge exceeds  $\sim 2.5$  C/cm<sup>2</sup>. One way to reduce this background (coming mainly from a well-localized area of the beampipe) would be to make the tungsten shield around the beam pipe thicker. Another way would be to change the field configuration in the interaction region. Both possibilities (among others) will have to be studied to find a way to mitigate this background. Another key result of the background studies is that the neutron flux thought the DIRC-like TOF photon detector and its front end electronics is  $10^{11}$  cm<sup>-2</sup> per year, which makes impossible the use of silicon photomultipliers (SiPM) which would be destroyed rapidly by this harsh environment.

Based on the studies presented in this thesis, the HAMAMATSU SL-10 MCP-PMT has been defined as the baseline photon detector for the DIRC-like TOF. One such device with 4 channels has been characterized in a dedicated test bunch at LAL. A time resolution of about 37 ps has been measured using a Wavepro 750ZI LeCroy digital oscilloscope and the new 16-channel USB WaveCatcher electronics which has been developed by LAL (CNRS/IN2P3) and CEA/IRFU (with a time resolution of about 10 ps per channel). A future version of these electronics will likely equip the DIRC-like TOF front-end crates. In addition, the timing of other photon detectors – a XP85012 MCP-PMT from Planacon and various  $1 \times 1$  mm<sup>2</sup> SiPM – has been studied. All of them have worse timing resolution and lifetime than the SL-10.

To confirm the simulation results, the DIRC-like TOF technique has been tested on a prototype, built and installed in the SLAC Cosmic Ray Telescope. A time resolution of about 70 ps per photo electron has been obtained. The good agreement between measurements and simulation shows that we understand the prototype well and that we do not miss any significant contribution to the timing resolution. This makes us confident that our full simulation of the *SuperB* DIRC-like TOF (which uses the same tools: physics and material properties) provides access to the main characteristics of this device.

# Bibliography

- [1] M. Kobayashi and T. Maskawa, “CP Violation in the Renormalizable Theory of Weak Interaction”, *Prog. Theor. Phys.* **49** (1973) 652–657.
- [2] N. Cabibbo, “Unitary Symmetry and Leptonic Decays”, *Phys. Rev. Lett.* **10** (1963) 531–533.
- [3] L. Wolfenstein, “Parametrization of the Kobayashi-Maskawa Matrix”, *Phys. Rev. Lett.* **51** (1983) 1945.
- [4] C. Amsler, M. Doser, M. Antonelli, D. Asner, K. Babu, H. Baer, H. Band, R. Barnett, E. Bergren, J. Beringer, *et al.*, “Review of particle physics”, *Physics Letters B* **667** (2008) no. 1-5, 1–6.
- [5] D. Derkach, “Mesure de l’angle gamma du triangle d’unitarité avec le détecteur *BABAR*”, *PhD thesis* (2010) .
- [6] V. Niess, “Global fit to ckm data”, July, 2011. EPS HEP 11, 2011, Grenoble, France.
- [7] **SuperB** Collaboration, M. Bona *et al.*, “SuperB: A High-Luminosity Asymmetric  $e^+e^-$  Super Flavor Factory. Conceptual Design Report”, [arXiv:0709.0451 \[hep-ex\]](https://arxiv.org/abs/0709.0451).
- [8] J. Seeman, “Pep-2 status and plans”, in *Particle Accelerator Conference, 1995., Proceedings of the 1995*, vol. 1, pp. 486–490, IEEE. 1995.
- [9] S. Kurokawa and E. Kikutani, “Overview of the kekb accelerators”, *Nuclear Instruments and Methods in Physics Research Section A: Accelerators, Spectrometers, Detectors and Associated Equipment* **499** (2003) no. 1, 1–7.
- [10] M. Zobov, D. Alesini, M. Biagini, C. Biscari, A. Bocci, R. Boni, M. Boscolo, F. Bossi, B. Buonomo, A. Clozza, *et al.*, “Test of ”crab-waist” collisions at the da $\phi$ ne  $\phi$  factory”, *Physical Review Letters* **104** (2010) no. 17, 174801.
- [11] K. Hirata, “Analysis of beam-beam interactions with a large crossing angle”, *Physical Review Letters* **74** (1995) no. 12, 2228–2231.

- [12] **SuperB** Collaboration, E. Grauges, F. Forti, B. Ratcliff, and D. Aston, “Superb progress reports–detector”, [arXiv:1007.4241v1](https://arxiv.org/abs/1007.4241v1).
- [13] B. Auberta *et al.*, “The babar detector”, *Nuclear Instruments and Methods in Physics Research A* **479** (2002) 1–116.
- [14] I. Nakamura, “Belle electromagnetic calorimeter and its belle2 upgrade”, in *Journal of Physics: Conference Series*, vol. 160, p. 012003, IOP Publishing. 2009.
- [15] P. Milenovic, J. Puzovic, D. Jovanovic, D. Maletic, G. Dissertori, and P. Adzic, “Performance of the cms ecal safety system for super modules sm0 and sm1”, *Nuclear Instruments and Methods in Physics Research Section A: Accelerators, Spectrometers, Detectors and Associated Equipment* **554** (2005) no. 1, 427–436.
- [16] P. Coyle, H. Kawahara, A. Lu, G. Lynch, G. Mueller, D. Muller, B. Ratcliff, and C. Simopoulos, “The dirc counter: a new type of particle identification device for b factories”, *Nuclear Instruments and Methods in Physics Research Section A: Accelerators, Spectrometers, Detectors and Associated Equipment* **343** (1994) no. 1, 292–299.
- [17] J. Vavra, “Focusing dirc design for superb”, tech. rep., SLAC-PUB-13763, 2009., and LDRD proposal, SLAC, 4.20, 2009.
- [18] R. Andreassen, N. Arnaud, D. Brown, L. Burmistrov, J. Carlson, C. Cheng, A. Di Simone, I. Gaponenko, E. Manoni, A. Perez, *et al.*, “Fastsim: Fast simulation of the superb detector”, in *Nuclear Science Symposium Conference Record (NSS/MIC), 2010 IEEE*, pp. 322–326, IEEE. 2010.
- [19] I. Adam *et al.*, “Dirc, the internally reflecting ring imaging cherenkov detector for babar”, *Nuclear Science, IEEE Transactions on* **45** (1998) no. 3, 657–664.
- [20] J. Schwiening *et al.*, “Performance of the babar-dirc”, *Nuclear Instruments and Methods in Physics Research Section A: Accelerators, Spectrometers, Detectors and Associated Equipment* **553** (2005) no. 1-2, 317–322.
- [21] C. Field, T. Hadig, M. Jain, D. Leith, G. Mazaheri, B. Ratcliff, J. Schwiening, and J. Va’vra, “Novel photon detectors for focusing dirc prototype”, *Nuclear Instruments and Methods in Physics Research Section A: Accelerators, Spectrometers, Detectors and Associated Equipment* **518** (2004) no. 1-2, 565–568.
- [22] J. Benitez, D. Leith, G. Mazaheri, B. Ratcliff, J. Schwiening, J. Va’vra, L. Ruckman, and G. Varner, “Status of the fast focusing dirc (fdirc)”, *Nuclear Instruments and Methods in Physics Research Section A: Accelerators, Spectrometers, Detectors and Associated Equipment* **595** (2008) no. 1, 104–107.
- [23] K. Inami *et al.*, “Cross-talk suppressed multi-anode MCP-PMT”, *Nucl. Instrum. Meth. A* **592** (2008) 247–253, [arXiv:0803.0594 \[physics.ins-det\]](https://arxiv.org/abs/0803.0594).

- [24] **GEANT4** Collaboration, S. Agostinelli *et al.*, “GEANT4: A simulation toolkit”, *Nucl. Instrum. Meth.* **A506** (2003) 250–303.
- [25] <http://geant4.web.cern.ch/geant4>.
- [26] E. I. Manaev, *General radio electronics*. Radio and Communication, Moscow.
- [27] D. V. Sivuhin, *General course of physics. Optics*. Nauka, Moscow.
- [28] Dispersion is the phenomenon in which the phase velocity of a wave depends on its frequency.
- [29] D. Brown, E. Charles, and D. Roberts, “The babar track fitting algorithm”, in *Proceedings of CHEP, 2000*.
- [30] F. Martinez-Vidal *et al.*, “The babar vertexing”, *BABAR Analysis Document* **102** (2001) .
- [31] M. Rama, “Look at the track hit efficiency and de/dx of the babardrift chamber”, May, 2010. <http://agenda.infn.it/getFile.py/access?contribId=57&sessionId=3&resId=0&materialId=slides&confId=2262>. XIII *SuperB* General Meeting - Isola d’Elba.
- [32] M. Rama, “Tracking and de/dx vs dch length”, December, 2009. <http://agenda.infn.it/getFile.py/access?contribId=133&sessionId=19&resId=0&materialId=slides&confId=1165>. XI *SuperB* General Meeting - LNF.
- [33] S. Kononov, “Status of farich”, May, 2010. <http://agenda.infn.it/getFile.py/access?contribId=9&sessionId=4&resId=0&materialId=slides&confId=2262>. XIII *SuperB* PID meeting, Isola d’Elba.
- [34] E. Kravchenko, “Test beam results on focusing aerogel”, May, 2011. <http://agenda.infn.it/getFile.py/access?contribId=77&sessionId=14&resId=0&materialId=slides&confId=3352>. XVII *SuperB* Workshop and Kick Off Meeting - La Biodola (Isola d’Elba) Italy.
- [35] J. Hubbell, H. Gimm, and I. Øverbø, “Pair, triplet, and total atomic cross sections (and mass attenuation coefficients) for 1 mev-100 gev photons in elements z= 1 to 100”, *Journal of physical and chemical reference data* **9** (1980) 1023.
- [36] J. Butcher and H. Messel, “Electron number distribution in electron-photon showers in air and aluminium absorbers”, *Nuclear Physics* **20** (1960) 15–128.
- [37] E. Storm and H. Israel, “Photon cross sections from 1 kev to 100 mev for elements z= 1 to z= 100.”, tech. rep., Los Alamos Scientific Lab., N. Mex., 1970.

- [38] O. Klein and T. Nishina, “Über die streuung von strahlung durch freie elektronen nach der neuen relativistischen quantendynamik von dirac”, *Zeitschrift fur Physik A Hadrons and Nuclei* **52** (1929) no. 11, 853–868.
- [39] M. Gavrila, “Relativistic k-shell photoeffect”, *Physical Review* **113** (1959) no. 2, 514.
- [40] F. Biggs and R. Lighthill *Preprint Sandia Laboratory* **113** (1990) no. 87, 0070.
- [41] V. Grichine, A. Kostin, S. Kotelnikov, et al. *Bulletin of the Lebedev Institute* (1994) no. 2–3, 34.
- [42] R. Sternheimer and R. Peierls, “General expression for the density effect for the ionization loss of charged particles”, *Physical Review B* **3** (1971) no. 11, 3681.
- [43] H. Messel and D. Crawford, “Electron photon shower distribution function, tables for lead, copper, and air absorbers”, *1970* .
- [44] S. Kelner, R. Kokoulin, and A. Petrukhin, “Bremsstrahlung from muons scattered by atomic electrons”, *Physics of Atomic Nuclei* **60** (1997) 576–583.
- [45] L. Urban, “A multiple scattering model in geant4”, *Preprint CERNOPEN-2006-077, Dec* (2006) .
- [46] H. Lewis, “Multiple scattering in an infinite medium”, *Physical review* **78** (1950) no. 5, 526.
- [47] J. Fernández-Varea, R. Mayol, J. Baró, and F. Salvat, “On the theory and simulation of multiple elastic scattering of electrons”, *Nuclear Instruments and Methods in Physics Research Section B: Beam Interactions with Materials and Atoms* **73** (1993) no. 4, 447–473.
- [48] I. Kawrakow and A. Bielajew, “On the condensed history technique for electron transport”, *Nuclear Instruments and Methods in Physics Research Section B: Beam Interactions with Materials and Atoms* **142** (1998) no. 3, 253–280.
- [49] S. Perkins, D. Cullen, and S. Seltzer, “Tables and graphs of electron-interaction cross sections from 10 ev to 100 gev derived from the llnl evaluated electron data library (eedl), z= 1–100”, tech. rep., Lawrence Livermore National Lab., CA (United States), 1991.
- [50] R. Ford and W. Nelson, 1985. SLAC-265.
- [51] V. Ivanchenko, S. Giani, M. Pia, L. Urban, S. Nieminen, and G. Mancinelli, “Geant4 simulation of energy losses of slow hadrons”, *CERN-99-121, INFN/AE-99/20* (1999) .

- [52] “Geant4 Physics Reference Manual.”  
<http://geant4.cern.ch/G4UsersDocuments/UsersGuides/PhysicsReferenceManual/html/PhysicsReferenceManual.html>.
- [53] P. Čerenkov, “Visible radiation produced by electrons moving in a medium with velocities exceeding that of light”, *Physical Review* **52** (1937) no. 4, 378.
- [54] C. Grupen and B. Shwartz, *Particle detectors*, vol. 26. Cambridge Univ Pr, 2008.
- [55] S. G. Manufacturers, “Tie-29: Refractive index and dispersion”, January, 2007.  
[http://www.us.schott.com/advanced\\_optics/english/download/schott\\_tie-29\\_refractive\\_index\\_v3\\_jan\\_2007\\_us.pdf](http://www.us.schott.com/advanced_optics/english/download/schott_tie-29_refractive_index_v3_jan_2007_us.pdf). TECHNICAL INFORMATION.
- [56] J. Cohen-Tanugi, M. Convery, B. Ratcliff, X. Sarazin, J. Schwiening, and J. Va’vra, “Optical properties of the dirc fused silica cherenkov radiator”, *Nuclear Instruments and Methods in Physics Research Section A: Accelerators, Spectrometers, Detectors and Associated Equipment* **515** (2003) no. 3, 680–700.
- [57] “Hamamatsu photonics, photomultiplier tube”, December, 2006. [http://sales.hamamatsu.com/assets/applications/ETD/pmt\\_handbook\\_complete.pdf](http://sales.hamamatsu.com/assets/applications/ETD/pmt_handbook_complete.pdf). hamamatsu PMT handbook.
- [58] M. Charles, R. Forty, *et al.*, “Torch: Time of flight identification with cherenkov radiation”, *Nuclear Instruments and Methods in Physics Research Section A: Accelerators, Spectrometers, Detectors and Associated Equipment* (2010) .
- [59] R. Forty and M. Charles, “Torch: a novel time-of-flight detector concept”, *CERN-LHCb-PUB-2009-030* .
- [60] T. Gys, “R and d status for the lhcb torch project”, *Journal of Instrumentation* **6** (2011) C10004.
- [61] A. Otte, J. Barral, B. Dolgoshein, J. Hose, S. Klemin, E. Lorenz, R. Mirzoyan, E. Popova, and M. Teshima, “A test of silicon photomultipliers as readout for pet”, *Nuclear Instruments and Methods in Physics Research Section A: Accelerators, Spectrometers, Detectors and Associated Equipment* **545** (2005) no. 3, 705–715.
- [62] F. Dal Corso, G. Simi, and R. Stroili, “Quick report on silicon g-apds (a.k.a. si-pm) studies”, September, 2010. <http://agenda.infn.it/getFile.py/access?contribId=107&sessionId=7&resId=3&materialId=slides&confId=2303>. XIV SuperB General Meeting - LNF.
- [63] L. Burmistrov, “Progress on full simulation of the forward dirc-like tof detector”, March, 2010. <http://agenda.infn.it/getFile.py/access?contribId=86&sessionId=67&resId=0&materialId=slides&confId=2026>. XII SuperB General Meeting - LAPP - Annecy.

- [64] S. Germani, “Fwd pid effects on emc”, May, 2011.  
<http://agenda.infn.it/getFile.py/access?contribId=108&sessionId=40&resId=0&materialId=slides&confId=3352>. XVII *SuperB* Workshop and Kick Off Meeting - La Biodola (Isola d’Elba) Italy.
- [65] F. Bogard and S. Wallon, “Superb fpid mechanical design & integration”, Juin, 2010. <http://agenda.infn.it/getFile.py/access?contribId=228&sessionId=44&resId=0&materialId=slides&confId=2262>. XIII *SuperB* General Meeting - Isola d’Elba.
- [66] D. Breton, E. Delagnes, and J. Maalmi, “Picosecond time measurement using ultra fast analog memories”, *Topical Workshop on Electronics for Particle Physics (TWEPP-09), Paris : France (2009)* .
- [67] D. Breton, E. Delagnes, J. Maalmi, K. Nishimura, L. Ruckman, G. Varner, and J. Va’Vra, “High resolution photon timing with mcp-pmts: A comparison of a commercial constant fraction discriminator (cfd) with the asic-based waveform digitizers target and wavecatcher”, *Nuclear Instruments and Methods in Physics Research Section A: Accelerators, Spectrometers, Detectors and Associated Equipment* **629** (2010) 123–132.
- [68] F. Halzen and A. Martin, *Quark and Leptons: An introductory Course in Modern Particle Physics*. Wiley-India, 2008.
- [69] M. Peskin and D. Schroeder, “Quantum field theory”, *The Advanced Book Program, Perseus Books Reading, Massachusetts* (1995) .
- [70] C. Bernardini, G. Corazza, G. Di Giugno, G. Ghigo, J. Haissinski, P. Marin, R. Querzoli, and B. Touschek, “Lifetime and beam size in a storage ring”, *Physical Review Letters* **10** (1963) no. 9, 407–409.
- [71] M. Boscolo, M. Antonelli, and S. Guiducci, “Simulations and measurements of the touschek background at daφne”, *EPAC02, Paris, France* (2002) .
- [72] F. Zimmermann and M. Zorzano, “Touschek scattering in hera and lhc”, *LHC Project Note* **244** (2000) .
- [73] S. Møller, “Beam residual gas interactions”, *CERN EUROPEAN ORGANIZATION FOR NUCLEAR RESEARCH-REPORTS-CERN* (1999) 155–164.
- [74] G. Montagna, M. Moretti, O. Nicrosini, A. Pallavicini, and F. Piccinini, “Light pair correction to bhabha scattering at small angle”, *Nuclear Physics B* **547** (1999) no. 1-2, 39–59.
- [75] R. Chytracek, J. McCormick, W. Pokorski, and G. Santin, “Geometry description markup language for physics simulation and analysis applications”, *Nuclear Science, IEEE Transactions on* **53** (2006) no. 5, 2892–2896.

- [76] R. Brun and F. Rademakers, “Root—an object oriented data analysis framework”, *Nuclear Instruments and Methods in Physics Research Section A: Accelerators, Spectrometers, Detectors and Associated Equipment* **389** (1997) no. 1-2, 81–86.
- [77] T. Bray, J. Paoli, C. Sperberg-McQueen, E. Maler, F. Yergeau, *et al.*, “Extensible markup language (xml) 1.0”, 2000.
- [78] V. Ezhela, S. Lugovsky, and O. Zenin, “Hadronic part of the muon g-2 estimated on the  $\sigma_{2003}^{total}$  ( $e^+e^- \rightarrow$ hadrons) evaluated data compilation”, *Arxiv preprint hep-ph/0312114* (2003) .
- [79] C. Caso *et al.*, “Particle data group”, *Eur. Phys. J. C* **3** .
- [80] H. Quinn *et al.*, “Babar physics book”, tech. rep., Stanford Linear Accelerator Center, Menlo Park, CA (US), 1998.
- [81] A. Stocchi private communication.
- [82] E. Paoloni, “Luminosity backgrounds”, February, 2009.  
<http://agenda.infn.it/getFile.py/access?contribId=24&sessionId=5&resId=0&materialId=slides&confId=959>. VIII SuperB General Meeting - Orsay.
- [83] G. Altarelli and F. Buccella *Nuovo Cimento* **34,6385** (1964) .
- [84] H. Burkhardt and J. Poole, “Proceedings of the third Workshop on LEP Performance’ CERN SL/93-19 (DI).”.
- [85] R. Kleiss and H. Burkhardt, “Bbbrem–monte carlo simulation of radiative bhabha scattering in the very forward direction”, *Computer physics communications* **81** (1994) no. 3, 372–380.
- [86] T. Jinno, T. Mori, T. Ohshima, Y. Arita, K. Inami, T. Ihara, H. Nishizawa, and T. Sasaki, “Lifetime-extended mcp-pmt”, *Nuclear Instruments and Methods in Physics Research Section A: Accelerators, Spectrometers, Detectors and Associated Equipment* **629** (2011) 111–117.
- [87] W. Myers, W. Swiatecki, T. Kodama, L. El-Jaick, and E. Hilf, “Droplet model of the giant dipole resonance”, *Physical Review C* **15** (1977) no. 6, 2032.
- [88] This methode has been proposed by J. Va’vra as well as the equation.
- [89] J. LeDuff, (1987). 2nd Advanced Accel. Physics Course, Berlin, F.R. Germany.
- [90] H. Bruck, “Circular particle accelerators”, (1966) .
- [91] M. Enrica Biagini, P. Raimondi, and J. Seeman, “Superb progress reports–accelerator”, [arXiv:1009.6178](https://arxiv.org/abs/1009.6178).

- [92] M. Boscolo, M. Biagini, P. Raimondi, M. Sullivan, and E. Paoloni, “Touschek background and lifetime studies for the superb factory”, *TH6PFP060, proceedings* .
- [93] I. Nakamura, “Radiation damage of pixelated photon detector by neutron irradiation”, *Nuclear Instruments and Methods in Physics Research Section A: Accelerators, Spectrometers, Detectors and Associated Equipment* **610** (2009) no. 1, 110–113.
- [94] C. A. Milardi *et al.*, “Experience with daφne upgrade including crab waist”, *Particle Accelerator Conference, Canada, 2009* (2009) .
- [95] M. Boscolo *et al.*, “Detectors for absolute luminosity measurement at daφne”, *Nuclear Instruments and Methods in Physics Research Section A: Accelerators, Spectrometers, Detectors and Associated Equipment* **617** (2010) no. 1-3, 453–456.
- [96] M. Boscolo *et al.*, “Luminosity and background measurements at the  $e^+ e^-$  daφne collider upgraded with the crab waist scheme”, *Nuclear Instruments and Methods in Physics Research Section A: Accelerators, Spectrometers, Detectors and Associated Equipment* **621** (2010) no. 1-3, 121–129.
- [97] M. Cargnelli *et al.*, “Kaonic atoms studies at daφne by the siddharta experiment”, *Nuclear Physics A* **835** (2010) no. 1-4, 27–34.
- [98] J. Va’vra, “Slac cosmic ray telescope facility”, January, 2010.  
<http://www.slac.stanford.edu/pubs/slacpubs/13750/slac-pub-13873.pdf>.  
SLAC-PUB-13873.
- [99] J. Va’vra, “A pixilated tof with lyso crystals”, March, 2010.  
<http://agenda.infn.it/getFile.py/access?contribId=91&sessionId=67&resId=0&materialId=slides&confId=2026>. XII *SuperB* General Meeting - LAPP - Annecy.
- [100] J. Va’vra, “Tof counter tests in crt”, September, 2010.  
<http://agenda.infn.it/getFile.py/access?contribId=91&sessionId=2&resId=0&materialId=slides&confId=2303>. XIV *SuperB* General Meeting - LNF.
- [101] J. Va’vra, “Pid summary”, September, 2010.  
<http://agenda.infn.it/getFile.py/access?contribId=9&sessionId=48&resId=0&materialId=slides&confId=2303>. XIV *SuperB* General Meeting - LNF.
- [102] J. Va’vra, “Tof with lyso + g-apd”, April, 2011.  
<http://agenda.infn.it/getFile.py/access?contribId=16&sessionId=8&resId=0&materialId=slides&confId=3410>. XVI *SuperB* Workshop (LNF).

- [103] J. Va'vra, L. Ruckman, K. Nishimura, G. Varner, D. Aston, D. Leith, and B. Ratcliff, "The focusing dirc with waveform digitizing electronics", *Proceedings of the TIPP09 International Conference, 2009* .
- [104] J. Benitez, I. Bedajnek, D. Leith, G. Mazaheri, B. Ratcliff, K. Suzuki, J. Schwiening, J. Uher, and J. Va'vra, "Development of a focusing dirc", November, 2006.  
<http://www.slac.stanford.edu/cgi-wrap/getdoc/slac-pub-12236.pdf>.  
 SLAC-PUB-12236, IEEE Nucl.Sci, Conference records, October 29.
- [105] J. Va'vra, J. Benitez, D. Leith, G. Mazaheri, B. Ratcliff, J. Schwiening, and K. Suzuki, "The focusing dirc the first rich detector to correct the chromatic error by timing, and the development of a new tof detector concept", September, 2007.  
<http://www.slac.stanford.edu/cgi-wrap/getdoc/slac-pub-12803.pdf>.  
 SLAC-PUB-12803, presented at Vienna conference on Instrumentation, Feb. 2007.
- [106] J. Hill, "Results from the k2k long–baseline neutrino oscillation experiment", *Arxiv preprint hep-ex/0110034* (2001) .
- [107] MITEQ, "Amplifier model: Am-1610-1000", October.
- [108] Mini-Circuits, "Coaxial low pass filter vlf-530", April, 2006.  
<http://www.chipfind.ru/datasheet/mini/vlf530.htm>. Datasheet.
- [109] D. Breton and E. Delagnes, "Ongoing r&d in orsay/saclay on ps time measurement: a usb-powered 2-channel 3.2 gs/s 12-bit digitizer", February, 2009.  
<http://agenda.infn.it/getFile.py/access?contribId=130&sessionId=6&resId=0&materialId=slides&confId=959>. VIII *SuperB* General Meeting - Orsay.
- [110] D. Breton, J. Maalmi, and E. Delagnes, "Picosecond time measurement using ultra fast analog memories: new results since orsay workshop", October, 2009.  
<http://agenda.infn.it/getFile.py/access?contribId=196&sessionId=33&resId=0&materialId=slides&confId=1742>. X *SuperB* General Meeting - SLAC.
- [111] D. Breton, J. Maalmi, E. Delagnes, and J. Va'vra, "Picosecond time measurement using ultra fast analog memories: new results since slac workshop", December, 2009. <http://agenda.infn.it/getFile.py/access?contribId=92&sessionId=23&resId=0&materialId=slides&confId=1165>. XI *SuperB* General Meeting - LNF.
- [112] D. Breton, L. Burmistov, and J. Maalmi, "Update of time measurement results with the usb wavecatcher board & electronics for the dirc-like tof prototype at slac", May, 2010. <http://agenda.infn.it/getFile.py/access?contribId=32&sessionId=9&resId=0&materialId=slides&confId=2262>. XIII *SuperB* General Meeting - Isola d'Elba.

- [113] D. Breton and J. Maalmi, “Electronics for the two-bar test”, September, 2010. <http://agenda.infn.it/getFile.py/access?contribId=92&sessionId=2&resId=0&materialId=slides&confId=2303>. XIV *SuperB* General Meeting - LNF.
- [114] D. Breton, L. Burmistrov, J. Maalmi, and V. Puill, “Mcp-pmt test bench at lal”, December, 2010. <http://agenda.infn.it/materialDisplay.py?contribId=127&sessionId=21&materialId=slides&confId=2902>. XV *SuperB* General Meeting - Caltech.
- [115] E. Delagnes, Y. Degerli, P. Goret, P. Nayman, F. Toussenel, and P. Vincent, “Sam: A new giga hz sampling asic for the hess-ii front-end electronics”, *Nuclear Instruments and Methods in Physics Research Section A: Accelerators, Spectrometers, Detectors and Associated Equipment* **567** (2006) no. 1, 21–26.
- [116] “Dropbox”, September, 2010. <https://www.dropbox.com/>. Free software.
- [117] P. Grieder, “Cosmic rays at earth”, *Cosmic Rays at Earth by PKF Grieder. Elsevier Science, 2001*. **1** (2001) .
- [118] “Network Time Protocol”, August, 2011. [http://en.wikipedia.org/wiki/Network\\_Time\\_Protocol](http://en.wikipedia.org/wiki/Network_Time_Protocol).
- [119] E. Lorenz, S. Natkaniec, D. Renker, and B. Schwartz, “Fast readout of plastic and crystal scintillators by avalanche photodiodes”, *Nuclear Instruments and Methods in Physics Research Section A: Accelerators, Spectrometers, Detectors and Associated Equipment* **344** (1994) no. 1, 64–72.
- [120] V. Puill, C. Bazin, D. Breton, L. Burmistrov, V. Chaumat, N. Dinu, J. Maalmi, J. Vagnucci, and A. Stocchi, “Single photoelectron timing resolution of sipm as a function of the bias voltage, the wavelength and the temperature”, *Nuclear Physics A Conference Proceedings (NDIP 2011)* (2011) .
- [121] N. P. Buslenko, *Monte-Carlo methods*. Fizmat, Moscow, 1962.
- [122] I. M. Sobol, *Monte-Carlo methods*. Fizmat, Moscow, 1978.

# Chapter 8

## Likelihood based particle selector

Any kind of detectors perform measurement of the given quality with some error. For example: the TOF detector measure the time with some precision due to this the PID would have some identification efficiency (when particle determined correctly) and miss identification probability (when particle wrongly determined). Intuitively one can say that if the purity of the selected particle sample is very hight which mean that number of wrongly determined particles is low the efficiency of the identification is low too. And vice versa: if the purity is low which mean that miss identification is high the identification is hight. In case of different physical analysis higher purity or higher identification efficiency needed. It would be very convenient to construct out of measured qualities variable which will define purity and efficiency of the selected particle sample. In **Likelihood** based selector this variable can be likelihood ratio  $R_{LH}$  defined by this equation:

$$R_{LH} = \frac{LH_1}{LH_1 + LH_2} = \frac{1}{1 + \frac{LH_2}{LH_1}} \quad (8.1)$$

Where  $LH_1$  and  $LH_2$  - likelihoods of the hypothesis (1) and (2) respectively.

Lets consider an example where probability density function (PDF) of the measurements are Gaussian. In such particular case the likelihood can be written like this:

$$LH = \frac{1}{\sigma\sqrt{2\pi}} \exp\left(-\frac{(t - t_{exp}(P, L, m, \{x, y, \phi, \theta\}_{int}))^2}{2\sigma^2}\right) \quad (8.2)$$

Where  $t$  - measured time,  $t_{exp}(P, L, m, \{x, y, \phi, \theta\}_{int})$  - expected time,  $\sigma$  - standard deviation (error of the  $(t - t_{exp})$  variable) in case of the FTOF  $\sigma$  defined by this equation (3.7). The expected time ( $t_{exp}$ ) is a function of the momentum, flight length, mass of the particle and track intersection position and angles with FTOF ( $\{x, y, \phi, \theta\}_{int}$ ). In order to keep precision of the  $t_{exp}$  in acceptable level one have to perform good track parameter reconstruction.

Likelihood distribution for two different observable separated apart by  $3\sigma$  depicted in the Figure 8.1. For convenience we centered at 0 and 3 the  $LH_1$  and  $LH_2$  respectively.

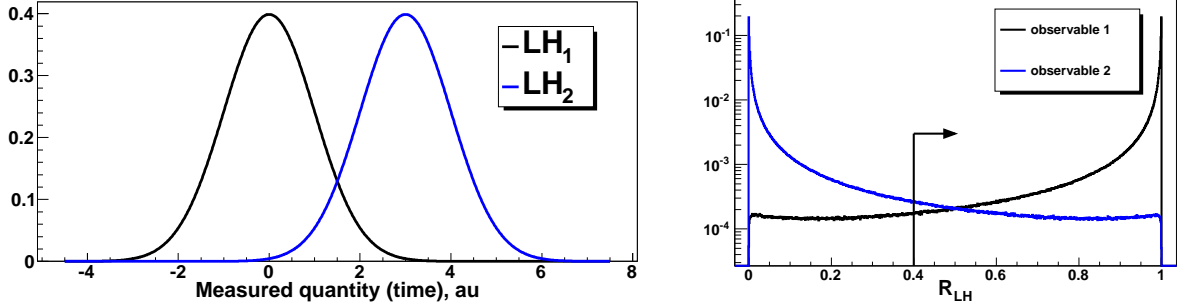


Figure 8.1: (Left) Likelihood distribution for two different observable separated apart by  $3\sigma$ . For convenience we centered at 0 and 3 the  $LH_1$  and  $LH_2$  respectively,  $\sigma = 1$ . (Right) Distribution of the Gaussian likelihood ratios  $R_{LH}$  for different observable.

Their normalized distribution likelihood ratios  $R_{LH}$  can be seen in the Figure 8.1. By cutting on this variable ( $R_{LH} > R_{cut}$ ) different efficiencies of the signal and background can be obtained. Using the one-to-one correspondence between  $R_{LH}$  and measured quantity  $t$  the correct identification efficiency (ID)  $\epsilon$  and miss identification probability (mis-ID)  $\eta$  can be calculated:

$$\epsilon = \int_{-\infty}^{t(R_{cut})} LH_1(t) dt \quad (8.3)$$

$$\eta = \int_{-\infty}^{t(R_{cut})} LH_2(t) dt \quad (8.4)$$

Where  $t(R_{cut})$  can be evaluated using this formula:

$$t(R_{cut}) = \frac{1}{k} \ln \left( \frac{1 - R_{cut}}{R_{cut}} + \frac{k}{2} \right) \quad (8.5)$$

One can see that integrals (8.3), (8.4) can be expressed via complementary error function, denoted \$\text{erfc}\$, using this and (8.5) the relevant equations are:

$$\epsilon = \frac{1}{2} \text{erfc} \left[ -\frac{1}{2\sqrt{2}} \left( k + \frac{2\lambda}{k} \right) \right] \quad (8.6)$$

$$\eta = \frac{1}{2} \text{erfc} \left[ \frac{1}{2\sqrt{2}} \left( k - \frac{2\lambda}{k} \right) \right] \quad (8.7)$$

Where  $\lambda$  defined like this:

$$\lambda = \ln \left( \frac{1 - R_{cut}}{R_{cut}} \right) \Leftrightarrow R_{cut} = \frac{1}{1 + e^\lambda} \quad (8.8)$$

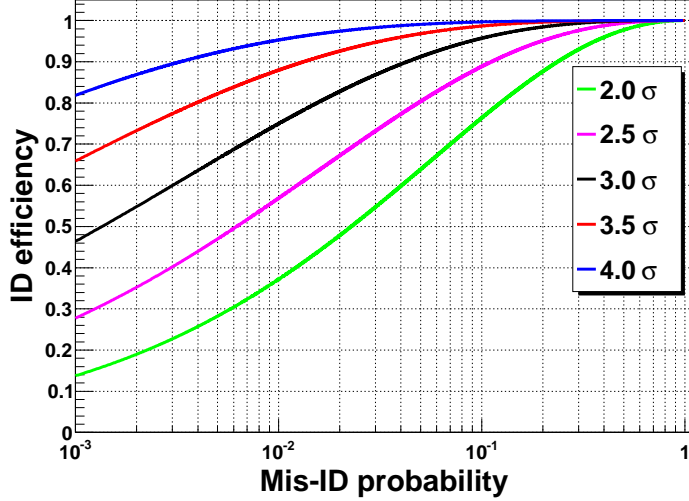


Figure 8.2: ID efficiency versus Mis-ID probability for different ' $\sigma$ ' separation.

There is a one-to-one correspondence between  $(\epsilon, \eta)$  and  $(k, R_{cut})$ :

$$k = \sqrt{2} [\operatorname{erfc}^{-1}(2\eta) - \operatorname{erfc}^{-1}(2\epsilon)] \quad (8.9)$$

$$\lambda = [\operatorname{erfc}^{-1}(2\epsilon) - \operatorname{erfc}^{-1}(2\eta)] [\operatorname{erfc}^{-1}(2\epsilon) + \operatorname{erfc}^{-1}(2\eta)] \quad (8.10)$$

Equation (8.9) shows that the number of ' $\sigma$ ' separation ( $k$ ) only needs the ID and mis-ID probabilities. Hence, changing the likelihood ratio threshold ( $R_{cut}$ ) changes ID/mis-ID power in a way that the separation remains constant. Figure 8.2 give a better idea of the variations of the ' $\sigma$ ' separation in the (mis-ID, ID) plane.

Two additional important point one have to remember. First: in case of combining information from several subsystems or measurements the total  $LH_{tot}$  is a product of likelihoods  $LH_i$ . Second: in reality the PDF function can be more complicated than simple Gaussian than in order to estimate ID efficiency and Mis-ID probability one can use Monte Carlo method [121, 122], which are very efficient for this kind of problem.



# Acknowledgements

My supervisor Achille Stocchi and co-supervisor Nicolas Arnaud deserve very warm words for giving me useful advises and for paying continuous attention to my scientific and non-scientific problems.

I gratefully acknowledge Jaroslav Va'vra and Oleg Bezshyyko who agreed to be the referees of this thesis. I thank Laurent Serin, Dominique Breton, Philippe Schune and Jean Sebastien Real for accepting to be part of the jury for this thesis.

I would like to thank all the *SuperB* members, especially Evgeniy Kravchenko, Sergey Kononov, Alexey Onuchin, Alexander Rakitin, Eugenio Paoloni, Rolf Andreassen, Andrea Di Simone, Douglas Roberts and David Aston for their useful advises and fruitful discussions during workshops.

Many thanks to the LAL B-physics community: Anne-Marie, Emi, Marie-Helene, Benoit, Sergey and many others.

During writing my thesis I worked in collaboration with LAL Instrumentation team and therefore I would like to thank Veronique Puill, Cyril Bazin, Nicoletta Dinu, Jean-Franois Vagnucci, Chamaut Vincent and others.

A lot of thanks to LAL electronics team and in particular to Dominique Breton and to Jihane Maalmi Di Bello. We spent wonderful time in San Francisco, it was great to hang out with you ;-).

My friends or BEER-friends :-) these messages are for you people!!! Nejc<sup>1</sup> and Michelle (thank you for Wednesday morning Vodka day), Andrey (it was very nice to spend 4 years together in same 'boat', finally you make me believe that not all people from Moscow are \*\*\* ;-)), Victor (thank you for good evenings in La Pacaterie) & Victor Kopp (thank you for Opeth and very nice Summer Holiday 2010), Lesha<sup>2</sup> (thank you for Absinthe party), Aurelien (I am not ashamed of what happened in Ukraine :-) I am glad that we spend this nice time together), Alejandro (thank you, man, for teaching me how to dance at night at SLAC :-) sorry but I need to thank you :-))), Nicolas (red tea at two o'clock at night at LAL... thanks for the company :-) ).

---

<sup>1</sup>Do you know the only person who can beat Chuck Norris and Bruce Lee simultaneously? If not, just ask me :-).

<sup>2</sup>Your are the only who survived after Absinthe party – now to get the Ph.D is just one step more.

Lots of thanks to my friends around the world who partly became virtual but yet very close: Dana, Vasja, Misha, Vitalik, Anton, Katja, Lena, Oksana.

My Ukrainian buddies: Katod, Chyzh, Dismal, Boroda, Sasha, Liza, Lena Nevinchana, Valentynka – you are the best of the best friends which I will never forget and probably will never find better than you. I miss you every single day and hope you miss me too :-). Your help in writing this thesis is just like dark matter – can not be seen but can be felt.

It is a pleasure for me to say “thank you very much” to my school teacher of physics Jaroslav Filimonovych and his son Volodymyr. These guys always inspired me and made me aware of the beauty of science.

I thank you Ira<sup>3</sup> and Slava<sup>4</sup>, for all of your support and for being with me during not simple moments of my life here in France.

I want to give special thanks to my mother, father and sister, who helped me very much in this PhD-adventure.

This thesis was really supported by all the people mentioned above and many others who deserve to be mentioned but somehow disappeared from the list :-(. Thanks to all of you!

---

<sup>3</sup>Could you please practise a little bit more in monopoly ;-), so then i can use at least half of my power :-))).

<sup>4</sup>Thank you for stopping me to talk about uncle Beri... and uncle Sta.... :-).